A STATIC MODEL OF HIGH GRADIENT MAGNETIC SEPARATION

by

© Jan Edward Nesset

A Thesis Submitted to the
Faculty of Graduate Studies and Research
in Partial Fulfilment of the Requirements for the Degree of
Master of Engineering.

Department of Mining and Metallurgical Engineering
McGill University
Montreal, Canada

March 1980

HE who binds to himself a joy
Does the winged life destroy;
But he who kisses the joy as it flies
Lives in eternity's sun rise.

'Eternity'

by William Blake

ABSTRACT

A fundamental physical model of the fully loaded condition of particle accumulation on cylindrical wires occurring in high gradient magnetic separation (hgms) is developed. Magnetic, fluid shear and gravity forces are included in the analysis. The approach is unique in that Blasius-type fluid shear on particles at the bottom of a changing boundary layer is considered.

Magnetically, the model allows for the more complex case of variable magnetic susceptibility as typified by the canted-antiferromagnetic behavior of hematite. The Frantz Isodynamic Separator is shown to be well suited for generating this complex susceptibility information.

The model is verified against the photographic evidence of buildup shapes of Friedlaender et al. for $Mn_2P_2O_7$ as well as by comparison with the measured recovery of hematite, chalcopyrite and sphalerite in an hgms batch separator employing a stainless steel expanded metal-type matrix.

A powerful development of the model is that loading (volume of accumulated material per unit volume of matrix) is uniquely defined by a dimensionless group, called the loading number, N_L. From direct measurement N_L proved superior to the dimensionless group proposed by Watson, $\frac{V_M}{U_\infty}$, as a measure of loading.

RESUME

Un modèle physique fondamental de condition de chargement "pleine capacité" pour l'accumulation de particules sur des fils cylindriques, se produisant lors de la séparation magnétique à gradient élevé (hgms), y est développé. Incluses dans cette analyse sont les forces; magnétiques, de cisaillement causé par le fluide et de gravité. L'approche est unique en son genre dû au fait que, le cisaillement de type 'Blasius' sur les particules dû au fluide a l'extrémité inférieure lors d'un changement frontalier de couche, entre en considération.

Magnétiquement, le modèle tient compte des cas plus complexes de susceptibilité magnétique variable typiquement représenté par le comportement "incliné-antiferromagnétique" de l'hématite. Le "Franz Isodynamic Separator" s'est montré des plus aptes à fournir cette complexe information de susceptibilité.

Le modèle est vérifié en le comparant aux preuves photographiques des formes de l'accumulation par Friedlaender et al. pour le $Mn_2P_2O_7$, tout comme par comparaison aux recouvrements mesurés pour l'hématite, la chalcopyrite et la sphalérite dans un hgms à séparation discontinue employant une matrice de métal déployé en acier inoxydable.

La puissance du modèle réside dans le fait que le chargement (volume de matériel accumulé par unité de volume de matrice) est défine uniquement par un groupe sans-dimension appelé nombre de chargement, N_L. Basé sur des mesures directes, N_L s'est avéré supérieur au groupe sans-dimension proposé par Watson, $\frac{V_M}{U_\infty}$, comme mesure de chargement.

ACKNOWLEDGEMENTS

The author wishes to express his sincerest gratitude and appreciation to Dr. J.A. Finch for guidance, encouragement and unfailing support throughout the course of this research.

Thanks are also due the staff, fellow graduate students and technicians of the Department of Metallurgical Engineering for their help on numerous occasions.

The assistance of Don Wilford (McGill) and Dr. J. MacKinnon (Concordia University) in obtaining magnetometer data is gratefully acknowledged as is the help of Alan Selby (McGill) with some mathematical complexities.

Finally, the loan of magnets from CANMET (Ottawa) and SALA Magnetics (Boston) plus the financial assistance of the Steel Company of Canada (Fellowship), the Natural Sciences and Engineering Research Council and Quebec Iron and Titanium Corporation (Fellowship) helped make this work possible, and are gratefully acknowledged.

TABLE OF CONTENTS

NOMENCLATURE

CHAPTER II

A	data fitted constant in buildup rate equation
a	bare wire radius
a_n	radius to n^{th} particle layer
b	particle radius
C_D	drag coefficient
F	volumetric packing fraction
$F(V_M)$	function describing the cumulative weight fraction of particles with magnetic velocity less than V_M
f	capture efficiency
f_s	fluid shear adjustment factor
f_{max}	maximum buildup to wire volume ratio
g	coefficient in Friedlaender drag equation
H_a	applied magnetic field
K	Stokes number $= 2b^2\rho_p U_\infty/9a\eta$
K_f	universal fibre parameter
L	matrix length
L/L_M	ratio of loading to maximum possible wire loading
M_w	wire magnetization
M_s	wire saturation magnetization
N_i	number of particles entering separator
N_o	number of particles leaving separator
n	counter or exponent
P	particle retention probability
R	particle accumulation radius
R_a	relative particle accumulation radius $= R/a$
R_{a_s}	saturation (i.e. maximum) relative particle accumulation radius
R_c	wire capture radius $\div a$
Re_p	particle Reynolds number
S	diameter of major fibre axis for non-cylindrical fibres
t	time
U	outer (potential) flow velocity
U_∞	free stream velocity
V	buildup volume
V_M	magnetic velocity $= 8\pi b^2\kappa H_a M_w/9a\eta$
V_w	wire volume
α	coefficient in drag equation
δ	nominal boundary layer thickness
δ_{99}	boundary layer thickness over which flow has regained 99% of outer flow velocity
η	fluid viscosity (absolute), cm^2/s
κ	particle (volume) susceptibility
ξ	capture radius for mechanical entrapment
ρ_f	fluid density
ρ_p	particle density
$>$	greater than
$<$	less than

CHAPTER III

A	scalar potential energy function (Equations (3.9,10,11) only)
A	field perturbation term $= 2\pi M_w/H_a$ for cylinders perpendicular to H_a
a	bare wire radius
a_n	radius to n^{th} particle layer
A_f	fractional cross-section of flow area
A_x	cross section of flow area
B^x	magnetic induction, gauss
B'	Blasius summation of θ terms
b	particle radius
C	constant in simplified force balance (Equation (3.2-8))
dms	mass of material retained on a segment in a time increment dt
F_M	magnetic force
F_{r_M}	radial component of F_M
F_{θ_M}	tangential component of F_M
F_G	gravitational force
F_{r_G}	radial component of F_G
F_{θ_G}	tangential component of F_G
F_D	fluid drag force
F_B	buoyancy force
$F_{\theta_{net}}$	net tangential force
$F_{r_{net}}$	net radial force
f	field parameter
f_b	fractional area of particle shear
g	gravitational constant
H	magnetic field, oersteds
H_a	applied magnetic field
H_r	radial component of H
H^r	tangential component of H
H_D	demagnetizing field $= NM_w$
h_c	coercive force, oersteds
K	empirical constant in wire magnetization (Equation (3.1-19))
$L(n)$	mass loading of n^{th} segment
L_m	maximum loading (mass) per unit length of wire $(= \gamma_m)$
L_{max}	maximum loading of segment
ℓ	inter particle layer distance (buildup model)
ℓ	distance between magnetic poles (magnetic theory)
ℓ	characteristic body dimension (fluid mechanics)
ℓ	length of wire per matrix screen
M^w	magnetization, emu/cm^3
M_p	particle magnetization, emu/cm^3
M_w	wire magnetization, emu/cm^3
M_{Pe}	effective M_p
M_o	spontaneous magnetization, emu/cm^3
m	magnetic moment, emu
m_r	residual magnetization, emu/cm^3
m_w	mass of screen
N	demagnetization factor

N_G	dimensionless ratio of magnetic-to-gravity force $= 2\sqrt{2}H_a^2\kappa A/a(\rho_p - \rho_f)g$
N_L	dimensionless ratio of magnetic-to-fluid shear force $= 2bH_a^2\kappa A/\rho_f U_\infty^{3/2}\nu^{1/2}a^{1/2}$, the 'loading number'
n	counter or exponent
p	fluid pressure
p_1, p_2	magnetic pole strength (unit)
r	particle accumulation radius
r	distance between poles p_1, p_2
r_a	relative particle accumulation radius $=$ r/a
r_{a_s}	saturation (equilibrium) r_a
r_n	radius to n^{th} particle layer
R_c	capture radius of wire ÷ a
R_{c_i}	initial R_c
Re^i	Reynolds number $= \rho U' \ell/\nu$
Re_p	particle Re
Re_w	wire Re
s	number of screens per segment
s_w	inter wire distance on screen
t	time
U	outer stream fluid velocity
U'	relative velocity (between particle and fluid)
U_r	radial component of U
U_θ	tangential component of U
U_∞	free stream velocity
u	velocity in y-direction
V	particle volume
V_B	nominal buildup volume
V_M	magnetic velocity $= 4b^2\kappa H_a^2 A/9a\eta$
v	velocity in x-direction
α	driving function in capture radius equation
α_A	Akoto's α
α_L	Luborsky's α
β	geometric correction factor for screens
γ_m	(mass) loading, g of particles/g of fully loaded wire
γ_V	(volume) loading, cm^3 of particles/cm^3 of fully loaded wire $= \gamma_m \rho_w/\rho_p$
∇	gradient operator
δ	nominal boundary layer thickness
δ_{99}	δ over which flow has regained 99% of U
ε	packing fraction
η	fluid viscosity (absolute), g/cm-s
θ	angle from front stagnation point, (degrees), radians
θ_c	minimum critical angle, (degrees), radians
κ	particle (volume) susceptibility, emu/cm^3-Oe
κ_e	effective κ, emu/cm^3-Oe
κ_p	particle κ, emu/cm^3-Oe
κ_m	medium κ, emu/cm^3-Oe
κ_∞	susceptibility extrapolated to infinite field strength (field dependent susceptibility)

μ	magnetic permeability
ν	fluid viscosity (kinematic), cm^2/s
ξ	transformation variable used in stream function
ρ	density
ρ_p	particle density
ρ_f	fluid density
Σ	summation operator
σ	magnetization, emu/g
σ_o	spontaneous magnetization, emu/g
τ	shear stress, dynes/cm^2
τ_o	shear stress at solid "wall", dynes/cm^2
ϕ	function
χ	susceptibility (mass), emu/g
χ_∞	particle susceptibility extrapolated to infinite field strength (field dependent susceptibility)
ψ	stream function
$\dot{m}$	particle flux rate entering segment, particles/s
$\dot{m}_o$	particle flux rate entering separator, particles/s

CHAPTER IV

D	solenoid diameter
d_a	actual cyclosizer cone cut-off diameter
d_∞	nominal cyclosizer cone cut-off diameter
$d_{g.m.}$	geometric mean diameter
d	diameter
f_1, f_2, f_3, f_4	cyclosizer correction factors
H	magnetic field strength, kOe, Oersteds
dH/dX	average field gradient, kOe/cm
H_{max}	maximum H in pole gap, kOe
I, i	current, amperes
I_{50}	current at which 50% of feed to Frantz Isodynamic reports to the magnetics chute, amperes
I_c	current applied to Hall crystal
K_1	crystal calibration constant for Hall equation
L	solenoid length
m	particle mass, g
n	number of coil windings
$\hat{n}$	normal unit vector
R_H	Hall constant, volt-cm/ampere-Oe
R	electrical resistance, ohms
r	length-to-diameter ratio of spheroids
t	Hall crystal thickness, cm
V_H	Hall potential, volts

CHAPTER V

f	field parameter
$\bar{f}$	integrated (volume) field parameter
γ_κ	loading determined using field dependent susceptibility
γ_{κ_e}	loading determined using effective susceptibility
γ/γ_m	ratio of loading to maximum possible wire loading = L/L_m

GLOSSARY

CHAPTER II

Trajectory models - models which predict separator recovery from mathematical descriptions of particle behavior in the viscinity of magnetized wire(s) based on the differential equations of particle motion.

Buildup models - predict hgms recovery based on static or probabilistic analyses of forces for particles assumed to have already arrived at the wire/buildup.

Magnetic velocity (V_M) - can be considered as the terminal velocity achieved by a spherical particle under the influence of a magnetic force and purely Stokesian fluid conditions.

Capture radius (R_c) - or capture cross-section, is the limiting radius or area about the wire from which all particles are captured, as determined from trajectory models.

Potential flow - mathematical analysis of flow which considers only incompressible, frictionless fluids. Approximates the real flow of many fluids and situations at distances well removed from solid boundaries.

Viscous flow - analysis which considers fluid stresses to be related to the velocity gradients. Approximates real flows near solid boundaries and at low Reynolds number.

Equilibrium or saturation buildup profile - the ultimate outline of particle buildup about a wire representing a stable balance of the acting forces.

Front or upstream buildup - particles collecting on the upstream side of a wire.

Back or downstream buildup - particles collecting on the downstream (wake) side of a wire.

Loading - the process of particle onto wire/buildup accumulation, often referred to in the context of "fully loaded" wires, i.e. the maximum mass (γ_m) or volume (γ_v) of particles capturable by a unit mass or volume of wire under the specified conditions.

CHAPTER III

Magnetization (M) - is the magnetic moment/unit volume of a substance. Materials are characterized magnetically according to their magnetization behavior as a function of some variable, for example, field strength or temperature.

Diamagnetic - materials have a small but negative linear response of magnetization to increasing field.

Paramagnetic - substances exhibit positive linear magnetization with increasing field.

Anti-ferromagnetic - materials are similar to paramagnetics aside from showing a reversed temperature dependence of susceptibility below a critical value called the Néel temperature.

Ferro, ferrimagnetics - have a large and non-linear magnetization which is also characterized by the phenomena of saturation and hysteresis.

Canted antiferromagnetics - are essentially anti ferromagnetics with a small ferromagnetic contribution dependent on the crystal orientation relative to the field.

Magnetic susceptibility (κ) - the way in which the magnetization (M) varies with field (H). κ is of special interest to the engineer as it shows the magnetic responsiveness of a material to the field.

Perturbation term (A) - is a field dependent parameter describing the extent to which a magnetic material disturbs the background field. Other factors effecting the magnitude of A are body geometry, field orientation and the magnetic properties of the material itself.

Stagnation point - in fluid mechanics, a mathematical point at which a streamline begins or ends. For the present case of a cylindrical rod in fluid cross-flow, the stagnation points occur at the solid/fluid boundary along the axis of symmetry in the flow direction.

Blasius solution - An analytical solution to the boundary layer equations available for certain cases of quite symmetrical flows. These solutions are exact in that they provide accurate (i.e. not averaged) descriptions of flow throughout the boundary layer.

Shear stress at the 'wall' (τ_o) - those stresses between the elements of fluid trapped next to a solid boundary and those elements moving in the adjacent layer. In the developed model, the outermost layer of mineral particles is considered to be the 'wall'.

Minimum critical angle of buildup (θ_c) - the angle measured from the front stagnation point, beyond which there exists either a repulsive radial component of net forces acting on a particle, or insufficient net attractive tangential force to keep the particle from being swept away. θ_c changes with distance away from the wire, eventually tending to zero.

Loading number ($N_L = 2bH_a^2\kappa A/\rho_f U_\infty^{3/2}\nu^{1/2}a^{1/2}$) - a dimensionless ratio of magnetic-to-fluid shear forces for a particle of radius, b, residing at the bottom of the boundary layer on a wire of radius, a, in a crossflow, U_∞. In the simplified model developed, the maximum loading (γ_v) is characterized by N_L alone.

Screen - ideally refers to a square weave of cylindrical wires and in practical terms is used to describe an expanded metal lath; a widely used matrix medium in mineral processing applications of hgms.

Matrix - the particle collection medium of hgms devices, be it expanded metal, steel wool, thin rods, etc.

Packing fraction (ε) - the fraction of the apparent or nominal buildup volume actually occupied by particles. Ideally, for close packed spheres $\varepsilon \approx 0.7$, however, the actual packing fraction for real minerals will be somewhat less.

Driving function (α) - the mathematical description of how capture radius decreases from the initial (bare wire) value as loading of the wire progresses, i.e. $R_c = R_{c_i}\alpha$ where R_{c_i} is the initial value of R_c.

Geometric correction factor (β) - a factor for screens which accounts for overlapping capture cross-sections of the individual wires as well as the loss of efficiency whenever the wires themselves overlap. The β correction is applied to the total length of wire per screen, ℓ_w.

CHAPTERS IV AND V

Magnetometer - strictly speaking, any device which measures the magnetic response of a material. In this study, magnetometer generally refers to devices, such as the Foner vibrating sample magnetometer, which are used for determining the magnetization of a bulk sample through indirect measurement and/or calibration with a standard. In contrast, the Frantz Isodynamic separator deflects an individual particle one of two ways, depending on its level of magnetization, thus permitting a direct calculation of the relevant property through a force balance.

'Effective' susceptibility (κ_e) - for field dependent susceptibility materials (e.g. canted antiferromagnetics) κ_e is the value of κ computed for an average (integrated) value of the field throughout the buildup volume. It gives the same predicted loading as when a unique value of κ for every particle location is computed.

'Magnetically cleaned' samples - real mineral samples carefully prepared on the Frantz Isodynamic separator so as to isolate fractions with very uniform magnetic properties (i.e. susceptibility) for controlled hgms study.

Field amplification - an increase in the background field near one wire due to the close proximity of neighbouring wires. This effect manifests itself in real matrices but has largely been ignored in the development of the field equations which apply to single wire cases.

LIST OF FIGURES

LIST OF TABLES

I. INTRODUCTION

High gradient magnetic separation (hgms) is now recognized as one of the major industrial advances in magnet technology since electromagnetic forces were first put to use separating materials. Already well established in applications such as kaolin processing[1,2], steel mill waste and process water filtration[3,4], such devices are on the threshold of enlarging their stature in mineral beneficiation. Potential uses appear to be the treatment of taconitic iron ores[5], the production of high purity wolframite concentrate[6] and the purification of industrial minerals by removal of the staining minerals.[7] Other possible applications are pyrite removal from coal[8], uranium upgrading[9], and pyrite and chalcopyrite recovery as impurities from molybdenite concentrate.[5]

At present, batch type hgms devices are employed. In the kaolin industry, capacities up to 20 TPH are reported.[10] Batch devices are well suited to feeds where the magnetic fraction is small but in many of the potential mineral processing applications this is not the case and continuous hgms devices are required. The first application of a full-scale continuous hgms device seems near.[10]

The advantages of the hgms design over prior art technology are twofold.[11] Firstly, the iron-clad solenoid (Figure 1-1) permits the uniform magnetization of a large throughput volume thus becoming attractive for high capacity applications. Roughly speaking, costs will escalate linearly with increased machine size while throughput

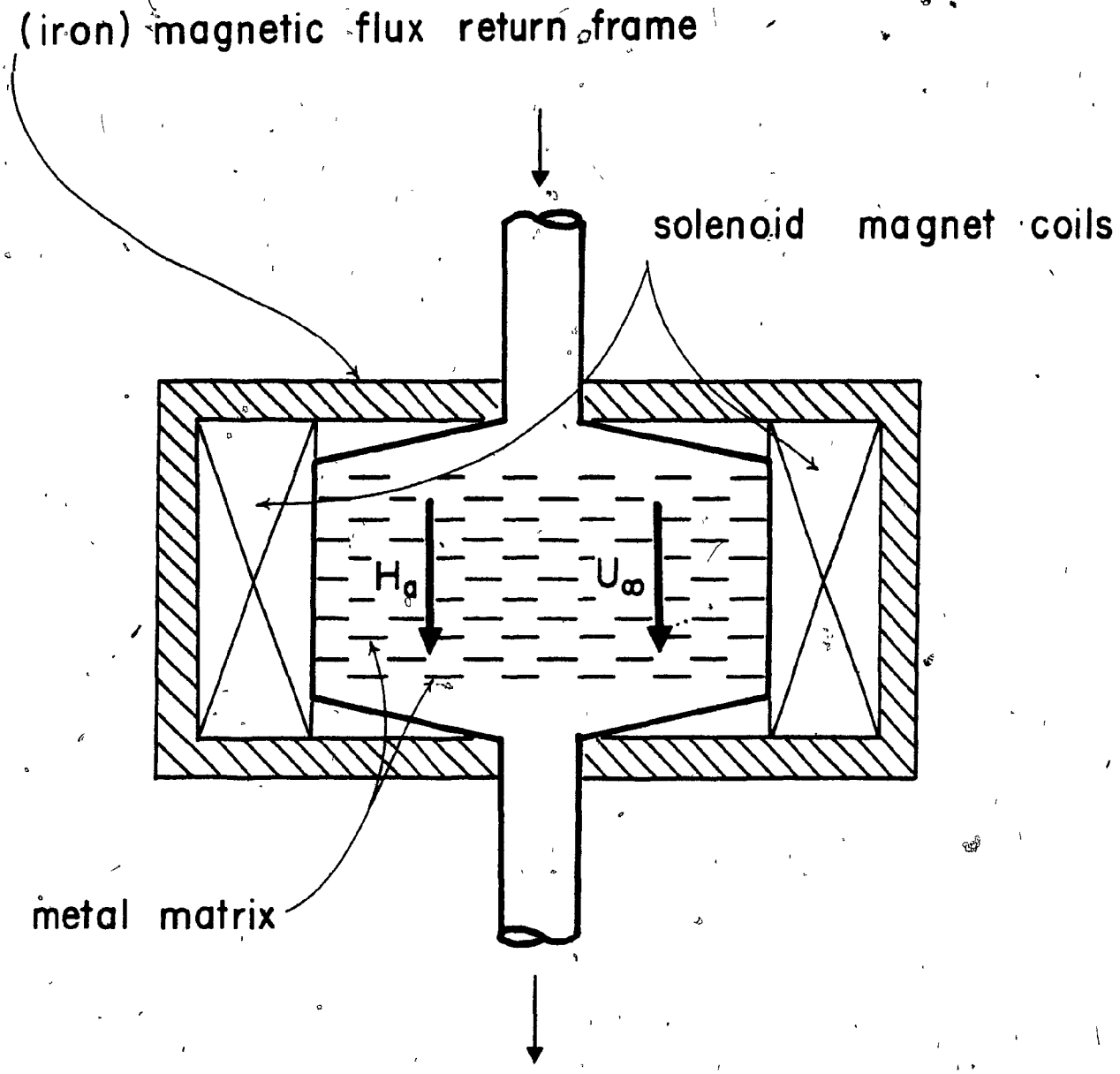

1-1 Iron clad solenoid design of hgms devices.

will go up as the square of the size.[12] Secondly, a solenoid-type design allows for close control over the competing forces in the working volume due to the large scale uniformity of field and flow conditions throughout.[13]

Accompanying the equipment development extensive mathematical modelling of the process has been undertaken. The ability to select equipment and predict the performance is clearly of great value. In some respects, the fact that the process is based on quite well defined forces (i.e. magnetic, fluid drag,gravity) lends hope to the eventual success of fundamental models. This is in sharp contrast to, say, flotation.[14]

The fundamental models can be conveniently divided into two areas; viz. trajectory (or dynamic) and build-up (or static) models. A complete description will require a combination of approaches.

Numerous trajectory models have been developed. They involve predictions of the limiting trajectories, or capture radii, of small magnetized particles as they are subjected to localized field and flow perturbations caused by the ferromagnetic matrix wires.

Less work has been done on modelling the buildup of these particles once they have arrived at the wires. This process is important, however, in that the ultimate buildup will determine the maximum loading of the wire and hence the total amount of material recoverable. Considerations of particle accumulation are also important in trajectory modelling where the changing hydrodynamic shape of wire plus particles is required.

Three principal orientations of field, flow and wire are of interest in hgms. These have been designated as the transverse (case A), the longitudinal (case B) and the axial or parallel (case C) configurations and are shown in Figure (1-2). The axial case has received particular attention for possible filtering of deoxygenated red blood platelets from whole blood since this orientation appears to minimize platelet damage.[15] This investigation concerns itself with the configuration receiving the major industrial and theoretical attention at present, namely case B.

The approach taken in the modelling has been to consider magnetic, fluid shear, and gravitational forces on particles at the bottom of the fluid boundary layer as it develops on the upstream side of a cylindrical wire. Downstream buildup is not considered in the analysis. Once predictions of equilibrium (i.e. maximum) buildup are made for a unit length of wire, the analysis is extended to predict recovery on a single wire screen and finally to a series of stacked screens or 'matrix'. This then allows the overall performance of a separator to be predicted.

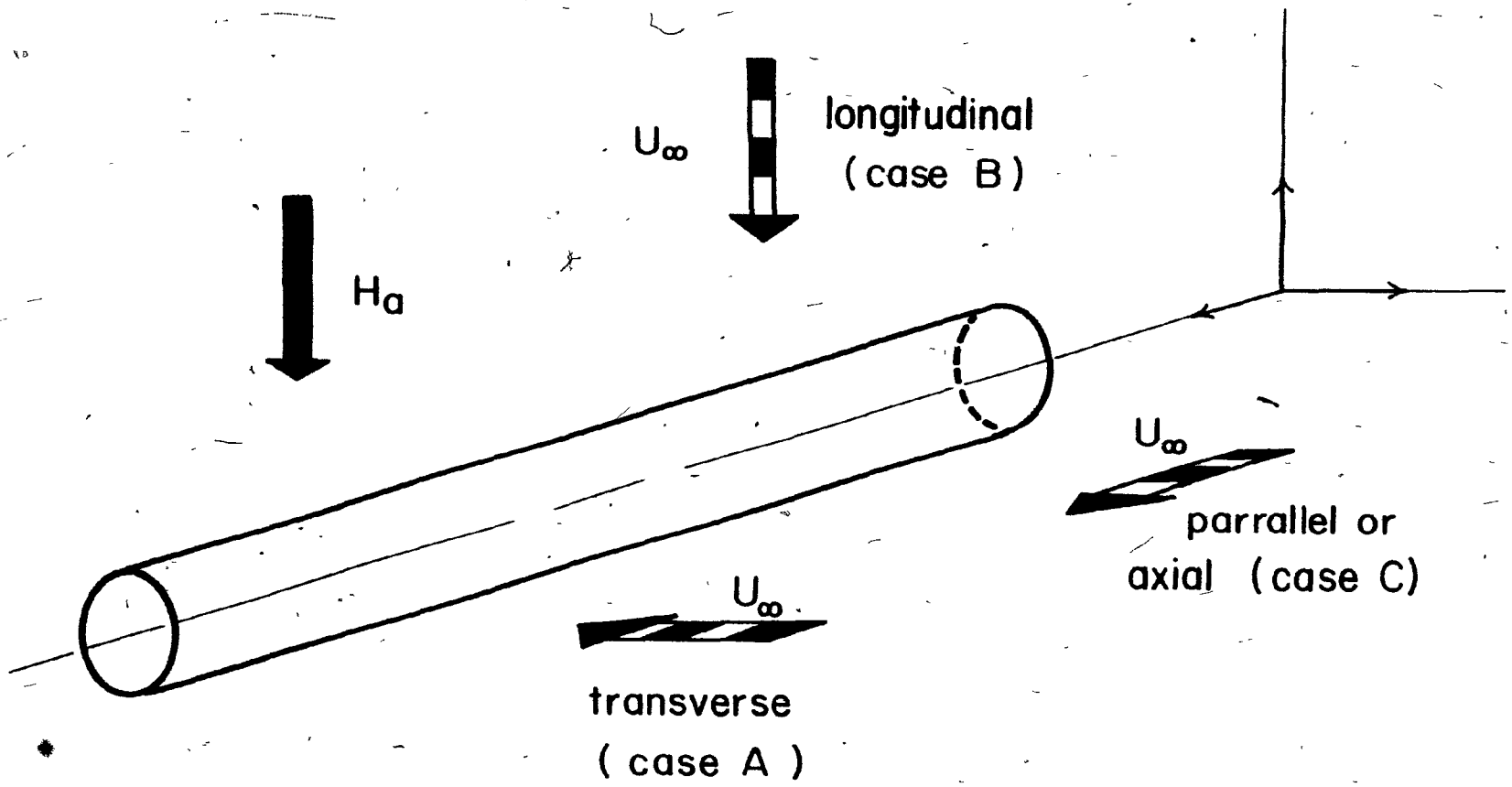

1-2 Principal orientations of hgms.

II. PREVIOUS WORK

2.1 Trajectory Models

In his mathematical study of electrostatic separation, Zebel[15] provided the framework subsequently used in the trajectory models of hgms. His analysis of particle motion under the influence of fluid and electrical forces was readily adapted by Watson to considerations of magnetic rather than electrostatic interactions.[17] This is possible because of the analogous fashion in which fields of magnetic and electrical energy will interact with a body of suitable material to create a dipole. In the vicinity of such a material, through the contribution of its own dipolar field, highly localized disturbances are created in the potential energy net. A particle of sufficiently exploitable properties (i.e. electrical conductivity, magnetic susceptibility) travelling near the disturbance may experience very large tractive forces provided its dimensions are adequately matched to the size of the field perturbation.

By considering magnetic and fluid drag effects only (gravity and inertia neglected) Watson found the trajectories of paramagnetics in the vicinity of a highly magnetized cylindrical ferromagnetic wire to be uniquely dependent on the parameter $\frac{V_M}{U_\infty}$. The 'magnetic velocity', $V_M = \frac{8\pi b^2 \kappa H_a M_w}{9a\eta}$, can be thought of as the terminal velocity a spherical particle would achieve in a stationary fluid due to the magnetic field alone, assuming Stokesian viscous drag. U_∞ is the undisturbed fluid velocity far from the wire.

In order to obtain exact solutions, Watson (and Zebel) chose to neglect the short range magnetic force term which becomes important very near the wire. Field strengths (H_a) in excess of those required for saturation magnetization (M_s) of the wire (i.e. $H_a > 2\pi M_s$) also simplified the resulting calculations since the wire magnetization becomes constant.

The concept of a limiting particle trajectory is used in defining a unitless capture radius, R_c, such that all particles passing within a capture cross-section $2R_c a$, where a refers to the wire radius, will be attracted toward and ultimately captured by the fibre. R_c is determined at a location sufficiently upstream from the wire to be magnetically and hydrodynamically undisturbed by the wire's presence. The dependence of R_c on $\frac{V_M}{U_\infty}$ as determined by Watson for bare wires and potential flow is shown in Figure (2-1).

To extend this single wire model to apply to an entire separator, a unit element of thickness, d_x, and volumetric packing fraction F, is integrated over the length, L, of the matrix. By assuming that for a randomly packed steel wool matrix 2/3 of the fibres would be correctly oriented (i.e. perpendicular to the field vector) Watson expressed the ratio of particles leaving a separator to those entering as:

$$\frac{N_o}{N_i} = \exp\left(-\frac{4FR_cL}{3\pi a}\right) \qquad (2\text{-}1)$$

The model is of restricted applicability to actual systems because it considers clean fibres only and fails to account for a

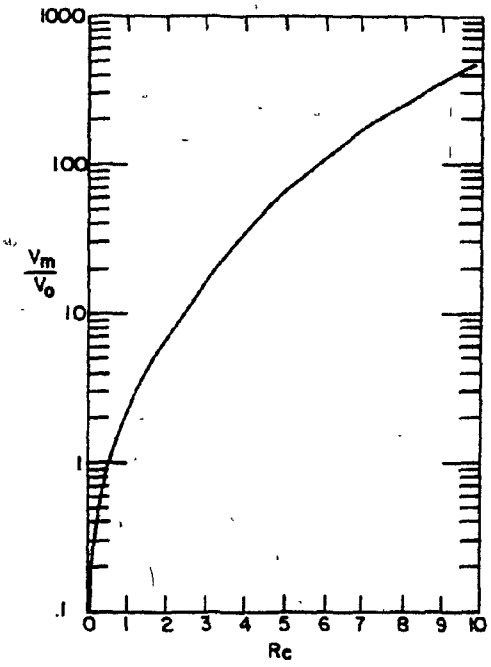

2-1 Watson's dependence of R_c on $\frac{V_M}{U_\infty}$ $(= \frac{V_M}{V_o})$.

decreasing R_c due to particle buildup. This decrease is a function of both time and position in the matrix. The usefulness of the trajectory approach to modelling hgms and the significance of $\frac{V_M}{U_\infty}$ and R_c have received much support from subsequent investigators.[18,19]

An extension of Watson's method to include the effects of buildup on particle trajectories and R_c has been performed by Luborsky and Drummond.[20] Figure (2-2) shows this relationship for increasing numbers of particle layers, n. It is evident that the capture cross section decreases but remains proportional to $\frac{V_M}{U_\infty}$ in the presence of retained material. Also shown is the case of magnetically unsaturated wires ($H_a = 2\pi M_s$ assumed) for which a numerical integration technique was required to solve the equations of motion. The curves suggest that for equivalent lower range $\frac{V_M}{U_\infty}$, a fibre at or below magnetic saturation will have a greater capture radius than will a fibre at fields well in excess of that required for saturation.

By assuming 1/3 of ribbon-like fibres (felt to geometrically more closely resemble the cross-section of steel wool strands than a cylindrical approximation) to be correctly oriented for capturing particles, Luborsky and Drummond write the total fractional recovery, R, of paramagnetics as

$$R = 1 - \exp\{-\frac{fFL}{3S}(R_c + \xi)\} \qquad (2\text{-}2)$$

where S is the diameter of the major fibre axis, and F, L and R_c are as per Watson's Equation (2-1).

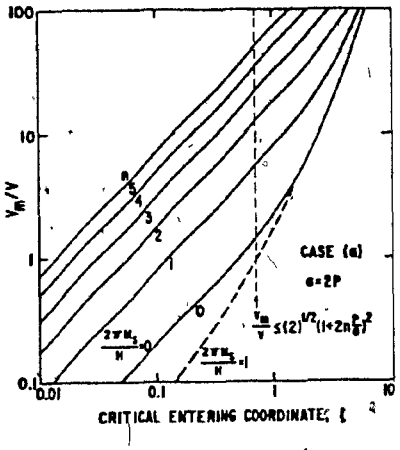

2-2 Luborsky and Drummond's effect of increasing particle layers (n) on R_c $(= \zeta)$ as a function of $\frac{V_M}{U_\infty}$ $(\frac{V_M}{V})$.

In order to permit comparison with an available body of $CuO-Al_2O_3$ experimental work they introduced the parameters f and ξ, where f is termed the 'capture efficiency' and represents the fraction of total fibres which perform as described in the model, and ξ is a capture radius for mechanical entrainment of particles. Both f and a separate constant in the expression for ξ were data fitted to yield the best possible agreement between model and experiment. A value of $f = .153$ produced a reasonable fit. The model predicted CuO recovery well but consistently overestimated CuO grade.

The approach of Luborsky and Drummond has been criticized in part by Watson[21] on account of their capture criterion and because the stability of the accumulated particles on the wire was not considered. In later work[22] Luborsky and Drummond do consider the stability of accumulated material as well as an averaged boundary layer effect. This results in a small improvement between experiment and theory. They reported the data fitting to be insensitive to the value of f chosen provided that an adjustable parameter was introduced into the expression for viscous drag in the boundary layer.

The different approaches to particle buildup will be covered in detail in the section on buildup models but the general conclusion is that for $H >> 2\pi M_s$ the limiting volume of material captured is dependant upon $\frac{V_M}{U_\infty}$ alone. To support this result Watson cites experimental evidence from clay systems (at high $\frac{V_M}{U_\infty}$) where an up to tenfold change in field strength and flow velocity varied the $\frac{V_M}{U_\infty}$ by a factor of 20.[21] The limiting amount of magnetics captured remained linearly dependent on $\frac{V_M}{U_\infty}$ with a correlation coefficient of 0.95 for 30 measurements.

A recent investigation by Cummings, Prieve and Powers[23] analyzed trajectories assuming creeping rather than potential flow behavior of the fluid medium. They found that capture cross-sections were considerably reduced since the particles feel the hydrodynamic effects of the wire much further upstream. In the vicinity of the wire, the no-slip criterion at the cylinder surface which is associated with creeping flow is physically more satisfying than the inviscid approximation. Potential flow is likely to be better at distances further away and for higher (flow) Reynolds numbers.

In order to account for both viscous and inertial fluid body forces at low to moderate Reynolds numbers, Clarkson, Kelland and King[24] superimposed a boundary layer on the solution for potential flow for elliptical fibre shapes. The model treats magnetically saturated wires as well as non-linear magnetization response to applied field for less than saturated wires. Gravitational and near-field magnetic effects are also included in the numerical calculations of particle trajectories.

Recovery is defined, as per Watson (Equation (2-1)), with a 'universal fibre parameter', K_f;

$$\% \text{ Recovery} = 100\left(1 - \exp \frac{(-2K_f F R_c L)}{\pi ab'}\right) \qquad (2\text{-}3)$$

K_f allows for random fibre-fibre interactions and orientation effects much as Luborsky's f (Equation (2-2)), and $\pi ab'$ is the cross-sectional area of the fibre. The influence of particle buildup on fluid flow is achieved assuming a changing elliptical shape of buildup while the capture radius is allowed to exponentially decrease toward zero for fully loaded wires.

By isolating closely sized fractions of fairly pure hematite (α-Fe_2O_3) for which they had obtained accurate magnetization data, Clarkson et al. showed very good correlation between predicted and measured recovery. K_f was fitted as a function of the particle-to-fibre size ratio.[25] Values of K_f from .01 to .06 were obtained for particle-to-fibre ratios of roughly 1 to 0.1.

The results in Figure (2-3) led Clarkson et al. to conclude that, for their and similar systems, assumptions of potential flow alone (without the superimposed boundary layer) were acceptable for particle sizes greater than 5 μm provided that the fraction of mechanical entrainment was not large. Below this size the 'shielding' effects of the boundary layer on particles from the otherwise very large near-wall drag forces of potential flow become increasingly significant and should be included. Their work also suggested that for similar hydrodynamic conditions to those investigated (low to moderate Reynolds number), gravitational and inertial forces could be neglected for less than 30 μm diameter particles.

An additional aspect of the Clarkson and Luborsky models merits comment. The fitted parameters (including orientation assumptions) suggest that 94-99 percent of the stainless steel wool filaments in an hgms filter do not contribute to particle capture as modelled. A sufficiently satisfactory discussion of this has yet to be provided but it has been reflected upon by Drehmel and Gooding.[26]

In an elegant study, Simons, Lawson and Treat[18] examined the dynamics of particle attraction assuming potential flow about a

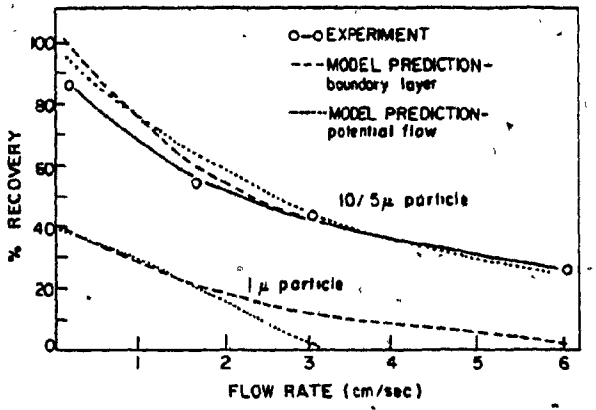

Hematite results: recovery versus flow rate, Particle size 10/5, applied field 1 kG, medium matrix.

2-3 Clarkson and Kelland's effect of boundary layer versus potential flow on recovery of hematite.

cylindrical wire. Included were inertial effects, gravity, as well as the consequences of the near-field magnetic force term. They established ranges of conditions for which it is permissable to neglect these considerations in calculations of R_c. Generally, for Stokes number, $K = \frac{2b^2 \rho_p U_\infty}{9a\eta}$ (a measure of particle inertia to viscous flow effects), greater than unity inertia should be accounted for while for K small (i.e. < 0.1) gravity can be neglected. Under conditions of $\frac{V_M}{U_\infty}$ below 10 and low K (say 0.1) inclusion of the short-range magnetic force term has a positive and increasing (with decreasing $\frac{V_M}{U_\infty}$) effect on the capture cross-section. Within the boundaries of these limitations, Simons et al. concluded that the relationships between R_c and $\frac{V_M}{U_\infty}$ developed by Watson and others were completely adequate.

In their mathematical study, Simons et al. also predicted the interesting occurrence of oscillatory particle trajectories (shown in Figure (2-4)) under conditions of both high $\frac{V_M}{U_\infty}$ and K such as might be experienced during hgms treatment of paramagnetic dusts in high velocity gas streams. This phenomenon has since been experimentally confirmed by them in a video recording of MnO_2 particles attracted by magnetized nickel wire in an air stream.[27]

Stekly and Minervini[28], in studying the shape effects of cylindrical and elliptical fibres on R_c, showed that the initial capture cross-section is determined by the projected frontal area of the wire and is largely independent of the aspect ratio of the major to minor axis (up to a ratio of approximately 4:1). However, bare wires with increasing aspect ratios but of constant volume produced a steady decline in the initial capture radius. Their results should enable

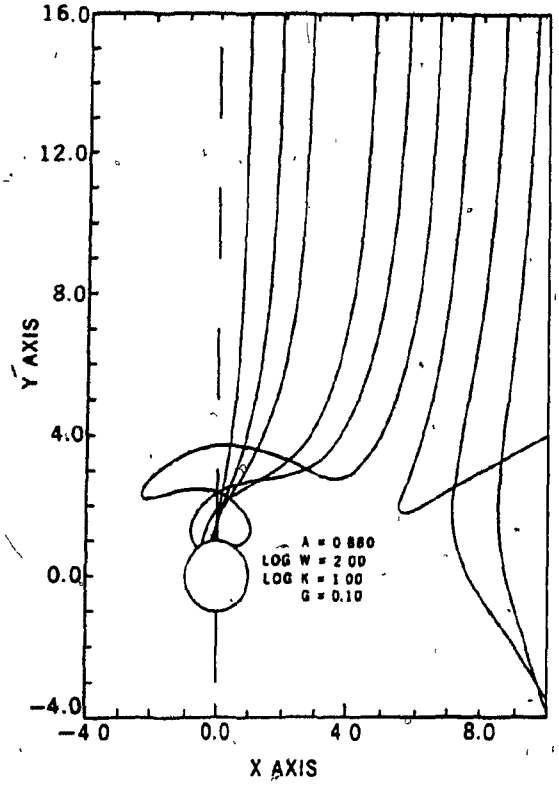

2-4 Predicted oscillatory behavior at high Stokes number (K) from Lawson et al.

the conclusions of studies on cylindrical wires to be more widely applied to other shapes of filamentary type matrixes since they suggest that only the wire dimensions perpendicular and not parallel to the field and flow significantly effect the capture cross-section.

2.2 Buildup Models

As discussed in the preceeding section on trajectory models, the use of single wire capture radii in predicting the performance of a large assemblage of filamentary stainless steel in hgms units requires rather hefty fitting factors to achieve compatability between theory and experiment. Efforts have also been directed toward relating the important system parameters to the maximum amount of material capturable on a single fibre. These are the so-called "buildup models"; some aspects of which have already been touched upon in reviewing the trajectory work of Luborsky and Drummond, Watson and Clarkson et al.

These two classifications (trajectory and buildup), far from being independent in an analysis of hgms, have usually been complementary in the modelling approaches to overall separator performance. Trajectory models provide initial capture cross-sections for a specified set of conditions and all particles entering the viscinity of the wire within this area are assumed captured. Buildup models then predict the profile of the accumulating material which in turn has a bearing on the hydrodynamics and hence (it is postulated) on the capture cross-section as seen by particles subsequently approaching the partially loaded wire. The second function of buildup models is to determine the maximum loading capability of a wire element, and hence the total mass recovery potential of hgms devices based on the limiting (or equilibrium) buildup profile.

Debate has focussed on both the profile of the accumulating material as well as the manner in which the capture radius, R_c, changes as loading progresses. Part of the problem has been the difficulty in obtaining experimental verification of buildup shapes[19], particularly for the configuration of greatest interest, longitudinal of case B.

Luborsky and Drummond

Early attempts at accounting for particle buildup involved guessing a suitable profile and then seeing the subsequent effect on calculations of particle trajectories and capture cross section. In their initial study[20], Luborsky and Drummond considered two possible fan-shaped geometries, shown in Figure (2-5), based, in part, on the observations of Himmelblau.[29] Case (a) fans out in a 90^o arc while case (b) assumes a narrower, blade-like buildup in which each layer holds the same number of particles. The fluid sees a changing radius, a_n, for each layer (n) of buildup for both cases given by:

$$a_n = a + 2bn$$

where a refers to the bare wire radius and b, the particle radius. They found that as loading progressed R_c decreased as:

$$R_c = \frac{V_M}{2U_\infty}\left(\frac{a}{a_n}\right)^2 \qquad (2\text{-}4)$$

for case (a) provided $\frac{V_M}{U_\infty} \leq 2^{1/2}\left(\frac{a_n}{a}\right)^2$ and as;

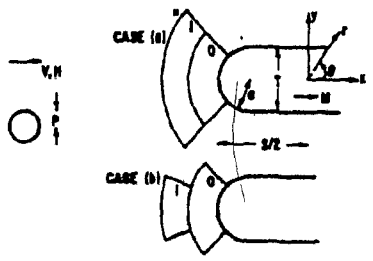

Schematic of ribbon-like fiber, infinite in z-direction, with approaching particle, showing two possible modes of build-up of particle layers; case (a) and (b).

2-5 Luborsky and Drummond's assumed fan-shaped buildup.

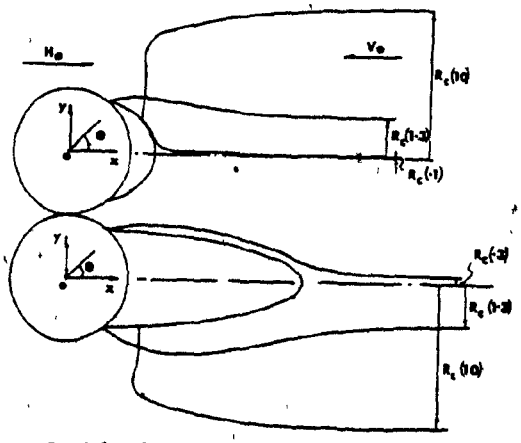

Particle orbits in the presence of captured material.

2-6 Watson's elliptical buildup assumption.

$$R_c = \frac{V_M}{2U_\infty}\left(\frac{a}{a_n}\right)^3 \qquad (2\text{-}5)$$

for case (b).

As noted previously in Section 2.1, Luborsky and Drummond used two data-fitted constants (viz. fibre efficiency and mechanical entrainment at zero field) to achieve a reasonable correlation between their filter model and the experimental $CuO\text{-}Al_2O_3$ recovery results of Oberteuffer.[30] For this they assumed the case (a) mode of buildup as no values of the adjustable parameters provided a good fit for case (b). Since the stability of the accumulated particles was not considered (an objection raised by Watson[21]), the maximum buildup profile and hence the fully loaded conditions of the filter could not be predicted.

After deciding that "the worst approximation in (their) modelling was the arbitrary configuration assigned to the buildup of particles on the fibers" Luborsky and Drummond[22] refined their earlier approach by considering a balance of drag and magnetic forces on the individual spherical particles within an average fluid boundary layer thickness.

On the upstream side of the ribbon-like wires the buildup was considered stable provided the magnetic force on a particle was radially attractive. Also, the magnetic force was required to exceed the Stokesian drag tangentially. The outer (potential) flow velocity, U, was reduced by a factor $\frac{b}{\delta_{99}}$ to account for a decreased velocity in the boundary layer of thickness, δ_{99}. Assumptions made were that $2b < \delta_{99}$ and that δ_{99} could be approximated, over the 90° region of interest,

as that given by Schlichting[52] for flow along a flat plate:

$$\delta_{99} = \pi^{1/2}\left(\frac{\pi a_n}{\mu\rho_f}\right)^{1/2}$$

Hence, the fluid shear force becomes proportional to:

$$b^2U^{3/2}\rho_f{}^{1/2}\eta^{1/2}$$

This is a different dependence than when Stokesian drag is considered alone, which has the shear related to:

$$bU\eta$$

Critical angles at which the components of tangential force exactly balanced were determined for each successive layer of particles.

The loci of these angles described the ultimate buildup profile of the captured material. The changing profile radius, a_n, was used to adjust the capture cross section of the wire for the incoming particles by the relationship for case (a) (Equation (2-4)).

Back capture was modelled in a similar fashion by balancing the radial components of magnetic and shear forces. The boundary layer thickness was approximated by that at the end of a flat plate. The results showed that a much greater amount of retained material could be expected downstream than upstream.

In fitting this revised model to the experimental recovery data of Oberteuffer a somewhat improved correlation was achieved after

the previously defined fibre efficiency factor ($f = .153$) was set to unity and an adjustment to the fluid shear force ($f_s = 0.25$) was employed instead. The effect was that of increasing the boundary layer thickness, δ_{99}, by a factor of 4 thereby reducing the velocity gradient and the shear force on the particles and increasing the amount of material captured.

In light of the somewhat better fit resulting from this approach where boundary layer considerations have provided a more physically satisfying model there remain several aspects meriting comment. Boundary layer theory requires that wire Reynolds numbers be considerably greater than unity and even then the resulting relationships are generally only applicable at a distance somewhat downstream from the leading edge of the object. For the ribbon-like fibres of Luborsky (.002 cm x .02 cm) which have been approximated as flat plates with buildup at the leading and lagging edges, the required conditions at the upstream and especially at the downstream location are suspect. Here, boundary layer separation, possible wake effects and the changing hydrodynamics occurring as a result of buildup at the fibre front could play a major role. Averaging the influence of the boundary layer has qualitatively led to the correct interactions between variables but in order for accurate buildup profiles to be predicted the shear stresses should probably be calculated as a function of particle position.

The predominance of back capture predicted by the Luborsky model has not been experimentally confirmed. It would seem that back capture modelling by this technique is inadequate and that attaching too much physical significance to the fitted parameters should therefore be viewed as hazardous.

Watson

In a series of papers following his initial study of capture[17], Watson examined the effects of including a probability of retention for particles having already collided with the fibre. This probability was coupled with the traditional capture radius to yield an overall or 'effective' value of R_c.[31] Figure (2-6) shows the assumed ellipsoidal cross section of buildup used to deflect fluid streamlines on the upstream side of the collection wire. Watson found the initial (bare wire) R_c was solely dependent upon $\frac{V_M}{U_\infty}$ and remained constant as the volume of buildup increased. This contrasts with Luborsky and Drummond's fan-shaped profile where R_c decreased in an inverse square manner with increasing accumulation radius.

A numerical technique was used to calculate inviscid flow over the profile divided into numerous surface elements. Boundary layer effects were not considered. Upon arriving in a magnetically (radially) attractive element, a tangential balance of magnetic, Stokesian drag and friction-like dissipative forces on a particle decided whether it remained or was swept away. A probability of retention per collision per element of surface could thus be determined and summed over the entire profile to yield the overall probability of retention, P, and a total effective capture cross section, $2R_cP$.

The results, illustrated in Figure (2-7), showed that for low $\frac{V_M}{U_\infty}$ (< 1) and small volumes of captured material the effective capture radius was small but tended to increase as buildup progressed. Watson attributed this phenomenon to an increase in surface area (and hence the number of retention sites) and the corresponding decrease in potential

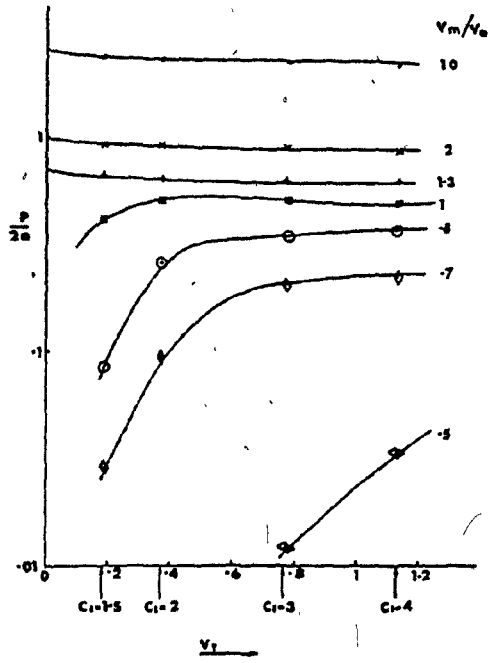

2-7 Watson's 'effective' R_c $(= \frac{P}{2a})$ as a function of the normalized volume of captured material (V_T) at various $\frac{V_M}{U_\infty}$ $(= \frac{V_M}{V_o})$. Ellipsoidal buildup assumed.

velocity associated with the assumed ellipsoidal shape. At higher $\frac{V_M}{U_\infty}$ (say > 1) and greater amounts of retained material, $2R_cP$ remained constant with increasing buildup volume.

The initial assumption of buildup profile shape is important and in a recent paper[32] Watson, after commenting on the limitations of his earlier study, which considered uniform growth in all surface elements, included several modifications to allow for growth to proceed independently starting from a bare wire condition. Again, employing the numerical technique which calculates inviscid flow velocities over any blunt-nosed profile, and including a boundary layer adjustment to the surface velocity as per Luborsky and Drummond, Watson calculated the probability of retention in each surface element. Particle contributions to a unit of area included those attracted directly onto it plus any migrating there from adjacent segments. The volume of each element was then allowed to increase in proportion to its retention probability thus generating a new profile for the buildup and a new flow distribution over it.

The model predicted continuous fan-shaped growth with final, rapid development into regions where the radial magnetic force becomes repulsive (see Figure (2-8)). Watson speculated, however, on the macroscopic stability of such outgrowths and one is lead to wonder about the applicability of the numerical technique in the region about the cusps. As in the earlier model for ellipsoidal profiles the effective R_c showed an initial increase (at low $\frac{V_M}{U_\infty}$) for reasons of increased surface area and the resulting decrease in velocity. Watson cites experimental evidence of Parker who noted an initial increase in the efficiency of

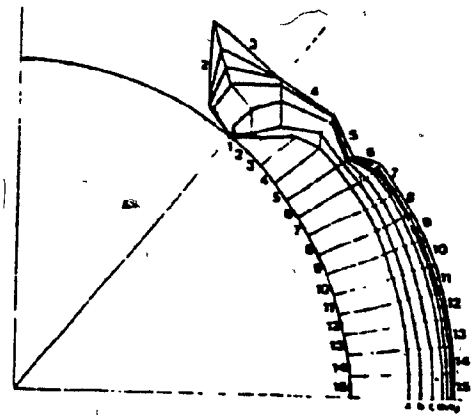

2-8 Watson's computed surfaces for growth model.

a clean filter. An obvious question would be that if growth of the overlaps does not occur (due to, say, instabilities) would the predicted capture cross section still show the initial increase?

As the volume of buildup, V, increased the effective R_c declined much like the Luborsky model and led to a similar relationship; viz.

$$R_{c_{effective}} = \frac{R_{c_{initial}}}{(1 + \frac{4V}{V_w})}$$

where V_w is the volume of the wire.

Overall, the conclusions of Watson's growth model support the fan-shaped profile of buildup and the considerably less complicated model of Luborsky and Drummond.

Stekly and Minervini, Clarkson and Kelland

In their previously mentioned investigation (see Section 2.1) concerning shape effects of a matrix wire on R_c, Stekly and Minervini[28] also studied material accumulation on the upstream side of the fibre. By assuming an elliptical profile of buildup they found that capture cross sections for both circular and elliptical wires showed an initial decrease followed by a levelling-off as buildup progressed. Stability and ultimate profile of the accumulated material were not considered.

In their trajectory approach, Clarkson and Kelland[25] also allowed for the influence of wire loading by adjusting the flow patterns to a changing elliptical shape on the upstream side while assuming zero capture at the back. The resulting capture radii were allowed to decrease

exponentially toward zero as a function of L/L_m, the ratio of material captured (L) to the maximum possible (L_m). This maximum was defined through a static particle force balance and included the effects of an averaged boundary layer thickness. It should be pointed out that in allowing R_c to be a maximum for bare wires and zero for 'fully loaded' ones, the approach of Clarkson and Kelland differs considerably from those of Watson, Luborsky and Drummond and others where relationships for the influence of buildup volume on capture radius do not necessarily lead to zero R_c at maximum buildup volume. The differences are especially evident at lower values of V_M/U_∞.

Cowen, Friedlaender, Jaluria

The desire for photographic evidence of buildup shapes and accumulation-rate data prompted Cowen et al.[34-37] to initiate a series of studies covering the three orientations of flow, field and wire axis of interest. They employed a hot-wire anemometer method and correllated heat loss from the wire undergoing loading with timed photographs of the buildup. Case B proved to be the most difficult experimentally. A lack of closely sized material ($Mn_2P_2O_7$), uneven accumulation on the wire, plus difficulties in obtaining sufficiently clear photographs prevented direct comparison with the available models. Fan-shaped, rather than elliptical buildup was observed on the upstream side and some downstream collection at higher flowrates (> 17 cm/s for 125 μm diameter cylindrical nickel wire) was also noted. The anemometer method, they concluded, was adequate for monitoring the initial rate of buildup but proved poor in determining the fully loaded condition.

Friedlaender, Takayasu, Rettig, Kentzer

These workers developed a video system with improved image resolution for continuous monitoring of particle accumulation on individual wires. All three orientations of field, flow and wire were studied for paramagnetic capture on cylindrical nickel wire.[38]

A rate equation for the relative accumulation radius, R_a (= radius of buildup along axis of symmetry ÷ radius of wire) was found for the parallel stream configuration (case C) to be

$$R_a^n = At + 1$$

where A and n were data-fitted constants which depended strongly on the magnetic field and slurry concentration, and t was buildup time. A model based on theory which considers a changing drag coefficient, C_D, for different ranges of particle Reynolds number, Re_p, was developed and shown to be consistent with the experimental results. This modification recognizes the fact that conditions in hgms devices are often such as to violate the assumption which permits Stokesian drag on particles (i.e. $Re_p < 0.2$) to be employed. Friedlaender et al. used a value for the drag coefficient given by,

$$C_D = gRe_p^{\alpha-2}$$

where α varied from 1 at low values of Re_p (< .3) to 2 at high values (> 10^3) and g was a coefficient between 24, at low Re_p, and .45 at high particle Reynolds number. Although a comparable method of analysis has

not yet been performed for cases A or B it should, in principle, be possible, and would result in models of broader applicability than those based on Stokesian considerations alone. Several follow-up papers[39,40] reported on the experimental results of work with para and ferromagnetics plus data on wake formation for case A. The photographs in Figure (2-9) show that case B upstream collection qualitatively fits a Luborsky or Watson model of fan-shaped buildup. Downstream collection increased with velocity, U_∞, and passed through a maximum while the upstream relative saturation accumulation radius, R_{as}, decreased continually with increasing U_∞ as shown in Figure (2-10). Interestingly, Friedlaender et al. found the average of front and back R_{as} to be largely independent of fluid velocity over the range considered, a phenomenon not yet seen in published operating data.

Liu, Oak, Lin

By using a model of buildup very similar to that of Luborsky and Drummond, Liu et al.[41] developed arguments for neglecting the decrease in capture radius with increased wire loading. Their model found that maximum buildup volume was usually reached before an appreciably large reduction in R_c occurred. In defining fluid drag forces, two cases of relative particle-to-wire size, b/a, were considered; namely (i) b/a close to 1 and (ii) b/a << 1. For larger particles (case (i)) the carrier fluid, it is argued, will pass through the interstices of the buildup and hence Stokesian drag on the spheres can be assumed. The flow field was not adjusted for the wire/buildup perturbation in balancing radial and tangential components of the forces.

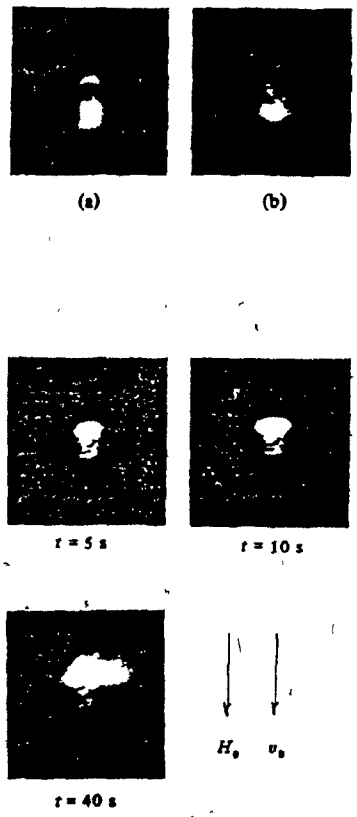

2-9 Friedlaender et al.'s sequence of Case B photographs of $Mn_2P_2O_7$ buildup. Field strength, 4.7 kOe; flow rate 1.5 cm/s at times of 5, 10 and 40 s. Photographs (a) and (b) are of saturation buildup at 17.7 cm/s and 35.1 cm/s, respectively.

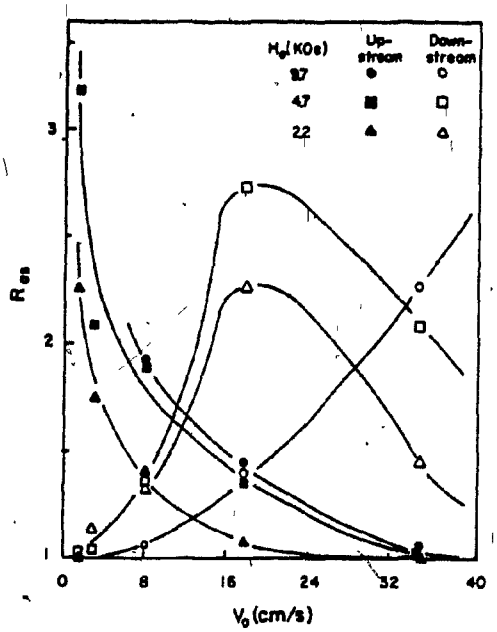

Saturation value of relative accumulation radius R_{as} of upstream and downstream collection is plotted versus slurry velocity v_0 ($Mn_2P_2O_7$, $c \approx 0.4$ g/l).

2-10 R_{as} as a function of U for upstream and downstream wire buildup (from Friedlaender et al.).

Figure (2-11) shows the manner in which the maximum relative buildup volume so determined, f_{max} (= volume buildup/volume wire), is a function of $(\frac{V_M}{U_\infty})^{2/3}$ for the assumptions listed on the diagram and that there exists a minimum value for buildup at roughly $\frac{V_M}{U_\infty} = 0.5$. For particles much smaller than the wire (case (ii)) Liu et al. included an averaged boundary layer effect as per Luborsky and showed that f_{max} depends both on $(\frac{V_M}{U_\infty})^{0.8}$ and $(\frac{\delta}{b})^{0.8}$, where δ is the boundary layer thickness and b the particle radius.

The overall filter model, developed for case (i) only, led Liu et al. to conclude that for quantitative performance predictions of hgms, capture radii variations with buildup volume could be neglected since the capability of the wire matrix in capturing particles remains high and practically unchanged up to buildup saturation (Figure (2-12)). Hence, maximum buildup volume was felt to be the most important factor to consider in the experimental verification of their model; an industrial coal beneficiation problem.

The effect of distributions in particle size, density and magnetic susceptibility was well handled by considering the magnetic velocity distribution of the feed stream (Figure (2-13)). If $F(V_M)$ is the function describing the cumulative weight fraction of feed with magnetic velocity less than V_M, then $1-F(V_{M_{minimum}})$ corresponds to the fraction captured when subjected to the condition that all particles with V_M greater than $V_{M_{minimum}}$ are retained in the filter. This $V_{M_{minimum}}$ is specified by the equilibrium wire loading as per Figure (2-11). The total weight fraction recovered by the separator is determined by numerically integrating $(1-F(V_{M_{minimum}}))$ for increments of feed.

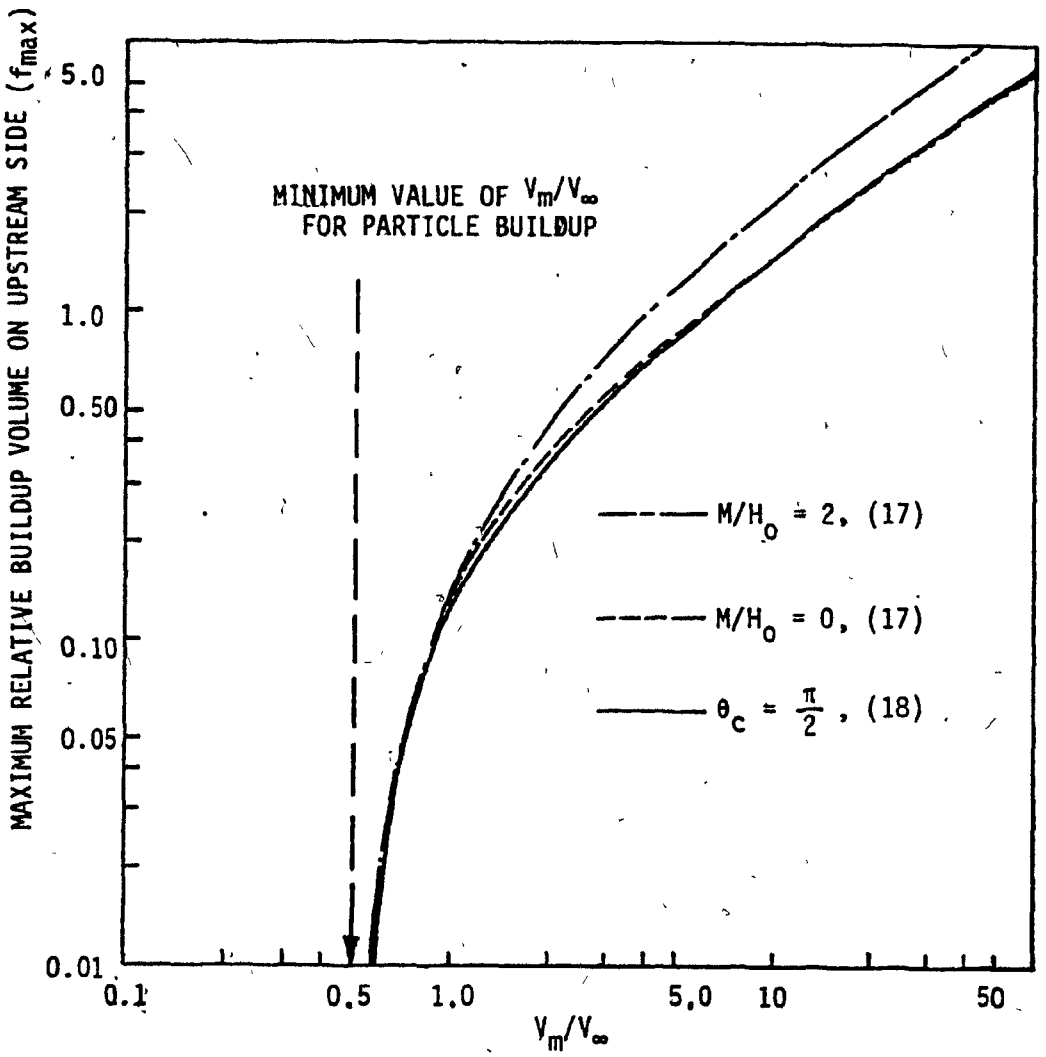

2-11 Liu et al.'s maximum relative buildup volume (f_{max}) as a function of $\frac{V_M}{U_\infty}$ ($= \frac{V_M}{V_\infty}$).

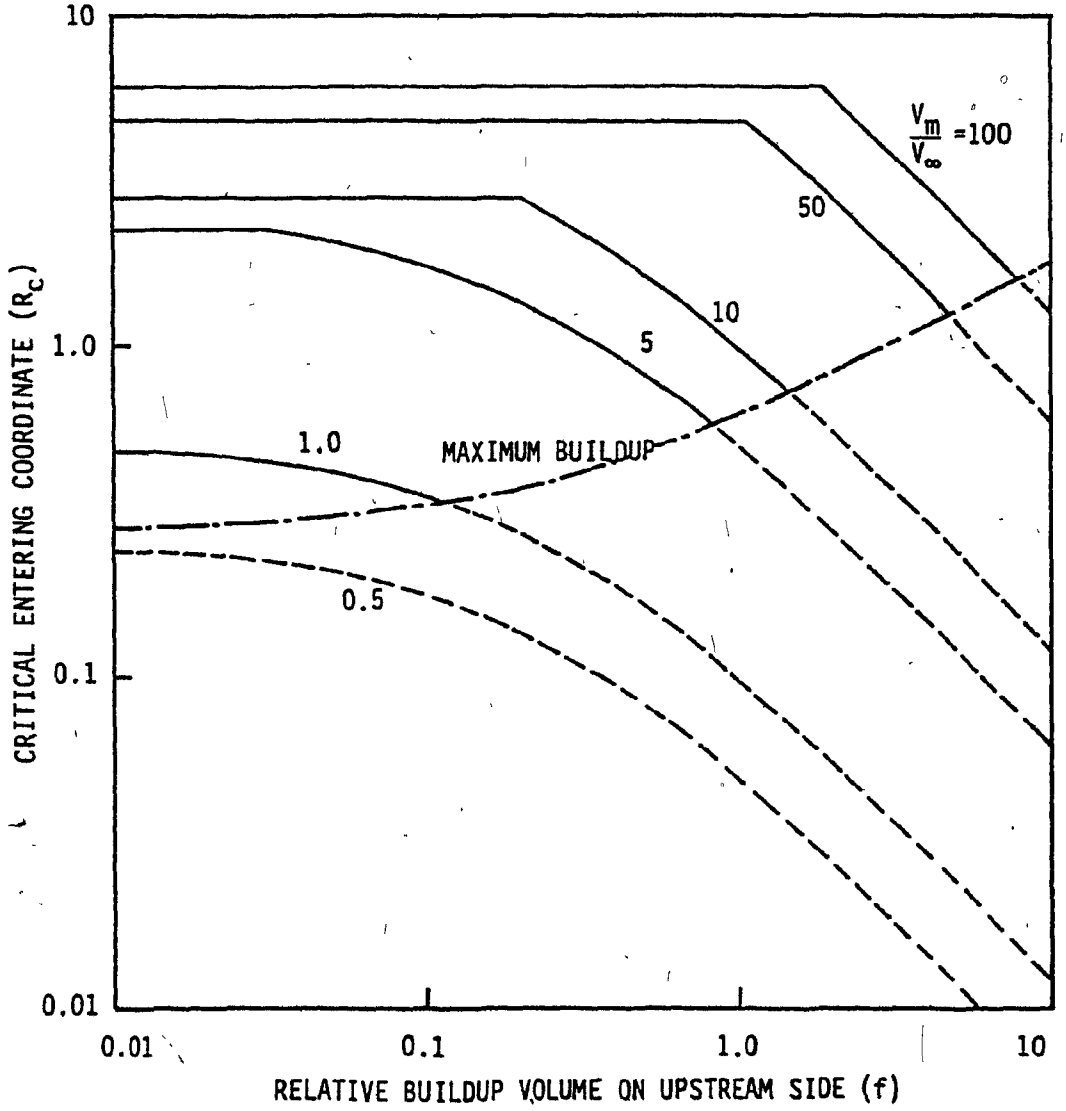

2-12 Liu et al.'s variation in R_c with relative buildup volume on the upstream side (f) at various $\frac{V_M}{U_\infty}$ $(= \frac{V_M}{V_\infty})$.

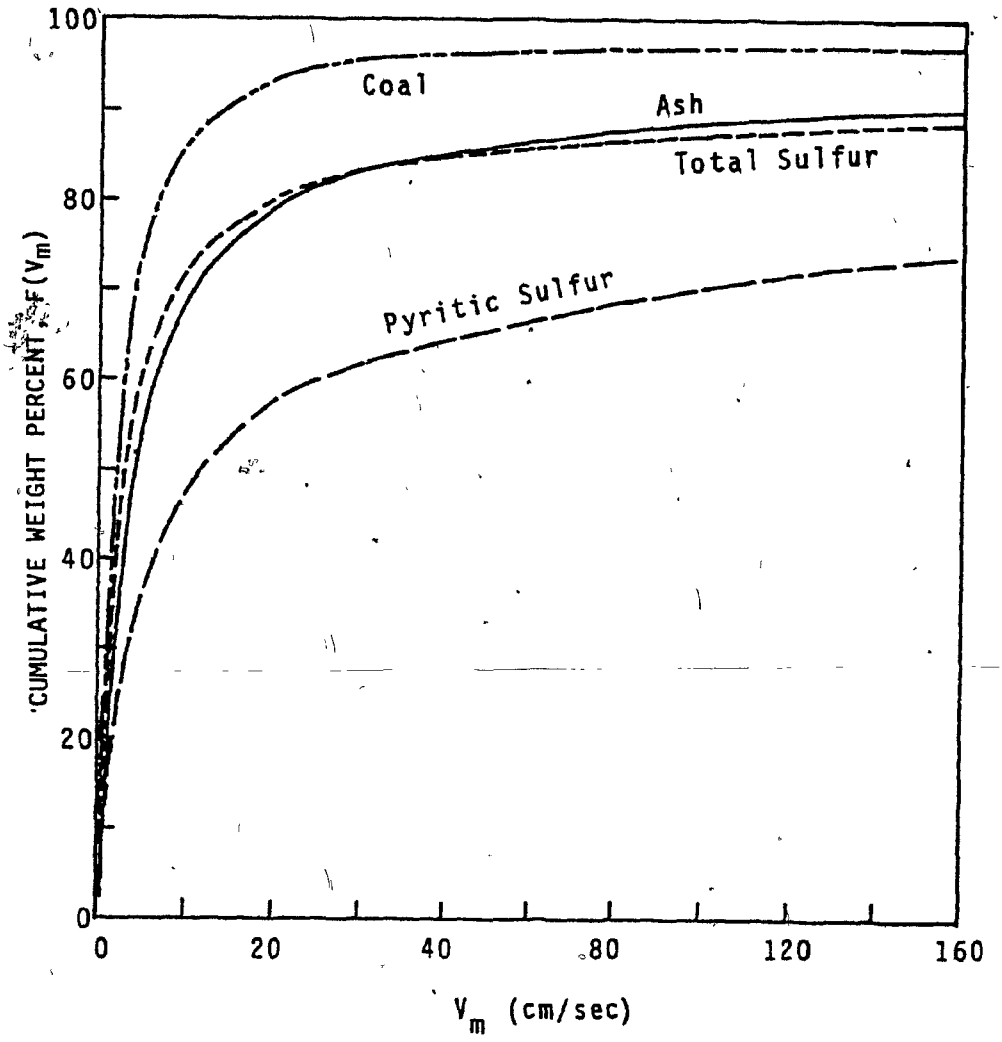

2-13 Liu et al.'s magnetic velocity distribution of pulverized feed coal.

Although Liu et al. argue that their approach is valid for the entire range of $\frac{V_M}{U_\infty}$ the experimental conditions were such that $\frac{V_M}{U_\infty}$ was, in general, considerably greater than unity. Conditions which would test both the model at lower $\frac{V_M}{U_\infty}$ and the postulation of a minimum $\frac{V_M}{U_\infty}$ of about 0.5 do not appear to have been investigated.

III. THEORETICAL CONSIDERATIONS

3.1 Forces

3.1.1 Magnetic Force

Principles

Coulombs Law states that the magnetic force, F_M, on a pole of strength p_1 a distance r from another pole, p_2, is given by the relationship;

$$\hat{F}_M = \frac{p \cdot p_2}{\mu r^2} \hat{r} \qquad (3.1\text{-}1)$$

where $\hat{r}$ is a unit vector* directed from p_2 toward p_1. The inverse constant of proportionality, the permeability, μ, has a defined value of 1 in a vacuum and can be taken as 1 in air (cgs units).

The magnetic field strength, H, is then given as the force on a unit pole, or:

$$\hat{H} = \frac{\hat{F}_M}{p} \qquad (3.1\text{-}2)$$

This leads to the definition of the unit of field strength, the Oersted (Oe), as the field required to exert a force of 1 dyne on a unit pole. A useful concept in representing H is that of 'lines of force' (i.e. lines to which a compass needle would be tangent) which by convention radiate from north toward south poles. A measure of H

---

*Note that the circumflex, ^, above a symbol in an equation denotes a vector quantity.

becomes the number of lines per unit area perpendicular to the field direction. As the field strength at the surface of a sphere of 1 cm radius centered on a unit pole is one Oersted, it follows that there must be 4π lines of force issuing from it since the area of the surface is 4π cm^2. A pole of strength p, therefore, has $4\pi p$ lines of force leaving it.

Though single poles are useful aids to thought, poles occur in nature always as pairs; therefore, the magnetic dipole is considered a more appropriate entity for study. For two poles, of strength +p and -p, separated by a distance ℓ along the unit vector $\hat{r}$ and perpendicular to a field of one Oersted, the magnetic moment, m, of the resulting free couple can be shown to be:

$$\hat{m} = p\ell\hat{r} \qquad (3.1\text{-}3)$$

In spite of their being difficult to quantify individually, the products of p and ℓ, the dipole moment, can be precisely measured and has been given the fundamental unit of emu (electromagnetic unit) or ergs/Oe in the cgs system of measurement.

A body subjected to a field will become magnetized in some proportion to that field due to the aligning of the dipoles of the material. Another useful quantity is the magnetic moment per unit volume or magnetization, M, where:

$$\hat{M} = \frac{\hat{m}}{\text{volume}} \qquad (3.1\text{-}4a)$$

Since volume is equivalent to cross sectional area times a length, ℓ, it follows from Equation (3.1-3) that M may also be expressed as the pole strength per unit area, i.e.:

$$\hat{M} = \frac{p}{\text{area}} \hat{r} \qquad (3.1\text{-}4b)$$

It is sometimes convenient to have the magnetization in terms of mass rather than volume, hence;

$$\hat{\sigma} = \frac{\hat{M}}{\rho} \qquad (3.1\text{-}4c)$$

where ρ is the density of the material and σ has units of emu/g.

Magnetization curves are very useful in identifying the various types of magnetic materials and may broadly be classified into either linear or non-linear responses of M versus H. In Figure (3-1) curve a) shows a diamagnetic material having, typically, $\frac{M}{H}$ of the order -10^{-6} emu/cm^3-0e. Curve b) could be the response of either a para- or anti-ferromagnetic for which $\frac{M}{H}$ is roughly 10^{-5} emu/cm^3-0e. Under normal conditions these substances retain no magnetism when the field is removed. The non-linear behaviour shown in Figure (3-1c) is that of a ferro- or ferri-magnetic for which M is of the order 10^6 times greater than for paramagnetics. Two other phenomena are also exhibited by these materials. At sufficiently large H the magnetization becomes constant at its saturation value, M_s. When the field is subsequently reduced to zero, ferro- and ferri-magnetics show hysteresis as the magnetization remains at some finite value, m_r in Figure (3-1c), called the residual magnetization or

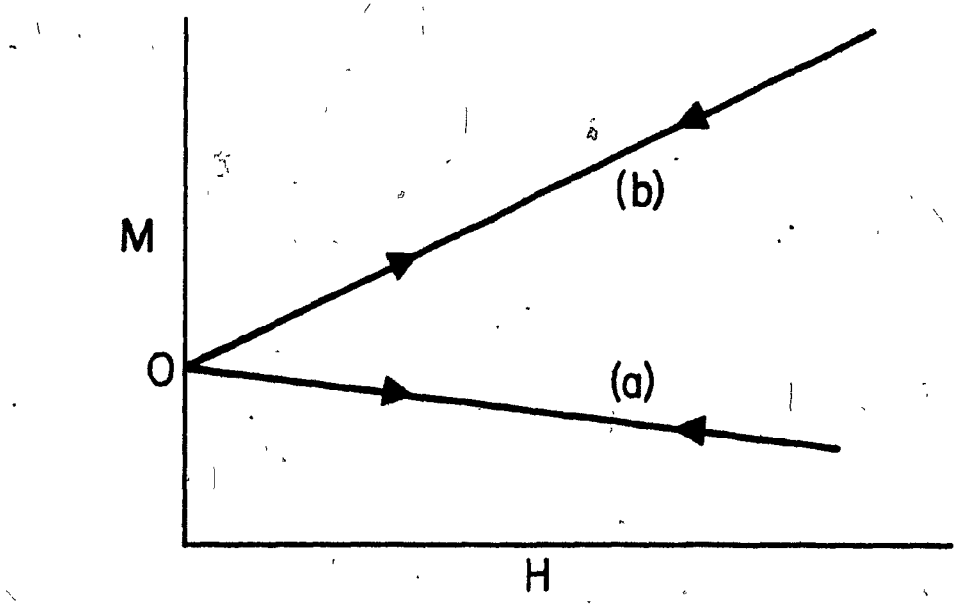

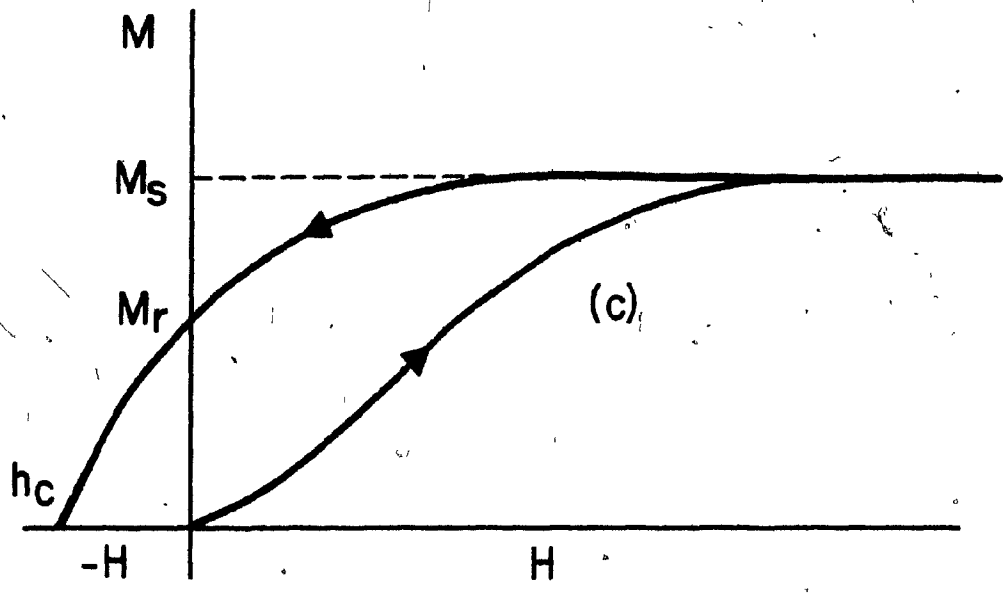

3-1 Magnetization behavior as a function of field for (a) diamagnetics, (b) paramagnetics and antiferromagnetics and (c) ferromagnetics and ferrimagnetics.

remanence. M can again be brought to zero by the application of a reverse field known as the intrinsic coercivity or simply the coercive force, h_c, in Figure (3-1c).

A material is characterized not only by M but also by the way in which M varies with H. This leads to the definition of magnetic susceptibility, κ, a parameter of great interest in the study of minerals as it shows the responsiveness of a material to the magnetic field. Magnetic susceptibility is commonly expressed in either of two ways, namely:

$$\kappa = \frac{\hat{M}}{\hat{H}} \qquad \text{volume susceptibility } \left(\frac{\text{emu}}{\text{cm}^3\text{-0e}}\right) \qquad \ldots\ldots(3.1\text{-}5a)$$

$$\chi = \frac{\hat{\sigma}}{\hat{H}} = \frac{\kappa}{\rho} \qquad \text{mass (or specific) susceptibility } \left(\frac{\text{emu}}{\text{g-0e}}\right) \qquad \ldots\ldots(3.1\text{-}5b)$$

Table (3-1) lists the ranges and average values of κ for various minerals.[42-44]

Referring again to a material in a field H, magnetized to a value M by the alignment of internal dipoles, one finds that an additional field now exists in the body. Since M can be considered as the pole strength per unit area and (Equation (3.1-4b)) thereby contributing $4\pi M$ lines of force, it follows that the net result of this plus the contribution due to the field itself is B lines of force per unit area, i.e.:

$$\hat{B} = \hat{H} + 4\pi\hat{M} \qquad (3.1\text{-}6)$$

TABLE 3-1

Magnetic Susceptibilities of Various Minerals

emu/cm^3-0ex10^6

Type	Telford et al.[42]	Taggart[43]	Andres*[44]
graphite	-8	-4.7,-30	-13
quartz	-1	175-438	-1.2, 27
rock salt	-1	-1.2	-1,-1.2
anydrite, gypsum	-1	-	-2.4,-4.8
calcite	-0.6 - -1.0	-1,-1.1	-9.8, 34
coal	2	-	-
clays	20	-	-
chalcopyrite	32	3.6	533,1680
sphalerite	60	-1.1	-1,-1.4
cassiterite	90	-	1,200,-1
siderite	100-310	320-550	378,246
pyrite	4-420	20-150	1,2.6,5
limonite	220	700-800	51,83
arsenopyrite	240	-	48,820,1430
hematite	40-3000	110-1,100	104,1500,3600
chromite	240-9400	-	71,350
franklinite	36,000	2,500-3,700	ferri-magnetic
pyrhotite	125,000	340-5,800	1,070
ilmenite	25,000-300,000	1500	450
magnetite	100,000-1,000,000	120,000-3,000,000	ferri-magnetic
galena	-	-2.6	-2.6

*Note - underlined values are for pure minerals.

Known as the magnetic induction or flux density of a material, B has units of Gauss (G) and represents the total field within the substance. Outside the body, since there is no material to magnetize, B simply equals H.

The ratio of B to H is termed the magnetic permeability, μ; that is

$$\mu = \frac{\hat{B}}{\hat{H}} \qquad (3.1\text{-}7)$$

which was first encountered in Equation (3.1-1). By combining Equations (3.1-5,6,7) the expression for μ is easily related to the magnetic susceptibility in the fashion:

$$\mu = 1 + 4\pi\kappa \qquad (3.1\text{-}8)$$

Note that although units of B, H and M are the Gauss, Oersted and $\frac{\text{emu}}{\text{cm}^3}$ respectively, they are numerically equivalent and no conversions are required.

Force on a Particle

The vector magnetic force on a magnetized body, $\hat{F}$, may be derived from a scalar potential (energy) function A, viz.

$$\hat{F} = -\nabla A \qquad (3.1\text{-}9)$$

where A is obtained by considering the energy involved when the material interacts with the field. That is;

$$A = \tfrac{1}{2}(\hat{m} \cdot \hat{H}) \qquad (3.1\text{-}10)$$

which, in integral form for a volume V, becomes;

$$A = \tfrac{1}{2} \int_V (\hat{M} \cdot \hat{H}) dV \qquad (3.1\text{-}11)$$

Substituting this expression for A into Equation (3.1-9) yields;

$$\hat{F} = -1 \nabla \int_V (\hat{M} \cdot \hat{H}) dV \qquad (3.1\text{-}12)$$

as the relevant equation for magnetic force.

Aharoni[45] has shown that the volume integral in Equation (3.1-12) may be evaluated exactly. However, the difference which results from assuming,

$$\hat{F} = \frac{V}{2} \nabla (\hat{M} \cdot \hat{H}) \qquad (3.1\text{-}13)$$

is not large and greatly simplifies the resulting component equations.

Magnetic Field

Consider the situation illustrated in Figure (3-2). A particle of radius b has its centre located a distance r from the centre of a wire of radius a, where θ forms the angle between the unit vectors

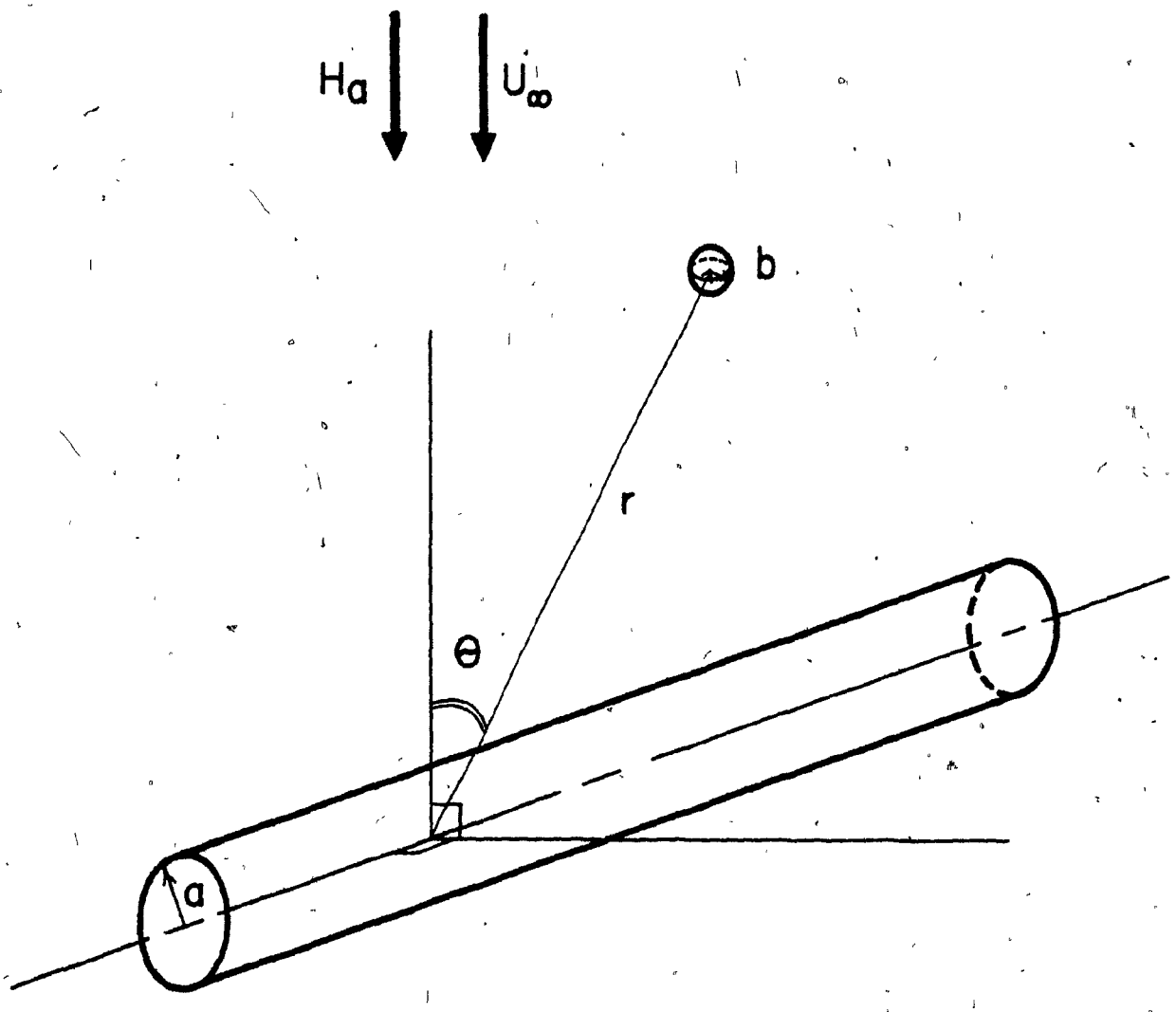

3-2 Idealized situation of a spherical particle near an infinitely long and cylindrical magnetized wire.

of r and the applied field, H_a. In cylindrical coordinates, the field components may be expressed as:[46]

$$\hat{H}_r = \hat{H}_a \cos\theta\left(1 + A\frac{a^2}{r^2}\right) \qquad (3.1\text{-}14a)$$

$$\hat{H}_\theta = -\hat{H}_a \sin\theta\left(1 - A\frac{a^2}{r^2}\right) \qquad (3.1\text{-}14b)$$

(Note: at this point vector notation is discontinued as no new vector quantities need to be introduced in the analysis of magnetic force). The perturbation term, A, for a cylinder is defined as;

$$A = \frac{\mu_w - \mu}{\mu_w + \mu} \qquad (3.1\text{-}15)$$

where the magnetic permeabilities of the wire, μ_w, and the background medium, μ, are given by Equation (3.1-7). For the case of water or air μ can be taken as unity leading to;

$$A = \frac{B - H}{B + H} \qquad (3.1\text{-}16a)$$

or, since $B = H + 4\pi M_w$ (Equation (3.1-6)):

$$A = \frac{4\pi M_w}{2H + 4\pi M_w} \qquad (3.1\text{-}16b)$$

Here M_w refers to the wire magnetization and H is the actual field inside the material after demagnetizing effects have been accounted for. The internal demagnetizing field, H_D, is that of the 'induced' poles and acts in opposition to the applied field, H_a, hence;

$$H = H_a - H_D$$

where

$$H_D = NM_w \qquad (3.1\text{-}17)$$

and N is the demagnetizing factor. Most shapes require N to be experimentally measured. Below saturation only ellipsoidal bodies magnetize uniformly thereby permitting N to be calculated exactly. Infinite length rods magnetized perpendicular to the long axis, have an exact demagnetizing factor of 2π.(47)

Hence, the expression for A to be used in Equations (3.1-14a,b) becomes;

$$A = \frac{2\pi M_w}{H_a} \qquad (3.1\text{-}18)$$

which is the ratio of demagnetizing to applied field. In the form, $\frac{Aa^2}{r^2}$, because of its strong dependence on r, this expression is often referred to in the literature as the 'near field' or 'short-range' term of the radial magnetic force.

Wire Magnetization

In the presence of an increasing field, the initial rate of magnetization for ferri and ferro-magnetics is geometry and field orientation dependent* while M_s, the saturation value to which M ulti-

*The initial rate of magnetization also depends on size when the dimensions approach those of the magnetic domains.

mately tends, is a characteristic of the material itself. Following the example of Clarkson[48], a simple exponential fit to experimentally measured curves was used to relate M_w and H, thus;

$$M_w = M_s \exp(-\frac{K}{H}) \qquad (3.1\text{-}19)$$

where K is an empirical constant. Upon substituting for H from Equation (3.1-17) one obtains:

$$M_w = M_s \exp(\frac{-K}{(H_a - 2\pi M_w)}) \qquad (3.1\text{-}20)$$

whence it is evident that the magnetization is a function of itself and requires a self-consistent calculation for its evaluation at a particular H_a.

Particle Magnetization

Traditionally most minerals have been considered either paramagnetic or diamagnetic. This means that, in accordance with Equation (3.1-5a), they magnetize in proportion to the field, i.e.;

$$M_p = \kappa H \qquad (3.1\text{-}21)$$

where the magnetic susceptibility, κ, is constant and M_p is the particle magnetization.

Most previous models[17,20,27] have made use of Equation (3.1-21) which has led to the following expression for magnetic force on para (and dia) magnetics,

$$F_M = -\frac{V}{2}\nabla(\kappa H \cdot H)$$

$$= \frac{V\kappa}{2}\nabla H^2 \qquad (3.1\text{-}22)$$

Strictly speaking, κ in Equation (3.1-22) should be expressed as

$$\kappa = (\kappa_p - \kappa_m)$$

where the subscripts p and m refer to susceptibilities of the particle and medium, respectively. In most instances of hgms, where the medium is either water or air (water is, in fact, slightly diamagnetic), $\kappa_m \ll \kappa_p$ and the approximation that $\kappa = \kappa_p$ may be safely used. In cylindrical coordinates, Equation (3.1-22) transforms to;

$$F_{r_M} = -2V\kappa H_a^2 \frac{Aa^2}{r^3}(\cos 2\theta + \frac{Aa^2}{r^2}) \qquad (3.1\text{-}23a)$$

$$F_{\theta_M} = -2V\kappa H_a^2 \frac{Aa^2}{r^3} \sin 2\theta \qquad (3.1\text{-}23b)$$

upon substitution for H from Equations (3.1-14a,b). These are the 'traditional' equations for magnetic force as employed by most workers. In trajectory models, the near-field term, $\frac{Aa^2}{r^2}$, is often dropped from F_{r_M} since r is large compared with a.

Work by Pastrana and Hopstock[49] on taconites has pointed out the importance of considering the field dependence of magnetic susceptibility. They suggested that a relationship of the form typically used to describe 'parasitic ferromagnetism' or 'canted anti-ferromagnetism' be used to describe particle magnetization. Hence, M_p can be represented

by the 2-parameter equation;

$$\sigma = \sigma_o + \chi_\infty H \qquad (3.1\text{-}24a)$$

where the spontaneous magnetization, σ_o, and the magnetic susceptibility extrapolated to infinite field strength, χ_∞, are constants in specific (i.e. mass) units. The equivalent relationship in volumetric terms is:

$$M_p = M_o + \kappa_\infty H \qquad (3.1\text{-}24b)$$

It was thought prudent to rework the expression for magnetic force (Equation (3.1-13)) taking into account the additional magnetization term, M_o, thus giving:

$$F_M = -\frac{V}{2} \nabla(M_o H + \kappa_\infty H^2) \qquad (3.1\text{-}25)$$

The assumption having been made that;

$$M_o H \equiv \hat{M}_o \cdot \hat{H}$$

which is equivalent to stating that the particle magnetizes isotropically and is free to orient itself with M_o parallel to the magnetic field vector. The detailed mathematics may be found in Appendix I with the results of transforming Equation (3.1-25) into cylindrical coordinates being;

$$F_{r_M} = -2VH_a \frac{Aa^2}{r^3}\left(\cos 2\theta + \frac{Aa^2}{r^2}\right)(\kappa_\infty H_a + fM_o) \qquad (3.1\text{-}26a)$$

$$F_{\theta_M} = -2VH_a \frac{Aa^2}{r^3} \sin 2\theta(\kappa_\infty H_a + fM_o) \qquad (3.1\text{-}26b)$$

where $$f = \frac{1}{2\left(1 + 2\frac{Aa^2}{r^2}\cos 2\theta + \frac{A^2a^4}{r^4}\right)^{\frac{1}{2}}}$$

and is termed the field parameter.

Note that Equations (3.1-26a,b) reduce to those for paramagnetics (Equations 3.1-23a,b) when M_o is set to zero and κ_∞ to κ. The field parameter f depends on both position and the near field term but for r large it tends toward 0.5.

The expressions for total magnetic force on paramagnetics obtained from Equations (3.1-23a,b) is:

$$F_{M_{total}} = \frac{V}{f} H_a^2 \kappa \frac{Aa^2}{r^3} \qquad (3.1\text{-}27)$$

and for canted anti-ferromagnetics becomes (from Equations (3.1-26a,b)):

$$F_{M_{total}} = \frac{V}{f} H_a^2 \frac{Aa^2}{r^3}(\kappa_\infty H_a + fM_o) \qquad (3.1\text{-}28)$$

Interestingly, one finds f appearing in both equations independent of the type of particle magnetization.

Equations (3.1-26a,b) and (3.1-27) also suggest that an 'effective' magnetization, M_{p_e}, defined as;

$$M_{p_e} = \kappa_\infty H_a + fM_o \qquad (3.1\text{-}29)$$

might be used to simplify the analysis of magnetic force for the field dependent case. When r is large, as in trajectory models, f could be taken as close or equal to 0.5.

Magnetic Force About a Wire

A material placed in a magnetic field becomes, due to its dipolar nature, a magnet itself, thereby setting up regions of attraction and repulsion in its vicinity. Using Equations (3.1-26a,b) the vector forces about a cylindrical stainless steel wire (a = .03 cm) were calculated for a typical situation, viz; field strength (H_a = 3000 Oe), particle size (b = .0005 cm), magnetization constants (κ_∞ = .000114 emu/cm^3-Oe, M_0 = 1.62 emu/cm^3), and perturbation term (A = 0.9).

Figure (3-3) shows these force vectors for one quadrant (the others are mirror images) about the wire in which the regions of attraction (parallel to $\hat{H}_a$) and repulsion (perpendicular to $\hat{H}_a$) are evident. From the dashed line representing the loci of zero radial magnetic force, i.e. the transition from repulsion to attraction, it can be seen that attraction extends to $\theta = 74^\circ$ at the wire surface. The extent to which the attractive region exceeds a 45° sector is determined by the relative magnitude of the near field term in Equation (3.1-26a). For instances where r is not large and A is near unity, the effect of the near field term in extending the attractive region is considerable and, in all likelihood, it should not be neglected. This caution is obviously more intended for buildup than trajectory models.

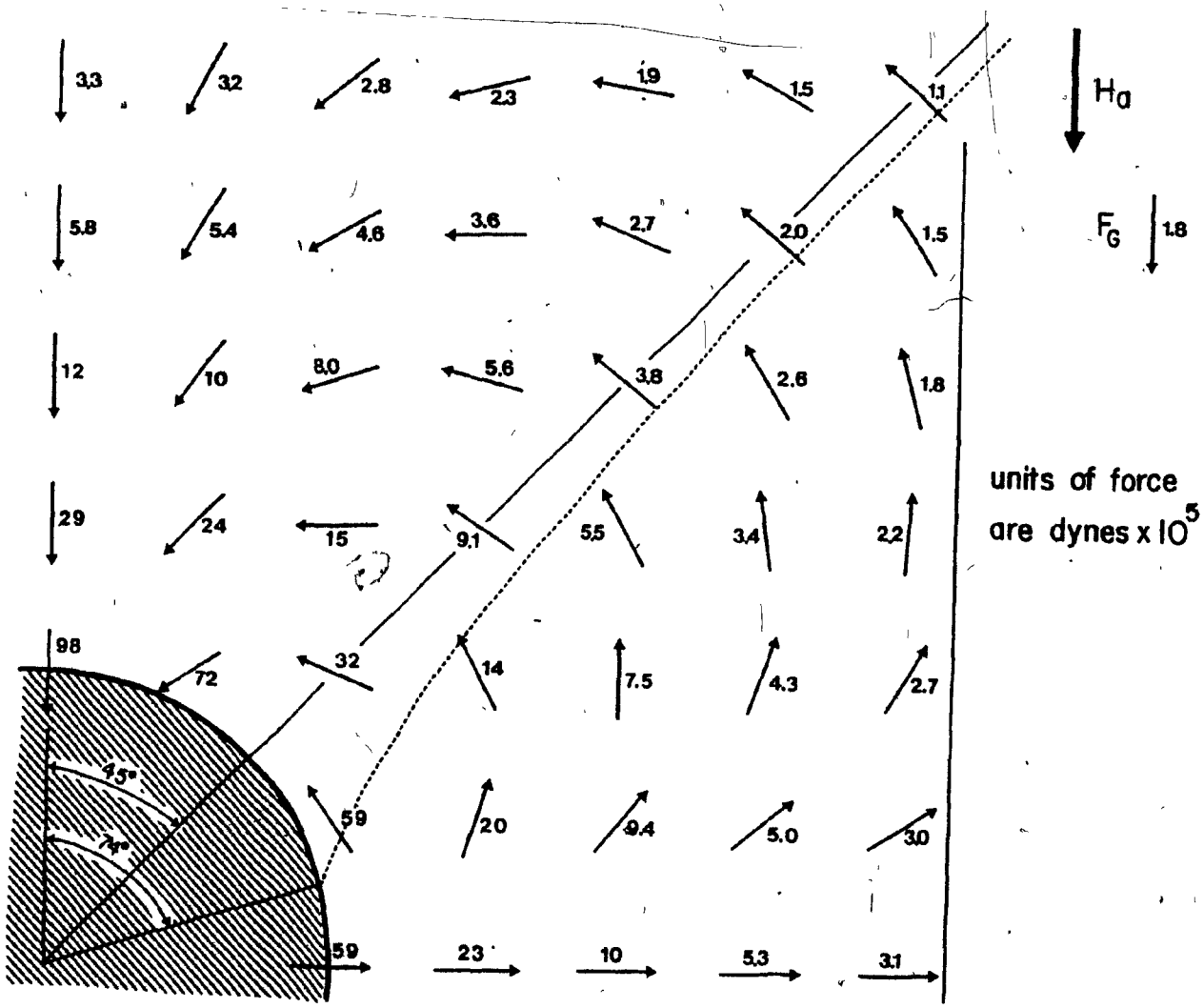

3-3 Magnetic force vectors in one quadrant about 600 μm diameter stainless steel wire. Data is for 'standard' test. Dashed line represents locus of zero radial magnetic force. Force units are dynes x 10^5.

3.1.2 Fluid Force Principles

When considering fluid flow around a body the problem is often simplified by assuming ideal (frictionless and incompressible) fluid behavior. Viscous forces are therefore neglected and this approximation, called potential flow, is often sufficient to realistically predict the flow patterns at sufficiently large distances from solid boundaries. Streamlines for ideal flow past a cylinder are shown in Figure (3-4).

The velocity components, in cylindrical coordinates, for this case are[50],

$$U_r = U_\infty \cos\theta\left(1 - \frac{a^2}{r^2}\right) \qquad (3.1\text{-}30a)$$

and

$$U_\theta = -U_\infty \sin\theta\left(1 + \frac{a^2}{r^2}\right) \qquad (3.1\text{-}30b)$$

where U_∞ is the undisturbed free stream velocity far from the cylinder and a, r and θ are as defined for the magnetic case. Note the existence of points of mathematical singularity, corresponding to flow stagnation points (marked S in Figure (3-4)), both upstream and downstream on the cylinder profile.

In making the conversion from ideal to real fluids it is necessary to consider the resistance to flow between adjacent fluid layers. For Newtonian fluids[51] (i.e. gasses, water and most single phase, non-polymeric fluids) this resistance in the x-direction is termed the shear stress, τ, and is proportional to the velocity gradient

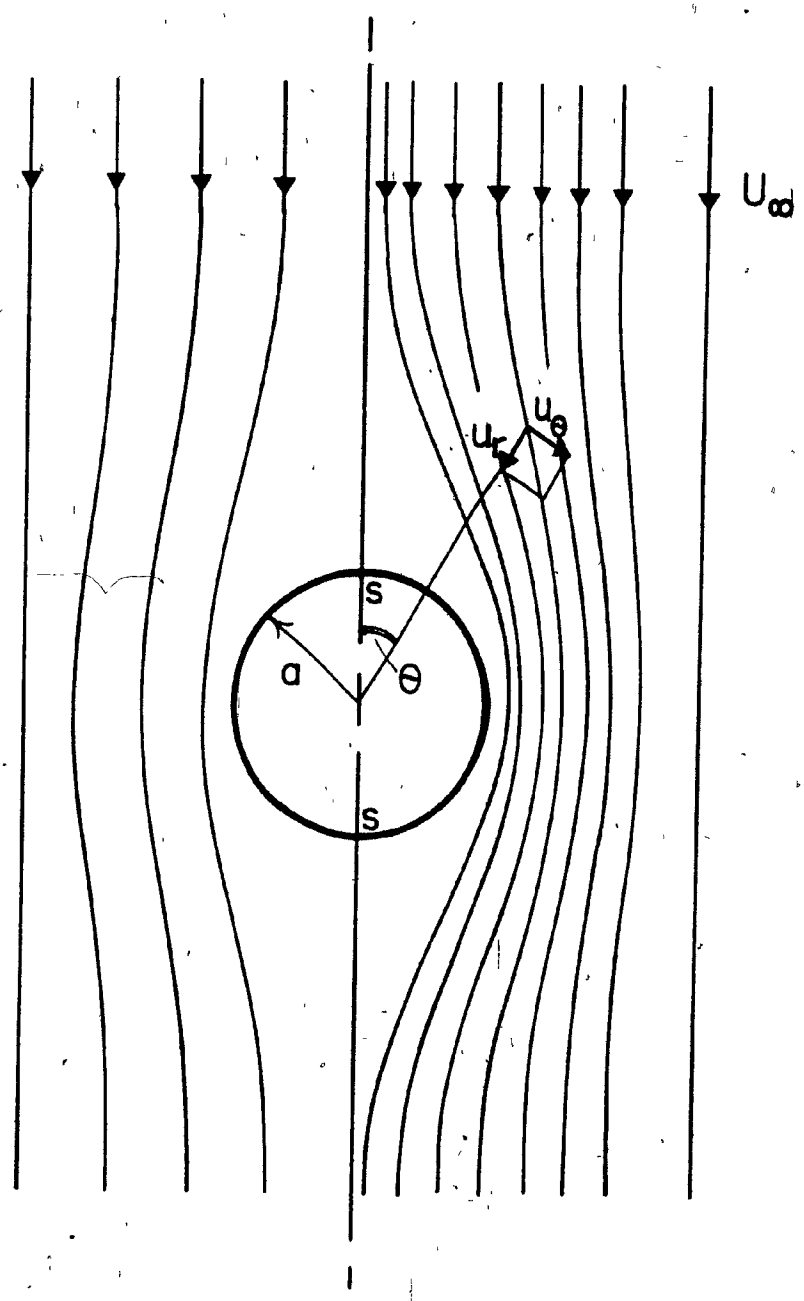

3-4 Flow streamlines for potential flow about a cylindrical wire.

(the rate of change of strain) in the y-direction, $\frac{\partial U}{\partial y}$. The constant of proportionality is the dynamic (or absolute) viscosity, η, so the equation for τ becomes:

$$\tau = -\eta \frac{\partial U}{\partial y} \qquad (3.1\text{-}31)$$

Fluid velocity at a rigid surface must of necessity be zero, the so-called 'no-slip criterion'. Further away the velocity must approach the main stream velocity. Viscous effects, therefore, predominate in the region adjacent to the surface where $\frac{\partial U}{\partial y}$ is large. This region of large velocity gradient, the 'boundary layer', is often assigned the nominal boundary layer thickness, δ_{99}, which represents the distance over which the velocity has recovered 99% of the outer flow velocity. Schlichting[52] gives an estimate of this thickness for a flat plate parallel to U_∞ as;

$$\delta_{99} = 5\left(\frac{\nu \ell}{U_\infty}\right)^{\frac{1}{2}} \qquad (3.1\text{-}32a)$$

or

$$\delta_{99} = \frac{5\ell}{(Re)^{\frac{1}{2}}} \qquad (3.1\text{-}32b)$$

where ℓ is the characteristic dimension, in this case length, ν is the kinematic viscosity and Re is the Reynolds number of the plate. Equations (3.1-32a,b) predict that δ_{99} will increase (thus decreasing shear) along the plate in proportion to $\ell^{\frac{1}{2}}$ while diminishing in relation to $Re^{\frac{1}{2}}$ if the Reynolds number alone is altered.

The ratio of fluid inertial to viscous forces is given by the Reynolds number, Re, where;

$$Re = \frac{U\ell\rho_f}{\eta}$$

$$= \frac{U\ell}{\nu} \qquad (3.1\text{-}33)$$

and ρ_f, the fluid density, relates the dynamic and kinematic viscosities according to

$$\nu = \frac{\eta}{\rho_f}$$

Consider the case of a cylindrical wire perpendicular to the flow direction in a free stream. For low wire Reynolds number, Re_w, of the order of unity and less, inertial effects can usually be neglected and flow around the cylinder is smooth. In the range of Re_w 2 to roughly 40 boundary layer separation from the surface gives rise to two circulating eddies immediately behind the cylinder, with flow becoming smooth again further downstream. Above Re_w 5000 inertial effects predominate in the fluid and there is complete turbulent mixing in the wake of the cylinder. In the intermediate region of Re_w 60 to 5000, the phenomenon of alternate shedding of the eddies in the wake occurs, the so-called 'Karman vortex street'. For bodies of increased bluffness, the effects of fluid inertia predominate at lower values of Reynolds number.

Typical ranges of operating conditions for wet hgms are wire diameters from 20 to 1000 μm and flow velocities from 1 to 20 cm/s.

For water, ($\nu = .01$ cm^2/s), this gives a three orders of magnitude range of wire Reynolds number, Re_w 0.2 to 200, and a value Re_w 60 as typical for an operation with 600 μm wire at 10 cm/s flow rate.(53)

Particle sizes treated by hgms have, typically, diameters of 1 to 50 μm, which also gives a three orders of magnitude variation in particle Reynolds number, Re_p, from .01 to 10. A 10 μm particle in a 10 cm/s flow has an Re_p of unity.

The fluid drag force, F_D, on a spherical particle of radius b in a uniform free stream can be calculated from Stoke's drag law(54);

$$F_D = 6\pi b\eta U' \qquad (3.1\text{-}34)$$

where U' is the relative velocity between the particle and fluid. Equation (3.1-34) applies for Reynolds numbers where the fluid inertia is not large, i.e. Re_p of 0.2 and less.

Trajectory models have made extensive use of the Stokes' relationship to describe fluid drag on particles. Considering the nature of the flow and the relatively large interfibre and interparticle distances, the approximation seems a valid one. The usefulness of Equation (3.1-34) is questionable, however, for particles residing at or near the bottom of a boundary layer where the flow is neither uniform nor free from the effects of nearby surfaces and other particles. A brief review of boundary layer theory seems in order.

Boundary Layer Equations

By considering the development of a boundary layer on a sur-

face where δ is small in comparison with the distance x (Figure (3-5)), the Navier-Stokes (N-S) equations (i.e. equations of motion for incompressible fluids) can be transformed into the relevant boundary layer equations. In two-dimensional flow the N-S equations are[55];

$$u \frac{\partial u}{\partial x} + v \frac{\partial u}{\partial y} = - \frac{1}{\rho_f} \frac{\partial p}{\partial x} + \nu \frac{\partial^2 u}{\partial x^2} + \nu \frac{\partial^2 u}{\partial y^2} \qquad (3.1\text{-}35a)$$

and

$$u \frac{\partial v}{\partial x} + v \frac{\partial v}{\partial y} = - \frac{1}{\rho_f} \frac{\partial p}{\partial y} + \nu \frac{\partial^2 v}{\partial x^2} + \nu \frac{\partial^2 v}{\partial y^2} \qquad (3.1\text{-}35b)$$

where u, v are x and y components of velocity, p is the pressure and ρ_f the fluid density.

The two left-hand terms represent inertial fluid forces whilst the first of the right-hand expressions is for pressure forces and the second and third are viscous stress terms. From the continuity equation (i.e. conservation of mass) one has:

$$\frac{\partial u}{\partial x} + \frac{\partial v}{\partial y} = 0 \qquad (3.1\text{-}36)$$

An order of magnitude estimate of terms shows that;

$$u = 0(U)$$

$$\frac{\partial}{\partial x} = 0(\frac{1}{x})$$

$$\frac{\partial}{\partial y} = 0(\frac{1}{\delta})$$

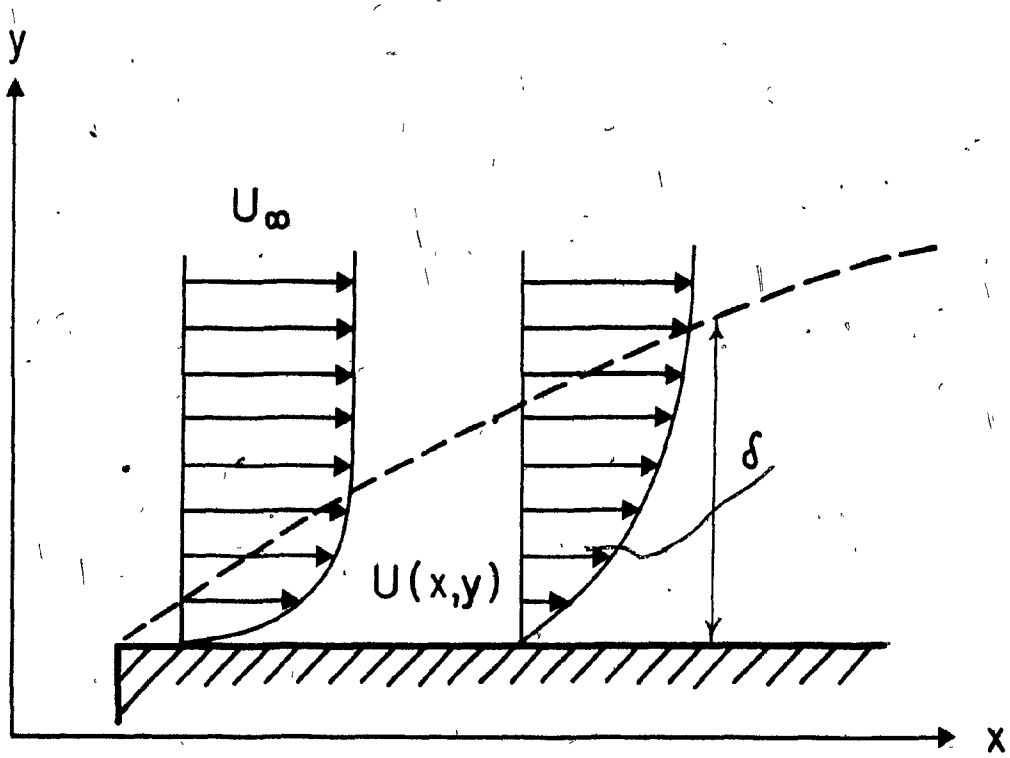

3-5 Development of a boundary layer of thickness δ from the leading edge of a flat plate.

where U is the velocity of the outer stream (i.e. beyond the boundary layer). Hence;

$$\frac{\partial u}{\partial x} = 0(\frac{U}{x})$$

and from the continuity equation;

$$\frac{\partial v}{\partial y} = 0(\frac{U}{x})$$

and

$$v = 0(\frac{U\delta}{x})$$

With these estimates the relative sizes of the terms in Equations (3.1-35a,b) become;

$$\frac{U^2}{x} + \frac{U^2}{x} = -\frac{1}{\rho_f}\frac{\partial p}{\partial x} + \nu\frac{U}{x^2} + \nu\frac{U}{\delta^2} \qquad (3.1\text{-}37a)$$

and

$$\frac{U^2}{x}\delta + \frac{U^2\delta}{x} = -\frac{1}{\rho_f}\frac{\partial p}{\partial y} + \nu\frac{U\delta}{x^3} + \nu\frac{U}{\delta x} \qquad (3.1\text{-}37b)$$

In Equation (3.1-37a) the first of the viscous stress terms is seen to be much smaller than the second and can be dropped. Hence, the x-component N-S equation becomes:

$$u\frac{\partial u}{\partial x} + \nu\frac{\partial u}{\partial y} = -\frac{1}{\rho_f}\frac{\partial p}{\partial x} + \nu\frac{\partial^2 u}{\partial y^2} \qquad (3.1\text{-}38a)$$

Upon comparing like terms of Equations (3.1-37a,b) it is seen that the inertia and viscous terms of the y-component equation are all

smaller by a factor $\frac{\delta}{x}$. They can, therefore, be neglected relative to the x-component terms and Equation (3.1-35b) is reduced to simply:

$$0 = -\frac{1}{\rho_f}\frac{\partial p}{\partial y}$$

This shows the pressure distribution in the boundary layer to be independent of the y-coordinate and the assumption is made that p simply equals the pressure in the outer flow. The relevant boundary layer equations are, therefore, (3.1-38a) and (3.1-36).

If the outer flow is a potential flow, the Bernoulli equation is valid, whence;

$$\frac{p}{\rho_f} + \tfrac{1}{2}U^2 = \text{constant}$$

from which:

$$-\frac{1}{\rho_f}\frac{\partial p}{\partial x} = U\frac{dU}{dx}$$

Substituting this result into Equation (3.1-38a) leads to an alternative form for the boundary layer equation:

$$u\frac{\partial u}{\partial x} + v\frac{\partial u}{\partial y} = U\frac{dU}{dx} + v\frac{\partial^2 u}{\partial y^2} \qquad (3.1\text{-}39)$$

The boundary conditions accompanying these equations are:

i) the no-slip condition at the wall, and

ii) the requirement that the velocity, u, must return to the outer flow velocity, U, far from the surface.

Strictly speaking, these relationships should not be used too near the leading edge (i.e. front stagnation point) of flow since the assumptions are no longer valid there. It can also be shown that the required assumption $\delta/x << 1$, is equivalent to $Re_w >> 1$.[56] As the Reynolds number approaches unity, the applicability of the boundary layer equations becomes more suspect. As already shown, there exist potential situations of slow flow rates and fine wires in hgms where this limitation would apply.

Solutions to the Boundary Layer Equations

These can be divided into exact and approximate types. Exact solutions are complete at all points over the entire range of the boundary layer and can be obtained by either analytical or numerical methods. However, there are relatively few exact analytical solutions due to the complexities of the non-linear equations involved.

Approximate solutions, on the other hand, satisfy the differential equations of motion only in the average over the boundary layer thickness. Integral relations such as momentum or energy equations provide mean value functions which can then be integrated over the boundary layer. In complex flow situations, these approximate methods often provide the only realistic means of obtaining boundary layer information. A popular approximate method is that by Karman and Polhausen[57,58], who use a fourth-order polynomial to represent the velocity profile in conjunction with the general momentum integral.

Exact solutions are available for a number of well defined situations such as flow over plates, wedges, cylinders, spheres and in wakes, laminar jets and channels. Finite difference and implicit methods

have been developed for solution by computers and these are considered to be as accurate as the analytical method.

For the case of a cylindrical body in a fluid stream with flow perpendicular to its axis there exists a particularly convenient method of analytical solution known as the Blasius solution.[59] It seemed appropriate, therefore, to try this approach in defining shear stress in the boundary layer since the required functions were readily available in the literature.

Blasius Solution[59]

In order to reduce the two boundary layer equations (Equations (3.1-36),(3.1-39)) to a single equation, a stream function, ψ, is introduced such that:

$$u = \frac{\partial \psi}{\partial y} \quad , \quad v = -\frac{\partial \psi}{\partial x}$$

Hence, Equations (3.1-36) and (3.1-39) are reduced to;

$$\frac{\partial \psi}{\partial y}\frac{\partial^2 \psi}{\partial x \partial y} - \frac{\partial \psi}{\partial x}\frac{\partial^2 \psi}{\partial y^2} = U\frac{dU}{dx} + \nu\frac{\partial^3 \psi}{\partial y^3} \qquad (3.1\text{-}40)$$

with the accompanying boundary conditions;

i) $\frac{\partial \psi}{\partial y} = 0 \quad , \quad \frac{\partial \psi}{\partial x} = 0 \qquad$ at $y = 0$

and

ii) $\frac{\partial \psi}{\partial y} = U(x) \qquad$ at $y = \infty$

Blasius' method now makes use of a power series expansion to define the outside potential flow about the cylinder, U(x). At the cylinder wall, the assumption is made that $\delta << a$. Hence, the following is obtained from Equation (3.1-30b):

$$U(x) = -U_\theta\Big|_{r=a} = 2U_\infty \sin\theta \qquad (3.1\text{-}41)$$

After introducing the expansion for sin θ, Equation (3.1-41) becomes;

$$U(x) = 2U_\infty\left(\theta - \frac{\theta^3}{3!} + \frac{\theta^5}{5!} - \frac{\theta^7}{7!} + \frac{\theta^9}{9!} - \frac{\theta^{11}}{11!} + \ldots.\right) \qquad (3.1\text{-}42)$$

for $\theta(=\frac{x}{R})$ in radians. The approximation to Equation (3.1-41) for successively including more terms in Equation (3.1-42) is shown in Figure (3-6). It is seen that the series as far as θ^5 (P^5 in the diagram) is sufficiently accurate in describing the sine function between 0^o and 90^o, the region of interest. In the present analysis the set of terms up to and including θ^{11} is used as the solution was readily available.

In analogy with Equation (3.1-42) the stream function is also chosen as a power series in making use of a similarity type of solution. Hence;

$$\psi(x,y) = \phi(\xi)$$

where

$$\xi = \frac{y}{r}\left(\frac{2U_\infty r}{\nu}\right)^{1/2}$$

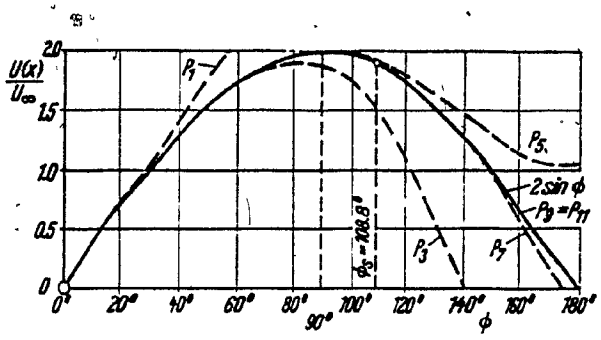

3-6 Approximations to the potential velocity distribution around a cylinder for including successively more terms in the expansion for sin ϕ in Equation (3.1-42) (from Schlichting).

and the boundary conditions have been adjusted accordingly. Expressions for u and v in terms of ψ are then obtained and substituted back into boundary layer Equation (3.1-41). The resulting system of simultaneous ordinary differential equations may be numerically solved to a high degree of accuracy and are considered to be exact solutions. Tabled values of the results, applicable to any symmetrically cylindrical shape, are provided by Schlichting.(60)

The shear stress at the wall, τ_o, can be found, since ψ is now known, from:

$$\tau_o = \eta \left.\frac{\partial u}{\partial y}\right|_{y=0}$$

$$= \eta \left.\frac{\partial^2 x}{\partial y^2}\right|_{y=0}$$

This leads to the following expression, valid from the stagnation point to the position of boundary layer separation:

$$\frac{\tau_o}{\frac{1}{2}\rho_f U_\infty^2}\left(\frac{U_\infty r}{\nu}\right)^{1/2} = 6.973\theta - 2.732\theta^3 + 0.292\theta^5 - .0183\theta^7$$

$$+ .000043\theta^9 - .000115\theta^{11} \qquad (3.1\text{-}43)$$

Note that the shear stress has been made dimensionless by means of the kinetic energy of the free stream, $\frac{1}{2}\rho_f U_\infty^2$. Sometimes called the 'dynamic pressure', it is a concept familiar in the application of the Bernoulli equation. Equation (3.1-43) is presented as curve A in Figure (3-7) which shows the site of maximum shear to occur

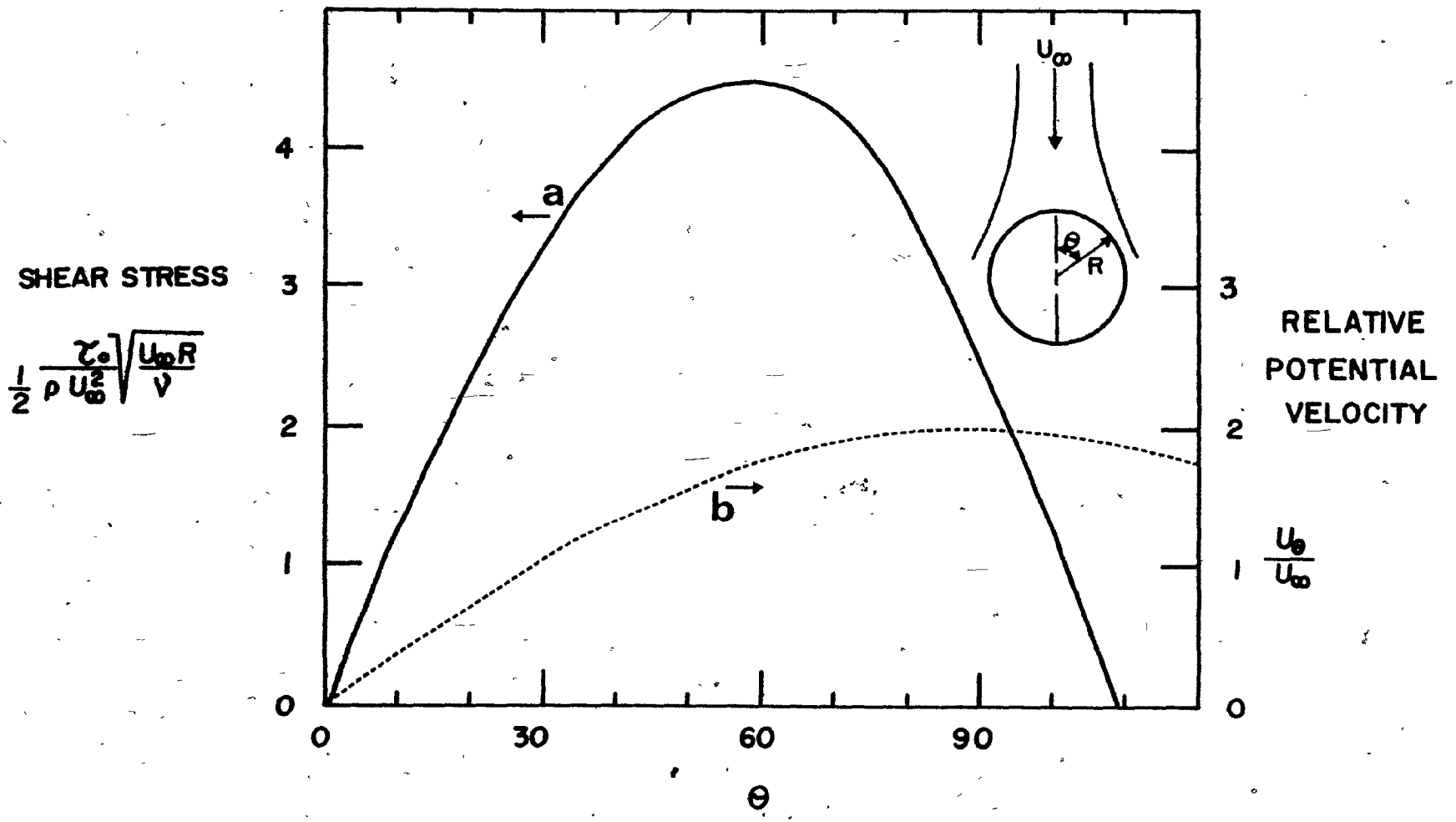

3-7 Variation in non-dimensional shear stress and relative potential velocity over the front of a cylinder.

at about 59°. Those models (i.e. Luborsky et al.[22], Liu et al.[41]) having average boundary layer thicknesses and adjusted velocities based on the outer flow velocity (U_∞) will have shear on particles varying in proportion to curve B in Figure (3-7) showing a maximum at 90°.

Note also that the point of separation for curve A where the shearing stress is no longer present since the boundary layer has lifted from the wall due to the adverse pressure gradient, occurs at approximately 109°. This is considerably beyond the region of interest for upstream modelling of particle buildup. For smooth cylinders, transition from a laminar boundary layer to a turbulent one begins at an Re_w of the order $3x10^5$ [61], well in excess of those encountered in hgms.

Drag Force on a Particle

The drag force, F_D, which results from a shear stress, τ_o, acting on an area, A, can readily be obtained by integration:

$$F_D = \int \tau_o dA \qquad (3.1\text{-}44)$$

By assuming that τ_o for a cylinder acts in a similar fashion on the 'wall of particles' building on a wire the drag force on a single particle has been determined in the following manner.

Consider the situation in Figure (3-8). A monolayer of particles of radius b resides on the surface of a wire of radius, a, with the stipulation that b is considerably less than a. One can assume that the disturbance to the boundary layer will be slight if the amplitude of the surface roughness, $\approx$ b, is small compared to the thickness

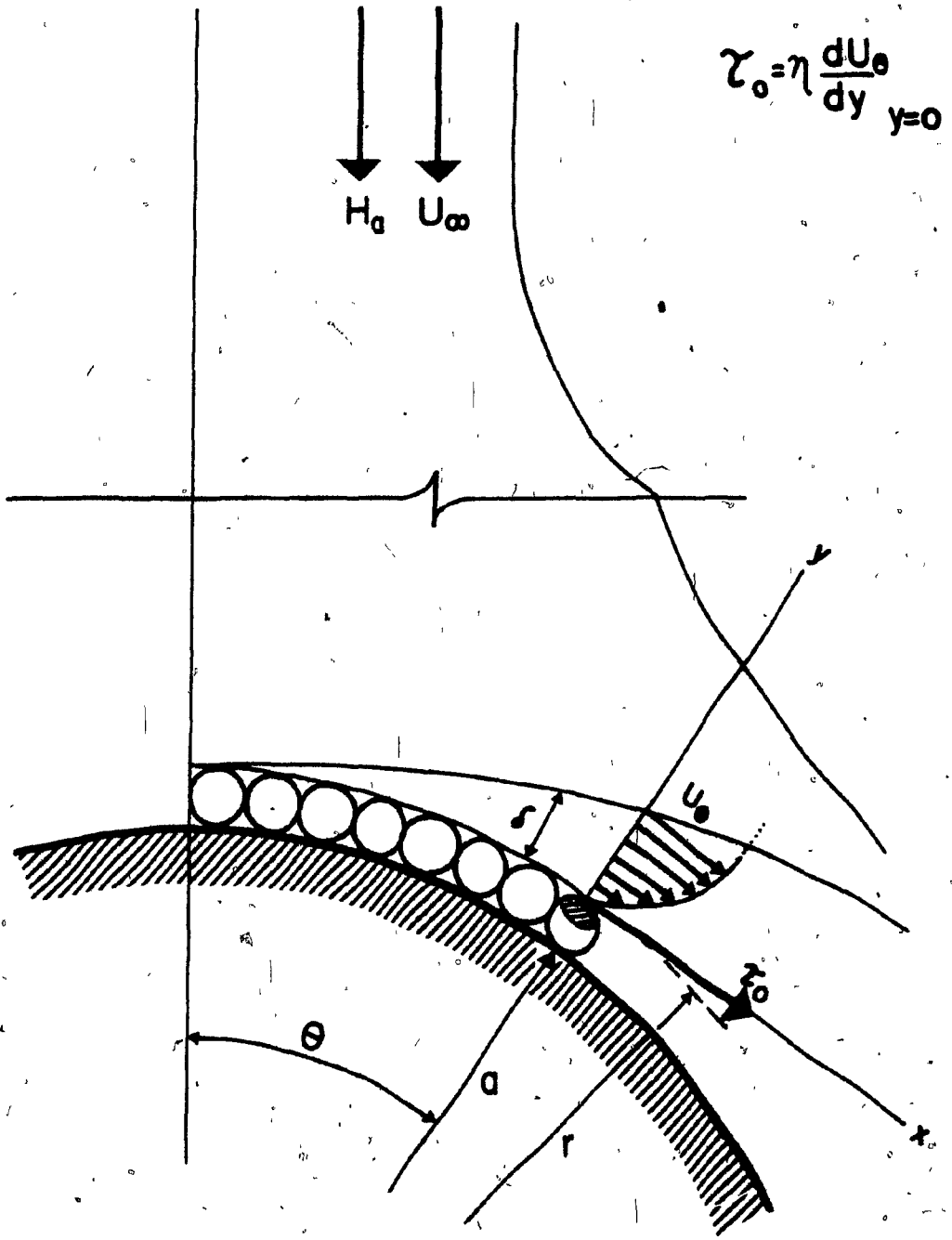

3-8 Shear stress (τ_o) acting on spherical particle residing at bottom of boundary layer on a cylinder.

of the boundary layer, δ. Very near the front stagnation point this condition will not be met since δ is very small. Calculations show that, typically, for 600 μm diameter wire at 10 cm/s flow rate, δ varies from 20 to 50 μm over the remaining portion of the cylinder front. A 10 μm particle would, therefore, yield a δ/b of from 0.25-0.1 and this roughness can be expected to give a somewhat larger τ_o than for the smooth case. However, the analysis is complex[62] and for low and moderate Re_w (say, < 2000) should not lead to appreciable error in τ_o if calculated with Equation (3.1-43).

The assumption is then made that τ_o is constant on any given particle thus permitting Equation (3.1-44) to be written:

$$F_D = f_b 4\pi b^2 \tau_o \qquad (3.1\text{-}45)$$

Assuming spherical particles, f_b is the fraction of the total surface ($4\pi b^2$) on which τ_o acts. To determine f_b one approach is to integrate the x-component of shear, $\tau_o \sin\theta$, over the upper half of the sphere, and divide by $4\pi b^2 \tau_o$. Hence[63],

$$f_b = \frac{\tau_o b^2}{4\pi b^2 \tau_o} \int_0^{\pi} \int_0^{\pi} \sin^2\theta \, d\theta d\phi$$

$$= \frac{\frac{\pi^2 b^2}{2}}{4\pi b^2}$$

$$= \frac{\pi}{8}$$

$$\approx 0.39 \qquad \text{.....(3.1-46)}$$

Arguably, eddy pools in the crevasses between particles should be considered which could reduce f_b below 0.39. The projected area of the spheres parallel to the flow, πb^2, might also be used thereby yeilding an f_b of 0.25. As no clear cut preference could be found the larger value was chosen.

An alternative form of Equation (3.1-45) is:

$$F_D = \frac{\pi^2}{2} b^2 \tau_o \qquad (3.1\text{-}47)$$

This relationship plus Equation (3.1-43) is then sufficient to describe the fluid drag on a single particle taking into account the changes in boundary layer behavior on the cylinder, i.e.:

$$F_D = \frac{\pi^2 b^2}{4} \rho_f U_\infty^{3/2} \left(\frac{\nu}{r}\right)^{1/2} (6.973\theta - 2.732\theta^3 + 0.292\theta^5 - .0183\theta^7 + .0000439\theta^9 - .000115\theta^{11}) \qquad .....(3.1\text{-}48)$$

A comparison between the fluid drag resulting from Equation (3.1-48) with that predicted by Stokesian drag with an averaged boundary layer thickness, $\delta = \left(\frac{\pi\nu r}{U_\infty}\right)^{1/2}$, as modelled by Luborsky and Drummond[22] and Liu et al.[41] is shown in Figure (3-9). The drag force, F_D, has been normalized to give;

$$\frac{F_D}{b^2 \frac{1}{2} \rho_f U_\infty^2} \left(\frac{U_\infty r}{\nu}\right)^{1/2}$$

in order that the curves be a function of θ only, the location on the wire. It is seen that the Blasius approach (curve A) predicts consider-

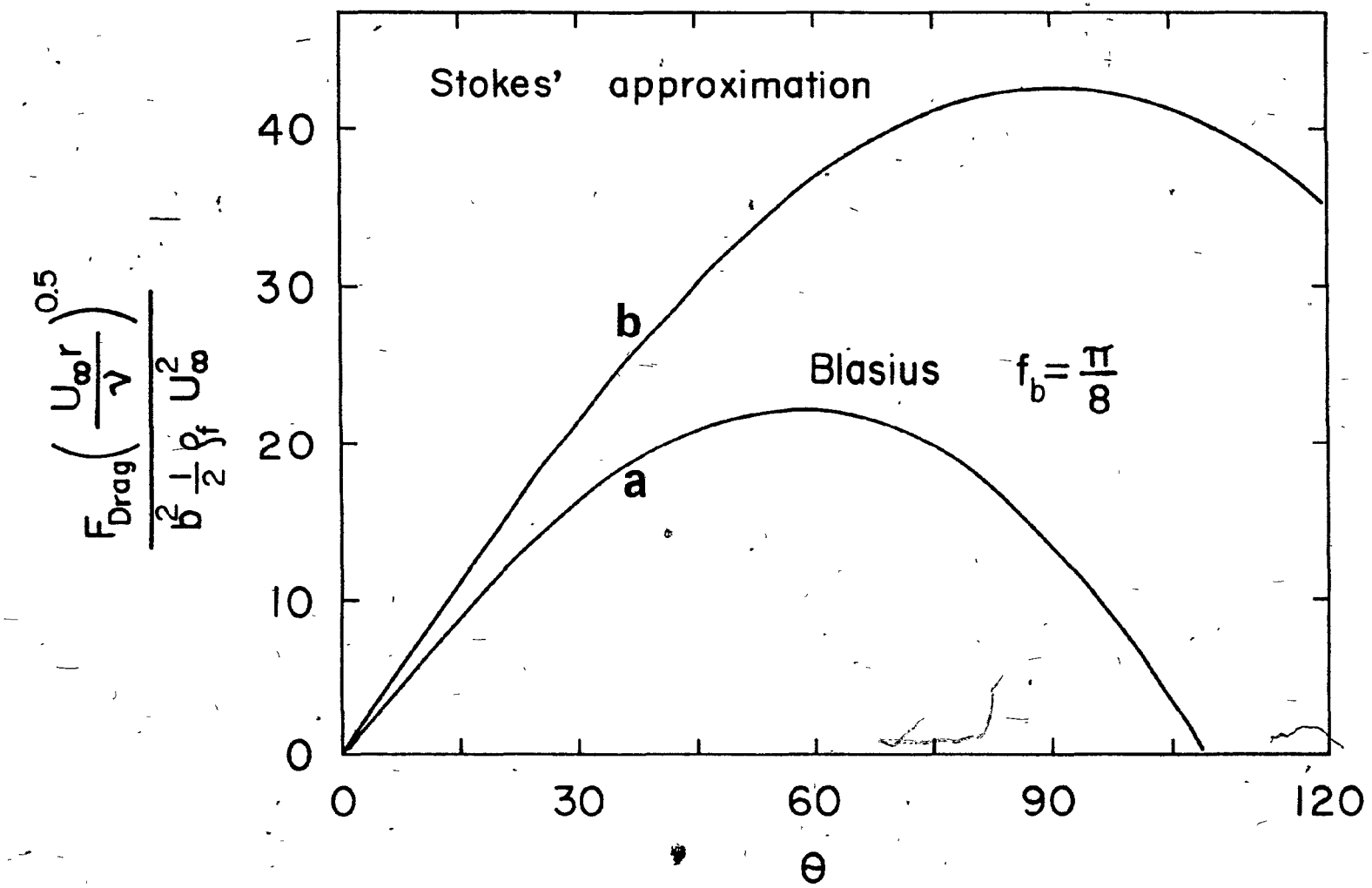

3-9 Non-dimensional drag force on spherical particle comparing Stokesian drag and an average boundary layer thickness with the Blasius solution having $f_b = .39$.

ably less shear on the particles than does modified Stokesian drag (curve B). The difference becomes increasingly significant for increasing θ, particularly beyond 45^{o}. As buildup in this sector (i.e. $> 45^{o}$) may be expected, the necessity for correctly modelling the fluid drag is self-evident.

3.1.3 Gravitational Force

The total gravitational force acting on a body is proportional to its mass;

$$F_{G_{total}} = - \text{mass } g$$

where g is the gravitational constant, usually taken as 980 cm/s^2. If the body is immersed in a fluid of density, ρ_f, an opposing buoyancy force, F_B, equal to the mass of the displaced fluid also acts, i.e.:

$$F_B = \text{volume } \rho_f g$$

Hence, the net gravitational force, F_G, is the sum of both effects, viz;

$$F_G = - \text{volume } (\rho_p - \rho_f)g$$

where ρ_p is the density of the body. For a sphere of radius b this net force becomes;

$$F_G = -\frac{4\pi b^3}{3}(\rho_p - \rho_f)g \qquad (3.1\text{-}49a)$$

and, when transformed into cylindrical coordinates:

$$F_{\theta_G} = \frac{4\pi b^3}{3}(\rho_p - \rho_f)g \sin\theta \qquad (3.1\text{-}49b)$$

$$F_{r_G} = -\frac{4\pi b^3}{3}(\rho_p - \rho_f)g \cos\theta$$

3.2 Development of the Model

3.2.1 Buildup on a Unit Length of Wire

In order to justify a static approach to material buildup the assumption is made that a particle has arrived at the wire surface and is stationary, at least momentarily. The issue as to how it has arrived, whether impacting from the fluid or migrating from an adjacent location, is not considered. If the net resultant of magnetic, gravitational, and fluid shear forces is toward a region of greater attractive force, then the particle remains on the wire, if not, it will be swept away. The surface where these forces are in equilibrium defines the so-called 'equilibrium profile' of the buildup, from which the maximum loading per unit length of wire may be readily determined. This idealized situation, with forces resolved into tangential and radial components, is illustrated in Figure (3-10).

θ-components

The net tangential force, $F_{\theta_{net}}$, is given by the summation of magnetic, gravity and fluid shear terms, i.e.:

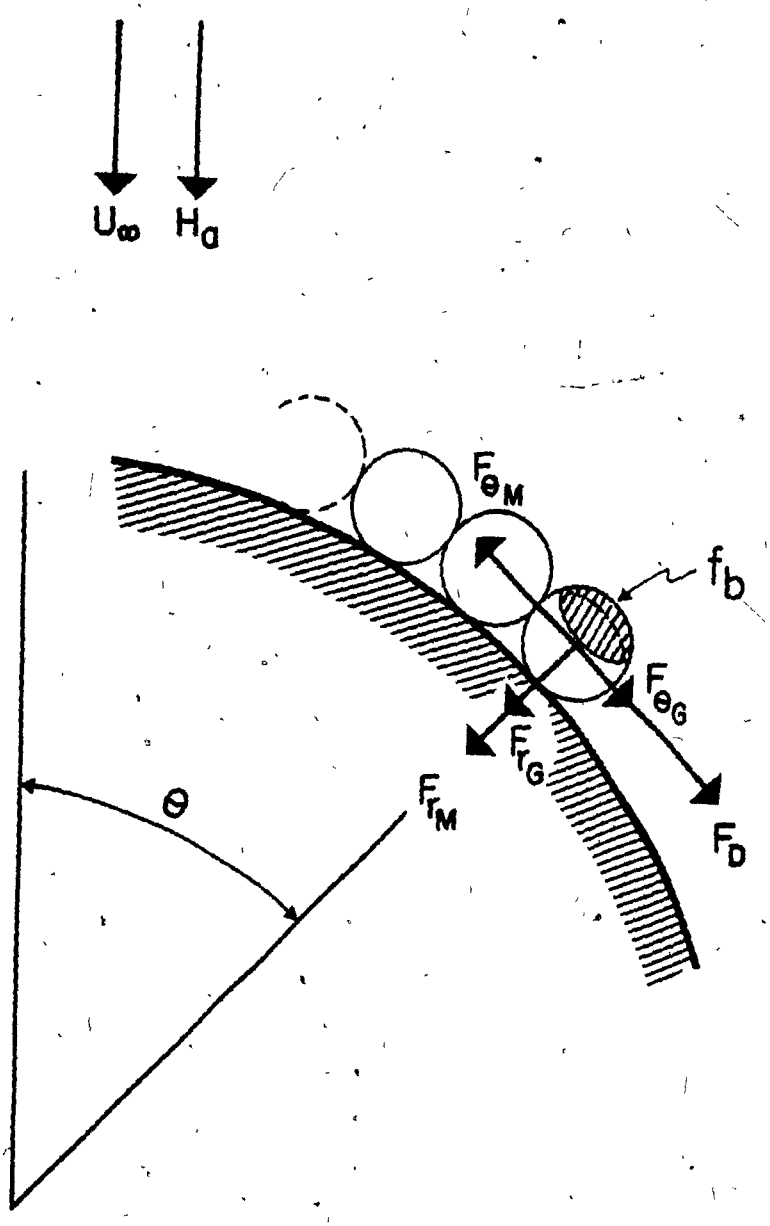

3-10 Force components acting on a spherical particle at rest on the cylinder wall.

$$F_{\theta_{net}} = F_{\theta_M} + F_{\theta_G} + F_D$$

Upon substitution for the individual forces (Equations (3.1-26b,49b,48)) this becomes:

$$F_{\theta_{net}} = -2VH_a \frac{Aa^2}{r^3} \sin 2\theta(K_\infty H_a + fM_o) + V(\rho_p - \rho_f)g \sin\theta + \frac{\pi^2 b^2 \rho_f}{4} U_\infty^{3/2} \frac{\nu^{1/2}}{r^{1/2}}(6.973\theta - 2.732\theta^3 + .292\theta^5 - .0183\theta^7 + .000043\theta^9 - .000115\theta^{11}) \quad .....(3.2\text{-}1a)$$

r-components

The net radial force, $F_{r_{net}}$, is comprised of magnetic and gravity terms only, hence:

$$F_{r_{net}} = F_{r_M} + F_{r_G}$$

After substituting for the individual forces (Equations (3.1-26a,49c)) one obtains:

$$F_{r_{net}} = -2VH_a \frac{Aa^2}{r^3}(\cos 2\theta + \frac{Aa^2}{r^2})(K_\infty H_a + fM_o) - V(\rho_p - \rho_f)g \cos\theta \quad .....(3.2\text{-}1b)$$

An attached particle will experience an attraction both radially toward the wire and tangentially toward the front stagnation point. By solving for θ at increasing r for the conditions $F_{\theta_{net}}$ and

$F_{r_{net}} = 0$ two sets of critical angles, θ_c, defining the regions of particle attraction about the wire will result. The loci of θ_c's are shown for the general case in Figure (3-11). Since a negative total net force is required for buildup (thereby satisfying both the aforementioned criteria) the equilibrium profile may be expected to follow the $F_{r_{net}} = 0$ curve (in Figure (3-11)) for initial layers and the $F_{\theta_{net}} = 0$ curve (in Figure (3-11)) for the final layers of accumulation.

Accomodating Particle Buildup

A discrete, layer-by-layer approach, as suggested by Luborsky[20] is used in adjusting the radius of buildup, r. By presuming that buildup occurs one layer at a time, it is implied that the profile of wire plus particles remains cylindrical from the point of view of the fluid flowing over the front. Although flow patterns and shear stresses at the sides and back will alter as a result of buildup, the upstream pressure distribution, and hence τ_o and U_∞, remain largely the same irrespective of changes occurring downstream.[64] A recent study of buildup shape by Watson[32] found that if the frontal surface, divided into numerous segments, was allowed to grow in proportion to the particle retention probability of each segment, the resulting shape was indeed similar to that of an expanding cylinder. This result also agrees with the time-sequence photographs in Figure (2-10) from Friedlaender et al.

It is felt that considerable evidence has accumulated to support the layer-by-layer approach as being both realistic as well as conceptually useful for calculation purposes.

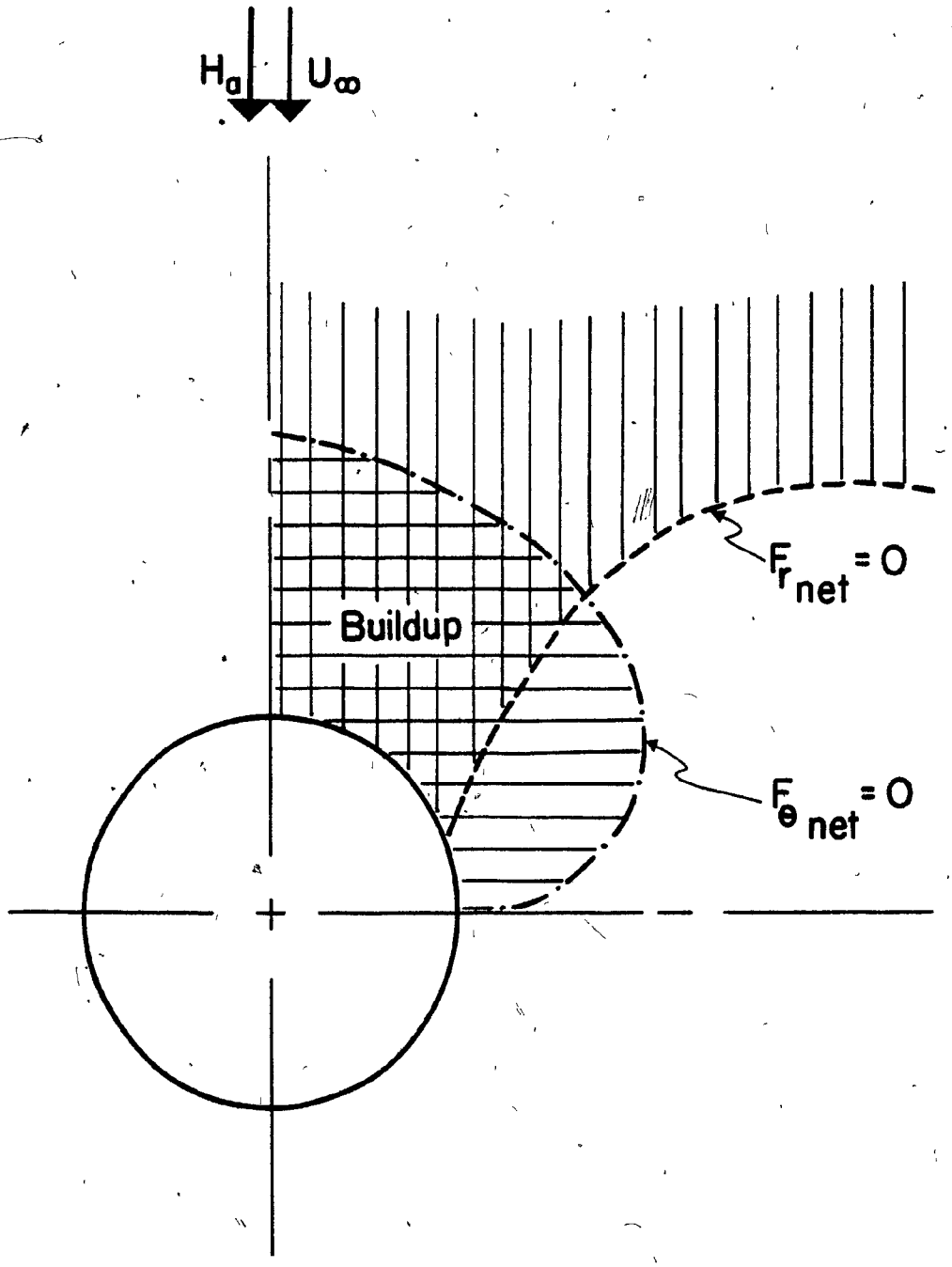

3-11 Loci of zero net radial and tangential forces in one quadrant about wire. Hatched regions show negative net force.

The distance from the centre of the wire, of radius a, to the centre of a particle, of radius b, on the n^{th} layer may be written;

$$r_n = a + b + (n - 1)b\ell \qquad (3.2\text{-}2)$$

where ℓ is the interlayer distance defined as:

$$\ell = \frac{\text{distance between the particle centres of adjacent layers}}{b}$$

A close-packing arrangement having $\ell = \sqrt{3}$ was assumed which is equivalent to a packing fraction of .698 or about 70% filling of the volume. In comparison, the void filling of randomly loose-packed spheres has been reported as around 55% by Kelly.[65] Empirical evidence of Friedlaender et al.[38] suggests a maximum packing efficiency of roughly 70% for buildup of various closely-sized oxides for the parallel stream configuration; while the theoretical maximum packing fraction for single-sized spheres has been reported as 74.1%.[66] The distance between adjacent rows of particles along the wire has also been taken as $b\ell$.

The effect on ℓ of a changing r as n increases is considered sufficiently small in comparison with ℓ itself to be neglected. It is also recognized that although the forces are assumed to be acting at the particle centre of mass the fluid shear acts on a surface somewhat further out. This small increase in radius has a minimal effect on decreasing the magnitude of F_D.

Once the minimum critical angle for each of the n layers, θ_n, has been determined (Equations (3.2-1a,b)) the total mass of particles per unit length of wire under fully loaded conditions, L_m, can be found from;

$$L_m = 2 \sum_{n=1}^{N} \left(\frac{2\pi b r_n \theta_n \rho_p}{3\ell}\right) \qquad (3.2\text{-}4)$$

where θ_n is in radians and ρ_p is the particle density. The factor of 2 arises from buildup on both sides of the stagnation point. It will also prove useful to define two additional loading parameters, γ_m and γ_v, relating the mass and volume of material per unit mass and volume of wire, respectively. Hence,

$$\gamma_m = \frac{L_m}{\pi a^2 \rho_w} \qquad (3.2\text{-}5)$$

and

$$\gamma_v = \gamma_m \frac{\rho_w}{\rho_p} \qquad (3.2\text{-}6)$$

where ρ_w is the wire density.

Development of a Loading Number

A significant simplification in the model predictions would be achieved if the loading could be related to a dimensionless 'loading number' much as Watson attempted to relate R_c and loading to the $\frac{V_M}{U_\infty}$ ratio.

Figure (3-11) suggests that buildup may be represented, to a first approximation, by a 90^o segment of constant radius r. The magnitude of r will roughly be determined by the curve $F_{\theta_{net}} = 0$, i.e. from

Equation (3.2-1a);

$$0 = -2VH_a^2 \kappa \frac{Aa^2}{r^3} \sin 2\theta + V(\rho_p - \rho_f) g \sin \theta + \frac{2\pi b^2 \rho_f U_\infty^{3/2} \nu^{1/2}}{r^{1/2}} \{B'\} f_b \quad \ldots\ldots (3.2\text{-}7)$$

where κ is the (field dependent, if applicable) susceptibility;

$$\{B'\} = \{6.973\theta - 2.732\theta^3 + .292\theta^5 - .0183\theta^7 + .000043\theta^9 - .000115\theta^{11}\},$$

and

$$f_b = \frac{\pi}{8}$$

Dividing through by $\frac{4\pi b^2}{3} \frac{\rho_f U_\infty^{3/2} \nu^{1/2}}{r^{1/2}}$ will result in a more convenient dimensionless form for Equation (3.2-7). Also, since maximum buildup is being considered it is sufficient to evaluate the above quantities at their location of maximum value over the range 0^o-45^o; namely at $\theta = 45^o$. Hence, Equation (3.2-7) becomes:

$$0 = -\frac{2bH_a^2 \kappa Aa^2}{\rho_f U_\infty^{3/2} \nu^{1/2} r^{5/2}} + \frac{b(\rho_p - \rho_f) g r^{1/2}}{\sqrt{2}\, \rho_f U_\infty^{3/2} \nu^{1/2}} + \underbrace{\frac{3}{2}\{4.24\} f_b}_{C = 2.50 \text{ (fluid)}} \quad (3.2\text{-}8)$$

(magnetic) (gravity)

By first considering only the magnetic and gravity terms and rearranging it can be shown that:

$$r_a^2 = \left(\frac{r}{a}\right)^2 = \left(\frac{2\sqrt{2}\, H_a^2 \kappa A}{a(\rho_p - \rho_f)g}\right)^{2/3}$$

$$= N_G^{2/3}$$

This is the desired order for r since nominal buildup volume (i.e. assuming 100% filling) can be related to r_a^2.

For a typical case of hematite recovery (viz; $H_a = 3000$ Oe, $\kappa = .000654$ emu/cm^3-Oe, $A \simeq 0.9$, $a = .04$, $\rho_p = 5.25$ g/cm^3, $\rho_f = 1$ g/cm^3, $g = 980$ cm/sec^2)N_G, the ratio of magnetic to gravity force in equilibrium at r_a, has a value of 90. This large N_G suggests that for the purpose of approximation the gravity term in Equation (3.2-8) may be neglected.

By equating magnetic and fluid terms only it can be readily shown upon rearranging Equation (3.2-8) that;

$$r_a^2 = \left(\frac{r}{a}\right)^2 = \left(\frac{2bH_a^2 \kappa A}{\rho_f U_\infty^{3/2} \nu^{1/2} a^{1/2}} \frac{1}{C}\right)^{4/5} = \left(N_L \cdot \frac{1}{C}\right)^{4/5} \qquad (3.2\text{-}10)$$

where

$$N_L = \frac{2bH_a^2 \kappa A}{\rho_f U_\infty^{3/2} \nu^{1/2} a^{1/2}} \quad \text{and} \quad C = 2.5 \qquad (3.2\text{-}11)$$

N_L is termed the loading number. It represents the ratio of magnetic to fluid shear forces required for an equilibrium buildup of radius r_a. A value of N_L equal to C would have r = a (i.e. bare wire) and suggests that a minimum loading number for buildup might be so defined (i.e. $N_{L_{min}} = C = 2.50$).

The nominal buildup volume per unit length of wire, V_B, is simply;

$$V_B = \frac{\pi r^2}{4} - \frac{\pi a^2}{4}$$

and when divided by the wire volume, πa^2, becomes;

$$\frac{V_B}{\pi a^2} = \frac{\text{Vol. buildup}}{\text{Vol. wire}} = \frac{1}{4}(r_a^2 - 1) \qquad (3.2\text{-}12)$$

where $r_a = \frac{r}{a}$

Converting from nominal to actual volume and mass of particles per cm^3 of wire requires a packing fraction, ε, whence;

$$\gamma_v = \frac{\varepsilon}{4}(r_a^2 - 1) \qquad (3.2\text{-}13)$$

and

$$\gamma_m = \frac{\varepsilon}{4}(r_a^2 - 1)\frac{\rho_p}{\rho_w} \qquad (3.2\text{-}14)$$

where ρ_w and ρ_p are wire and particle densities, respectively. Replacing r_a^2 in Equations (3.2-13,14) yields the following for the loading parameters γ_v and γ_m:

$$\gamma_v = \frac{\varepsilon}{4}\{(\frac{N_L}{C})^{4/5} - 1\}(\frac{cm^3 \text{ particles}}{cm^3 \text{ wire}}) \qquad (3.2\text{-}15)$$

$$\gamma_m = \frac{\varepsilon}{4}\{(\frac{N_L}{C})^{4/5} - 1\}\frac{\rho_p}{\rho_w}(\frac{g \text{ particles}}{g \text{ wire}}) \qquad (3.2\text{-}16)$$

These relationships suggest that the loading of the wire may be quantified by one dimensionless grouping, N_L.

N_L may be split into the more familiar groupings already discussed; the a to b ratio, the wire Reynolds number, Re_w, and the magnetic to fluid velocity ratio, $\frac{V_M}{U_\infty}$. Hence;

$$N_L = \frac{9}{\sqrt{2}}\left(\frac{a}{b}\right)\left(\frac{1}{Re_w}\right)^{1/2}\frac{V_M}{U_\infty} \qquad (3.2\text{-}17)$$

where $$\frac{V_M}{U_\infty} = \frac{4b^2\kappa H_a{}^2 A}{9a\eta U_\infty}$$

and $$Re_w = \frac{2aU_\infty\rho_f}{\eta}$$

Liu et al.[41] have shown for $\frac{a}{b}$ not large and Stokesian particle drag that $r_a{}^2$ is dependant upon $\left(\frac{V_M}{U_\infty}\right)^{2/3}$. The preceeding analysis shows that when boundary layer considerations are important, namely at greater $\frac{a}{b}$ and Re_w considerably above unity, these additional groupings assume importance and enter into the expression.

3.2.2 Recovery Through a Length of Wire Screens

It now remains to extend the analysis for maximum buildup on a unit length of wire to predictions of how a regular assemblage of wires will recover particles. Consider the matrix constructed in a regular fashion as shown in Figure (3-12) with uniform flow velocity, U_∞, throughout the cross-sectional area, A_x. This configuration is typical of expanded metal matrices.

For the modelling, U_∞ remains unchanged throughout the separator volume, no magnetic interactions between wires are considered and buildup on a given screen proceeds without interference from any

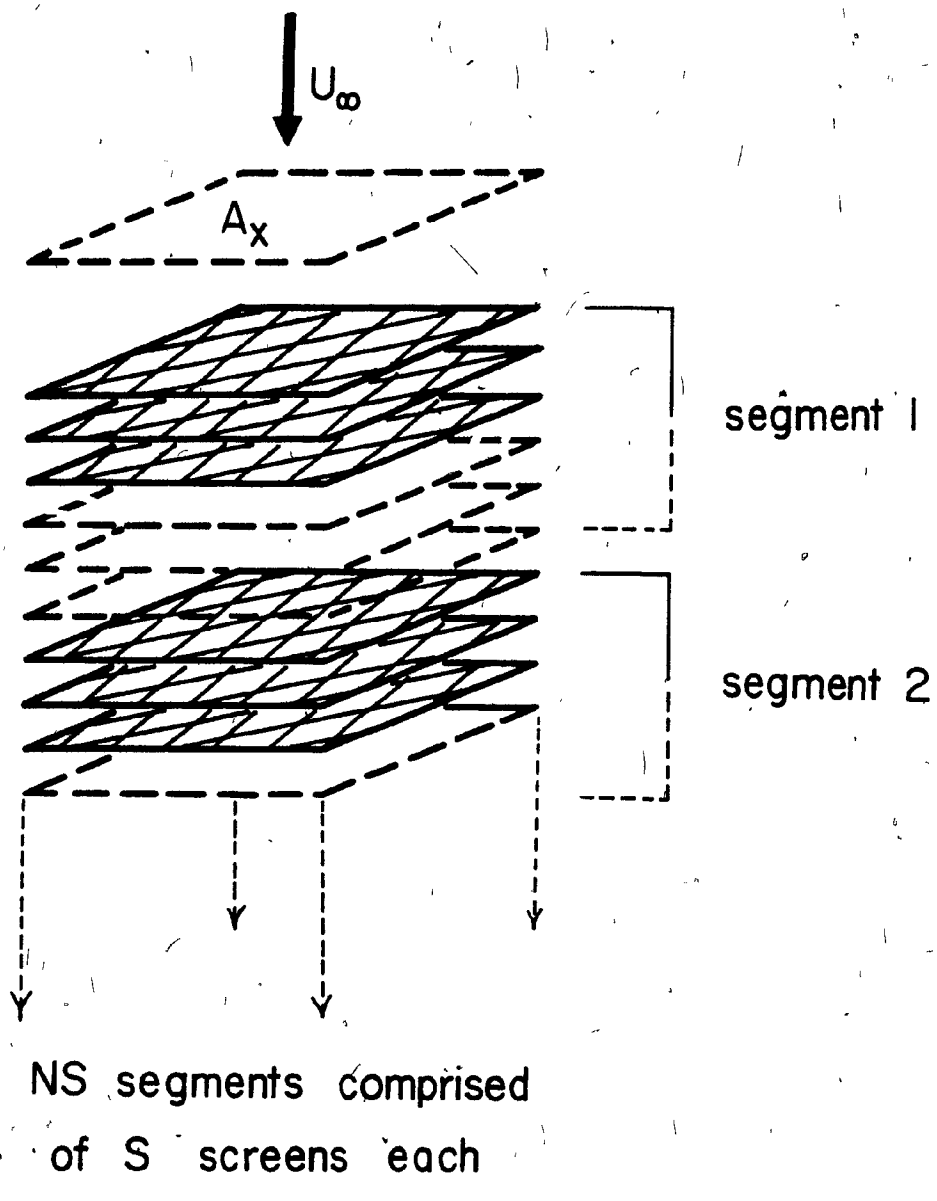

3-12 The piecewise nature of the matrix. A total of NS segments, each segment comprised of S screens.

other. Although each of these factors can be expected to have some effect they are judged to be of secondary importance.

Equations of Recovery

Consider again the situation in Figure (3-13). It is convenient to deal with the matrix in a piecewise manner; i.e. on the basis of NS segments, each segment comprised of S screens behaving identically. This approach simplifies the development of the equations and bears a physical resemblance to the actual situation. In principle, therefore, the recovery on a single screen could be measured. A cautionary note is that there must be sufficiently greater numbers of segments than screens per segment for all but the simplest situations in order that the analysis be valid.

At time, t, in an increment, dt, the amount of material retained within a segment, n, will be;

$$dms(n)_t = \dot{m}(n)_t A_f(n)_t S\, dt \qquad (3.2\text{-}18)$$

where $A_f(n) = \dfrac{\text{effective capture area of } n^{th} \text{ screen}}{A_x}$

$\dot{m}(n)$ = flux of particles to the n^{th} segment

S = screens per segment

If $A_f(n)$ remains constant with respect to time, $\dot{m}(n)$ becomes simply;

$$\dot{m}(n) = \dot{m}_o(1 - A_f)^{n-1}$$

where $\dot{m}_o$ is the flux to the first segment. For the more general case where $A_f(n)$ changes with time, t, the flux to the n^{th} segment may be evaluated from:

$$\dot{m}(n) = (\dot{m}_o - \sum_{i=1}^{n-1} (\frac{dms(i)}{dt})) \qquad (3.2\text{-}19)$$

Equation (3.2-18) transforms, therefore, to;

$$dms(n)_t = (\dot{m}_o - \sum_{i=1}^{n-1} (\frac{dms(i)}{dt}))_t A_f(n)_t S\, dt \qquad (3.2\text{-}20)$$

and since $\dot{m}_o$ is usually constant it is seen that only $A_f(n)_t$ needs to be determined for each segment at each increment in time.

It will prove useful to define several other loading parameters; the loading of segment n at time t;

$$L(n)_t = \sum_{o}^{t} dms(t)_n \qquad (3.2\text{-}21)$$

and the fractional loading of the same segment:

$$\frac{L(n)_t}{L_{max}} = \frac{L(n)_t}{L_m S \ell_w} \qquad (3.2\text{-}22)$$

Here, the maximum loading of a segment, L_{max}, is the product of the (mass) loading per unit length, L_m (Equation (3.2-4)), the total length of wire per screen, ℓ_w, and the number of screens per segment, S.

Fractional Capture Area of a Single Screen, A_f

The concept of a capture radius has been previously introduced (in Section 2) and it follows that each unit length of wire will have an associated "capture area" as a fraction of the total flow cross-section. Particles flowing past in the time increment, dt, will be recovered in proportion to this fraction. A screen can simply be regarded as a finite length of wire, ℓ_w, with a resulting fractional capture area, A_f, given by;

$$A_f = \frac{2R_c a \ell_w}{A_x} \cdot \beta \qquad (3.2\text{-}23)$$

where β is a geometric correction factor which allows for overlapping capture areas and is, therefore, a function of R_c and the screen geometry.

Capture Radius, R_c

Watson[17] has shown that for bare wires, R_c may be approximated by;

$$R_c = \frac{1}{2}\frac{V_M}{U_\infty} \qquad \text{for } \frac{V_M}{U_\infty} \leq (2)^{1/2} \qquad (3.2\text{-}24)$$

when the near field term in the magnetic force equation is neglected. R_c is somewhat greater at lower $\frac{V_M}{U_\infty}$ when the near field term is included; however, Equation (3.2-24) affords a reasonable approximation. For $\frac{V_M}{U_\infty}$ greater than $2^{1/2}$ the capture radius is indeterminate, a mathematical singularity, and must be solved numerically. However, Liu et al.[41] found that by neglecting the short range terms in both magnetic and

fluid drag equations R_c was given by:

$$R_c = \frac{3\sqrt{3}}{4}\left(\frac{V_M}{U_\infty}\right)^{1/3} \qquad \text{for } \frac{V_M}{U_\infty} > 1.0 \qquad (3.2\text{-}25)$$

Figure (3-14) (from Liu et al.) compares the approximations as per Equations (3.2-24,25) with the full numerical solution including the near field term (A = 1.0). For this study the simplicity in estimating R_c from these relationships precluded the complexity involved in obtaining the precise values.

To achieve a continuous set of functions for determining initial R_c, Equations (3.2-24,25) were solved simultaneously to yield $\frac{V_M}{U_\infty} = 4.19$. Hence, initial capture radius was defined as:

$$R_{c_i} = \frac{V_M}{2U_\infty} \qquad \text{for } \frac{V_M}{U_\infty} \leq 4.19 \qquad (3.2\text{-}26a)$$

$$R_{c_i} = \frac{3\sqrt{3}}{4}\left(\frac{V_M}{U_\infty}\right)^{1/3} \qquad \text{for } \frac{V_M}{U_\infty} > 4.19 \qquad (3.2\text{-}26b)$$

As shown by Luborsky and Drummond[20], and Stekly and Minervini[28] R_c will decrease with buildup as fluid is deflected further and further from the large field gradients and hence large magnetic forces in the vicinity of the wire. Various relationships exist for describing the manner in which the initial capture radius is decreased but, in general, they are either a function of the buildup radius, r_a, or of the loading ratio, $\frac{L}{L_{max}}$, of the wire. For this study the term 'driving function', given the symbol α, is applied to these relationships.

Hence, the capture radius at any time during loading will be given by:

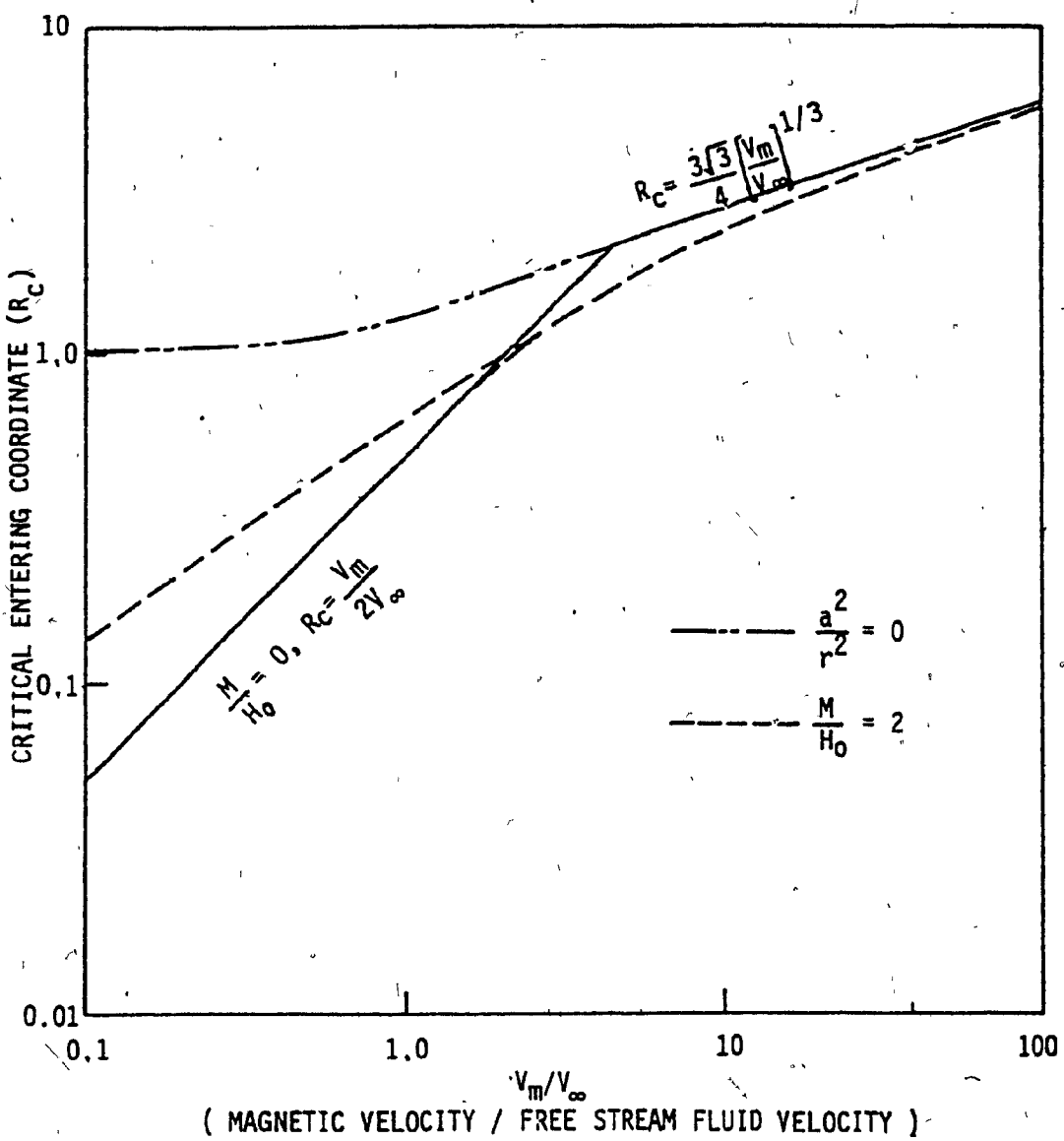

3-13 Liu et al.'s approximate solution of critical entering coordinate R_c as a function of $\frac{V_M}{U_\infty}$ $(= \frac{V_M}{V_\infty})$.

$$R_c = R_{c_i}\,\alpha \qquad (3.2\text{-}27)$$

Driving Function, α

The relationship found by Luborsky and Drummond[20] and used by others (e.g. Liu et al.[41]) for the change in R_c with increasing buildup radius, r_a, is;

$$\alpha_L = \left(\frac{1}{r_a}\right)^2$$

where $r_a = \frac{r}{a}$, and r is the radius at $\theta = 0^o$.

Watson[32] showed that α may increase initially but is for practical purposes adequately represented by α_L.

Akoto[67] has suggested a linear function based on the loading ratio, i.e.;

$$\alpha_A = 1 - \frac{L}{L_{max}}$$

Clarkson and Kelland[25] chose a function of $\frac{L}{L_{max}}$ with an exponential decrease toward zero as loading progressed toward the maximum.

It is readily seen that the Luborsky relationship does not tend to zero for maximum buildup radius, r_{as}. In practical terms, however, capture of particles has ceased so the effective R_c must by definition be zero.

Watson[31] has suggested combining a probability of sticking to the wire with the probability of arriving there, as given by the

capture radius, to yield an 'effective' capture radius. The definition of R_c in this study (Equation (3.2-27)) shall be the effective value, which always tends to zero at maximum loading.

Stekly and Minervini[28] showed that R_c decreased steadily as the frontal projected area of buildup increased. Since the frontal area of an idealized 90^o segment is proportional to the radius of buildup, r_a, to the first power, a relationship for α proportional to r_a is obtained by considering the following limits;

i) $r_a \to r_{as}$ for $\alpha \to 0$ (fully loaded wire)

ii) $r_a \to 1$ for $\alpha \to 1$ (bare wire)

The simplest form of such a function is:

$$\alpha = \frac{r_{as} - r_a}{r_{as} - 1} = (1 - \frac{(r_a - 1)}{(r_{as} - 1)}) \qquad (3.2\text{-}28)$$

It will prove more useful to have α in terms of the loading ratio, $\frac{L}{L_{max}}$, to be computed for each screen segment at each increment in time. By considering a 90^o sector of buildup in which the mass of particles will be proportional to this volume (i.e. packing density remains constant), it is possible to write:

$$\frac{L}{L_{max}} = \frac{\text{volume buildup}}{\text{max. volume buildup}}$$

$$= \frac{\frac{\pi}{4} r_a^2 - \frac{\pi}{4}}{\frac{\pi}{4} r_{as}^2 - \frac{\pi}{4}}$$

$$= \frac{r_a^2 - 1}{r_{as}^2 - 1}$$

Rearranging and solving for r_a yields;

$$r_a = \{\frac{L}{L_{max}}(r_{as}^2 - 1) + 1\}^{1/2}$$

and substituting this back into Equation (3.2-28) results in:

$$\alpha = (1 - \frac{\{(\frac{L}{L_{max}}(r_{as}^2 - 1) + 1)^{1/2} - 1\}}{(r_{as} - 1)} \qquad (3.2\text{-}29)$$

The limits of α for very small and very large buildup are:

i) for $r_{as} >> 1$ (i.e. very large maximum buildup)

$$\alpha \to \{1 - (\frac{L}{L_{max}})^{1/2}\}$$

ii) for $r_{as} \to 1$ (i.e. very small maximum buildup)

$$\alpha \to \{1 - \frac{L}{L_{max}}\}$$

Limit ii) is the same result as Akota's (i.e. α_A) and is felt to be more applicable for small maximum buildup where there are approximately equivalent numbers of (unisized) particles per layer.

Liu et al.[41] have pointed out that for large $\frac{V_M}{U_\infty}$ (i.e. > 4.19, Equation (3.2-26b)), R_c will remain constant with loading until a critical value of $\frac{L}{L_{max}}$ is reached. Above this loading, capture radius decrease will proceed toward zero when $\frac{L}{L_{max}} \to 1$ according to Equations (3.2-27,29). This critical value is arrived at by solving for $\frac{L}{L_{max}}$ when equating (3.2-26a,b,27,29); hence;

$$\left(\frac{L}{L_{max\ critical}}\right) = \left\{\frac{\left((r_{as} - 1)\left(1 - \frac{3\sqrt{3}}{V_M\ 2/3}\right) + 1\right)^2 - 1}{2\left(\frac{M}{U_\infty}\right)}\right\} \Big/ (r_{as}^2 - 1) \quad \text{.....(3.2-30)}$$

Geometric Correction Factor, β

The wire screen, approximated as a square weave of cylindrical wires shown in Figure (3-15), requires a correction to account for both overlapping wires and capture areas since the buildup model has assumed infinitely long wires.

For an interwire distance, S_w, and wire radius, a, a unit grid has an area:

$$(S_w + 2a)^2$$

The total number of unit grids in a cross-sectional area, A_x, is therefore:

$$\#\ grids = \frac{A_x}{(S_w + 2a)^2} \qquad (3.2\text{-}31)$$

An expression for the mass of a unit grid, with wire density ρ_w, is simply;

$$2\pi a^2 (S_w + a)\rho_w$$

if no overlapping of the wires occurs at corners, and;

$$2\pi a^2 (S_w + 2a)\rho_w$$

if overlapping is assumed.

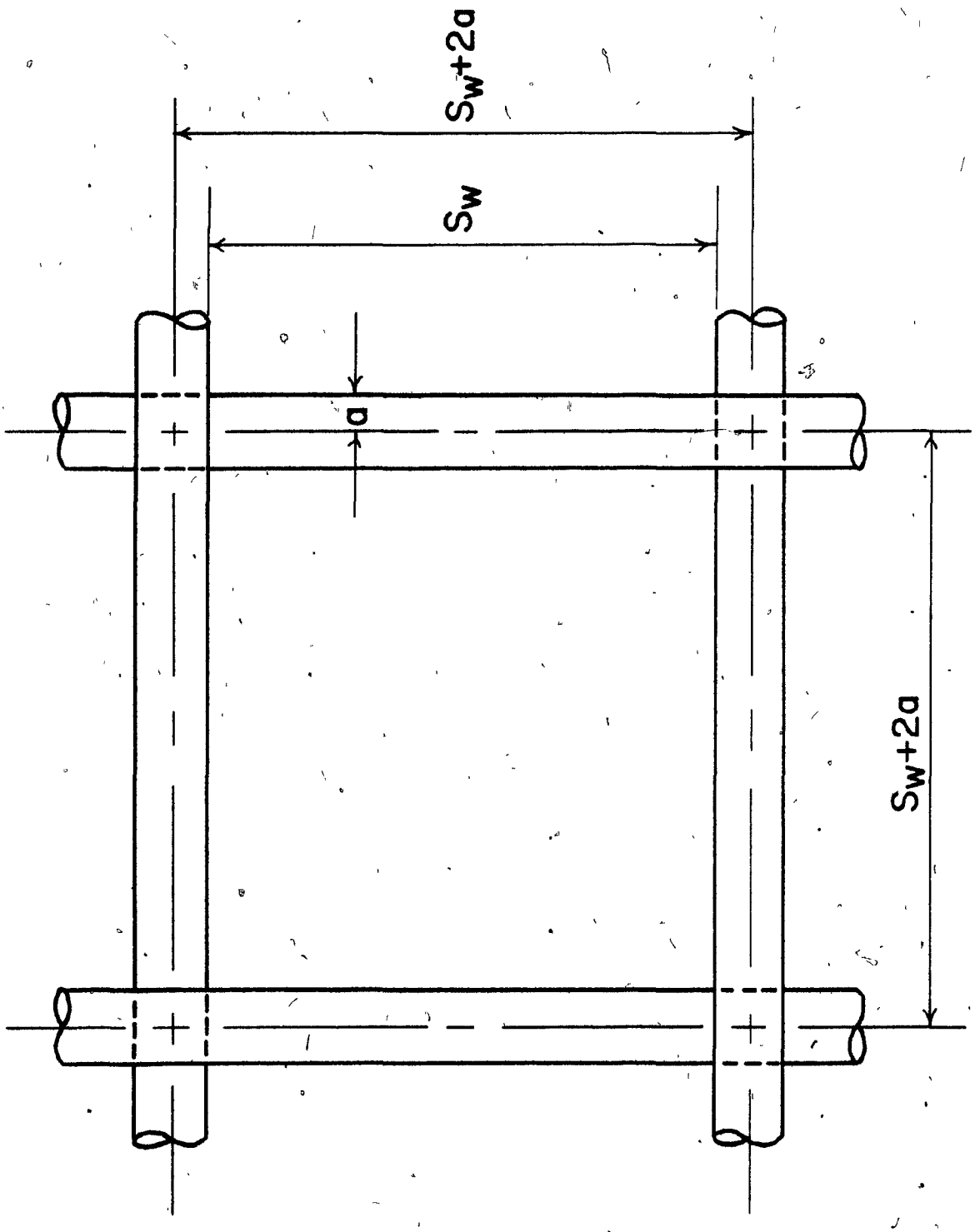

3-14 Unit grid of a matrix screen.

For a screen of total mass, m_w, the number of unit grids will be;

$$\#\text{ grids} = \frac{m_w}{2\pi a^2(S_w + a)\rho_w} \quad \text{(no wire overlap)}$$

and $$\#\text{ grids} = \frac{m_w}{2\pi a^2(S_w + 2a)\rho_w} \quad \text{(with wire overlap)}$$

Equating both these expressions with Equation (3.2-31) yields an alternate form for the area of a unit grid, $(S_w + 2a)^2$, viz;

$$(S_w + 2a)^2 = \frac{2\pi a^2(S_w + a)\rho_w A_x}{m_w} \quad \text{(no wire overlap)} \quad (3.2\text{-}32a)$$

and $$(S_w + 2a)^2 = \frac{2\pi a^2(S_w + 2a)\rho_w A_x}{m_w} \quad \text{(with wire overlap)} \quad (3.2\text{-}32b)$$

from which it is possible to solve for the interwire spacing, S_w. Hence;

$$S_w = \frac{1}{2}(Z + Z^2 - 4aZ)^{1/2}) - 2a \quad \text{(no wire overlap)} \quad (3.2\text{-}33a)$$

and $$S_w = Z - 2a \quad \text{(with wire overlap)} \quad (3.2\text{-}33b)$$

where $$Z = \frac{2\pi a^2 \rho_w A_x}{m_w}$$

To determine the fractional capture area, A_f, of a unit grid, one must consider the situation of R_c both greater than and less than one, shown in Figures (3-16,a,b). For $R_c > 1$ it is seen that 4 of the overlap (shaded) regions must be subtracted from the sum of the individual areas of each length of wire, i.e.:

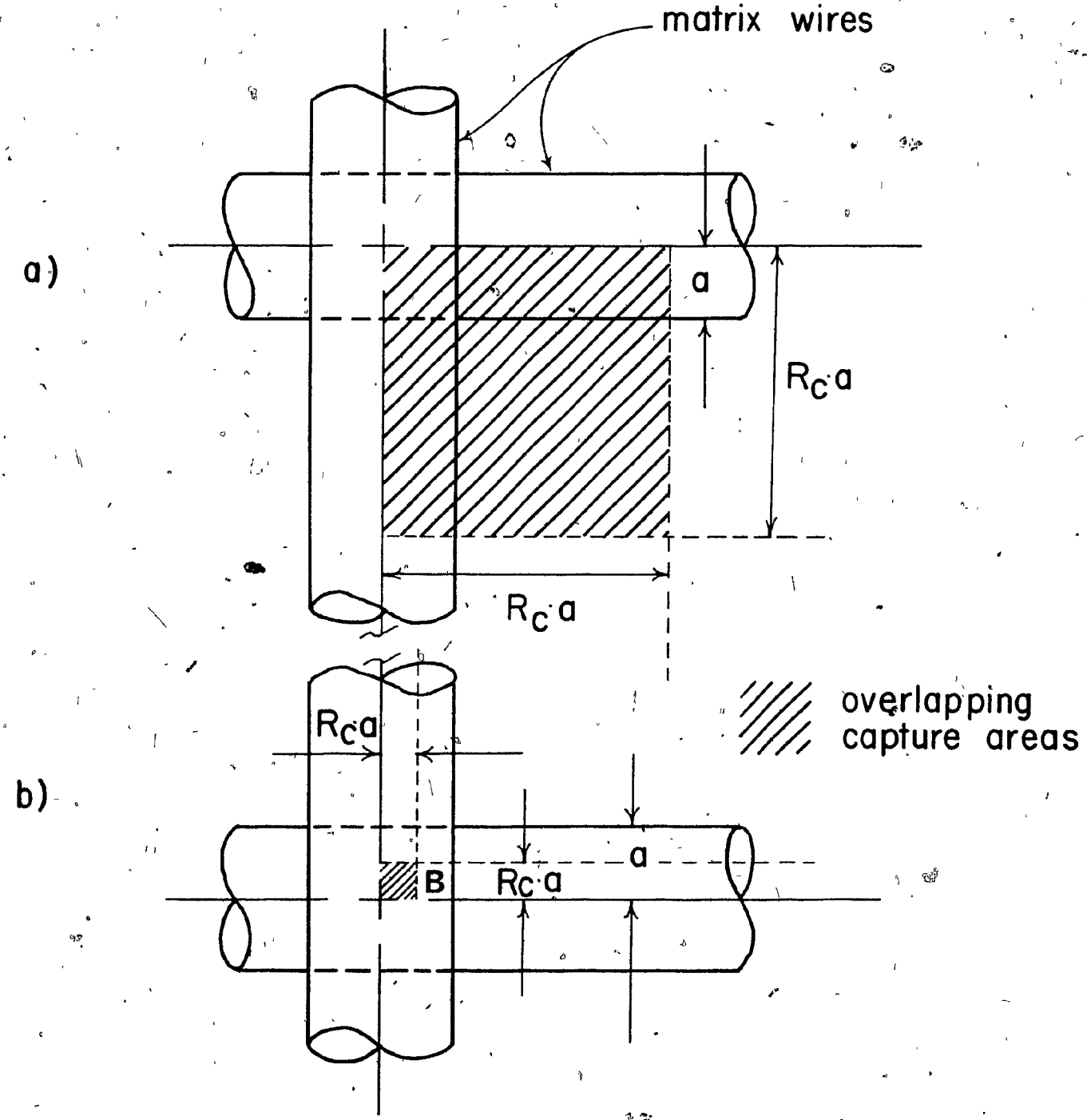

3-15 a) Overlap of capture areas (hatched region) for $R_c > 1$.
b) Overlap of capture areas (hatched region) for $R_c \leq 1$.

$$A_f = \frac{\text{capture area}}{\text{area of unit grid}}$$

$$= \frac{4(S_w + 2a)R_c a - 4(R_c a)^2}{(S_w + 2a)^2}$$

$$= \frac{4R_c a(S_w + 2a - R_c a)}{(S_w + 2a)^2} \qquad R_c > 1 \qquad (3.2\text{-}34a)$$

For $R_c \leq 1$, 4 of the overlap (shaded) areas plus 4 of the areas marked B must be subtracted from the total of the individual areas contributed by the sides of the unit grid, hence:

$$A_f = \frac{4(S_w + 2a)R_c a - 4(R_c a)a}{(S_w + 2a)^2}$$

$$= \frac{4R_c a(S_w + a)}{(S_w + 2a)^2} \qquad R_c \leq 1 \qquad (3.2\text{-}34b)$$

Replacing $(S_w + 2a)^2$ in Equations (3.2-34a,b) with Equations (3.2-32a,b) and including ℓ_w, the length of wire per screen, where;

$$\ell_w = \frac{m_w}{\pi a^2 \rho_w}$$

leads to the following relationships for the fractional area of capture:

$$A_f = \frac{4R_c a m_w}{2\pi a^2 \rho_w A_x}\beta$$

$$= \frac{2R_c a \ell_w}{A_x}\beta \qquad (3.2\text{-}23)$$

β, the geometric correction factor, is given by;

i) for no wire overlap;

$$R_c > 1 \qquad \beta = \frac{(S_w + 2a - R_c a)}{(S_w + a)} \qquad (3.2\text{-}35a)$$

$$R_c \leq 1 \qquad \beta = \frac{(S_w + a)}{(S_w + a)}$$

$$= 1 \qquad \ldots\ldots (3.2\text{-}35b)$$

ii) for wire overlap;

$$R_c > 1 \qquad \beta = \frac{(S_w + 2a - R_c a)}{(S_w + 2a)} \qquad (3.2\text{-}35c)$$

$$R_c \leq 1 \qquad \beta = \frac{(S_w + a)}{(S_w + 2a)} \qquad (3.2\text{-}35d)$$

Expanded metal matrices exhibit considerable wire overlap so this case, illustrated in Figure (3-17) with β as a function of $\frac{S_w}{a}$, is considered for the present study. Since 'blinding' of the screen openings occurs at $\beta = 0.5$ (i.e. the capture area equals the flow cross-section) it is suggested that Figure (3-17) could serve as a guide to designing the inter-fibre distance of a matrix. At a given $\frac{S_w}{a}$, little increase in filter efficiency would be expected at an R_c which yielded a β much below 0.5.

For this study, recognizing that the expanded metal unit grids are not perfect squares, the $\frac{S_w}{a}$ ratio is roughly 13.5 which yields a value of $\beta \approx 0.94$ for R_c typically 1 or less.

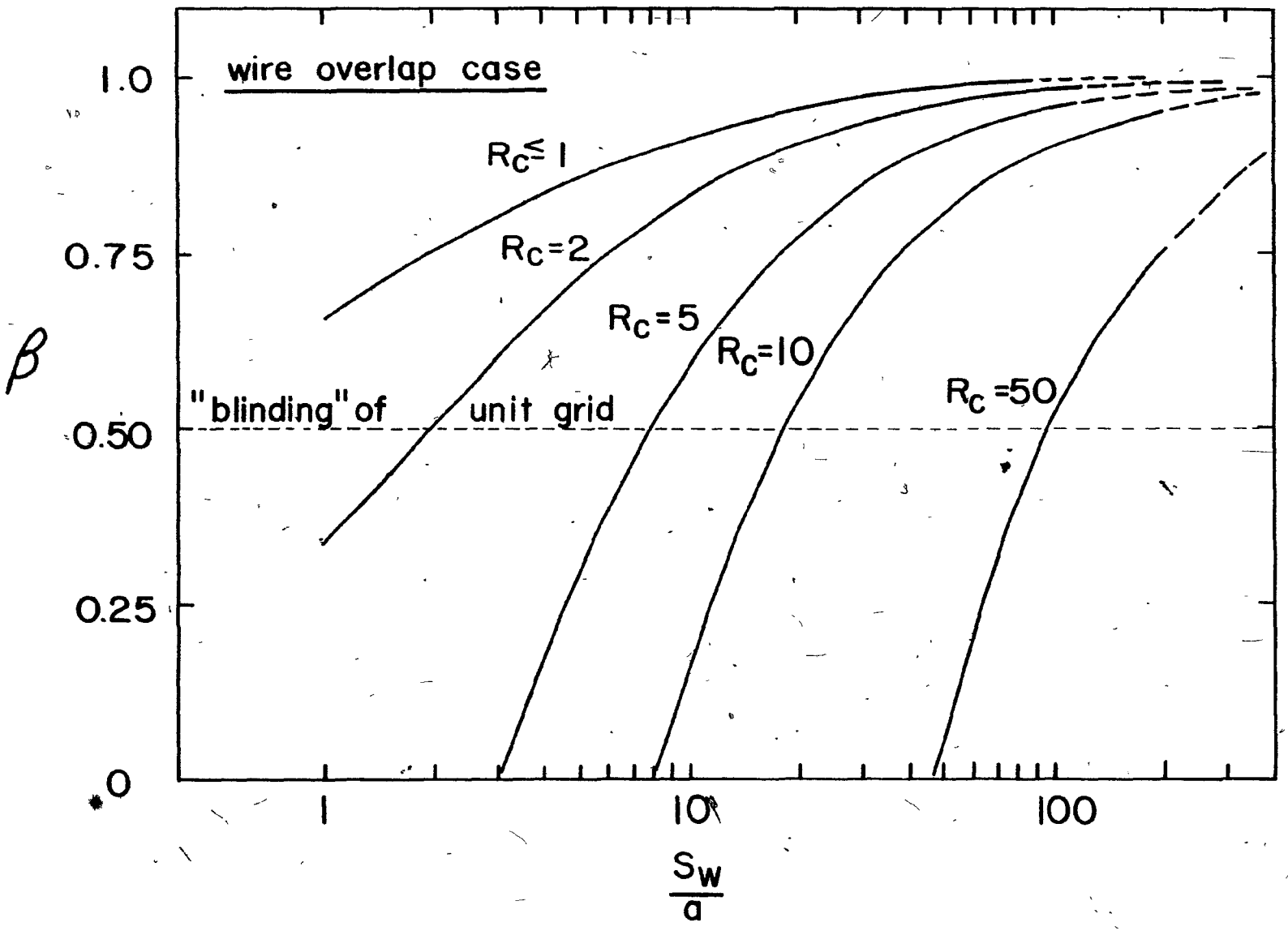

3-16 The geometric correction factor, , as a function of s_w/a for various R_c (overlapping wire case).

3.2.3 The Computer Model

The computer programme, written in Fortran WAT5 language on the McGill University System for Interactive Computing (MUSIC), was prepared in a fully conversational mode for user access from remote teletype terminals and CRT units. A general flow diagram of the programme appears in Figure (3-18). Detailed outlines of the sections labelled Parts 1, 2, and 3 are found in Figures (3-19,20,21), respectively.

Part 1 begins by calculating various parameters from the 16 entered variables. Values for wire magnetization, M_w, and the perturbation term, A, are determined from Equations (3-18,20) by Newton's method (see Appendix II) for converging on the root of the relevant equation. The program then calculates the required forces and their derivatives to find radial and tangential critical angles, θ_c (Equations (3.2-1a,b)), for each layer of particles. A modified Newton's method is used to solve for θ_c since the exact derivatives are not easily determined. As magnetic force diminishes with increasing r, the tangential θ_c also decreases until a preselected stop criterion is reached (usually 10^o) at which point the buildup is assumed complete and the calculation sequence stops. Selecting a stop criterion avoids the singularity at the front stagnation point and since no buildup of significance occurs at $\theta_c < 10^o$ no error is introduced.

Part 2 determines the equilibrium buildup profile as well as the maximum loading per unit length of wire, L_m, by choosing the lesser of the critical angles, either tangential or radial, for each of the n layers. The locus of these minimum θ_c gives the buildup profile. Values of minimum θ_c are then used to calculate the total number and mass of particles in each layer and the results are summed according to Equation

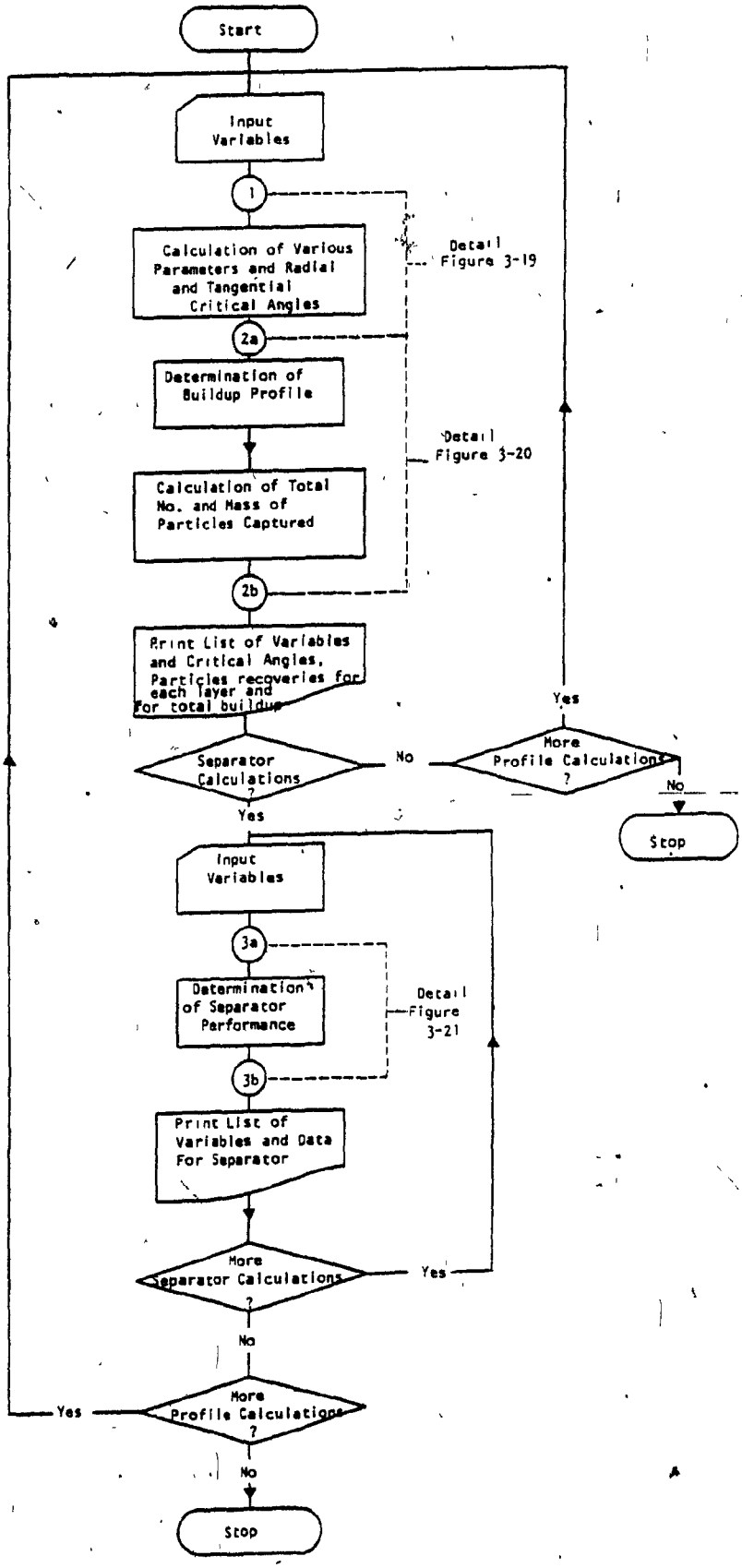

3-17 General flow chart of computer program MAG6.

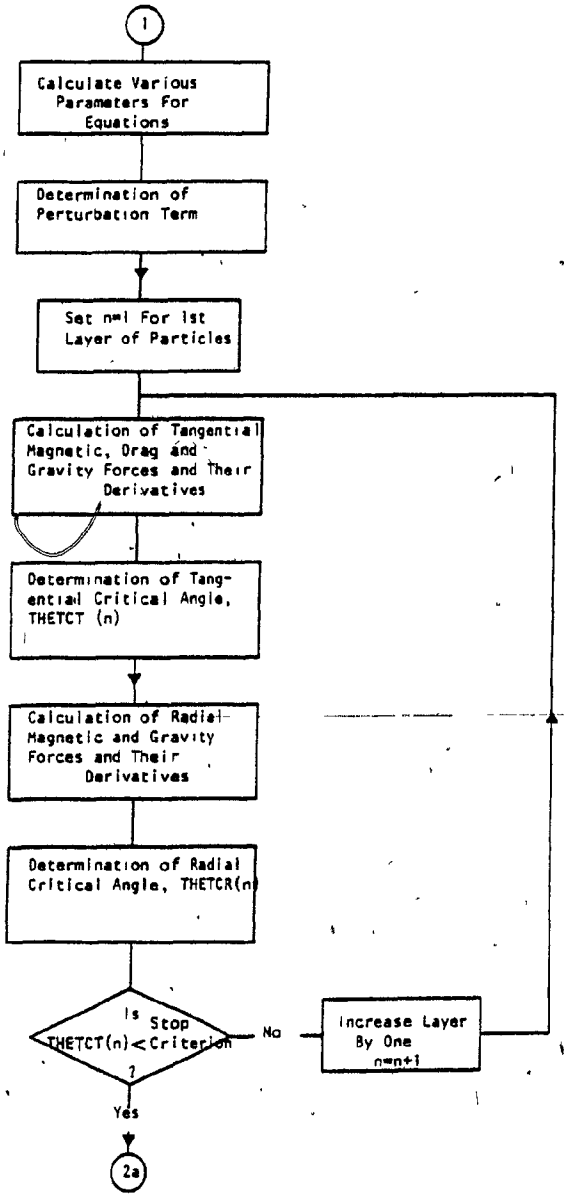

3-18 Detailed flow chart of Part 1 of computer program.

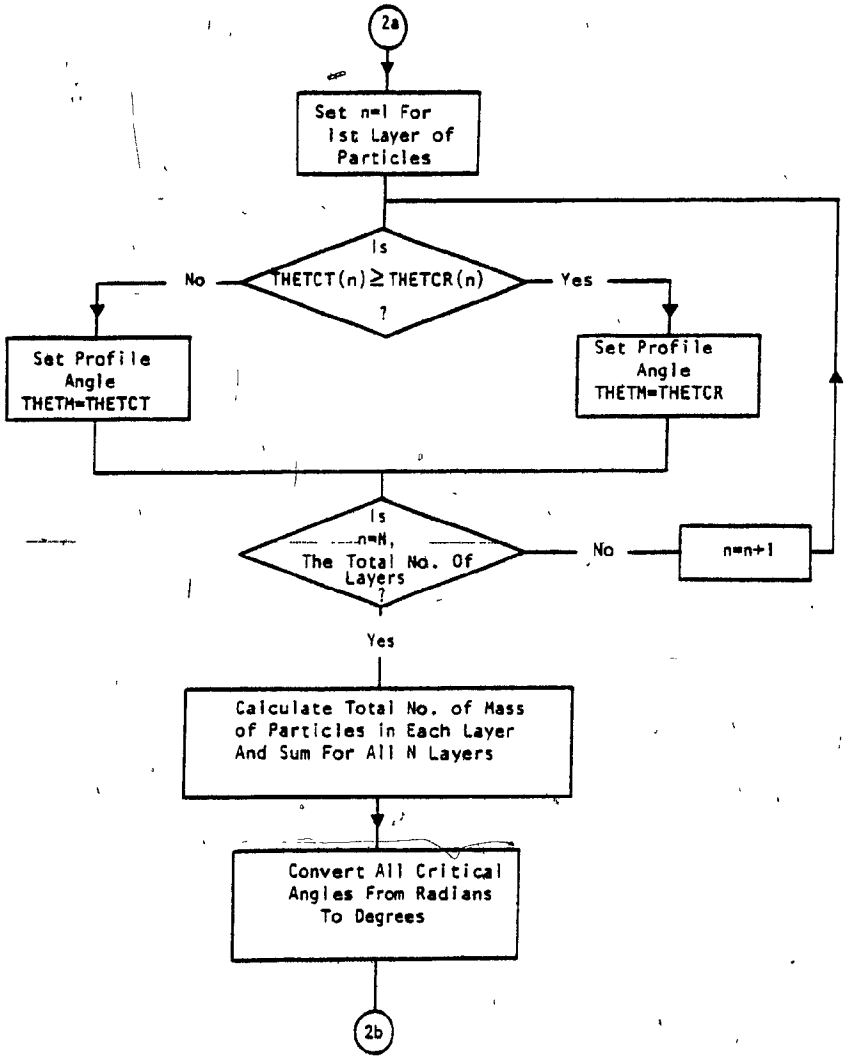

3-19 Detailed flow chart of Part 2 of computer program.

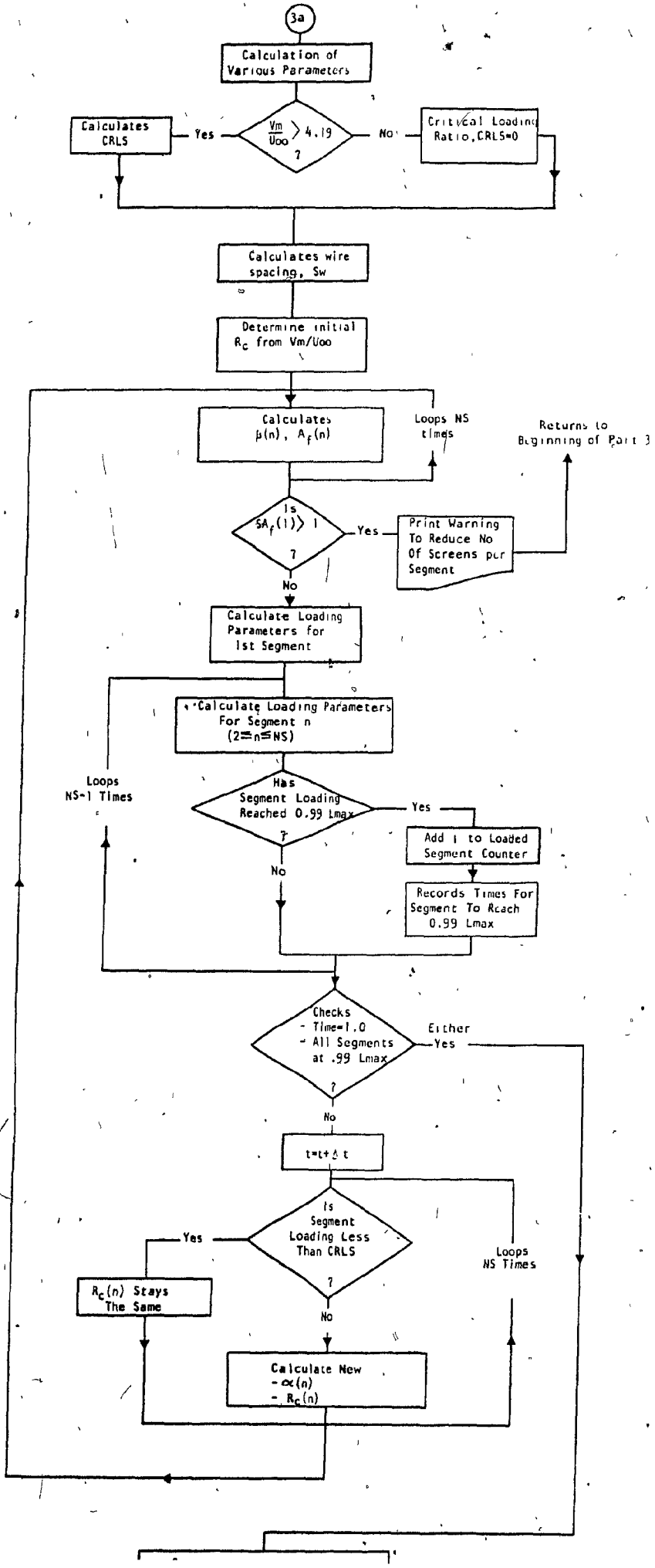
3a
Calculation of Various Parameters
Calculates CRLS
Yes
Vm/Uoo > 4.19 ?
No
Critical Loading Ratio, CRLS=0
Calculates wire spacing, Sw
Determine initial Rc from Vm/Uoo
Calculates β(n), Af(n)
Loops NS times
Returns to Beginning of Part 3
Is SAf(1) > 1 ?
Yes
Print Warning To Reduce No Of Screens per Segment
No
Calculate Loading Parameters for 1st Segment
Calculate Loading Parameters For Segment n (2≤n≤NS)
Loops NS-1 Times
Has Segment Loading Reached 0.99 Lmax ?
Yes
Add 1 to Loaded Segment Counter
Records Times For Segment To Reach 0.99 Lmax
No
Checks - Time=1.0 - All Segments at .99 Lmax ?
Either Yes
No
t=t+Δt
Is Segment Loading Less Than CRLS ?
Yes
Rc(n) Stays The Same
No
Calculate New - α(n) - Rc(n)
Loops NS Times

1 of

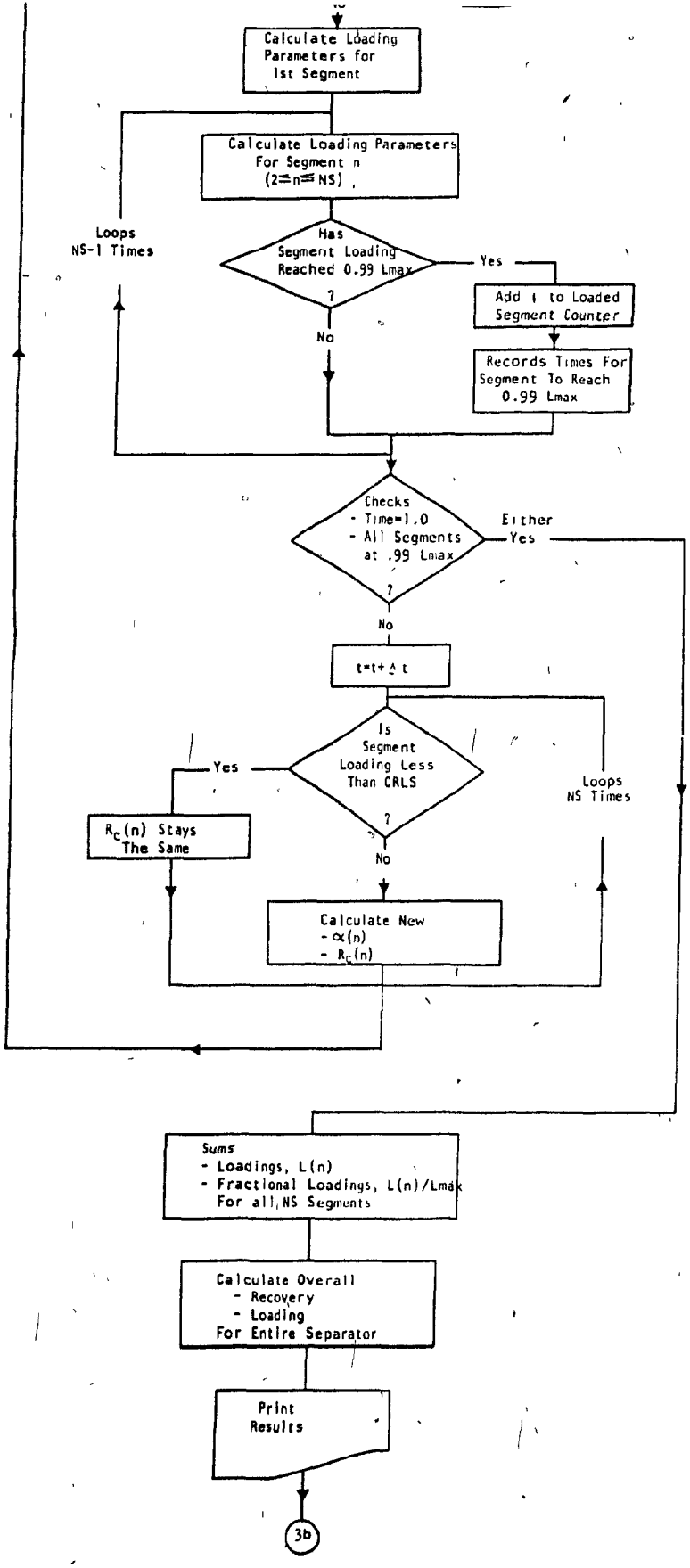

3-20 Detailed flow chart of Part 3 of computer program.

(3.2-4) to yield L_m. As calculations involving θ_c are in radians the angles are converted to degrees prior to printout.

Part 3 extends the calculations from loading per unit length of wire to overall recovery of material throughout a length of wire screens. An additional set of entered parameters (6) is required for this section.

The separator length is made up of segments, each segment comprised of a specified number of screens, which requires the loading per unit length of wire determined in Part 2 be converted to a maximum segment loading, L_{max}.

Recovery to each segment is calculated for successive time increments, dt, in accordance with Equation (3.2-20). The fractional capture area, A_f, is based on the capture radius (R_c), loading ratio (L/L_{max}), and geometric correction factor (β) at the end of the previous time increment. Figure (3-22), for typical conditions and a less than fully loaded matrix, shows the effect on predicted recovery of varying the number of time increments and segments for a 40 screen configuration. Fifty time increments and forty segments were judged to be a good compromise between accuracy (i.e. less than 1% relative error) and computer-time economics.

After each dt, segment loadings (L) are compared with 0.99 L_{max} which, for practical purposes, represents a fully loaded segment. If $L \geq .99\ L_{max}$ the time required to reach this condition is recorded. Should all segments load to 0.99 L_{max} the matrix is considered fully loaded and the calculations terminate.

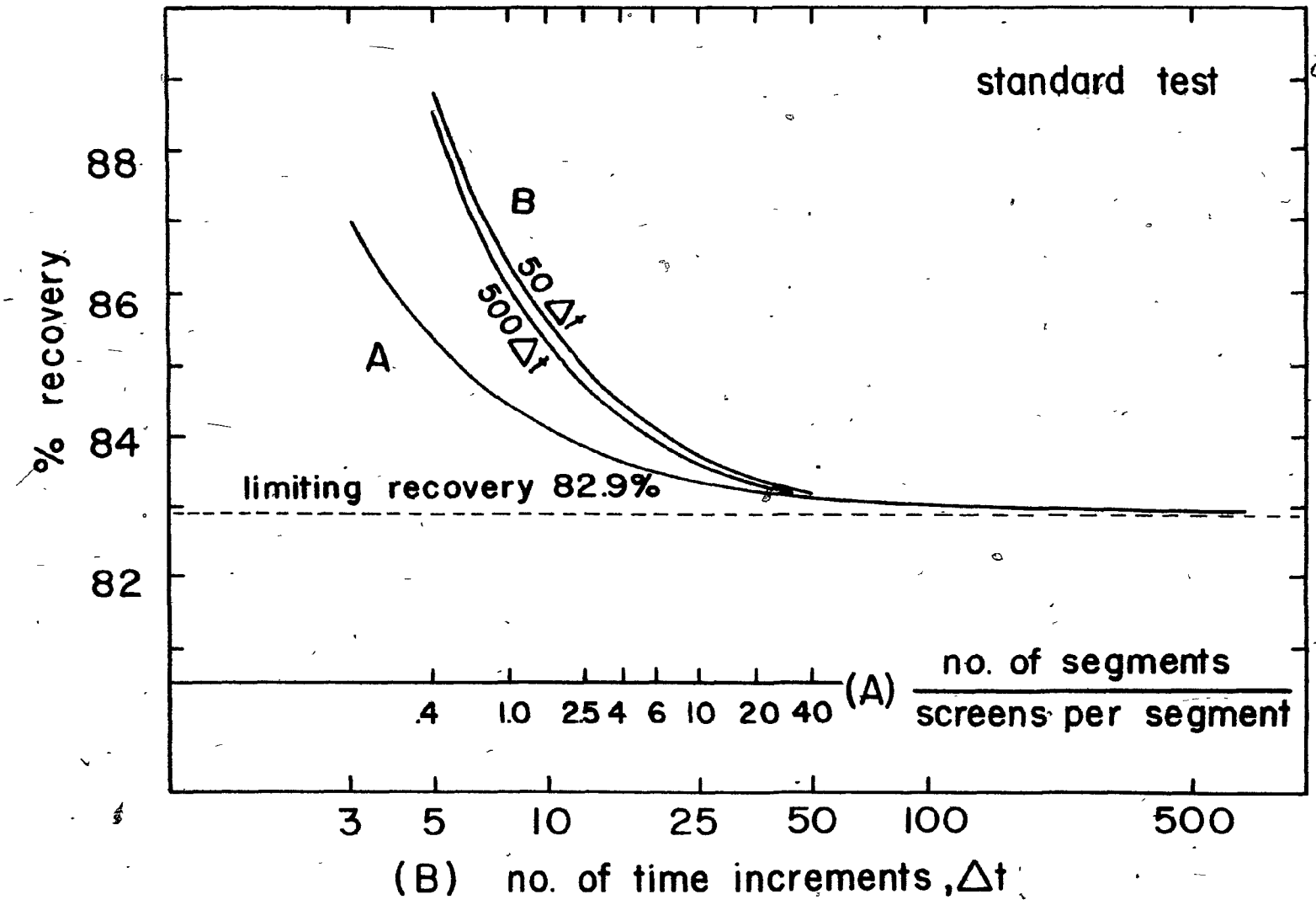

3-21 Influence on recovery predictions of the number of time increments and matrix segments chosen for Part 3 of the computer program. Test conditions are those for the standard test for hematite, 20 grams of feed and a 40 screen matrix.

Finally, Part 3 sums the individual segment L values to give overall separator loading and material recovery. A default condition arises if the product of the fractional area of loading (A_f) and the number of screens per segment (S) is greater than one. This avoids violating the mass balance for the segment.

Variables

The loading and profile determination calculations (Parts 1 and 2) require 16 entered "variables", listed in Table (3-2), and allow for the investigation of particle diameter, density and magnetization; wire diameter, density and magnetization; fluid viscosity, velocity and density; particle packing arrangement, background field strength and gravity.

Six additional variables must be entered for the evaluation of separator performance (Part 3); namely, feed mass, single screen mass and diameter, and the number of segments, screens per segment and time increments. A listing of these may also be found in Table (3-2).

Coded internal-programme variables with a description of each are listed in Table (3-3). A printout of the entire programme (MAG6) is appended (Appendix IV) including a sample hardcopy of the conversational input/output.

TABLE 3-2

Entered Variables in MAG6 Programme

Parts	Symbol in Equations	Programme Variable	Description
1 and 2	$2b$	DIAP	-particle diameter (cm)
	ρ_p	RHOP	-particle density (g /cm^3)
	κ_∞^p	CHIP	-particle susceptibility extrapolated to infinite field (emu/cm^3-Oe)
	M_o	SIGP	-particle spontaneous magnetization (emu/cm^3)
	f_b	SF	-fractional shear of area of spherical particle ($4\pi b^2$)
	$2a$	DIAW	-wire diameter (cm)
	ρ_w	RHOW	-wire density (g /cm^3)
	M_s^w	WMAGS	-wire saturation magnetization (emu/cm^3)
	K	AH	-wire magnetization constant (Oe)
	ν	ETAF	-fluid viscosity (Stokes) (cm^2/sec)
	U_∞	VELF	-fluid velocity (cm/sec)
	ρ_f	RHOF	-fluid density (g /cm^3)
	ℓ^2	ELLSQ	-square of interlayer packing distance as a multiple of particle radius, b (cm^2)
	H_a	HO	-background field strength (Oe)
	g	G	-gravitational constant (0 or 980 cm/sec^2)
	-	DTHETS	-stop criterion for tangential critical angle (degrees)
		Total: 16	
3	$\dot{m}_o$ *	FM	-feed mass (g)
	m_w	SM	-mass of one screen (g)
	S	SS	-number of screens per segment
	-	NS	-number of segments
	$(\frac{4A_x}{\pi})^{1/2}$ **	DIAV	-screen diameter (cm)
	-	M	-number of time increments
		Total: 6	

* The flux rate is equivalent to the feed mass since the total time equals one unit of time.

** A_x is the cross sectional area of the flow.

TABLE 3-3

Internal Variables in MAG6 Programme

Part	Symbol in Equation	Programme Variable	Description
1 and 2	-	THETAS	-stop criterion (radius)
	b	RP	-particle radius (cm)
	a	RW	-wire radius (cm)
	v	VOLP	-particle volume (cm^3)
	$-\frac{8}{3}\pi b^3 H_a a^2$	FMTI	-mag force (tangential) term #1
	$K_\infty H_a$	FMT2	-mag force (tangential) term #2
	$M_o f^a$	FMT4	-mag force (tangential) term #4
	$A^o \sin 2\theta/r^3$	FMT3	-mag force (tangential) term #3
	$A(\cos 2\theta + Aa^2/r^2)/r^3$	FMR3	-mag force (radial) term #3
	$M_o f$	FMR4	-mag force (radial) term #4
	H^o	H	-internal (wire) mag field (Oe)
	f(H)	FH	-function f(H) in Newton's method
	f'(H)	DFH	-derivative of f(H) in Newton's method
	g(H)	GH	-function g(H) in Newton's method
	-	DELH	-Abs (g(H)-H)/g'(H)) x 100 convergence criterion
	A	AA	-field perturbation term $\frac{2\pi M_f}{H_a}$
	r	R(N),RR	-radius from wire center to layer N
	n	N	-particle layer buildup counter
	$2A \cos 2\theta/r^3$	DFMT3	-derivative of FMT3
	f	FACT	-factor, f, in mag force eq's
	F_{θ_M}	FMT	-tangential component of magnetic force (dynes)
	-	DFMT	-derivative of FMT
	$-2A \sin 2\theta/r^3$	DFMR3	-derivative of FMR3
	F_{r_M}	FMR	-radial component of magnetic force (dynes)
	-	DFMR	-derivative of FMR
	θ	THETCT(N)	-tangential critical angle (radians)
	$(9.861 \ldots + .000050^9)$	SSC1	-shear stress term #1
	$\rho_f (U_\infty^3 \nu/8r)^{0.5}$	SSC2	-shear stress term #2
	-	DSSC1	-derivative of SSC1
	F_D	FDT	-drag force (dynes)
	-	DFDT	-derivative of drag force

.....(cont'd.)

TABLE 3-3 (cont'd.)

Part	Symbol in Equation	Programme Variable	Description
	$F_G \sin\theta$	FGT	-tangential component of gravity force (dynes)
	-	DFGT	-derivative of FGT
	$-F_G \cos\theta$	FGR	-radial component of gravity force (dynes)
	-	DFGR	-derivative of FGR
	$F_{\theta_{net}}$	FT	-net tangential force and function f(θ) in Newton's method
	$h(\theta)$	DFT	-derivative of FT and function h(θ) in Newton's method
	$g(\theta)$	GT	-function g(θ) in Newton's method
	-	DELT	-Abs(g(θ)-)/g(θ) x 100 convergence criterion
	$F_{r_{net}}$	FR	-net radial force and function f(θ) in Newton's method
	$h(\theta)$	DFR	-derivative of FR and h(θ) in Newton's method
	$g(\theta)$	GR	-function g(θ) in Newton's method
	θ	THETCR(N)	-radial critical angle (radians)
	ℓ	ELL	-square root of ELLSQ
	θ_c	THETM(N)	-minimum of radial and critical angles for a layer N (radians)
	-	PN(N)	-no. of particles in layer N
	-	PM(N)	-mass of particles in layer N
	-	PNT	-total no. of particles on layers 1 → N
	L_m	PM(N)	-total mass of particles on layers 1 → N
	-	DTHECT(N)	*-THETCT(N) in degrees
	-	DTHECR(N)	-THETCR(N) in degrees
	-	DTHETM(N)	-THETM(N) in degrees
		Total: 52	
3	ℓ_w	LPS	-length of wire per screen (cm)
	A_x	XAREA	-total cross sectional area of screen (and flow) (cm^2)
	κ	CHIPO	-particle susceptibility at H_a

.....(cont'd.)

TABLE 3-3 (cont'd.)

Part	Symbol in Equation	Programme Variable	Description
	V_M/U_∞	VMUF	-ratio of magnetic to fluid velocity
	L_{max}	LMAX	-maximum loading per segment (g)
	dt	DT	-increment of time
	t	TT	-time
	-	FLT	-time for segment to reach .99 L/L_{max}
	r_{as}	BMA	-radius of maximum buildup (at $\theta = 0^o$)(cm)
	(L/L_m)critical	CRLS	-critical loading ratio of segment
	-	KO	-counter
	-	KJ1	-counter
	-	KS	-number of segments having reached .99 L/L_{max}
	S_w	FSP	-inter wire distance in screen (cm)
	R_c	RC	-wire capture radius (dimensionless)
	L	LS	-loading of segment (g)
	β	BETA	-geometric screen correction factor
	A_f	FAREA	-effective capture area ÷ A_x
	-	EFA	-product of A_f and S for first screen (default test)
	dms	DMS	-increment of mass captured on segment during time, dt (g)
	Σdms	SDMS	-sum of incremental mass recoveries for segment (g)
	L/L_{max}	RLS	-ratio of segment loading to maximum segment loading
	α	ALPHA	-capture radius driving function
	-	SLS	-sum of segment loadings at time = 1, ΣL
	-	SRLS	-average segment loading for separator (g)
	-	PFMR	-percent recovery of feed mass

IV. DETERMINATION OF MODEL PARAMETERS

4.1 Magnetic Parameters

4.1.1 Field Measurements

Generally, when using the cgs convention for defining the primary magnetic field, that in a solenoid is an H field, in Oersteds, since there is little if any contribution by induction. In contrast, the field in the gap of a conventionally-wound iron-yoke electromagnet is a B field, in Gauss, due to the $4\pi M$ contribution of the magnetized iron to the flux per unit area. For simplicity, the fields measured in both solenoids and conventionally wound electromagnets will be referred to as H fields.

A variety of magnetometers and gaussmeters are available for the measurement of magnetic fields, from fractions of a gamma (10^{-5} Oe) to several hundred kOe. One of the most common and versatile devices for use in the intermediate range is the Hall probe. It makes use of an effect (the 'Hall effect') occurring in all current carrying conductors in the presence of a transverse magnetic field.

Consider the rectangular conductor with four wire connections illustrated in Figure (4-1) where the thickness, t, is much less than the other dimensions and the field vector, $\hat{B}$, makes an angle, θ, with the unit vector normal to the plate, $\hat{n}$. If a current, I_c, is appplied in the two leads as shown a 'Hall potential', V_H, due to the deflection of the electron path in the conductor, is observed across the other two leads according to:[68]

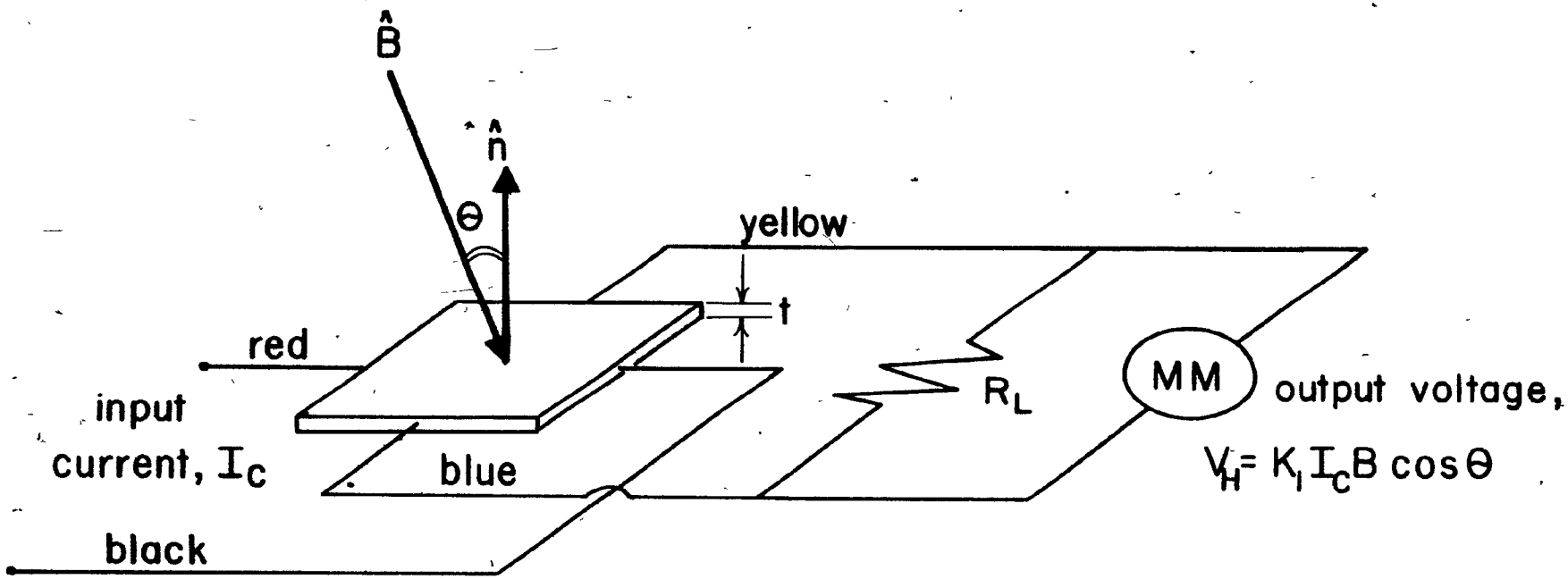

4-1 The Hall effect probe.

$$V_H = \frac{R_H}{t} I_c (\hat{n} \cdot \hat{B}) \qquad \text{(volts)} \qquad (4.1\text{-}1)$$

R_H, the Hall constant, is a property of the material and is much larger in semi-conductors than other substances. For a given Hall crystal (i.e. fixed R_H and t), at constant current, this emf becomes a measure of the field strength. Hence, Equation (4.1-1) may be rearranged to;

$$H = \frac{V_H}{K_1 I_c \cos \theta} \qquad (4.1\text{-}2)$$

where K_1 is a constant to be determined by calibration in a known magnetic field. For Hall probes, in general, the linearity between V_H and H is good to within one percent and only becomes markedly non-linear for fields exceeding 10 to 20 kOe, depending on the crystal.

Hall Probe Calibration

A suitable Hall probe (model HR-66, Ohio Semitronics Inc.) was calibrated against a known magnetic field determined with a rotating-coil gaussmeter. The magnet, a conventional water-cooled unit with conical pole pieces for increased range, produced a maximum field of 13 kOe across the one-inch gap. A schematic illustration of the calibration set up appears in Figure (4-2). The Hall probe, located in the gap close to the pole face such that θ in Equation (4.1-2) equalled zero, was hooked up to a constant DC durrent source (200 ± 1 milli-amperes). For optimum probe linearity a 16 ohm resistor was connected in parallel with the voltmeter measuring V_H across the crystal.

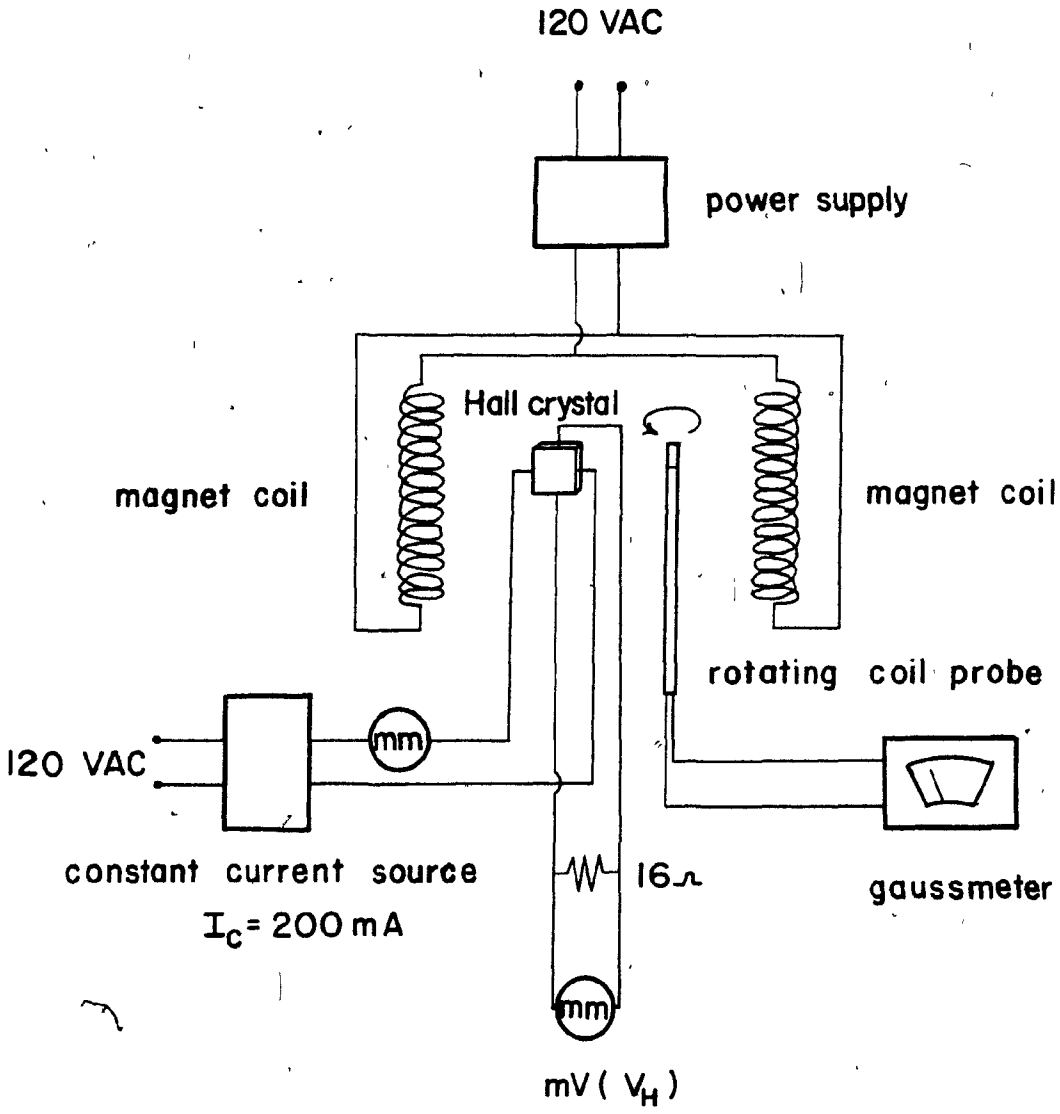

4-2 Schematic of calibration set-up showing Hall probe and magnet coils.

The calibration curve, shown in Figure (4-3), is judged to be linear for H up to 10 kOe, above which a positive deviation from straight line behavior occurs. Hence, the Hall probe calibration yielded (in kOe);

$$H = 25.88 \times \text{volts} \qquad (4.1\text{-}3)$$

for $H \leq 10$ kOe

with a standard error of ± 0.05 kOe. K_1 (Equation (4.1-2)) is, therefore, 1.932×10^{-4} volts/ampere-Oersted and may be used to deduce the relationship between field and Hall emf for other input currents. In the region H > 10 kOe where the calibration deviates from linear behavior, the correct value of H versus V_H should be read directly from Figure (4-3).

Superconducting Solenoid

The experimental equipment for tests at fields up to 20 kOe consisted of a superconducting solenoid, of 8 cm i.d. and 30 cm length, whose operation and characteristics have been described in considerable detail elsewhere.[69] Over the middle half of a long solenoid the field is very uniform and tends to a value at the ends about half that at the centre. The field at the centre of a coil of diameter, D, and length, L, can be calculated from (in Oersteds);[70]

$$H = \frac{4\pi ni}{10\,L}\left(\frac{L}{(D^2 + L^2)^{1/2}}\right) \qquad (4.1\text{-}4)$$

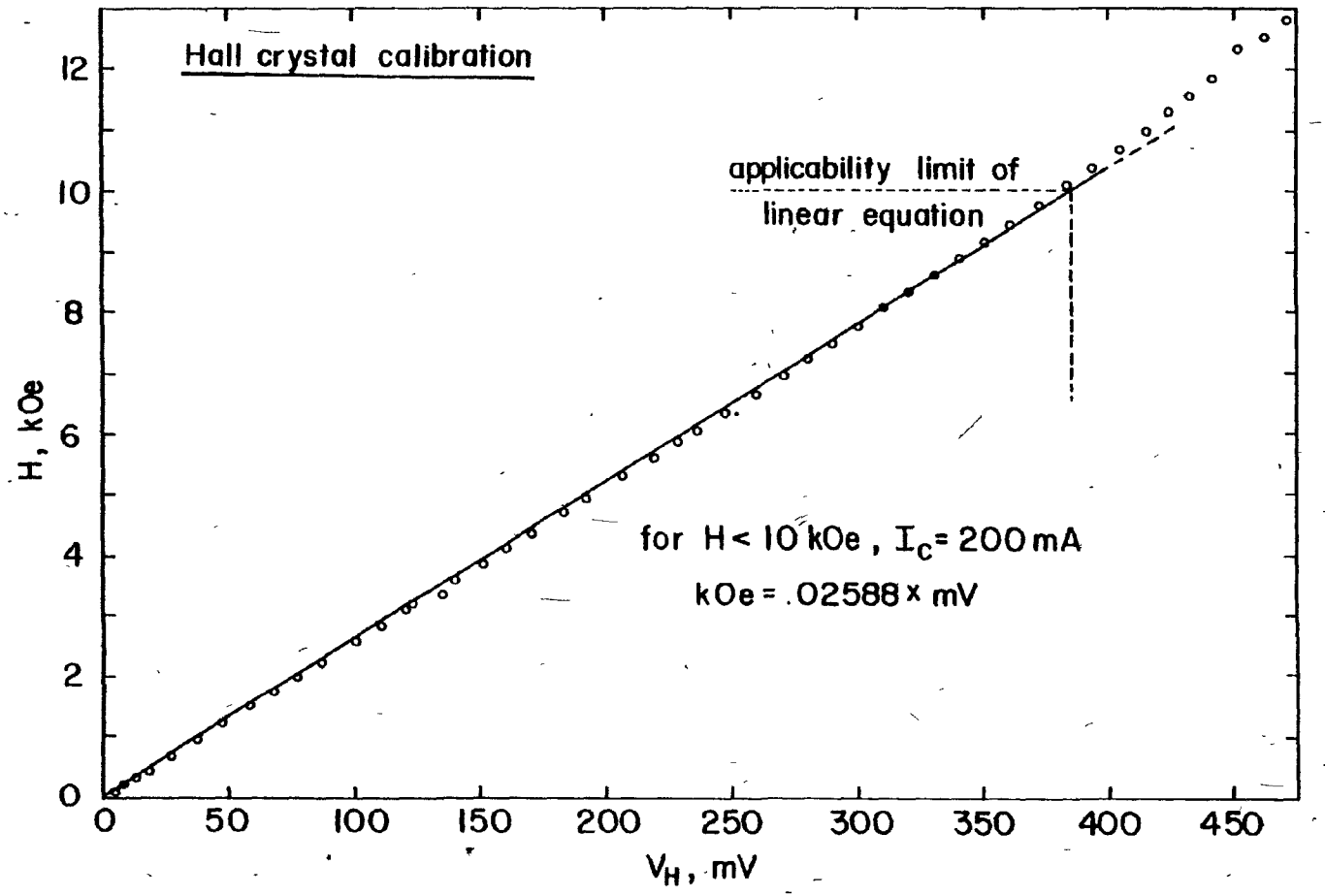

4-3 Calibration curve for Hall probe. V_H versus H.

where n is the number of windings and i the current in the wire. It is obvious from Equation (4.1-4) that, everything else constant, the field produced within the magnet will increase in direct proportion to the input current. The advantage of superconducting solenoids (i.e. zero coil resistance) over conventional ones is that they avoid the cooling requirements associated with ohmic heating ($\alpha i^2 R$, where R is the coil resistance) and large power draw which become significant in the latter at fields greater than 1-2 kOe.

Figure (4-4) shows the results of a field measurement survey along the axis of the magnet bore. Note that over the central half (15 cm) the field decreases less than 5% from maximum while the deviation from H_{max} over the middle one-sixth (5 cm) is negligible. During all testwork the matrix was located in this central region of very uniform field.

With the Hall probe positioned along the bore axis at the location of maximum field, the solenoid was calibrated as a function of input current* and yielded the results of Figure (4-5). A linear regression gave;

$$H = .6508 \times \text{amperes} \qquad (4.1\text{-}5)$$

with H in kOe and a standard error of estimate ± .05 kOe. Despite the calibration range in field being only to 13 kOe, the excellent linearity of H versus current suggests that Equation (4.1-5) may readily be applied

*Although a superconductor has essentially zero resistance, a supplementary resistance of 0.2 ohms external to the magnet coil is part of the overall circuit to allow proper control of the current-generated field.

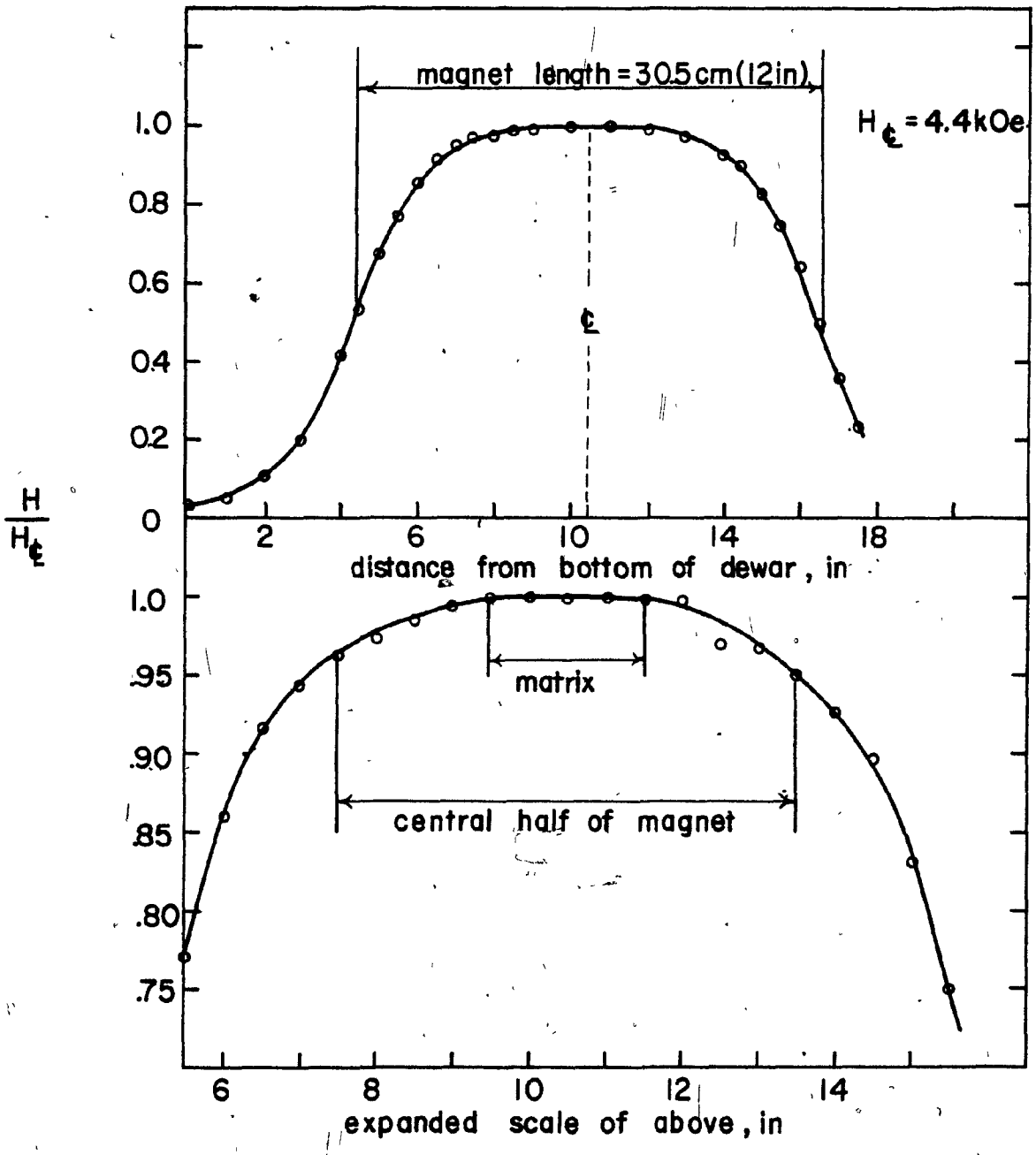

4-4 Variation in H through the bore of the superconducting solenoid.

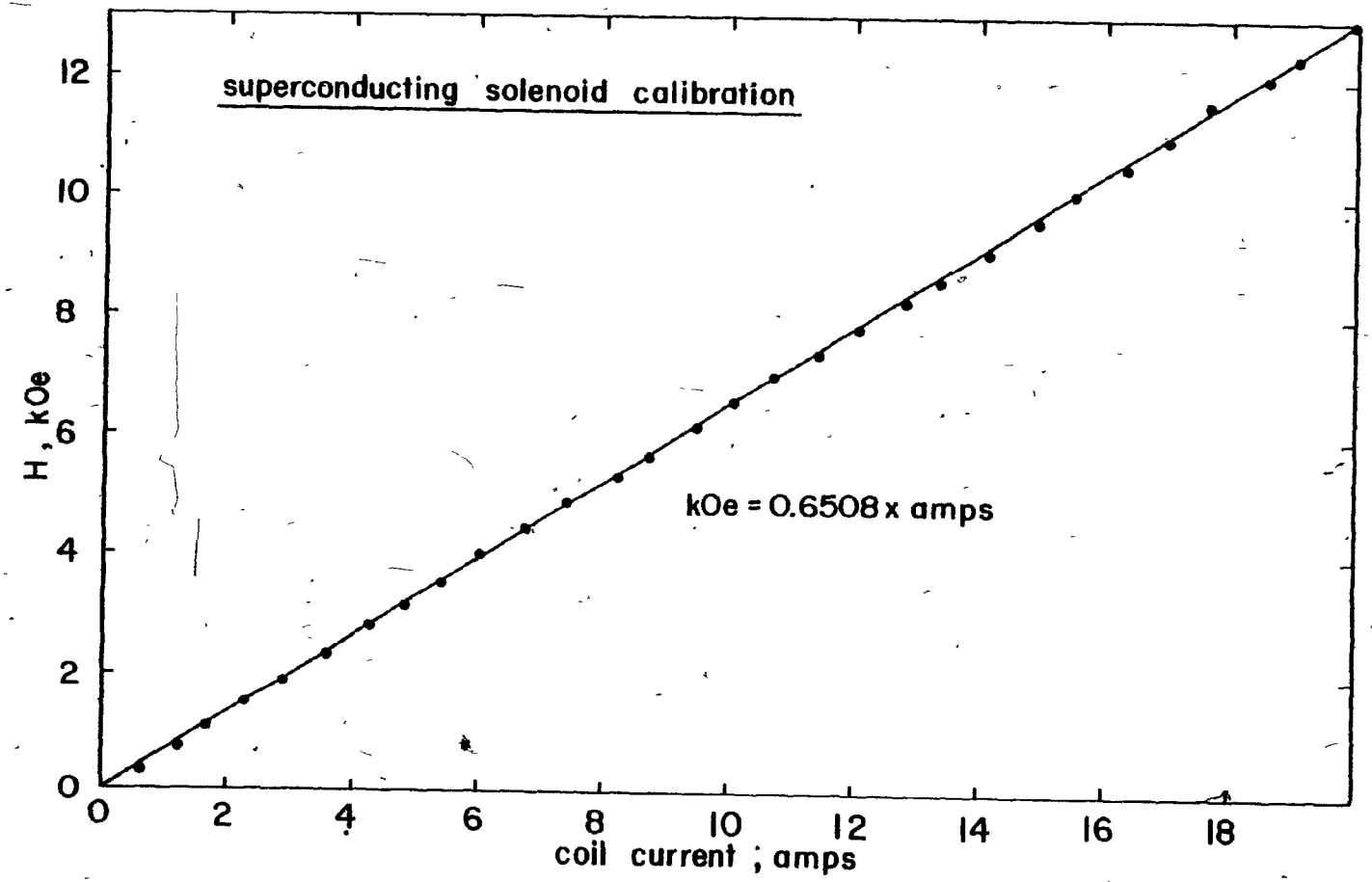

4-5 Calibration curve for superconducting magnet. H versus input current.

over the entire 20 k0e (i.e. 30 ampere) range of the magnet.

Permanent Magnet

A smaller, ferrite, permanent magnet solenoid was used for exploratory testwork in studying the loading behavior of hematite on expanded metal screens. The central bore of 5.7 cm i.d. and length 18.4 cm exhibited a lesser degree of field uniformity than the relatively longer superconducting solenoid. Figure (4-6) shows the results of field measurement surveys along both the axis and the side wall of the bore. The field is uniform to within ± 5% of the centre-line maximum, 776 Oersteds, over the middle 5 cm.

Frantz-Isodynamic Separator

This laboratory device, best known for its geological and mineralogical application in achieving precise separations of minerals of different magnetic susceptibilities[71], has also been used to provide an indication of the amenability of a mineral mixture to processing by magnetic methods in general[72], and by hgms in particular.[73]

The separation of particles occurs in a tray positioned lengthwise in the gap (approximately 25 cm long) between specially designed pole pieces of a powerful electromagnet. The cross-section of these 'isodynamic' poles is such that the changing field gradient exactly balances changes in the magnetic field to yield a constant product and hence uniform magnetic force throughout the gap. Since gravity, the only opposing force (adjusted by changing side slope of

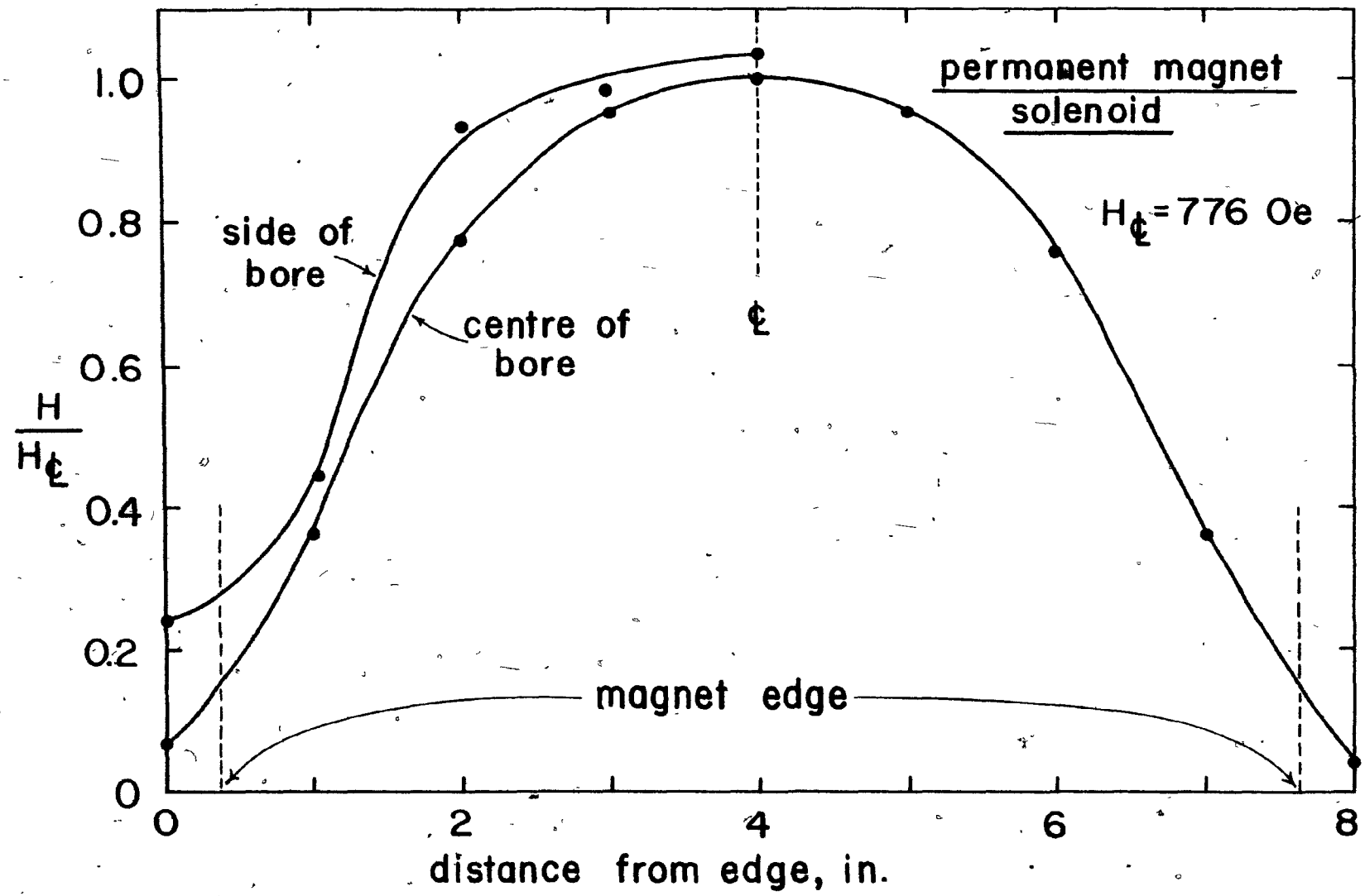

4-6 Variation in H through the bore of the permanent magnet solenoid.

the device) also remains constant, a separation of particles is achieved which is totally independent of their mass and solely a function of individual magnetic susceptibility.

In addition to a field versus input-current calibration of the Frantz-Isodynamic, detailed surveys were done of H both longitudinally and transversely in the gap. Input current was measured with a $3\frac{1}{2}$ digit multimeter which provided much improved current control over the original instrument ammeter. The precision of separations could thus be more closely monitored.

Longitudinal variation of H in the pole gap appears in Figure (4-7). It shows that particles enter and exit under essentially zero field conditions while being exposed to a constant H (longitudinally) in the separation zone. A splitter in the tray parts the feed into magnetic and non-magnetic fractions. Beyond this point the field smoothly and rapidly decreases allowing for continuous removal of both products.

An indication of the transverse variation in field appears in Figure (4-8). A word of caution is in order since these attempts at measuring field gradients were made with a probe over whose dimensions (0.5 cm) there sometimes occurred a significant variation in the field. An averaged value of H, and hence $\frac{dH}{dx}$, was in fact measured, but the location of maximum field may nonetheless be determined and is seen (Figure (4-8)) to occur at position -0.1. Over the width of the tray, positions -0.1 to +0.5, the gradient roughly doubles as H is halved, a result in keeping with the isodynamic nature of the poles.

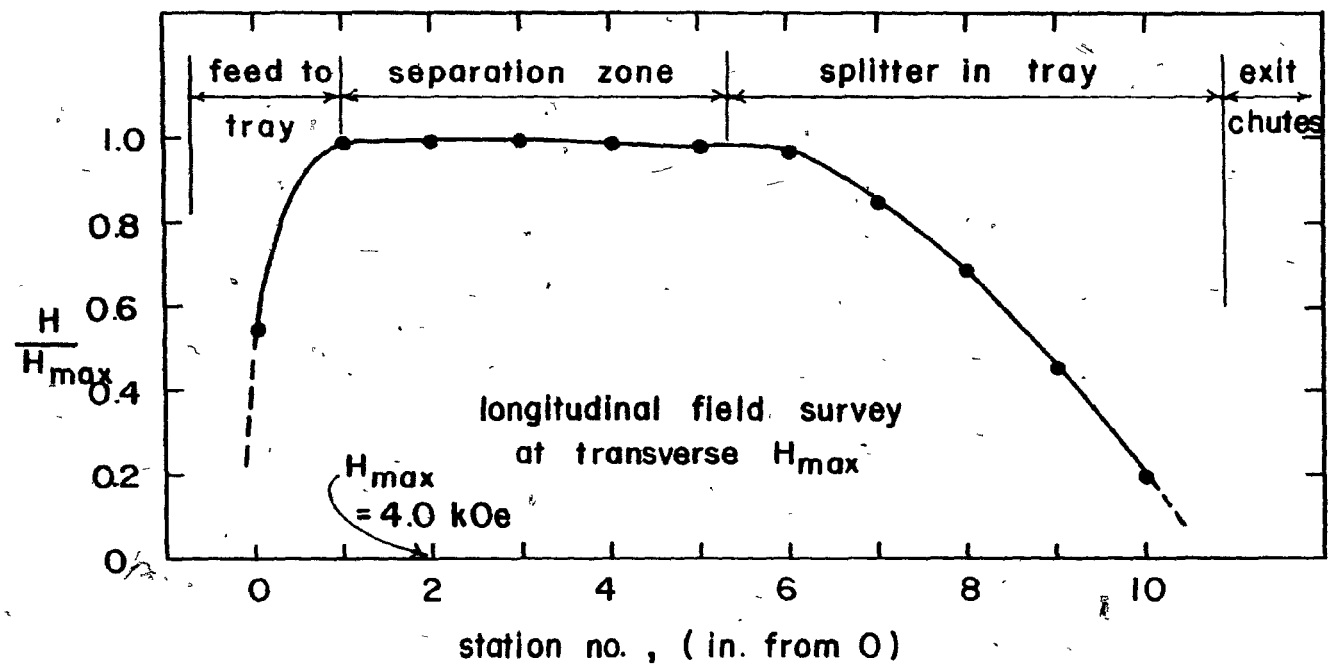

4-7 Longitudinal variation H in pole gap of the Frantz Isodynamic separator.

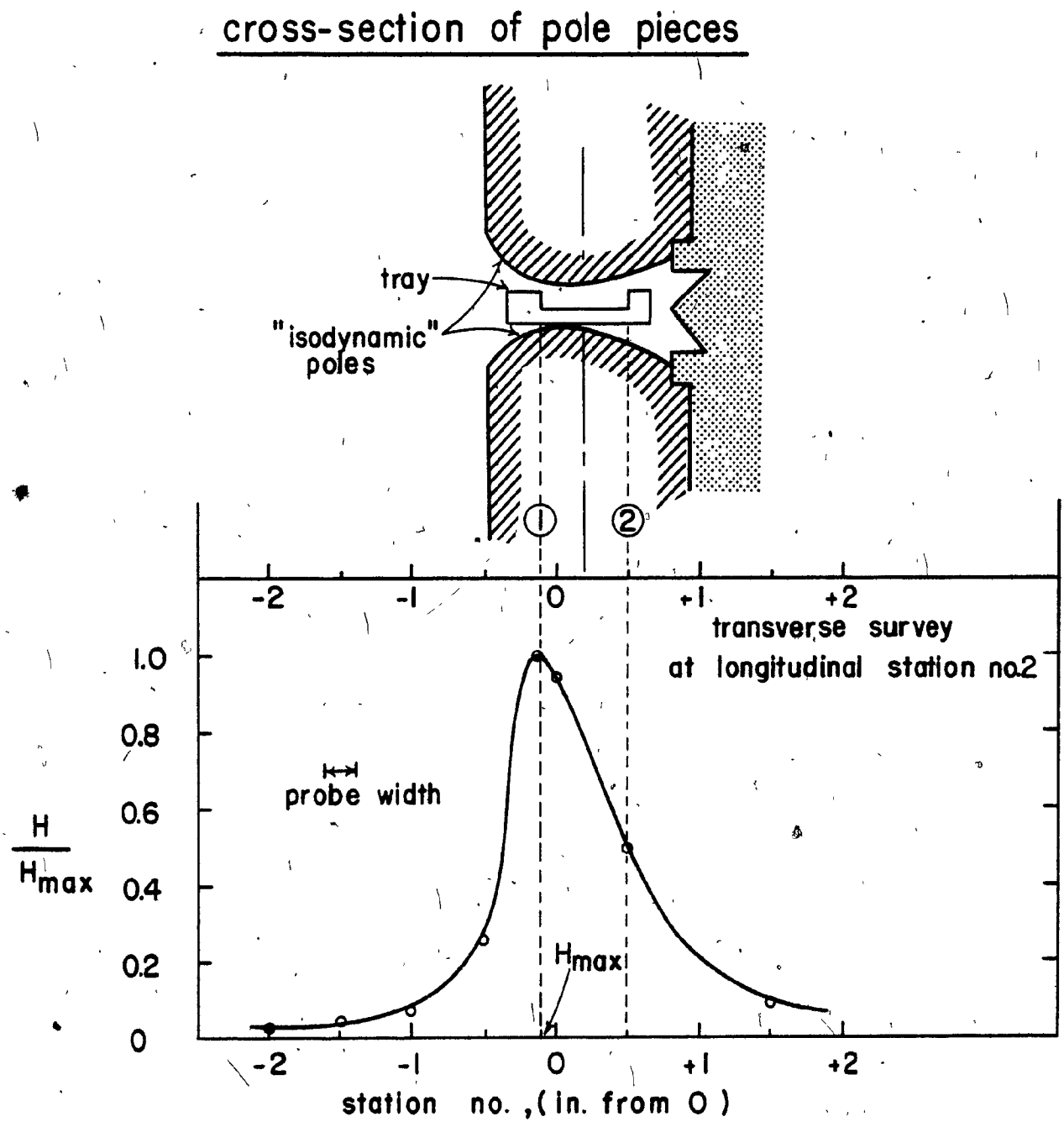

4-8 Transverse variation in H in pole gap of the Frantz Isodynamic separator. Measurements taken at longitudinal station #2 (1 station equals 2.54 cm).

The averaged gradient for this gap region, $\overline{\frac{dH}{dx}}$, was determined as a function of H_{max} by locating the Hall probe in the gap at positions -0.1 and +0.5. The resulting regression (5 measurements) through the origin (Figure (4-9)) gave, in kOe/cm;

$$\overline{\frac{dH}{dx}} = .2728\ H_{max} \qquad (4.1\text{-}6)$$

Field calibration of the Frantz-Isodynamic was performed with the Hall probe positioned at maximum transverse and longitudinal H. The curve (Figure (4-10)) was judged to be linear from 0.5-8.0 kOe according to;

$$H = 12.30 \times \text{amperes} \qquad (4.1\text{-}7)$$

where H, in kOe, has a standard error of ± .05 kOe.

The extent of hysteresis (also shown in Figure (4-10)) suggests that for accurate work an increasing current always be used to reach a required value. Expanded-scale curves (Figures (4-11,12)) are provided for the regions of H between 0-0.5 kOe and 8.0-13.0 kOe, respectively.

Since the Hall probe calibration itself only reached 13 kOe the region beyond this limit has been estimated and appears as a dashed line in Figure (4-10). The operating limit of the device appears to be about 1.6 amperes due to both magnetic saturation of the yoke and excessive heating of the coils.

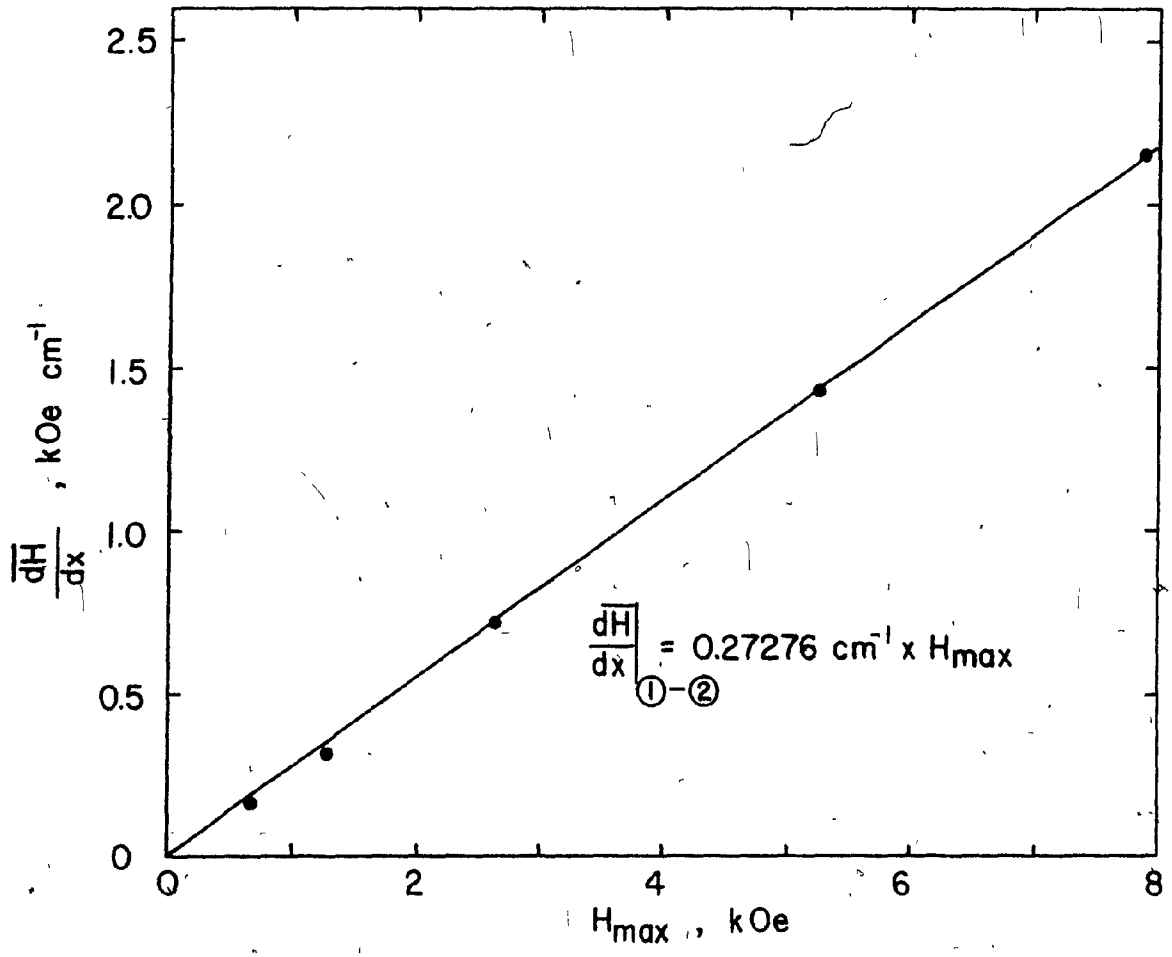

4-9 Average field gradient, $\overline{\frac{dH}{dx}}$, as a function of H_{max} for the Frantz Isodynamic separator.

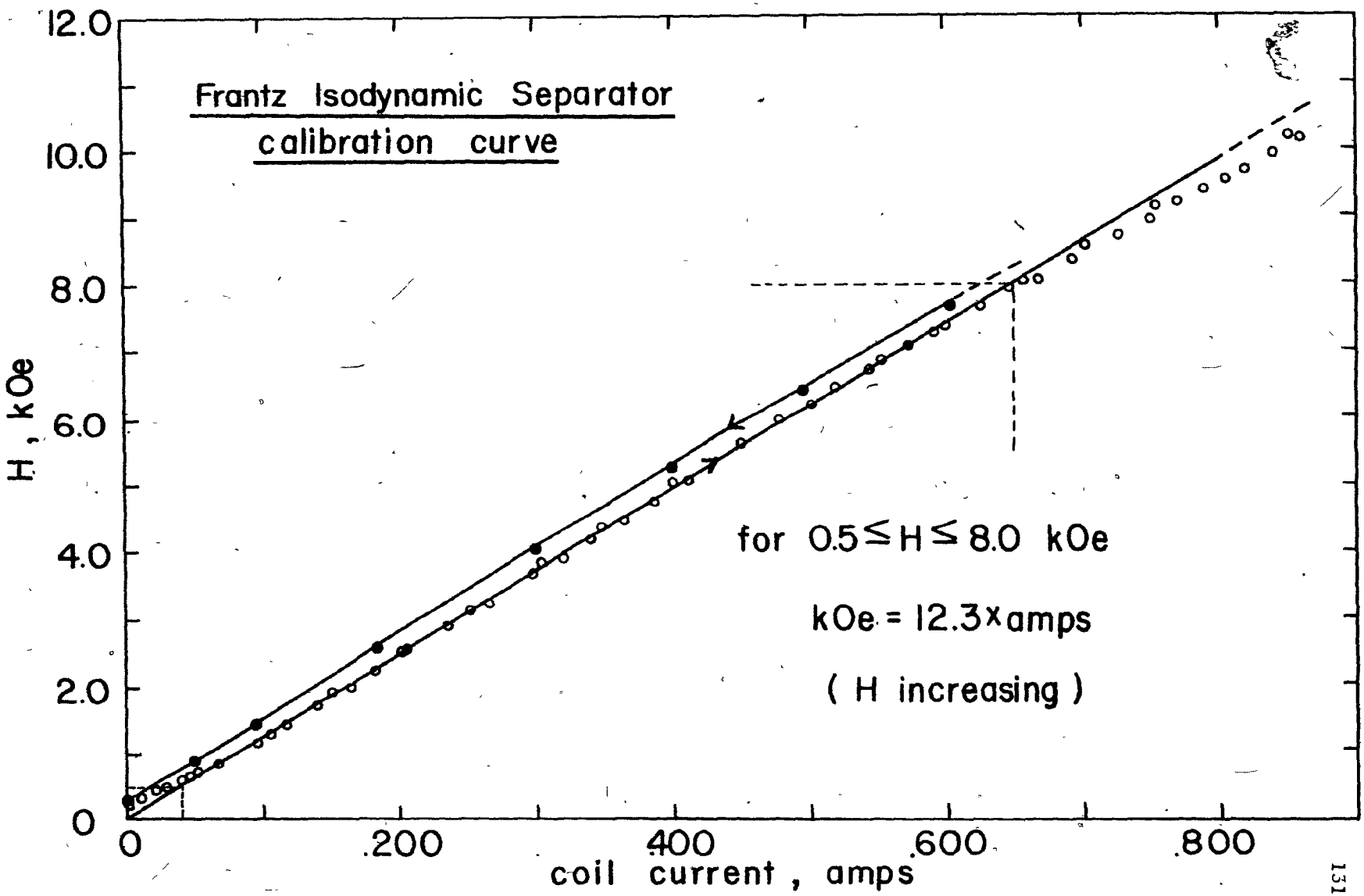

4-10 Calibration curve for Frantz Isodynamic separator, H versus input current, 0.5-8.0 kOe.

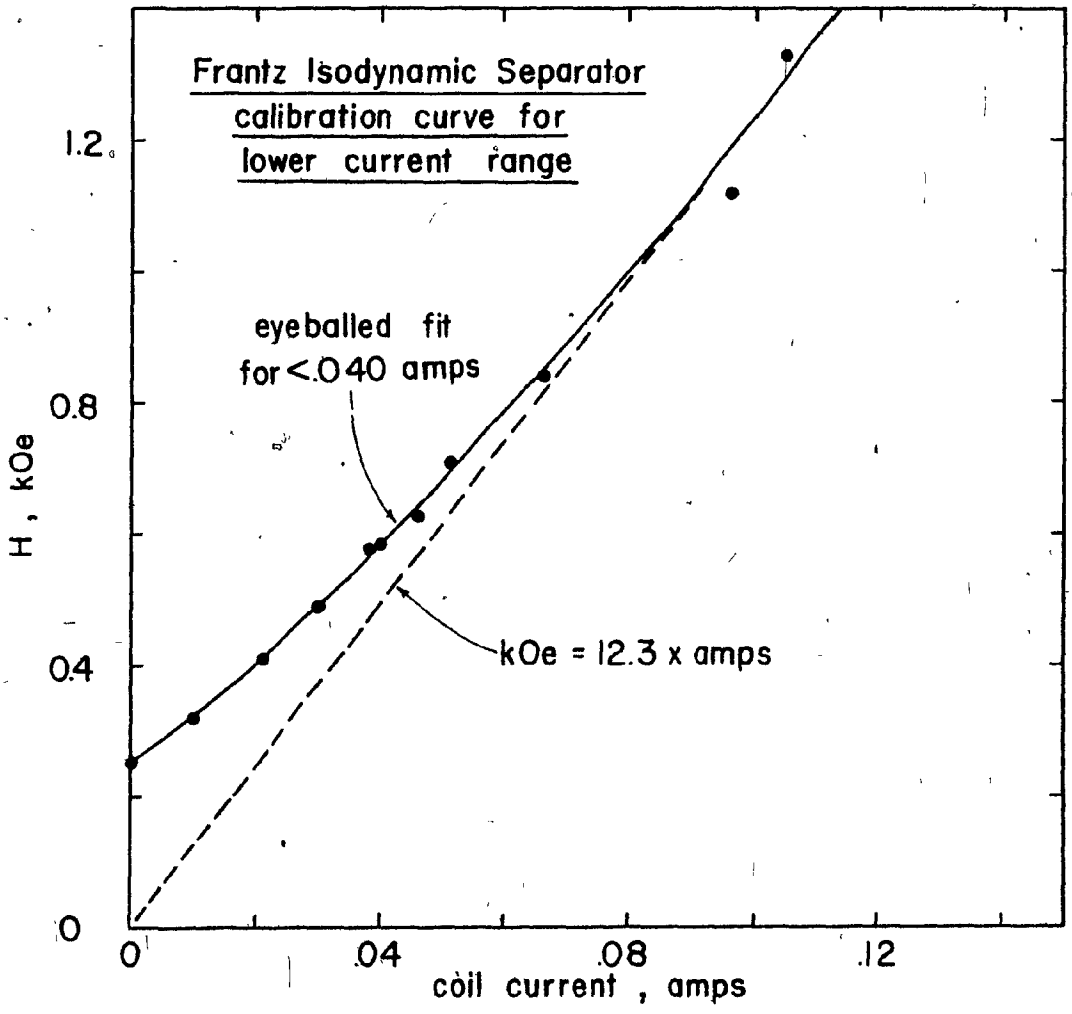

4-11 Calibration curve for Frantz Isodynamic separator, H versus input current, 0-0.5 kOe.

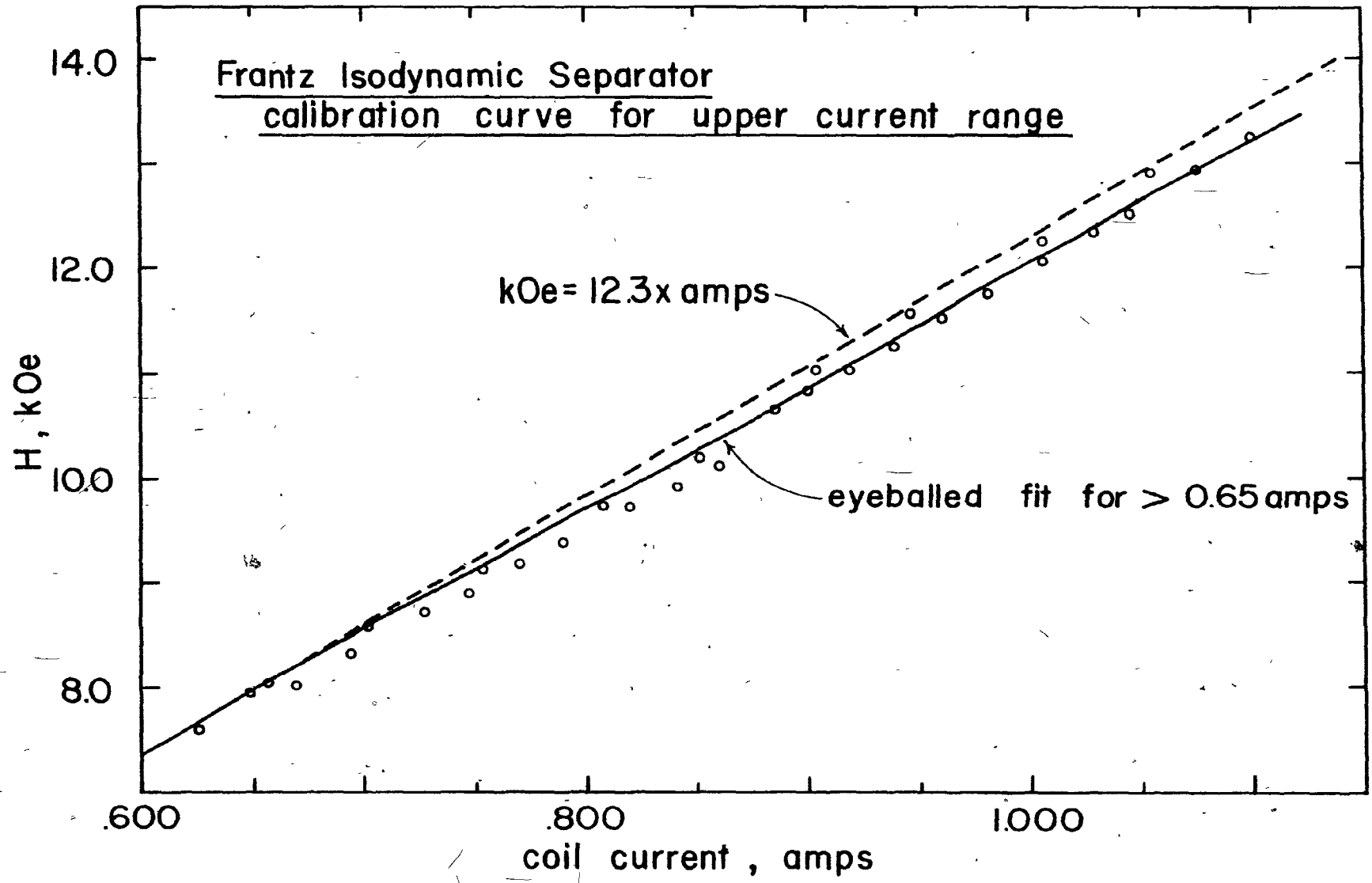

4-12 Calibration curve for Frantz Isodynamic separator, H versus input current, 8-13 kOe.

4.1.2 Particle Magnetization Measurements

As seen from Table (3-1), the reported magnetization behavior of a mineral may vary by up to three orders of magnitude. Andres[44] discusses the subject in detail. In previous times of less sophisticated magnetic separators it was sufficient to classify minerals as either 'strongly, weakly or non-magnetic'.[74] Only the strongly magnetic ones (e.g. magnetite, pyrrhotite, ilmenite) were amenable to separation. However, hgms devices have extended the range of magnetically recoverable minerals to include even the previously non-magnetics. Thus, the use of handbook values is at best risky and the accurate magnetization data required for prediction purposes should be obtained by direct measurement of the samples to be treated.

The testwork was largely concerned with a sample of Carol Lake (Labrador) specular hematite ore previously cleaned of silica and ground to minus 400 mesh by Partridge.[75] Subsequent size classification on a Warman Cyclosizer produced five closely sized fractions of fairly pure ($\sim$ 95% Fe_2O_3) hematite.

Each fraction was then magnetically 'cleaned' on the Frantz Isodynamic by first passing the samples through at a low current setting (0.1 amperes) to remove any highly magnetic material such as magnetite. Retreatment of the non-magnetic fraction followed at a sufficiently high current setting (0.3 amperes) to pull the hematite into the magnetics chute but leaving the silica and other minor contaminants to report as non-magnetics. Table (4-1) shows the resulting weight split for each cone as well as the overall average. The procedure is time consuming (up to several weeks for one cone fraction of 50-75 g) due to

TABLE 4-1

Magnetic Cleaning of Cyclosizer Cone Fractions (Hematite).
Weight Percent of Products.

	Weight Percent of Product		
Cyclosizer Cone #	Magnetics @ 0.1A	Non-Magnetics @ 0.3A	Magnetics @ 0.3A
1	2.0	0.7	97.3
2	1.9	2.2	95.9
3	2.2	7.1	90.7
4	2.1	6.4	91.5
5	4.2	1.5	94.3
average	2.5	3.6	93.9
description	Fe_3O_4	mostly SiO_2, some Fe_2O_3, some 'pipe scale'	~ pure Fe_2O_3

i) low throughput rate on the Frantz Isodynamic; ii) frequent stoppages for removing magnetite buildup from the tray; and iii) the required low-humidity and free-flowing condition for particles, especially at finer sizes.

Magnetization measurements were made using both a force balance method, i.e. the Frantz Isodynamic, and a magnetic induction technique, the Foner vibrating sample magnetometer.

Vibrating Sample Magnetometer

The Foner magnetometer[76] is a device of high precision (± 0.5% relative accuracy claimed) which determines magnetization properties by monitoring the voltage (on an x-y plotter) induced in a set of stationary detection coils by the moving dipole field of a sample vibrating perpendicularly between the coils in a uniform field. Samples were contained in a threaded Teflon holder 3 cm in length, 0.64 cm o.d. and 0.25 cm i.d. Care was taken to completely fill the volume with sample to avoid movement of the material relative to the holder. Any relative movement would result in a reduced vibration rate for the sample and hence a decreased signal from the coils. Sample size ranged from .09 to .16 g.

Calibration was with a high purity nickel plug of known mass (.128 g) and saturation magnetization[77] (54.39 emu/g). Foner claims an absolute instrument accuracy of ± 1% by this calibration method. Readings from the x-y plotter for the nickel standard were judged to be within ± 0.1 emu which translates to an accuracy of ± 1.4% at saturation. Repeatability of hematite measurements after repositioning and recalibration of the pickup coils was ± 2.5%.

Since the magnetometer measures bulk magnetization of the sample, the presence of any strongly magnetic material (such as magnetite), in even minute quantities, will drastically influence the apparent magnetization of a magnetically weaker material. The complete removal of, for example, all free magnetite from the hematite was, therefore, essential to obtaining reliable magnetization data.

A typical magnetization curve for hematite (cone #1) is shown in Figure (4-13). The considerable degree of weak ferromagnetism and hysterisis is evident. This results in the magnetic susceptibility, given by the slope of a line from the origin to a point on the curve, decreasing as the magnetizing field is increased.

The actual magnetization curves were fitted to a rearranged form of Equation (3.1-24a), describing field-dependent susceptibility, namely;

$$\chi = \chi_\infty + \frac{\sigma_o}{H}$$

where $\chi = \frac{\sigma}{H}$

To obtain the constants χ_∞ and σ_o, χ was least-squares fitted to the inverse field. Table (4-2) lists values of χ_∞ and σ_o for the cone fractions and although some variation is evident it is seen that no definite trend of values with respect to particle size occurred. Average values were, therefore, determined for use in the modelling: $\chi_\infty = 2.18 \times 10^{-5}$ emu/g-Oe($\kappa_\infty = 1.14 \times 10^{-3}$ emu/cm^3-Oe) and $\sigma_o = 0.308$ emu/g ($M_o = 1.62$ emu/cm^3).

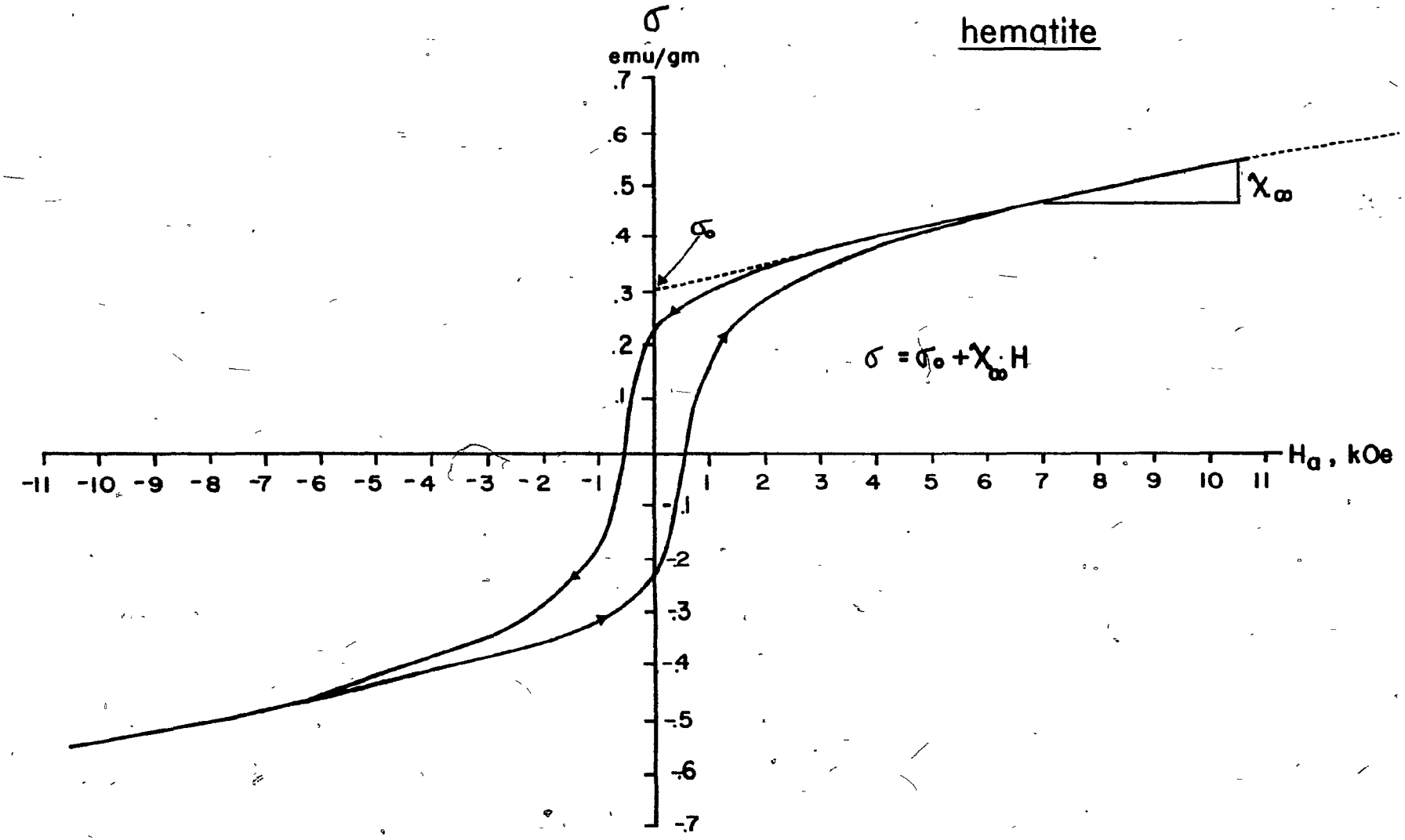

4-13 Typical magnetization curve for hematite. Labrador-hematite, cyclosizer cone #1 material.

TABLE 4-2

Susceptibility and Magnetization Parameters of Hematite (Regression for 3.0 to 10.0 kOe Data).

Cone #	$K_\infty x10^3$ (emu/cm^2-Oe)	M_o (emu/cm^3)	$\chi_\infty x10^6$ (emu/g-Oe)	σ_o (emu/g)
#1	1.27	1.62	24.2	.307
#2	1.26	1.61	23.9	.306
#3	1.09	1.44	20.8	.273
#4	1.03	1.60	19.6	.305
#5	1.07	1.85	20.3	.351
average	1.14	1.62	21.8 ± 2.1	.308 ± .028
#2 not 'magnetically cleaned'	1.14	6.36	21.7*	1.21**
-#5 slimes	0.96	9.10	18.3*	1.73**

*regression 9-10 kOe
**regression 7-10 kOe

A comparison between two magnetically 'as is' samples and a 'cleaned' sample is shown in Figure (4-14) with corresponding values of χ and σ_o appearing in Table (4-2). The -#5 fraction is too fine for 'cleaning' on the Frantz-Isodynamic while the 'as is' #2 cone material contained roughly 1% free magnetite. While χ_∞ remains about the same for contaminated and cleaned sample, note the much larger values of σ_o for uncleaned materials. The importance of removing strongly magnetic impurities from bulk samples is clearly evident.

A sample of magnetite isolated from the same ore had the magnetization curve shown in Figure (4-15). The saturation magnetization, 91.1 emu/g, compares well with published values of 91-92 emu/g.[78]

Frantz Isodynamic Separator

Since the path travelled by an individual particle is determined by the net resultant of magnetic and gravity forces, an estimate of particle susceptibility may be made using the Frantz Isodynamic. Hess[71] gives the approximation for mass susceptibility, χ(emu/g-Oe) as;

$$\chi = \frac{2 \sin \theta \times 10^{-5}}{I^2} \qquad (4.1\text{-}8)$$

where θ is the side slope of the device and I the minimum input current, in amperes, for which a particle reports to the magnetics chute. It is not known whether the constant, 2×10^{-5} amp^{2}emu/g-Oe, is mathematically derived or results from a calibration against the susceptibility of a standard.

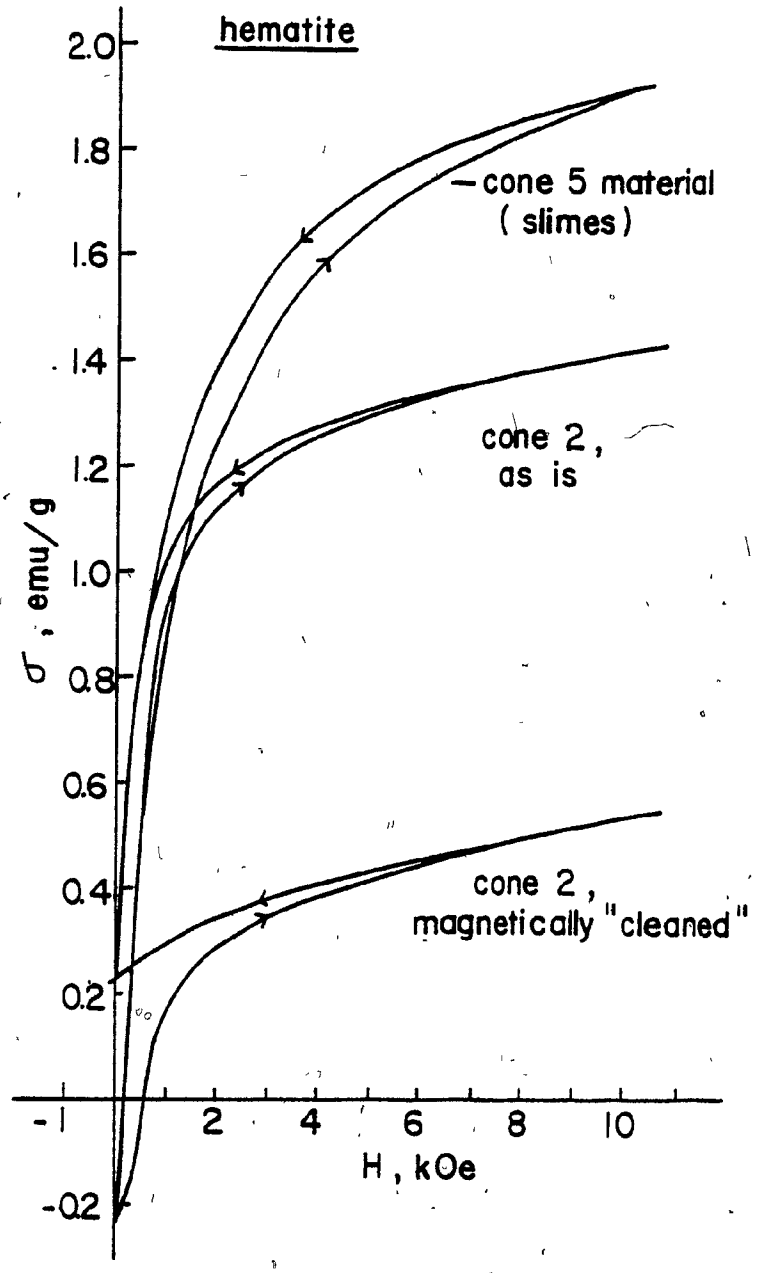

4-14 Magnetization curves for 'cleaned' and 'as is' cone #2 hematite, and minus cone #5 (slimes) material.

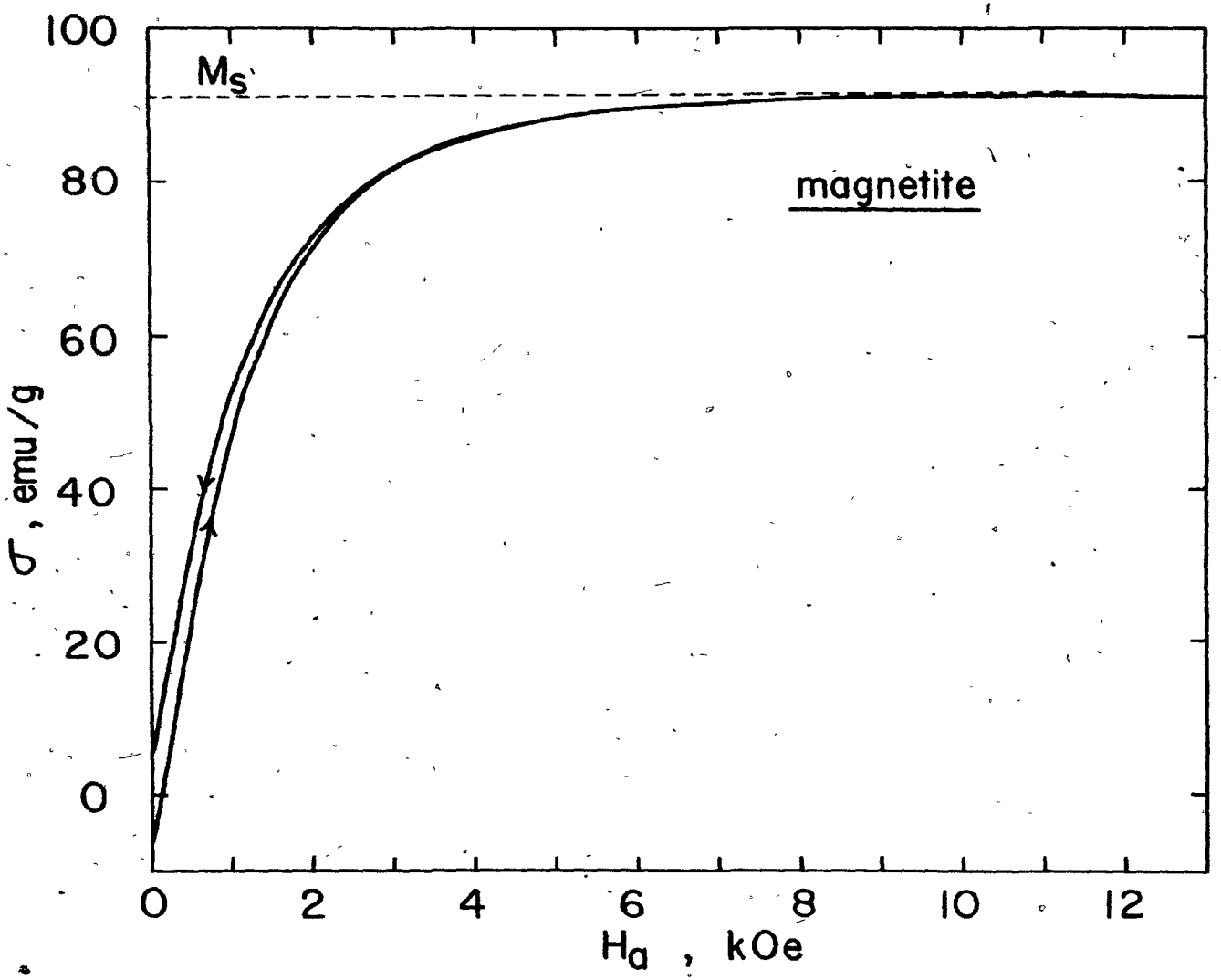

4-15 Magnetization curve for magnetite isolated from Labrador ore sample.

When treating materials exhibiting field dependent susceptibility with a Frantz it must be recognized that since H changes, χ will also change with particle position in the pole gap. A decision is required as to the critical location at which a balance between magnetic and gravity forces should be struck. An argument is made for selecting the centre-line of the chute. As all particles enter at this location, one which experiences an exact balance between forces will travel along the centre-line and have a 50-50 chance of reporting to either side of the chute splitter. The current at which 50% of the feed sample goes each way, the I_{50}, is taken as a measure of the balanced forces and can be used to determine susceptibility. Essentially, this is the same approach as used for paramagnetics.[69,79]

Consider a single particle in the chute of the Frantz Isodynamic. A balance of gravity and magnetic forces yields:

$$- mg \sin\theta = \frac{m}{2} \nabla(\sigma.H) \qquad (4.1\text{-}9)$$

For field dependent susceptibility of the form;

$$\sigma = \sigma_o + \chi_\infty H \qquad \text{(from Equation (3.1-24a))}$$

after substitution into Equation (4.1-9) and differentiating, one obtains;

$$-g \sin\theta = \frac{\sigma_o}{2} \frac{dH}{dx} + \chi_\infty H \frac{dH}{dx}$$

the assumption being that $\sigma_o H = \sigma_o \therefore H$ (see Equation (3.1-25)). Rearranging gives;

$$- \sin \theta = \sigma_o \left(\frac{1}{2g} \frac{dH}{dx}\right) + \chi_\infty \left(\frac{H}{g} \frac{dH}{dx}\right) \qquad (4.1\text{-}10)$$

as the expression relating side slope (θ) to the magnetization parameters σ_o and χ_∞.

In order to evaluate $\frac{dH}{dx}$ and $H\frac{dH}{dx}$ as functions of current (I_{50}), use is made of the isodynamic nature of the pole design, where by definition:

$$H \frac{dH}{dx} = \text{constant} \qquad (4.1\text{-}11)$$

Solving this differential equation for the following boundary conditions (from Figure (4-8) at the positions of maximum chute width), i.e.;

B.C.

i) $H = H_{max}$ at $x = 0$ cm

ii) $H = \frac{H_{max}}{2}$ at $x = 1.52$ cm

yields the solution:

$$\frac{H}{H_{max}} = (1 - (.493\ \text{cm}^{-1})x)^{1/2} \qquad (4.1\text{-}12)$$

An underestimation of the maximum field (Equation (4.1-7)) will occur since the width of the Hall probe (0.5 cm) is considerably greater ($\sim 4x$) than the H_{max} peak (Figure (4-8)). From Equation (4.1-12) and Figure (4-8) an estimate is made that H_{max} is low by 6-13%. Assuming

an average 10% underprediction, Equation (4.1-7) for the Frantz Isodynamic has been revised to give:

$$H_{max} = 12.3 \times \text{amperes} \times 1.1$$

$$= 13.5 \times \text{amperes} \qquad \ldots\ldots (4.1\text{-}13)$$

for field in kOe.

The second boundary condition for Equation (4.1-11) now changes to;

$$\text{ii)} \quad H = .454\, H_{max} \qquad \text{at } x = 1.52 \text{ cm}$$

which yields the revised solution:

$$\frac{H}{H_{max}} = (1 - (.525\ \text{cm}^{-1})x)^{1/2} \qquad (4.1\text{-}14)$$

for field in the gap.

It is readily evident that;

$$\frac{dH}{dx} = - \frac{(.262\ \text{cm}^{-1})}{(1 - (.525\ \text{cm}^{-1})x)^{1/2}} H_{max}$$

and

$$H \frac{dH}{dx} = - (.262\ \text{cm}^{-1}) H_{max}^{2} \qquad (4.1\text{-}16)$$

Evaluating Equation (4.1-15) at the splitter location, $x = 0.76$ cm, and then substituting the necessary values for H_{max}, g, $\frac{dH}{dx}$, $H \frac{dH}{dx}$ in Equation (4.1-10) yields;

$$\sin\theta = (2.33\ \sigma_o)I_{50} + (4.88\times10^4\ \chi_\infty)I_{50}^2 \qquad (4.1\text{-}17)$$

as the relationship for determining field dependent susceptibility parameters from the Frantz Isodynamic. Note that, unlike the Hess relationship where sin θ is proportional to I_{50}^2 (Equation (4.1-8)), Equation (4.1-17) has sin θ varying with I_{50} as a second order polynomial through the origin.

If σ_o is zero, Equation (4.1-17) reduces to;

$$\chi_\infty = \frac{20.5 \sin\theta \times 10^{-6}}{I_{50}^2} \qquad (4.1\text{-}18)$$

which is virtually identical to the Hess equation for χ. It would appear that Equation (4.1-17) is a more general form for χ determination applicable to both field-dependent and field-independent susceptible materials.

I_{50} values for the hematite were determined by successively retreating the non-magnetics fraction of the originally 1 g samples at small incremental increases in current until all the sample had reported to magnetics. The I_{50} could then be read from a plot of the resulting 'magnetic profile' at 50 cumulative weight % to magnetics versus current. The procedure was repeated for a range of side slopes, θ, which is equivalent to measuring susceptibilities at different H.

Results generated in this fashion proved very repeatable. A standard error in the I_{50} readings of ± .007 amperes was determined from the pooled variance of 35 measurements for cone fractions #1 and #2. This included up to 4 repeats for a given sample at θ from 5^o to

45^{o}. Due to the similar behavior of all sizes suggested by the magnetometer study (Table (4-2)) the remaining cone fractions (#3,4,5) were not investigated.

Following Equation (4.1-17) the results of I_{50} and θ were data fitted to a second order polynomial, and are shown in Figure (4-16). This gave;

$$\sin \theta = 1.20\, I_{50} + 1.07\, I_{50}^{2} + .012 \qquad (4.1\text{-}19)$$

from which the magnetization parameters could readily be calculated:

$$\sigma_{o} = .515 \text{ emu/g} \pm .03$$

$$\chi_{\infty} = 21.9\text{x}10^{-6} \text{ emu/g-Oe} \pm 1.8\text{x}10^{-6}$$

The ranges are due to the uncertainty associated with the maximum field estimate on the Frantz Isodynamic. Note that the 40^{o} and 45^{o} values of I_{50} were not included in the regression since these steep angles appeared to exceed the operating limit of the device (see Figure (4-16)).

A comparison between Frantz Isodynamic and magnetometer generated σ_{o} and χ_{∞} appears in Table (4-3). While χ_{∞} values are virtually identical, the Frantz method yields σ_{o} almost 70% larger than the magnetometer value.

Figure (4-17) shows hematite susceptibility, χ, and magnetization, σ_{p}, calculated from the χ_{∞} and σ_{o} values of Table (4-3). Note

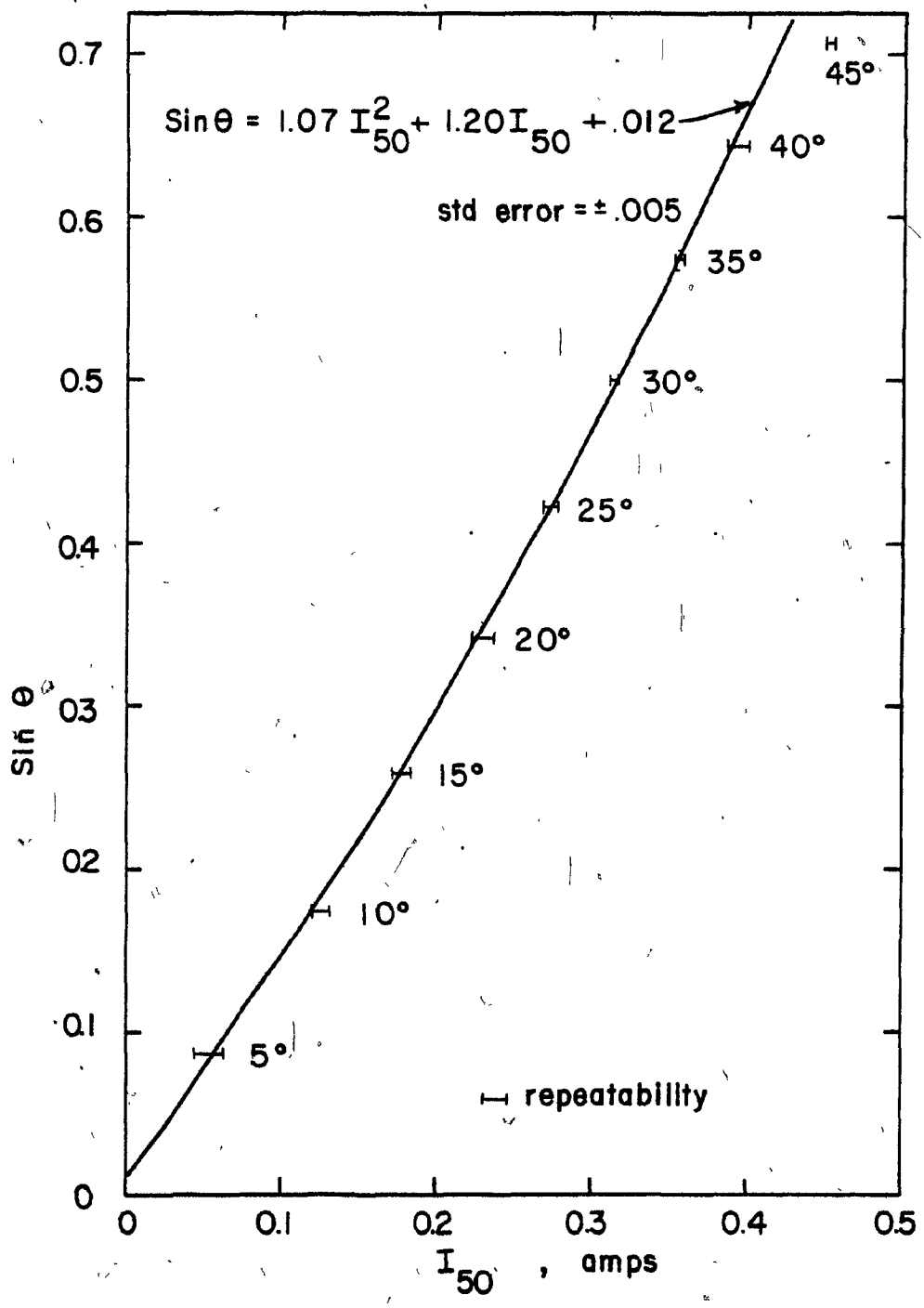

4-16 Sin θ versus I_{50} for hematite sample on the Frantz Isodynamic separator. θ is the side slope.

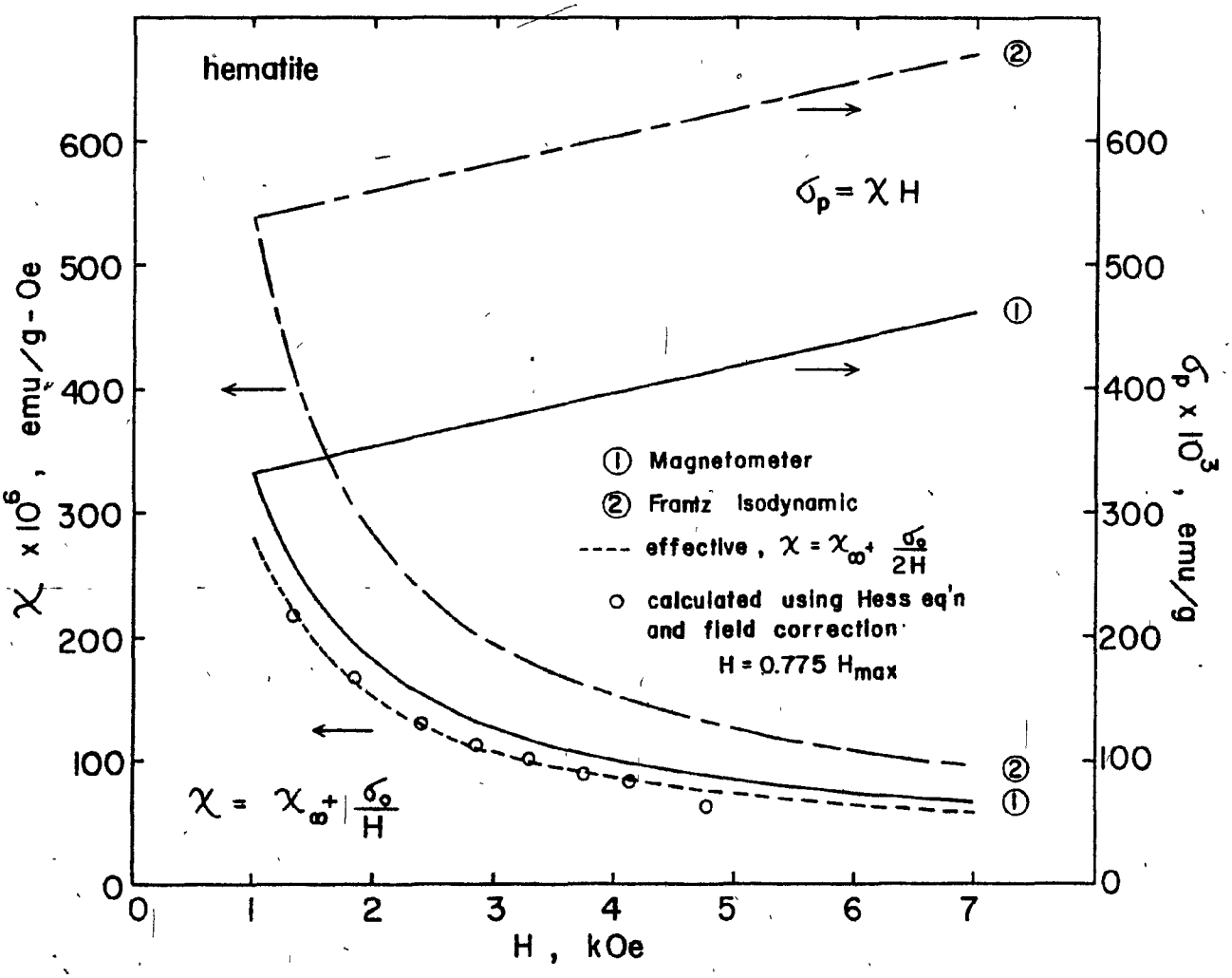

4-17 Comparison between magnetometer and Frantz Isodynamic susceptibility and magnetization for hematite.

TABLE 4-3

Average Magnetization Parameters for Hematite. Magnetometer and Frantz Isodynamic Data.

Method	$\chi_\infty x10^6$/emu/g-Oe	σ_o(emu/g)
Magnetometer	21.8 ± 2.1	.308 ± .028
Frantz Isodynamic	21.9 ± 1.8	.515 ± .03

TABLE 4-4

Magnetization Parameters of Other Mineral Samples. Magnetometer Data.

Mineral	$\chi_\infty x10^6$	$\sigma_o x10^3$	Field	Sample Origin
ilmenite	66.1	243	> 2 KOe	Allard Lake, Que.
sphalerite	6.95	68.9	> 4 KOe	Geco Mines, Ont.
chalcopyrite	4.10	97.6	> 4 KOe	Geco Mines, Ont.

the large field dependence of χ, especially for H below 5 kOe. Treating susceptibility as a constant in this region would be a poor approximation as already cautioned by Pastrana and Hopstock.[49] Particle magnetization, σ_p, based on magnetometer σ_o and χ_∞, is seen to be about two-thirds that calculated from the Frantz data.

If the Hess relationship is used to calculate χ a correction is required since the field at the splitter location is less than the maximum (i.e. $H_{splitter} = 0.775\ H_{max}$). Values calculated in this manner (shown as circles in Figure (4-17)) represent an 'effective' susceptibility which may be approximated from χ_∞ and σ_o by:

$$\chi_{eff} = \chi_\infty + \frac{\sigma_o}{2H} \qquad \text{(from Equation (3.1-2a))}$$

χ_{eff} is shown as the dashed line in Figure (4-17) and is seen to agree closely with the Hess points. The advantage of being able to easily go from the effective value to the magnetization constants or vice versa via Equations (4.1-8) and (4.1-17) using the proper adjustments is obvious.

Other Samples

The magnetization behavior of a number of mineral samples from a previous study by Dobby[79] were also examined on the vibrating sample magnetometer. The purpose was to generate input data for the model to permit a comparison between predictions and the experimental results of Dobby for ilmenite, sphalerite and chalcopyrite.

Although, magnetically, none of these minerals are called antiferromagnetics, the analysis of their magnetization in terms of

χ_∞ and σ_o permits the separation of paramagnetic effects from possible ferromagnetic contributions of any impurities. The results are seen in Table (4-4). Some hysteresis was noted for the ilmenite. It is also noteworthy that these samples were not as free of minute quantities of impurities as was the hematite in that they had been used for considerable test work since their original preparation by Dobby. Some contamination can, therefore, be expected to have influenced the measurement.

4.1.3 Wire Magnetization Measurements

The measurement of the magnetic behavior of ferromagnetics below saturation is somewhat complicated by the necessity of accounting for demagnetizing effects in the samples. As explained in Section 3.1, the demagnetization factor, N, relates the demagnetizing field, H_D, to the magnetization, H_w, through:

$$H_D = NM_w \qquad (3.1\text{-}17)$$

N may only be calculated for ellipsoidal shapes, since only they experience uniform magnetization throughout.

A cylindrical rod can be considered as a prolate spheroid for which the demagnetizing factor perpendicular to the long axis has been given by Stoner[80] as;

$$N = 2\pi - \frac{2\pi}{(r^2 - 1)}\left[\frac{r}{(r^2 - 1)^{1/2}} \ln\{(r + (r^2 - 1)^{1/2}) - 1\}\right] \qquad .....(4.1\text{-}20)$$

where r is the length-to-diameter ratio. For r very large (i.e. infinitely long rod);

$$N \approx 2\pi$$

Within a non-ellipsoidal body, the internal field, and hence the magnetization, is non-uniform and consequently H_D must be estimated through measurement. During initial magnetization the internal field is very small in comparison with H_a and H_D so it is possible to write

$$H_a \simeq H_D$$

$$= NM_w$$

It is evident that the N may be estimated from the initial slope of the magnetization curve:

$$\left.\frac{dM_w}{dH_a}\right|_{initial} = \frac{1}{N} \qquad (4.1\text{-}21)$$

Infinitely long rods, for which N equals 2π, should therefore exhibit magnetization curves of initial slope $\frac{1}{2\pi}$ or 0.159 emu/cm^3-0e.

Nickel Standard, Nickel and Stainless Steel Wire Matrices

The calibration standard was a cylindrical high-purity nickel plug of length 0.340 cm and diameter 0.245 cm with a known saturation magnetization of 484.1 emu/cm^3. The measured initial magnetization slope

(at $H_a \leq 1.5$ kOe) of 0.215 emu/cm^3-Oe was in excellent agreement with the value of 0.212 emu/cm^3-Oe calculated from Equation (4.1-20) having $r = 1.39$. This good agreement suggested a method for obtaining valid magnetization curves of infinitely long rods (required by the model) from the measured magnetization slopes of the relatively short and not quite cylindrical cross-sections of the samples. The transformation was necessary to achieve compatability between real wire magnetization and the perturbation term $(\frac{2\pi M_w}{H_a})$ for the infinite-wire model at fields below saturation.

The procedure used was to first determine the initial slope $(= \frac{1}{N})$ from the measured magnetization curves of both matrix samples (nickel wire and stainless steel mesh). From this, the demagnetizing field, $H_D (= NM_w)$, and internal field $(= H_a - H_D)$ as a function of M_w could be found. The applied fields necessary to generate the same M_w in infinitely long rods was then calculated by adding the demagnetizing field, H_D $(= 2\pi M_w)$, to the previously determined internal field values. These magnetization versus applied field curves for infinite rods were then fitted to the simple exponential relationship suggested by Clarkson[33];

$$M_w = M_s \exp(-\frac{K}{H}) \qquad (3.1\text{-}19)$$

where K is an empirical constant, H the internal field $(= H_a - 2\pi M_w)$ and M_s the saturation magnetization. Curves showing the measured and corrected magnetization behavior are shown in Figures (4-18) and (4-19) together with the fits to Equation (3.1-19). Values of K and M_s are presented in Table (4-5). It is seen that the nickel wire saturates

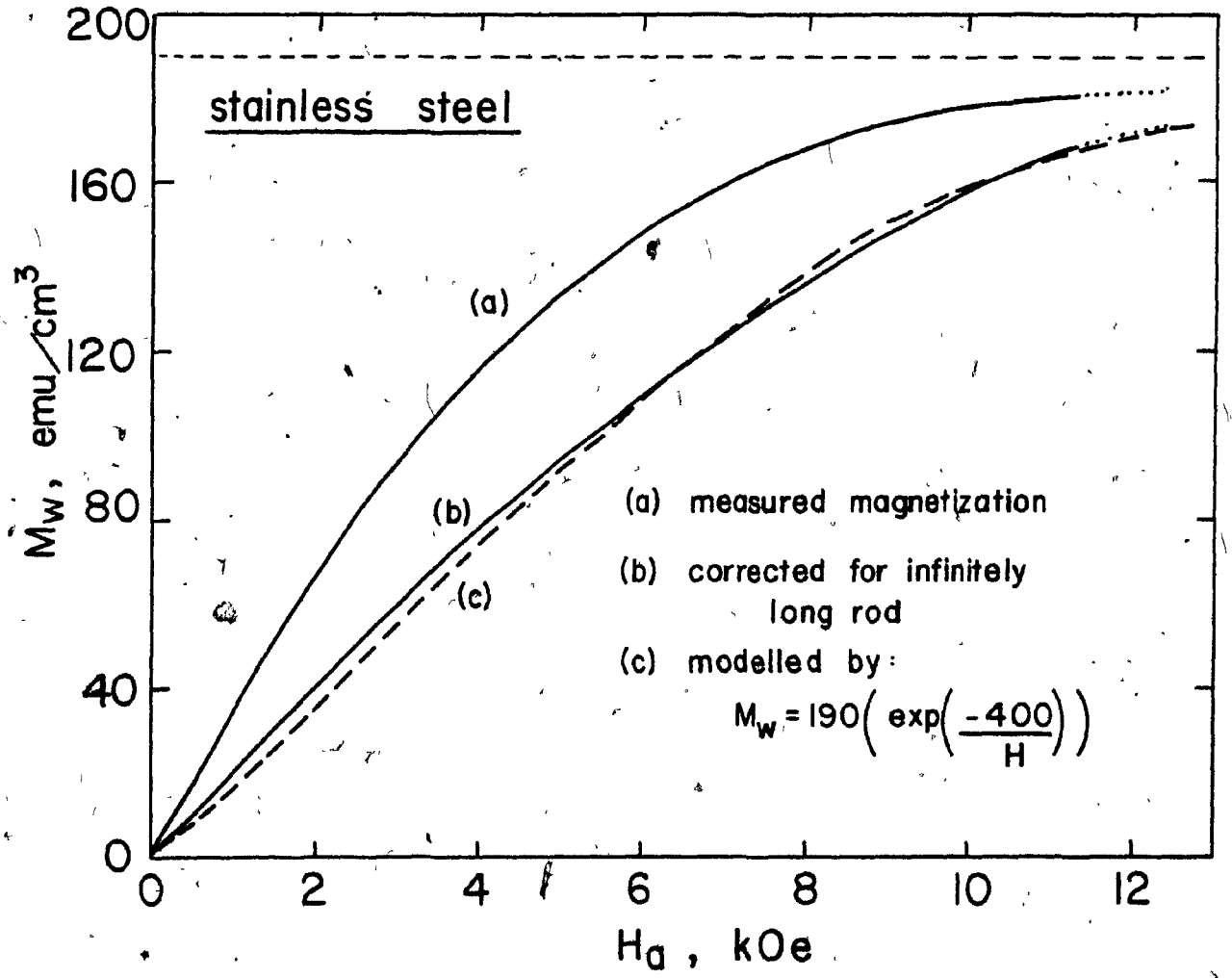

4-18 Magnetization curves for stainless steel matrix.

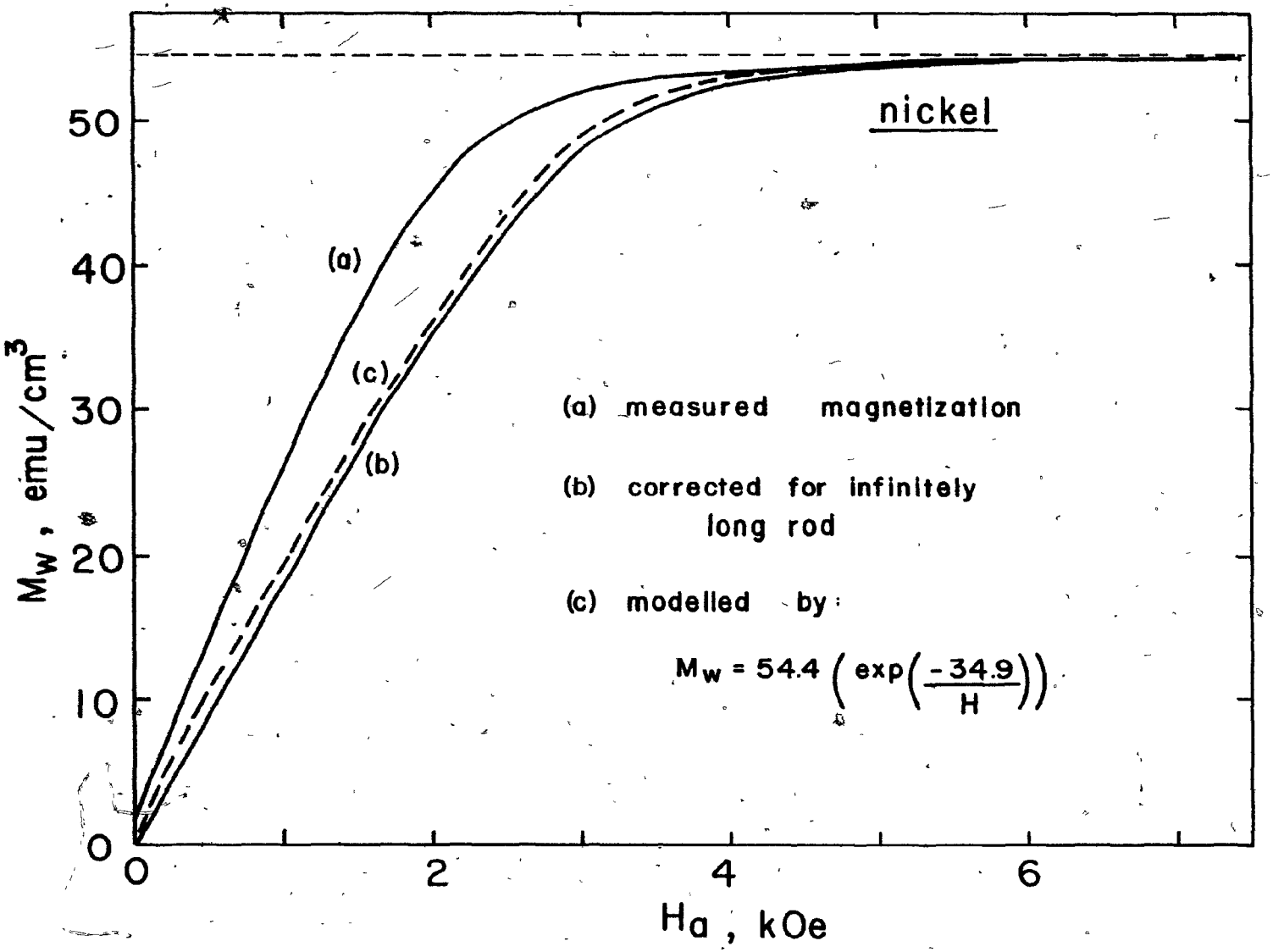

4-19 Magnetization curves for nickel wire.

TABLE 4-5

Values of M_s and K for Stainless Steel Mesh and Nickel Wire.

Magnetization Constants* for Eq. (3.1-19)		Matrix Type	
		Nickel Wire	Stainless Steel Wire Mesh
M_s	(emu/cm^3)	484	1472
	(emu/gm)	54.4	190
K	(Oe^{-1})	34.9	400

*The lower limit of applicability for Eq. (3.1-19) appears to be $\sim$ 900 Oe ($=H_a$).

quickly (at 3-4 kOe) to a value approaching 54.4 emu/g while the stainless steel begins, at 10-12 kOe, to saturate toward a magnetization estimated at 190 emu/g.

4.2 Particle Size Measurement

4.2.1 The Cyclosizer

Closely sized fractions of real minerals for the test work were generated with a hydraulic cyclone elutriator, the Warman Cylcosizer, described in detail by Kelsall and McAdam.[81] This device, consisting of 5 cyclones in series, separates up to 100 g* of feed at a time into a roughly $1/\sqrt{2}$ decreasing series of 5 sizes in the subsieve, 50-8 μm*, range. It is claimed[81] that Stokes' Law applies to classification in the cyclones where large centrifugal forces and high fluid shear result in rapid classification times (20-40 minutes) with minimal dispersion problems.

The unit is precalibrated to a silica standard with a nominal cut-off size for each cyclone (d_∞) based on infinite elutriation time and a set of standard operating conditions. Correction factors are then required for the conditions; i.e. water temperature (f_1), specific gravity (f_2), flowrate(f_3) and running time (f_4), which differ from the standards in order to generate a set of actual cut-off diameters, d_a, for each of the cones, viz;

$$d_a = d_\infty \cdot f_1 \cdot f_2 \cdot f_3 \cdot f_4 \qquad (4.1\text{-}22)$$

*Nominal values for silica, the calibration standard.

In theory then, each cone fraction contains those particles of equivalent-settling size which lie between its own cut-off size, d_{a_n}, and that of the previous cone, $d_{a_{n-1}}$. A geometric mean size, d_{gm}, defined as;

$$d_{gm_n} = (d_{a_n} \times d_{a_{n-1}})^{1/2} \qquad (4.1\text{-}23)$$

was used to characterize the size distribution of particles within the fraction n.

The operating conditions, correction factors, cut-off sizes, and geometric means for the hematite are presented in Table (4-6). The very fine #5 cyclone undersize was collected for the first 20 litres (approximately 2 minutes) of operation.

Table (4-6) shows the largest correction factor to be for specific gravity as a result of the large density difference between hematite (5.25) and the silica standard (2.65). Up to 10 cyclosizer runs of 50 g feed lots were required to produce the 20 to 60 grams of each cone fraction needed for the experimental runs.

4.2.2 The Sedigraph

In order to further investigate the ability of the Cyclosizer to generate closely-sized fractions and as a check on the calculated equivalent Stokesian diameters, the size distribution of each of the cone fractions was determined on an x-ray sedimentometer; the Micromeritics SediGraph 5000D.

TABLE 4-6

Cyclosizer Operating Conditions and Calculated Size Fractions for Hematite.

	Cut-off Sizes			
Cone #	d_∞ (μm)	d_a	Range	d_{gm}
1	39.7	26.1	26.1-37*	31.1
2	30.2	19.8	19.8-26.1	22.7
3	22.5	14.8	14.8-19.8	17.1
4	15.5	10.2	10.2-14.8	12.3
5	12.1	8.0	8.0-10.2	9.0
-5	-		-8.0	-

*Feed sample is undersize from screening at 400 mesh.

Variable	Operating Value	Correction Factor
water temp.	14.6°C	$f_1 = 1.073$
specific gravity	5.26	$f_2 = 0.622$
flow rate	11.6 litres/min	$f_3 = 1.000$
running time	60 minutes	$f_4 = 0.985$

This device employs a finely collimated x-ray beam to measure the change with time of particle settling concentration in a sample cell. The cell also descends relative to the beam so as to minimize the time required for analysis. Additional operating details are given by Olivier et al.[82] The size distribution reports on an x-y plotter as cumulative weight % finer than versus the equivalent Stokesian diameter. Particle sizes of 0.2 to 50 μm can be determined; the range depending on the relative specific gravity difference between solid and liquid and also the liquid viscosity.

A 0.2% Calgonite-in-water solution and 15-20 minutes of stirring ensured complete dispersion of the particles prior to measurement. Each sample was run twice. Sedigraph results for the cone fractions are shown in Figure (4-20). Also indicated are the calculated Cyclosizer size ranges. Note the considerable overlap of progressive size fractions plus the presence of ∿ 10% oversize material in each of the cones. The #1 and #2 cones show less of a difference than the others, possibly a result of the feed having been dry screened to minus 400 mesh (nominally 37 μm) before cyclosizing.

Agreement between the Cyclosizer and the Sedigraph is better across the total size distribution of all cones than for the individual fractions; the Sedigraph showing wider ranges and somewhat larger mean sizes, especially for the finer cones.

It is worth remembering that only truly spherical particles obey Stokes' Law and that deviations will occur for any other shape. The equivalent Stokes diameter merely represents the size of a sphere which would settle at the same rate as the particle under observation.

PARTICLE SIZ' ISTRIBUTION

SAMPLE IDENTIFICATION hematite - magnetically cleaned on Frantz Isodynamic

Density _____ g/cc LIQUID water - 0.2% calgonite

Viscosity _____ cp

Preparation 15 min stirring before analysis

2 runs for each cone

DATE _____

BY _____

TEMPERATURE _____ °C

RATE _____ START DIA. _____ µm

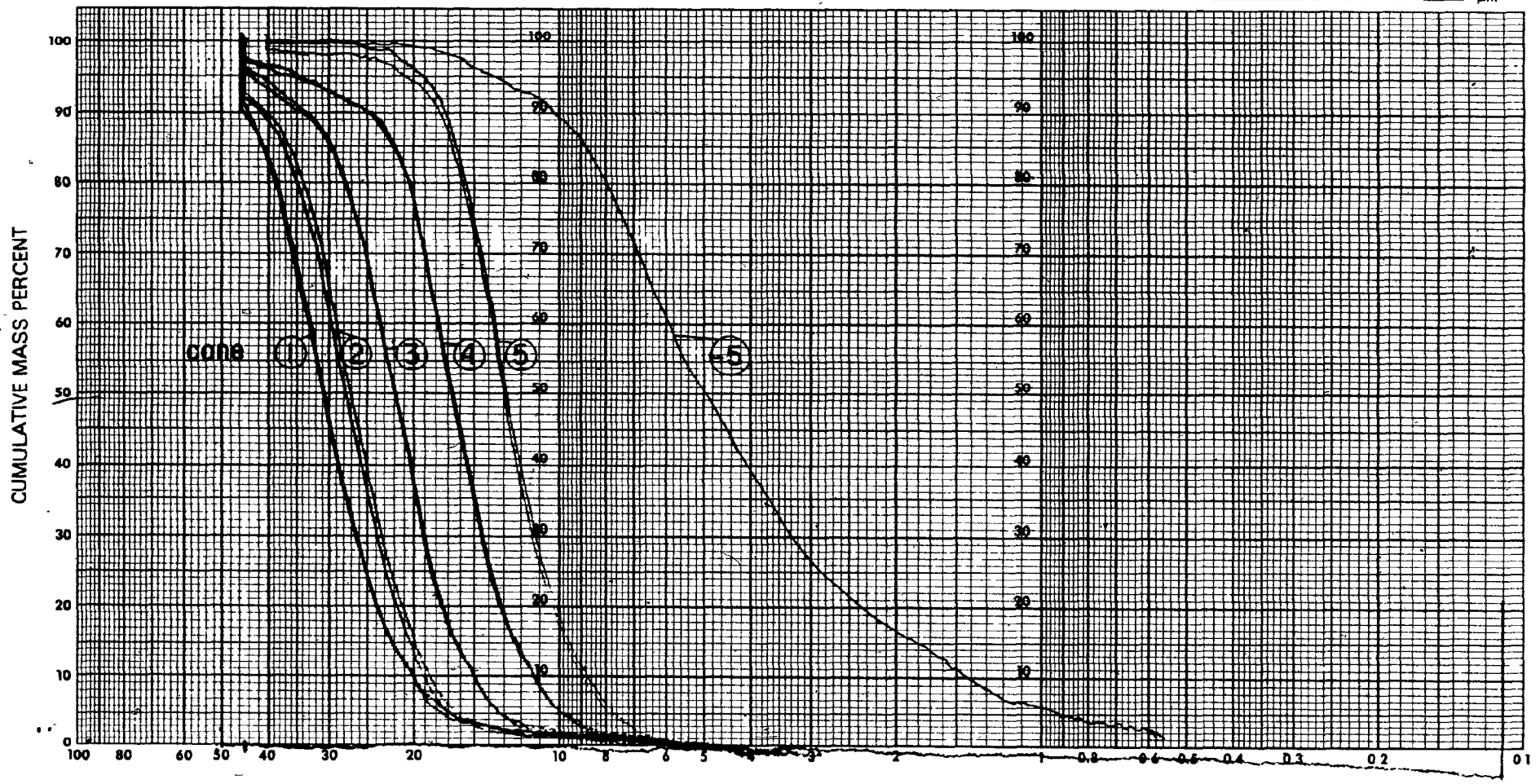

4-20 Sedigraph cumulative size distributions of cyclosizer cone fractions for hematite.

micromeritics®
instrument corporation
5680 goshen springs road • norcross georgia 30071 • USA
telephone 404/448-8282 • telex 70-7450

Form 500/42701

For real particles the term 'diameter' is a far from rigidly specified parameter and will to a large degree depend on the measurement system as pointed out by Allen.[83]

Scanning electron microphotographs of the hematite particles (Figure (4-21)) serve to illustrate their deviation from true sphericity. Note the angularity and variety of shapes present for this 20-30 μm diameter #2 cone material.

For ilmenite, sphalerite and chalcopyrite, the Dobby[69] Cyclosizer data on particle size were used.

4.3 Measurement of Other Parameters

4.3.1 Fluid Velocity

Average velocities through the cannister were calculated from measured volumetric flows over a period of time. A set of different internal-diameter bored plugs was used to adjust the velocity over the range of interest, 2-20 cm/s. These were readily interchangeable in the exit piping. Flow was from a constant head tank positioned 2 metres above the matrix cannister and discharged freely into a collection vessel about 0.5 metres below the cannister.

4.3.2 Particle Densities

The specific gravity of hematite was determined on a Berman torsion-type density balance.[84] Toluene (C_7H_8) was used as the displacement liquid because of its low surface tension (29 dynes/cm) giving easy wetting. The specific gravity of the Carol Lake hematite was thus accurately determined to be 5.250 ± .021 g/cm^3, which compares well with the range of 4.9-5.3 reported[85] for hematites in general.

4-21 Scanning Electron Micrograph of hematite. Cyclosizer cone #2 (~ 30 μm diameter) particles.

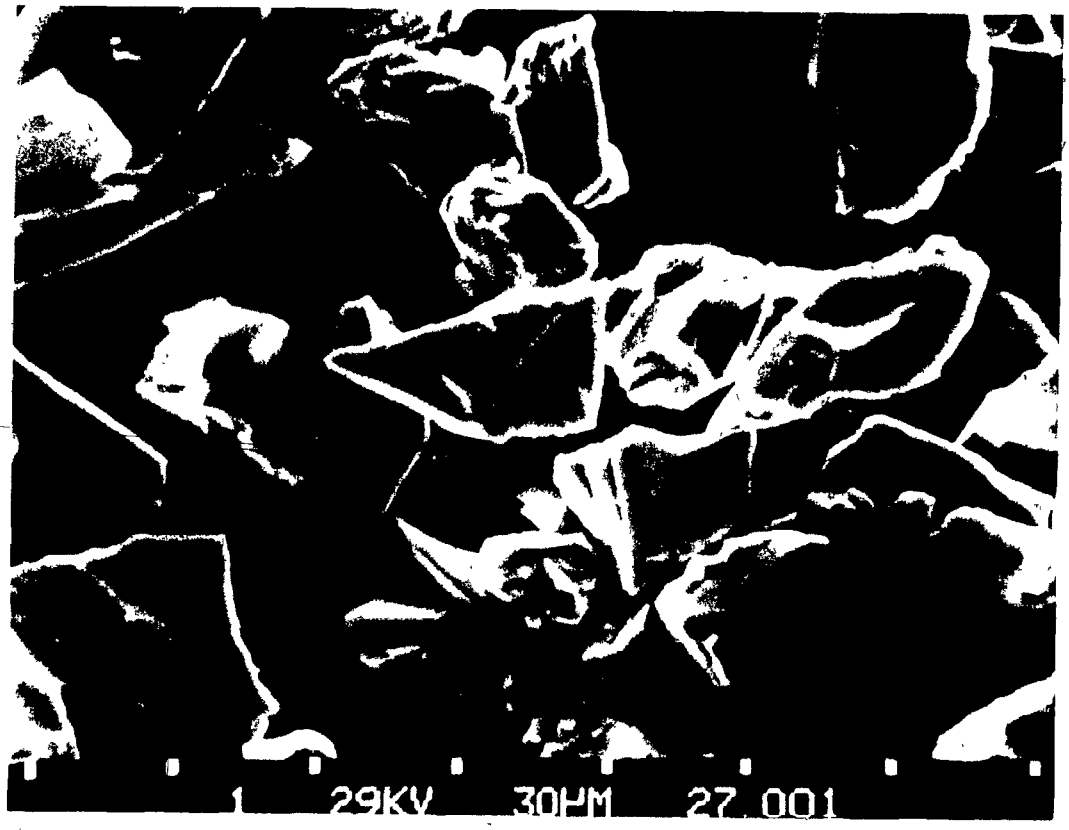
29KV 30UM 27 001

Density measurements for the other minerals of interest, using conventional specific gravity bottles and water, are listed in Table (4-7). Except for the chalcopyrite, reproducibility of the results was good.

4.3.3 Wire Size, Diameter, Density

A photograph of a single expanded metal screen appears in Figure (4-22) with relevant properties listed in Table (4-8). The cross-section of the wire, sketched in Figure (4-23), is that of a skewed diamond having one long ($\approx$ .09 cm) and one short side ($\approx$ .06 cm) projecting toward the flow. The question of a suitable wire diameter for use in the model remains. It was decided, after examining alternatives such as hydraulic radius and equivalent volume diameters, to select a diameter which gave the correct number of unit grids to a screen, i.e. 35.* From Equation (3.2-31), taking s_w, the inter-wire spacing, as 0.5 cm* for the 3.78 cm diameter screen, it is readily evident that;

$$\# \text{ grids} = \frac{(3.78)^2 \pi}{(.58)^2 \, 4}$$

$$= 33$$

if the wire diameter, 2b, is chosen as .08 cm.

For modelling on nickel wires, a density of 8.90 g/cm^3 (86) and a diameter of 125 μm was used.

---

*Values determined by measurement on an expanded metal screen.

4-22 Expanded metal screen. Diameter 3.78 cm.

TABLE 4-7

Mineral Densities.

Mineral	Specific Gravity
hematite	5.25 ± .02
ilmenite	4.81 ± .02
sphalerite	4.00 ± .02
chalcopyrite	4.1 ± .2

TABLE 4-8

Other Properties of Stainless Steel Expanded Metal Mesh.

Property	Value
screen diameter	3.78 cm
screen mass	1.41 g (average)
wire diameter	.08 cm
wire specific gravity	7.75

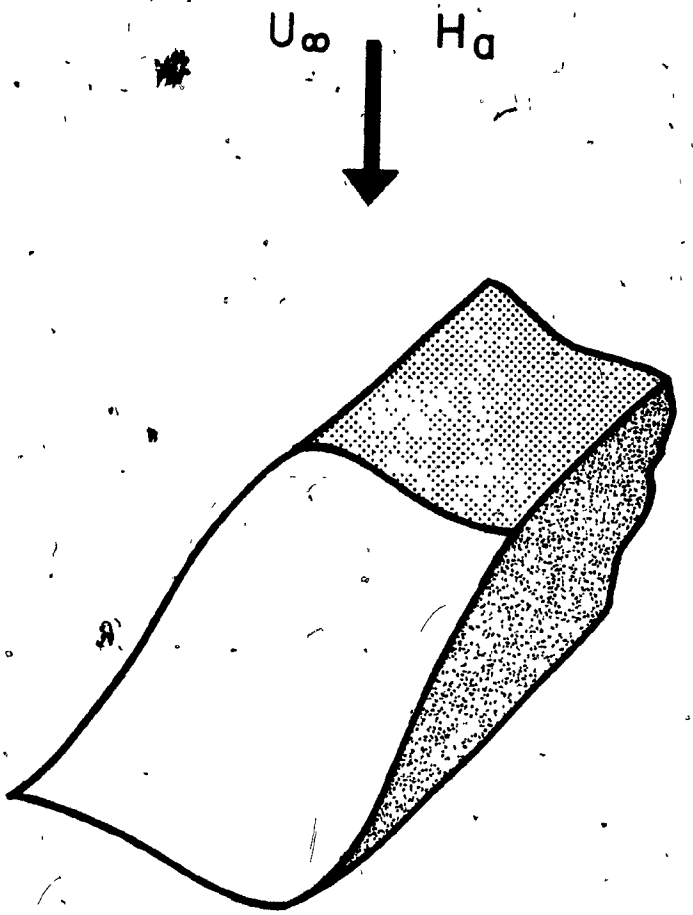

4-23 Sketch of expanded metal strand in cross-section. Note 'diamond-like' shape.

V. MODEL PREDICTIONS VERSUS EXPERIMENTAL RESULTS

5.1 Buildup on a Unit Length of Wire

5.1.1 Equilibrium Buildup Profile

Standard operating conditions which might be typical of an hgms installation treating a hematitic iron ore were defined as:

particle diameter, 2b	= 10 μm
particle density, ρ_p	= 5.25 g/cm^3
magnetization parameters, χ_∞	= 114×10^{-6} emu/cm^3-0e
σ_o	= 1.62 emu/cm^3
applied field, H_a	= 3000 0e
flow velocity, U_∞	= 10 cm/s
fluid density, ρ_f	= 1 g/cm^3
fluid viscosity, ν	= .01 S
wire diameter, 2a	= 600 μm (stainless steel)
gravitational acceleration, g,	= 980 cm/sec^2

For this 'standard' test, the model predicted the equilibrium buildup profile shown in Figure (5-1a). The presence of material considerably beyond 45° to either side of the upstream stagnation point, is particularly significant.

With the field increased from 3 to 9 k0e the magnitude of buildup increases but the extent of accumulation beyond 45°, especially close to the wire, is less (Figure (5-1b)). Also, the profile tends to

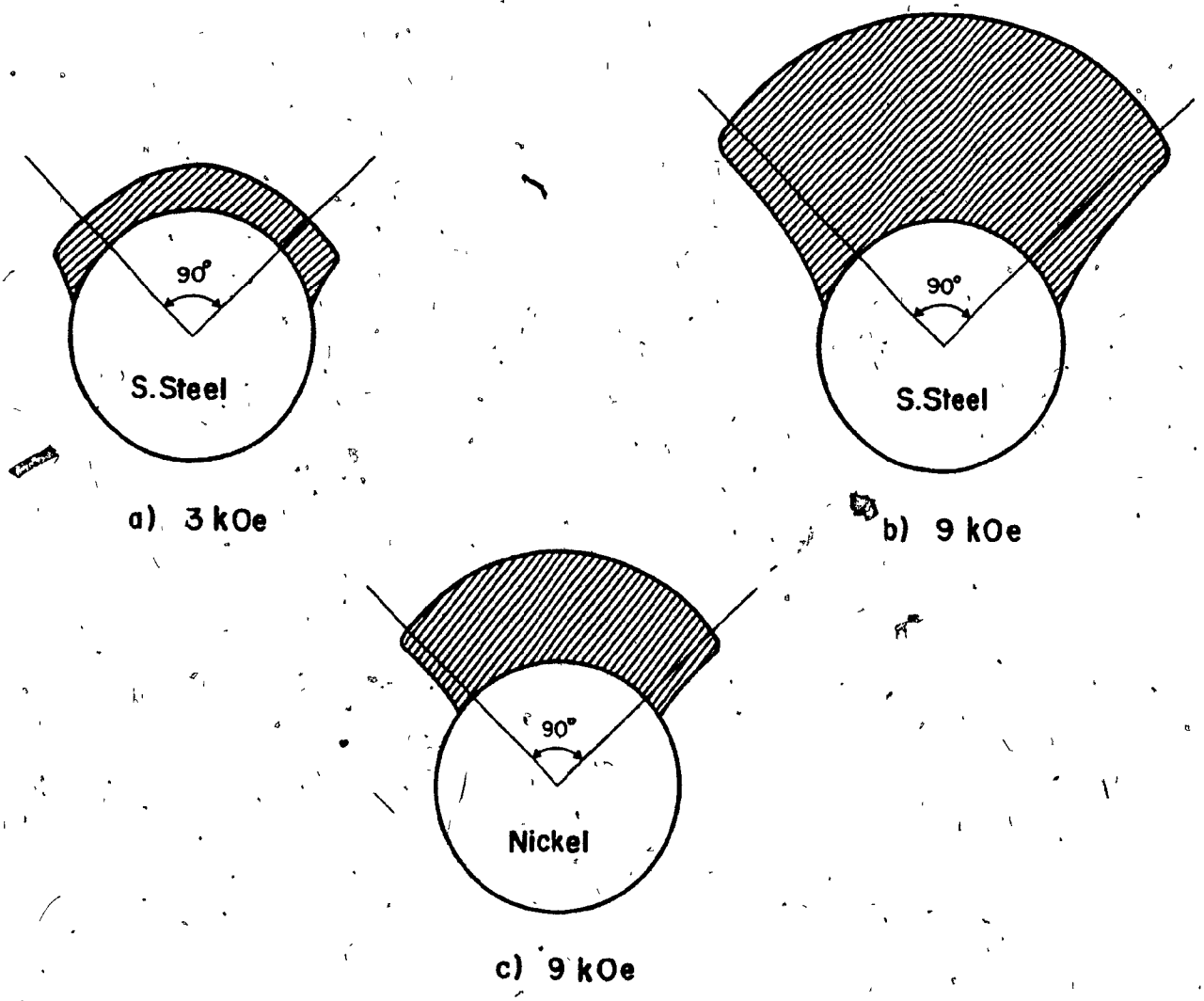

5-1 Equilibrium buildup profile, standard test.
a) 3 kOe, stainless steel wire
b) 9 kOe, stainless steel wire
c) 9 kOe, nickel wire

bulge more at the very front although this is not as evident from the figure as from the numerical results themselves. If identical nickel wire (M_s = 484 emu/cm^3) replaces the stainless steel (M_s = 1472 emu/cm^3) buildup at 9 kOe is considerably less as evident from Figure (5-1c).

Interestingly, if the wire is bottom fed rather than top fed (i.e. the sign of gravity is reversed) the standard test predicts 16% more buildup at 3 kOe and 8% at 9 kOe. The explanation is that for bottom feeding, gravity adds to the tangential magnetic component thereby helping to oppose the fluid drag.

5.1.2 Comparison with the Work of Friedlaender et al.

A set of photographs of their video images of manganese pyrophosphate ($Mn_2P_2O_7$) buildup on single strand nickel wire was made available by Friedlaender and Takayasu.[87]

Magnetic susceptibility of the $Mn_2P_2O_7$ was taken as that measured by Friedlaender et al.[88], $\chi = 83\times10^{-6}$ emu/g-Oe rather than the reported handbook value[89] ($\chi = 102\times10^{-6}$ emu/g-Oe) since assaying by atomic absorption (42.3% Mn ± .3%) showed the material to be somewhat different from stoichiometrically perfect $Mn_2P_2O_7$ (38.7% Mn). An x-ray powder diffraction study, which identified the material as having an $Mn_2P_2O_7$ crystal structure with a small amount of impurity (possibly another phosphate), and the atomic absorption were performed on a sample provided by Friedlaender.

Sedigraph size analysis showed a Stokesian size distribution with a mid-point (50%) value of 8.0 μm and a 10%-90% range of 4.0-13 μm (Figure (5-4)). These sizes correlate well with those already reported

for the material[38] by other sizing methods. The specific gravity was taken as 3.71; that for pure manganese pyrophosphate. Our own nickel wire magnetization data (Table (4-5)) were used. The properties of interest were felt to have been sufficiently defined to permit a valid comparison between the photographic evidence and the model.

Previous velocity measurements reported by Friedlaender et al. have been for average flow rates through the sample delivery tube. More recent measurements[90] of velocity at the wire location (i.e. the centre line) have shown these to be greater than the averages by roughly a factor of two. These more recent centreline values were used for the modelling.

A comparison between the Friedlaender photographs and the model predictions of equilibrium buildup at 5 kOe and various flow velocities appear in Figures (5-2a,b,c) and (5-3a,b,c). In general, the traced outlines are in good agreement with the model profiles. Both experiment and theory agree on the occurrence of buildup beyond the 90^{o} sector; the experiments showing more accumulation than predicted for distances further from the wire surface.

Results of saturated relative accumulation radius, R_{as}, for $Mn_2P_2O_7$ have also been reported by Friedlaender et al.[39], where R_{as} is the radius of buildup measured at the stagnation point divided by the wire radius. In addition to the published values at 2.2, 4.7, and 9.7 kOe, a set of unpublished data at 5 kOe were also made available by Friedlaender.

The comparisons of R_{as} versus U_{∞}, including the effects of the size distribution, are shown in Figures (5-5a,b,c). Experimental

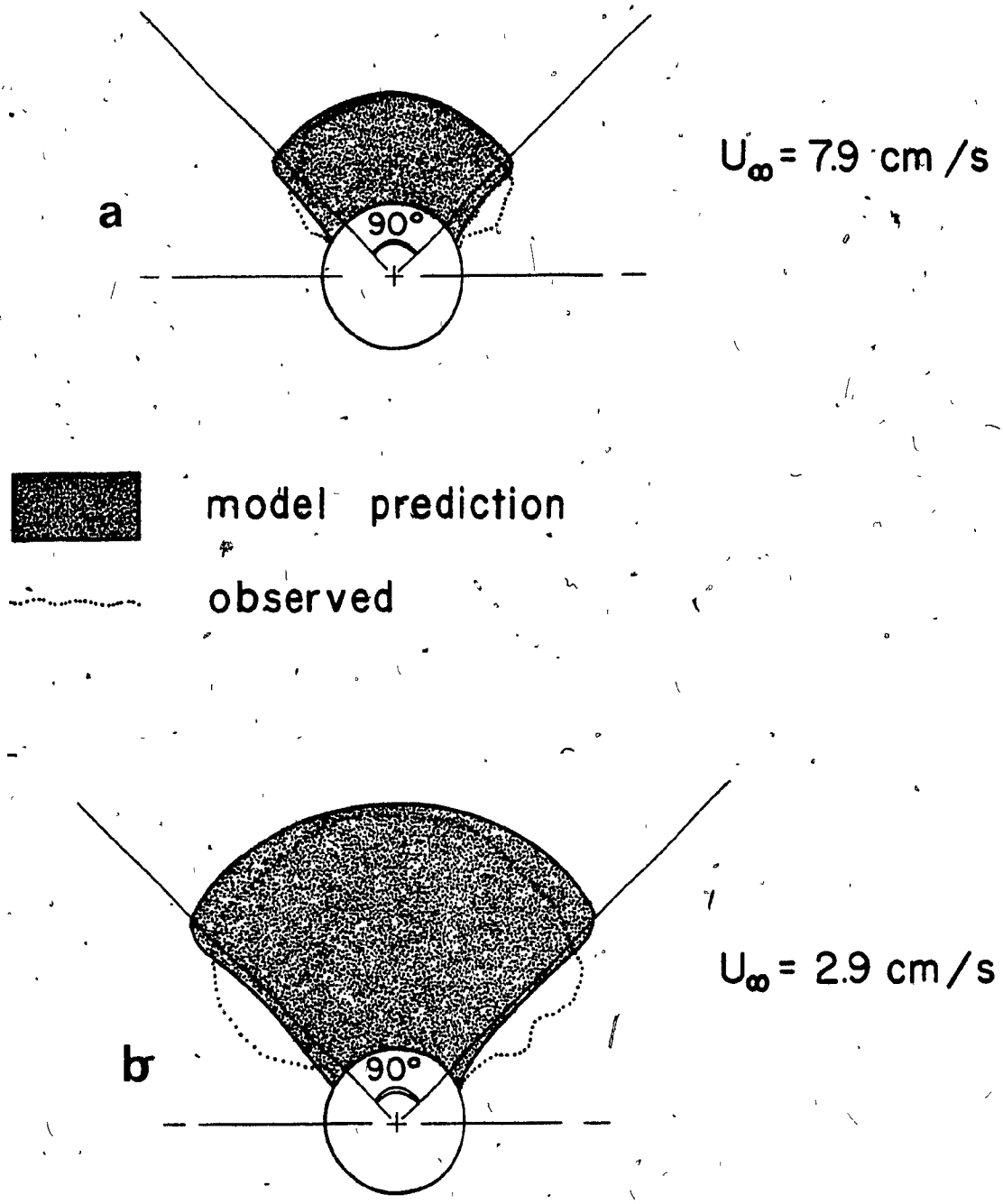

5-2 $Mn_2P_2O_7$ equilibrium buildup profile (upstream).
a) model prediction at 7.9 cm/s
b) model prediction at 2.9 cm/s
c) model prediction at 23.3 cm/s

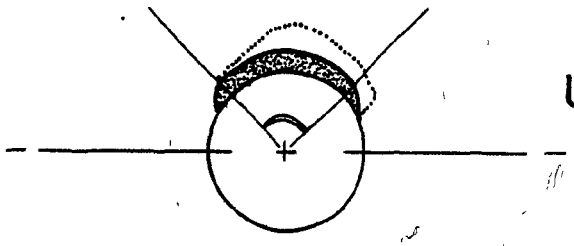

model prediction

observed

5-3 $Mn_2P_2O_7$ buildup photograph (from Friedlaender et al.).
a) at 7.9 cm/s
b) at 2.9 cm/s
c) at 23.3 cm/s

(a)

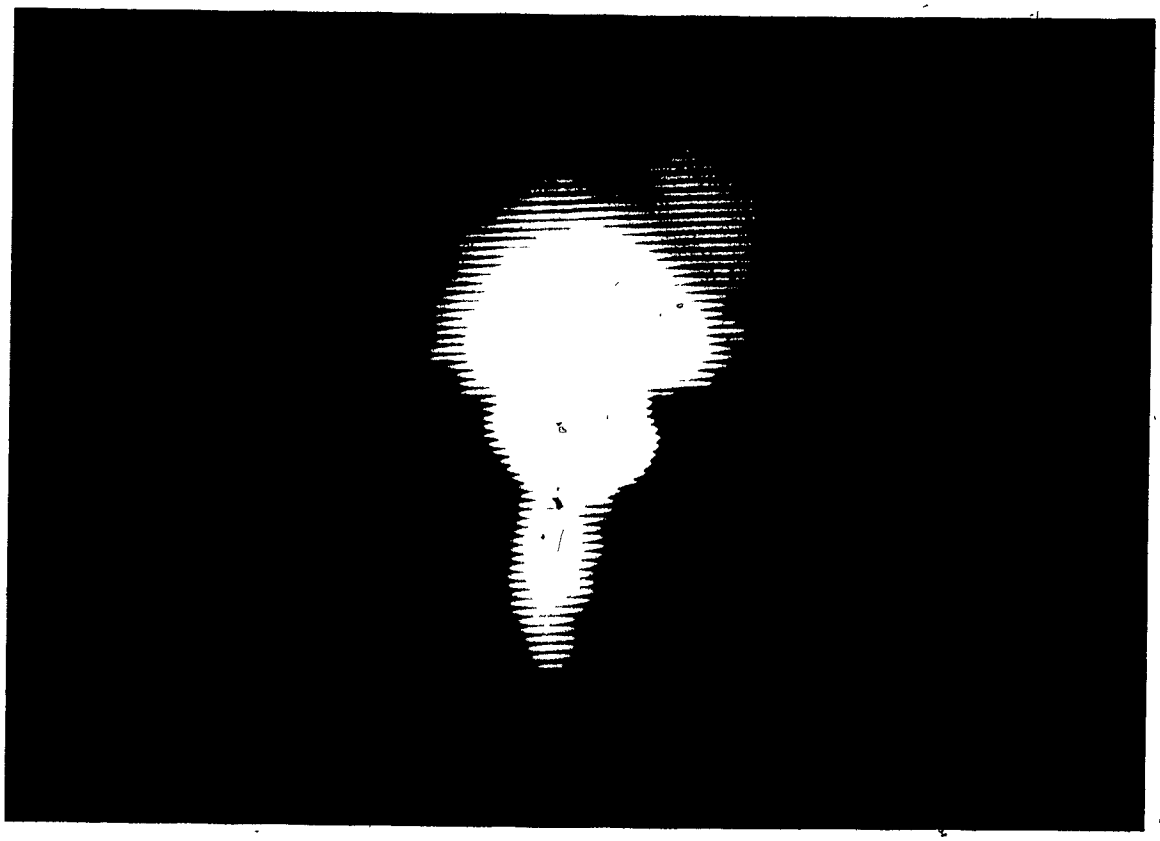

a

(b)

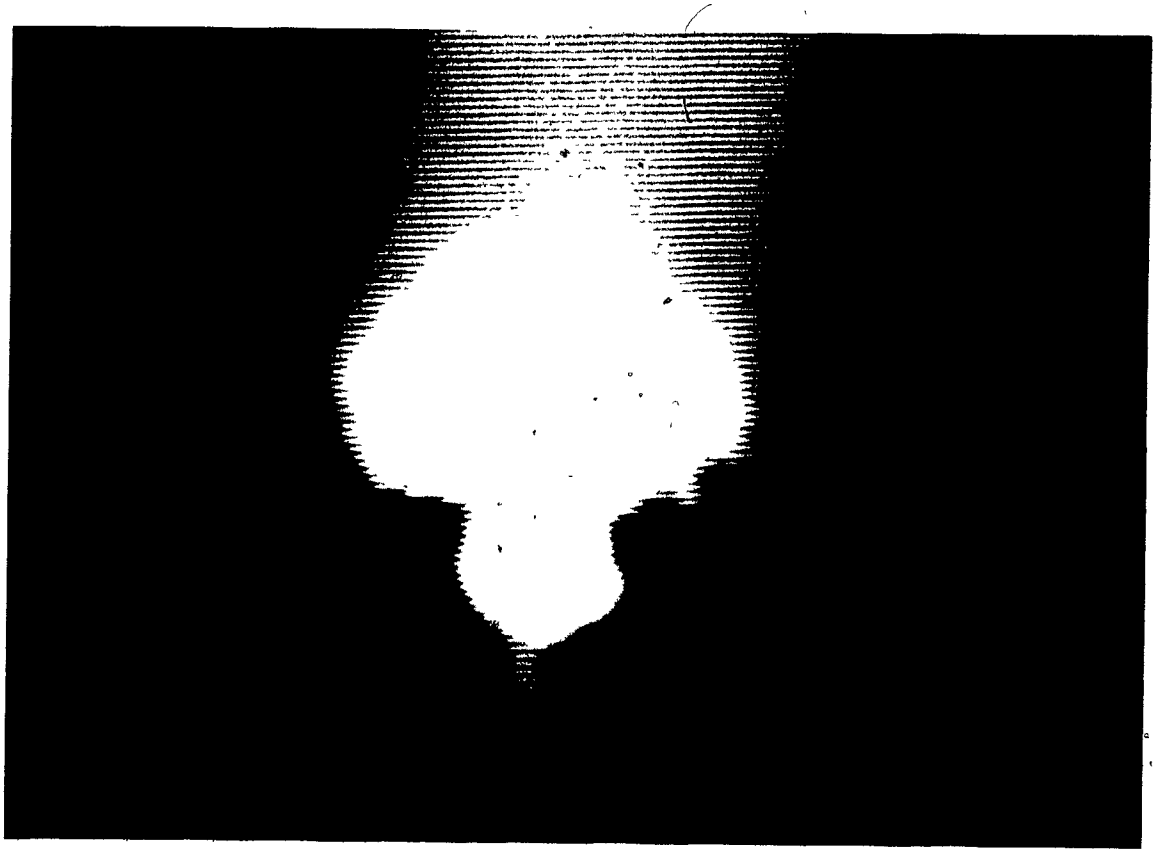

b

(c)

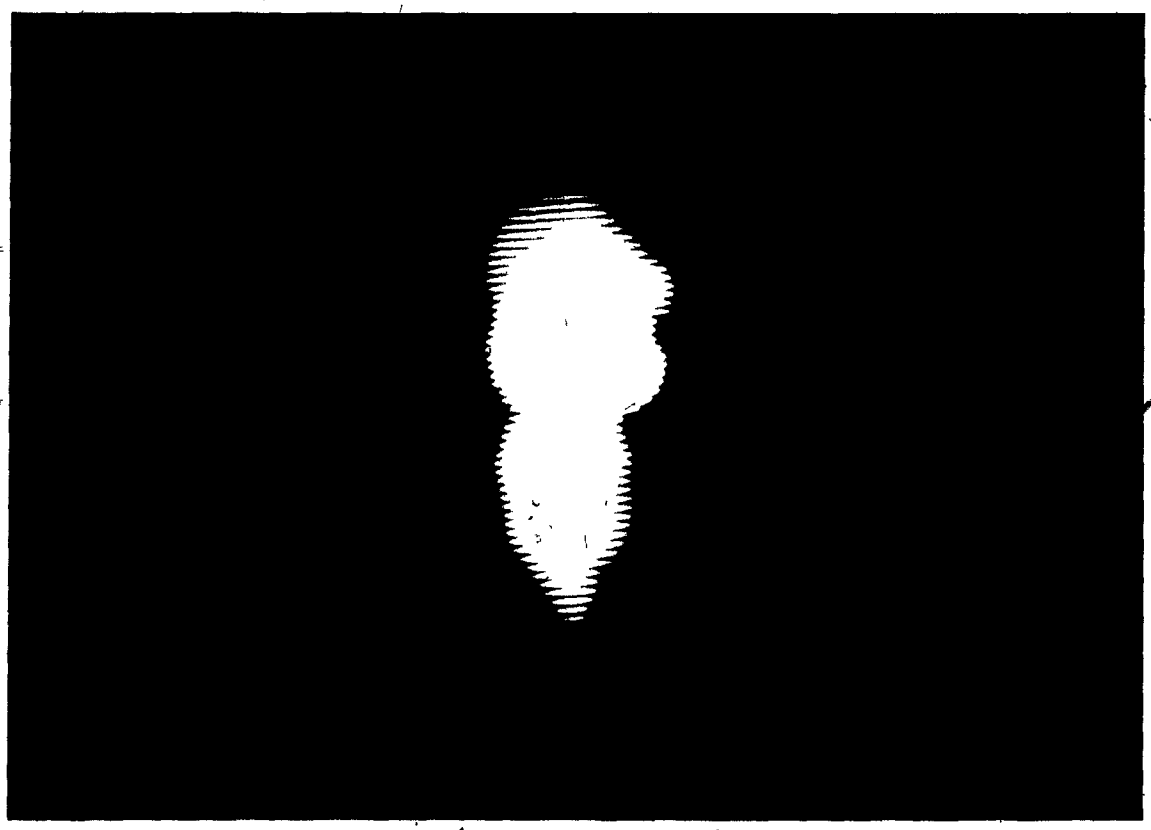

C

PARTICLE SIZ' ISTRIBUTION

Friedlaender's

SAMPLE IDENTIFICATION manganese pyrophosphate , $Mn_2P_2O_7$ DATE

Density g/cc LIQUID water - .05 % calgonite Viscosity cp BY

Preparation stirring before analysis ① - 30 min , ② - 35 min , ③ - 60 min TEMPERATURE °C

RATE START DIA µm

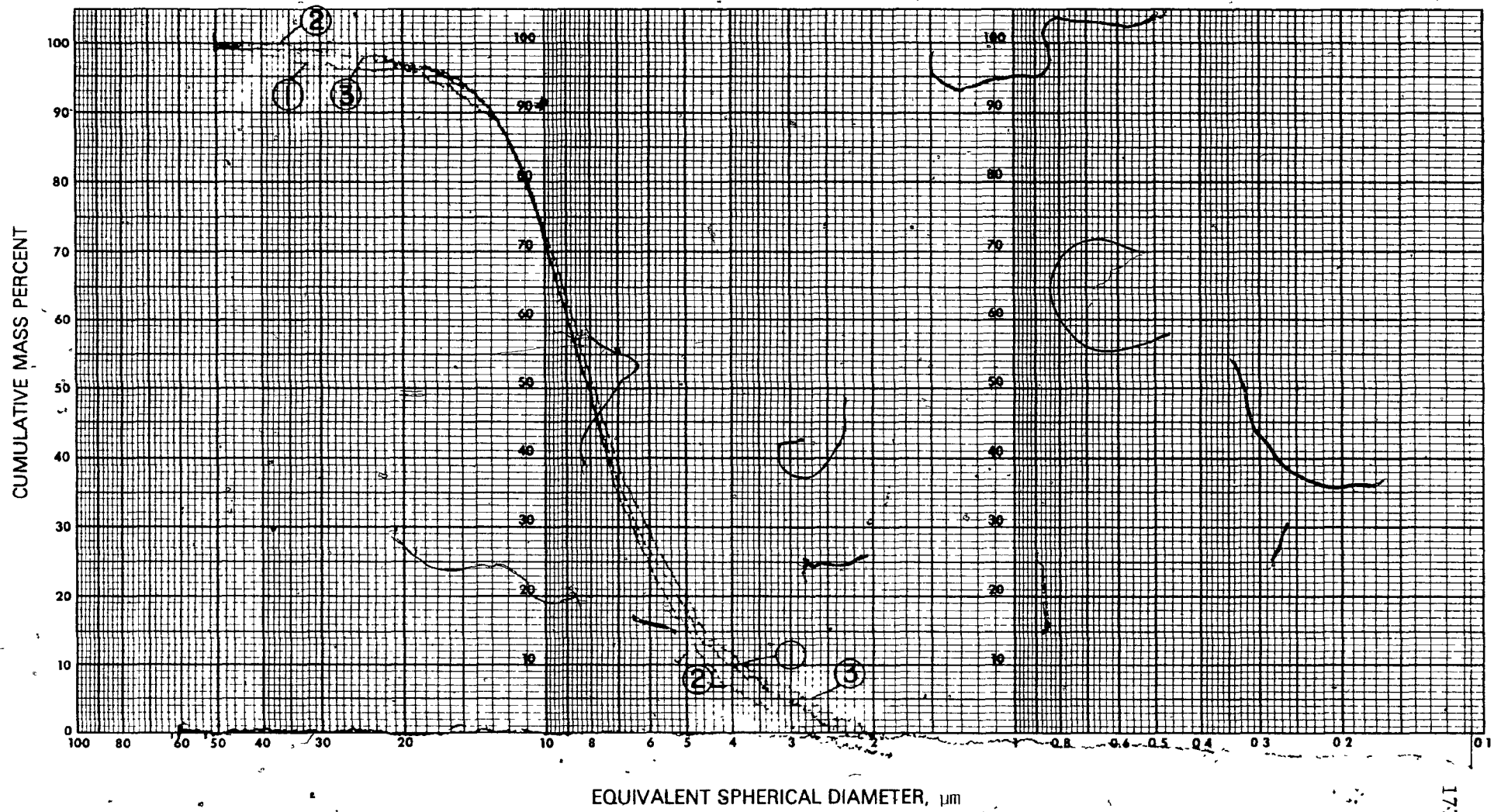

5-4 Sedigraph cumulative size distribution of $Mn_2P_2O_7$.

micromeritics®
instrument corporation
5680 goshen springs road • norcross georgia 30071 • USA
telephone 404/448 8282 • telex 70 7450

Form 500/42701

values for 4.7 and 5 kOe appear together. This is not felt to be a serious misrepresentation as some values of R_{as} at the higher field, contrary to expectation, are less than those at the lower field. This, it is felt, gives some indication of the uncertainty associated with their measured values.

Agreement between the theoretical curves and experimental points is judged to be good; both defining similar shapes and ranges of R_{as} for the flow velocities investigated. The restriction that $Re_w >> 1$, required by boundary layer theory, limits the model from being applied at very low flows. At high velocity, the model predicts a bare wire condition ($R_{as} = 1$) at a lower flow rate than is experimentally observed. Agreement is seen to improve considerably when the effect of the size range is incorporated.

5.1.3 Field Dependent versus Constant Susceptibility

Also investigated were the consequences of assuming constant rather than field dependent magnetic susceptibility for materials exhibiting magnetic behavior of the form;

$$\kappa = \kappa_\infty + \frac{M_o}{H} \qquad (5\text{-}1)$$

Since the magnetic field varies with location around a wire, the susceptibility of an individual particle will depend on its position relative to the wire. The program performs the detailed calculations once κ_∞ and M_o have been specified. It would prove useful to have an "effective", and constant, value for κ for all particles collected. Such a susceptibility, κ_e, would depend solely on the applied field and

would predict the same loading as if each particle had a unique κ. Following Equation (3.1-29), such an effective susceptibility is defined by;

$$\kappa_e = \kappa_\infty + \bar{f}\frac{M_o}{H_a} \qquad (5\text{-}2)$$

where $\bar{f}$ is the average field parameter, f, through the buildup volume.

The ratio of predicted wire loading using κ_e to that for variable susceptibility κ, $\frac{\gamma_{\kappa e}}{\gamma_\kappa}$, is shown as a function of H_a in Figure (5-6) for selected values of $\bar{f}$. Magnetometer values were used for the hematite magnetization parameters. It is seen that for $\bar{f} = 1$ a large overestimation (157% at 3 kOe) of loading is made, an effect which decreases with increasing H_a. The $\bar{f} = 1.0$ curve represents the error incurred if susceptibility as measured directly by (say) a magnetometer is used for prediction purposes, without accounting for the effect on magnetic susceptibility of the non-uniform field. A value of $\bar{f} = 0.42$ was judged to yield $\frac{\gamma_{\kappa e}}{\gamma_\kappa}$ sufficiently close to 1.0 ($\pm$ 5%) to be acceptable over the range 3-12 kOe. The value $\bar{f} = 0.42$ was also confirmed for ilmenite (magnetometer data) and hematite using the Frantz Isodynamic data, and it is tentatively proposed that $\bar{f} = 0.42$ holds true for most cases of interest at these fields. An alternative way of viewing $\bar{f}$ is that the effective field throughout the buildup volume is $\frac{H_a}{\bar{f}}$ or 2.4 H_a.

At higher fields, say H_a > 7 kOe, a better value of $\bar{f}$ seems to be 0.45 which yields $\frac{\gamma_{\kappa e}}{\gamma_\kappa}$ within a few percent of unity.

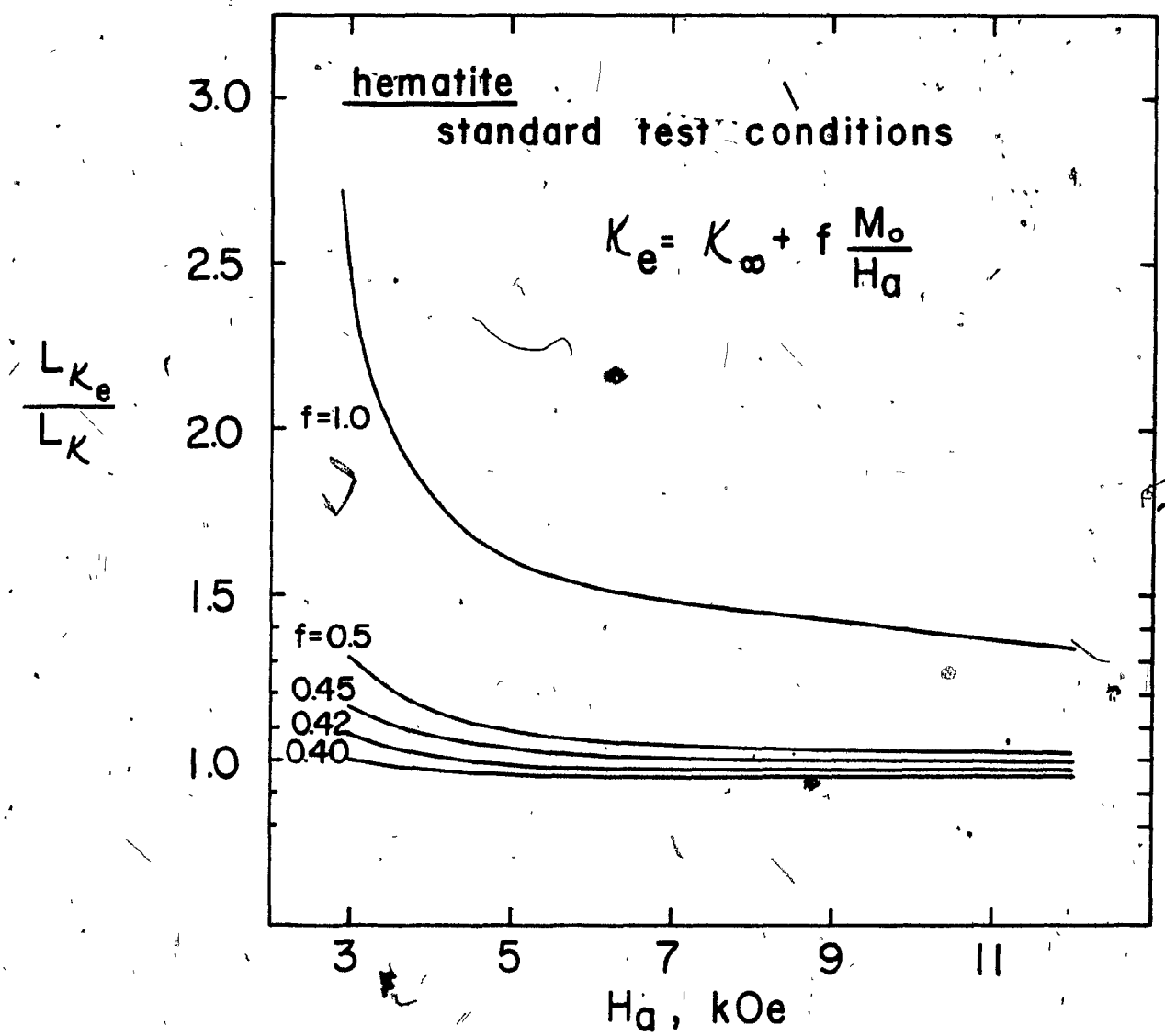

5-6 The ratio of loading with an effective susceptibility (L_{K_e}) to actual susceptibility (L_K), for various f as a function of applied field, H_a.

5.1.4 Loading as a Function of N_L

The equilibrium wire loading, γ_v (cm^3 of material/cm^3 of wire) given by Equation (3.2-6), was determined using the full model for a series of 93 'tests' covering the wide range of conditions and minerals cited in Table (5-1). γ_v has been plotted against the loading number, $N_L = \frac{2bH_a^2 \kappa A}{a^{1/2}\rho_f^{1/2}\eta^{1/2}U_\infty^{3/2}}$, (Figure (5-7)) with $A = \frac{2\pi M_w}{H_a}$ and κ as the effective susceptibility (κ_e with $\bar{f} = 0.42$). Also shown (solid line) is the simplified relationship for γ_v (Equation (3.2-15), i.e. zero gravity and buildup in a 90° sector assumed);

$$\gamma_v = \frac{\varepsilon}{4}\left\{\left(\frac{N_L}{2.5}\right)^{4/5} - 1\right\} \qquad (3.2\text{-}15)$$

The volume packing fraction, ε, has been taken as 0.7 for uni-sized spheres (see Section (3.2.1)).

In addition to suggesting a minimum $N_L = 2.5$ required for particle collection, Figure (5-7) shows the computer experimental points to closely describe a curve remarkably consistent with, though somewhat above, the simplified relationship of Equation (3.2-15) for γ_v.

In order to test the viability of N_L as a descriptor of equilibrium loading, a set of experiments using closely sized hematite (described in Tables (4-3,6,7)) was conducted with a small (4 screen) matrix so as to insure the attainment of fully-loaded conditions. These four stainless steel expanded metal screens, of uniform mass (1.39 g each), were sandwiched between similar, and essentially non-magnetic, aluminum screens. The purpose of the aluminum screens, 4 upstream and 2 downstream, was to minimize fluid-flow end-effects on the stainless steel screens sandwiched in the middle.

TABLE 5-1

Range of Conditions Used in Modelling γ_v for Various Minerals.

Mineral (# tests)	Range of Parameters					
	b (μm)	κ (x10^6 emu/cm^3-0e)	H_a (k0e) (A)	a (cm)	ν* (s)	U_∞ (cm/s)
hematite (25 tests)	5-35	454-190	2-9 (.88-.81)	.015-.12	.005-.015	2.5-15
ilmenite (23 tests)	7.5-13	564-416	2-5 (.88-.89)	.04	.01	4-30
sphalerite (21 tests)	5-22.5	27.8	6.5-25 (.87-.36)	.04	.01	9.9
chalcopyrite (24 tests)	3.8-20	16.8	5-22.5 (.89-.40)	.04	.01	5.7

*Fluid density taken as 1 g/cm^3 in all cases.

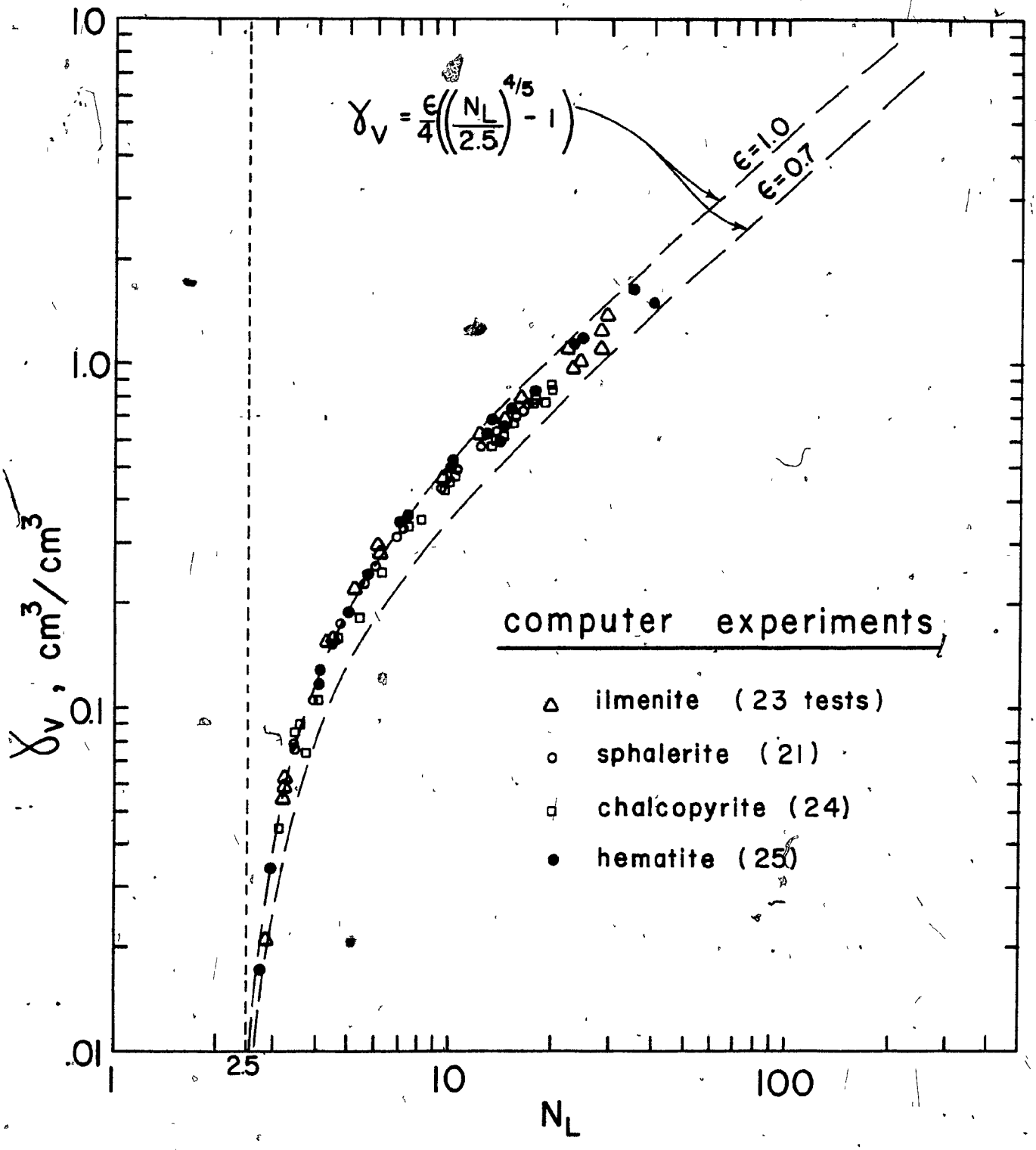

5-7 Full model predictions of γ_V versus N_L for various minerals.

Exploratory work on the permanent magnet with #2 cone hematite at 4 cm/s flowrate consisted of numerous runs of increasing feed mass. From this a loading curve of grams of magnetics retained versus grams fed was obtained. The results suggested that feeding 20-30 times the equilibrium loading mass was required in order for the matrix to reach equilibrium conditions.

Estimates of γ_v for each of the 8 planned tests were obtained from Figure (5-7). These were increased by the factor of 20 suggested by the exploratory work to give the feed mass used in the experiments. Due to the limited quantity of prepared material, recycling of the non-magnetics product during testing was required for some runs in order to achieve the target feed. Sodium silicate (added as 1 kg/tonne solids) plus vigorous agitation of the slurry prior to feeding assured adequate dispersion of the particles. Test conditions, including repeats, are listed in Table (5-2) and Appendix III. A Sala Magnetics Inc. (model 10-15-20) unit at CANMET (Ottawa, Ontario) was used for the testwork.

As in the exploratory run, some physical entrapment at zero field and retention of particles with no matrix present (under some conditions) should be accounted for. Since these adjustments, albeit small, have yet to be determined, the tests reported must be considered preliminary. Interestingly, the phenomenon of capture with no matrix seems to be the result of sufficiently large field gradients in the vicinity of the inside edge of the iron collars which are part of the Sala magnet design.

The experimental results are plotted in Figure (5-8) as γ_v against N_L together with the computer modelled points for hematite and the curve of the loading Equation (3.2-15). A bar connecting two

TABLE 5-2

Loading versus N_L and $\frac{V_M}{U_\infty}$ for Hematite.

Test	2b* (cm)	U_∞ (cm/s)	H_a (Oe)	γ_m (g/g)	γ_v (cm^3/cm^3)	N_L**	$\frac{V_M}{U_\infty}$ ***
A	.00123	15.2	2580	.081	.120	3.4	.180
B	.00228	2.9	2580	1.89	2.79	75.7	3.24
C	.00123	2.9	2580	1.28	1.89	40.8	.942
D	.00228	15.2	6710	.638 .709 .665	.942 1.047 .982	21.4	1.71
E	.00228	15.2	2580	.201	.297	6.3	.618
F	.00123	12.0	4240	.363	.536	9.1	.391
G	.00123	15.2	4240	.194	.286	6.4	.309
H	.00123	8.0	4240	.604	.892	16.8	.587

* Cyclosizer data.
** Based on $M_o = 2.70$ emu/cm^3, $\bar{f} = 0.42$.
***Based on $M_o = 2.70$ emu/cm^3, $\bar{f} = 0.50$.

See Appendix III (Section 6) for complete results of CANMET runs.

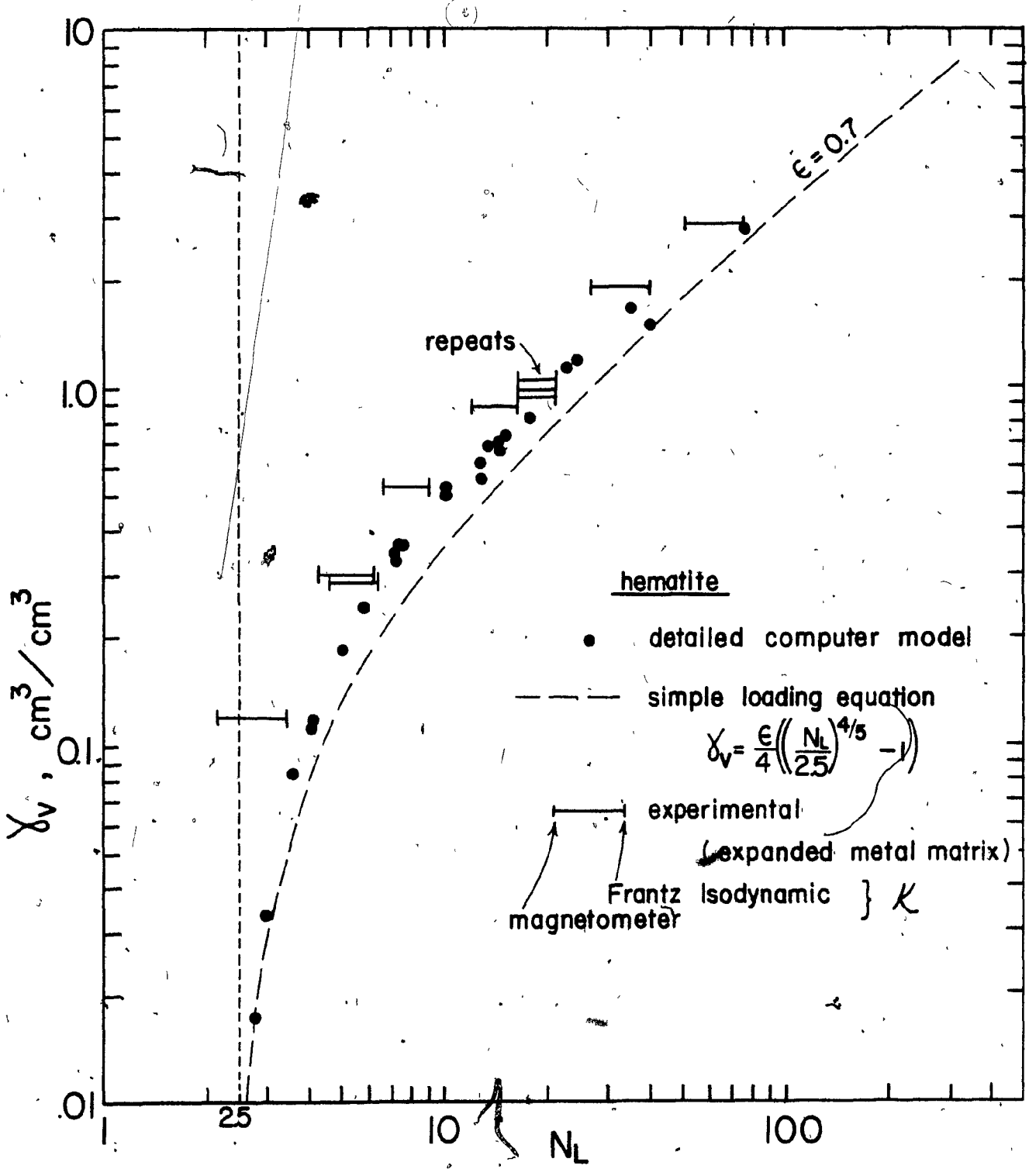

5-8 Full model predictions and experimental results of γ_v versus N_L for hematite. The simplified loading equation is also shown with $\epsilon = 0.7$.

points is associated with each experiment; the smaller value having N_L based on the effective susceptibility determined with magnetometer data while the larger value is for κ_e based on the Frantz Isodynamic data (see Appendix III for complete results). The results are in very good agreement with the predicted curves which, one is reminded, are for buildup on infinitely long cylindrical wires. Reproducibility of the repeat tests (set D) was good; ± 5% standard error for the amount captured and ± .2% of the total mass fed. Some levelling-off for γ_v values at high N_L can be expected if these points drop somewhat for the reasons previously cited. Attention is drawn to tests E and G which, for different experimental conditions, have virtually the same N_L (6.3 and 6.4)*; the γ_v's are the same (0.297 and 0.286) to within the reproducible error. Watson's $\frac{V_M}{U_\infty}$ for these tests, however, differs by a factor of two (0.618 and 0.309).** Note also test pair E and H for which $\frac{V_M}{U_\infty}$ is about the same (.618 and .587) but having N_L almost tripling (6.3 and 16.3). Experimentally, γ_v was 0.297 and 0.892 for E and H, respectively.

5.2 Recovery through a Length of Screens

A good indication of separator performance may still be obtained from the size of the $\frac{V_M}{U_\infty}$ ratio, a widely accepted indicator. A set of four computer 'tests' having increasing $\frac{V_M}{U_\infty}$ was run for hematite with the purpose of viewing how the predicted loading varied internally as a function of

---

*Frantz Isodynamic data, $M_o = 2.70$ emu/cm^3 and $\kappa_\infty = .000115$ emu/cm^2-Oe, $\bar{f} = .42$.

**Based on κ_e with $\bar{f} = 0.5$ since trajectory models, for which $\frac{V_M}{U_\infty}$ was developed, assumes particles are far from wire.

distance into the matrix. This information is readily obtained from the computer printout which also lists the individual segment loadings, L/L_m ($= \gamma/\gamma_m$).

From Figure (5-9) it is seen that at low $\frac{V_M}{U_\infty}$ (curve 1, $\frac{V_M}{U_\infty} =$ 0.15) the 40 segments of the separator have loaded to about the same extent, $\frac{\gamma}{\gamma_m}$ of 0.32 to 0.47), well below saturation for 5 g of feed. As field and flow change such that $\frac{V_M}{U_\infty}$ increases, the loading curves (numbers 2, 3 and 4) assume a shape which approaches that of an advancing front of saturated screens. It is evident from this type of simulation that unless the $\frac{V_M}{U_\infty}$ is high (say >> 1) the overall matrix will not be fully loaded for reasonable quantities of feed. A fully loaded matrix can always be achieved for all $\frac{V_M}{U_\infty}$ provided sufficiently large amounts of material are fed but the % recovery will be correspondingly low. Typically, conditions which predicted 20-90% recovery of 20 g of hematite on 40 screens had $\frac{\gamma}{\gamma_m}$ from 0.6 to 0.9 for the overall matrix.

5.3 Recovery Predictions versus Experiment

A comprehensive body of experimental work by Dobby[69] provided a good basis for comparison between measurement and model prediction. The experimental procedure has been reported in detail elsewhere [79] and may be described as a constant-head gravity-fed batch operation. A non-magnetics product was first collected before shutting the field off and flushing the collected magnetics product from the matrix. Flowrate was adjusted by means of calibrated bored plugs in the discharge line.

Dobby's matrix consisted of 39 stainless steel expanded metal screens, identical to those previously described, of average weight 1.51 g.

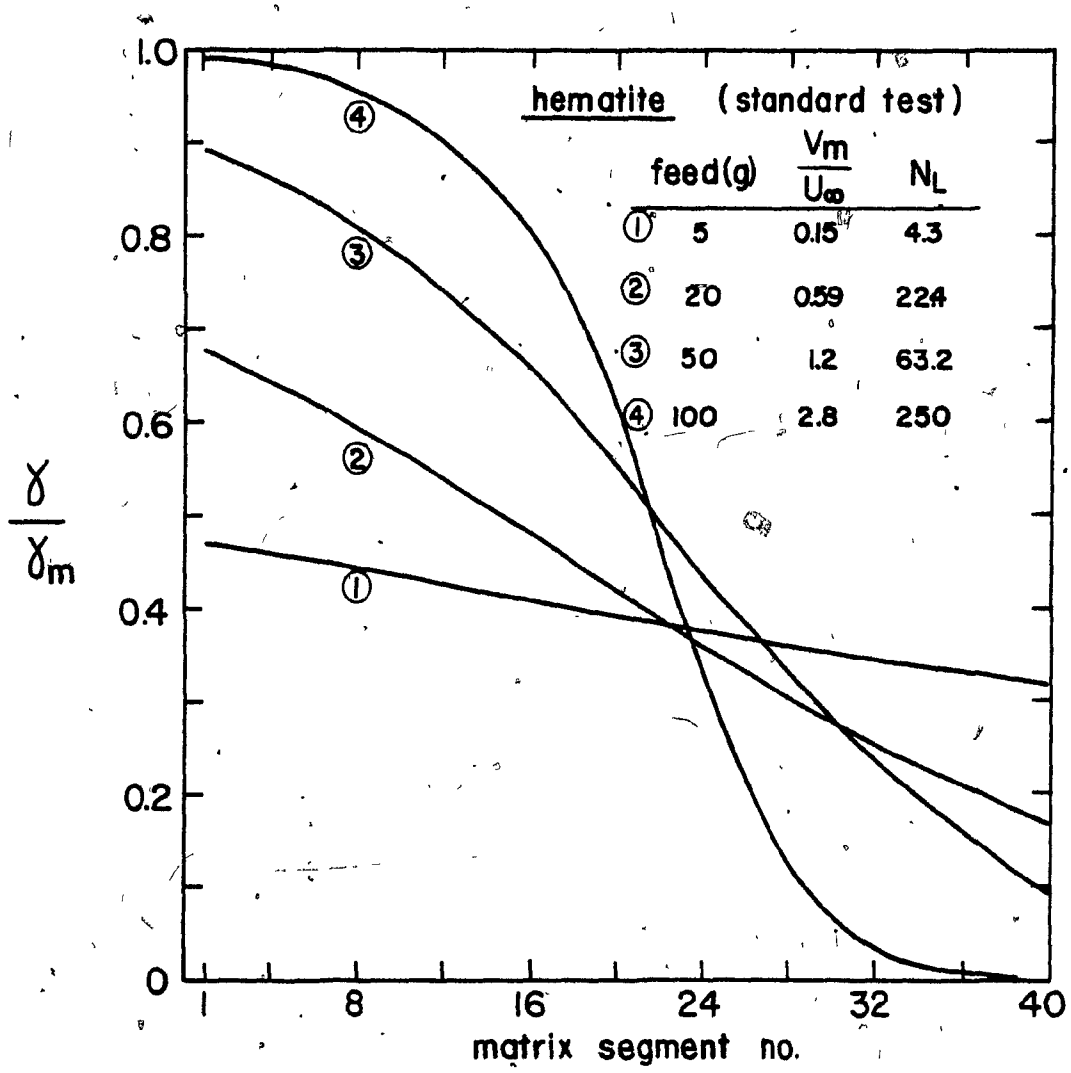

5-9 Variation in $\frac{\gamma}{\gamma_m}$ of the individual matrix segments for various $\frac{V_{M.}}{U_\infty}$

Typically, he fed 20 g of closely sized uni-mineral samples whose relevant properties have already been presented (Tables (4-2,4,7)). In comparison, the similar testwork of the present study employed a 40 screen matrix of average weight 1.41 g. The magnetometer magnetization data were used for the model.

Experimentally measured recovery of hematite as a function of particle diameter is compared with predicted results in Figures (5-10a,b). As a measure of the uncertainty of sizing the calculated size range of each Cyclosizer cone fraction is shown in bar form. The predicted curve falls somewhat below the measured values for both the 3 kOe-9.9 cm/s and 2.1 kOe-5.5 cm/s cases; however, the range in particle size over which recovery increases from 0 to 100% and the trend of the increase is similar between experiment and model.

The relationship between applied field and recovery of 22.8 μm diameter hematite at 9.9 cm/s appears in Figure (5-11a). The experimental curve is seen to level out at about 80% recovery while the model tends toward 100%. However, the considerable influence of particle size on the predictions is evident from the dashed lines which represent the range (9-14.4 μm) of this Cyclosizer fraction. Size effects would be expected to contribute to less than 100% recovery at higher fields. Similarly, Figure (5-11b) for 20 μm ilmenite at 9.9 cm/s, shows good agreement between model and experiment. The trend of the predictions in both ilmenite and hematite cases is to underestimate at low and to overestimate at high % recovery.

Figure (5-12a) shows the effect of flow velocity on the same 20 μm ilmenite at 2.0 and 3.0 kOe. Again, predicted recovery compares

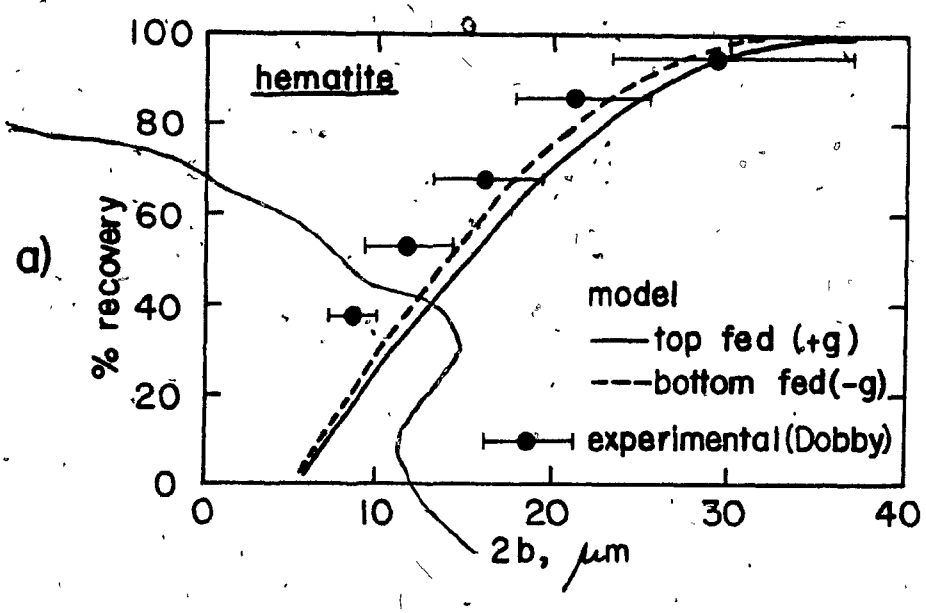

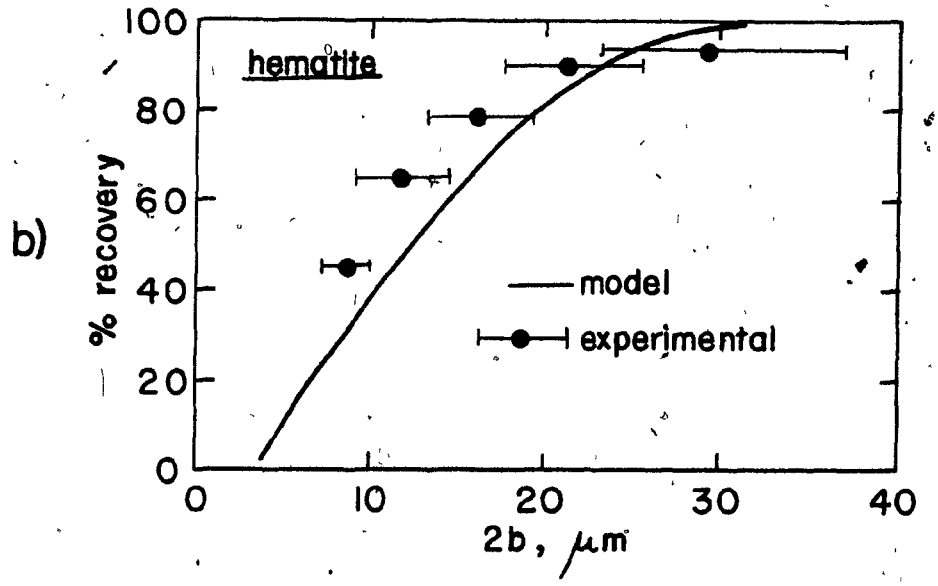

5-10 Experimental versus predicted recovery for hematite. Effect of particle diameter.
a) H_a = 3.0 kOe, U_∞ = 9.9 cm/s
b) H_a = 2.1 kOe, U_∞ = 5.5 cm/s

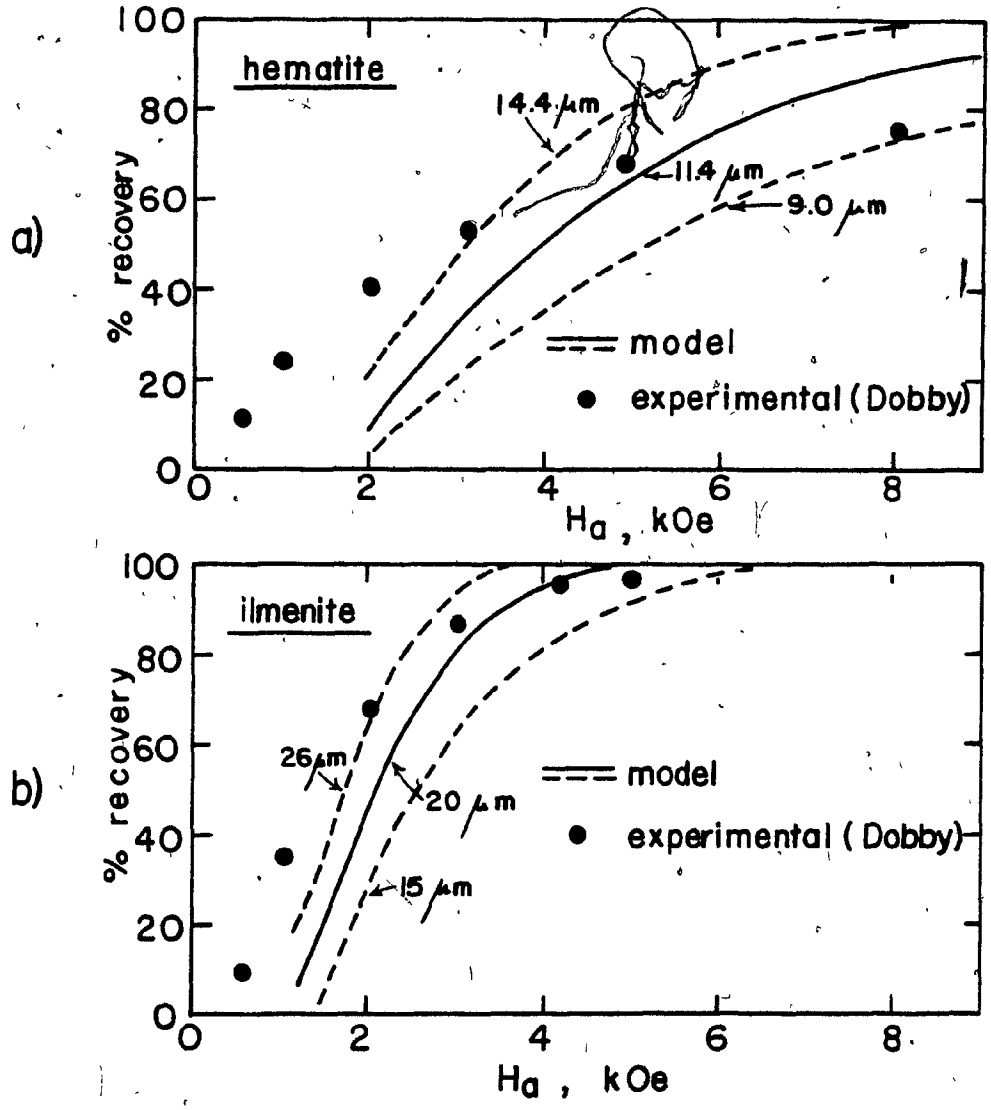

5-11 Experimental versus predicted recovery. Effect of applied field.
a) hematite, 2b = 11.4 μm, U_∞ = 9.9 cm/s
b) ilmenite, 2b = 20.0 μm, U_∞ = 9.9 cm/s

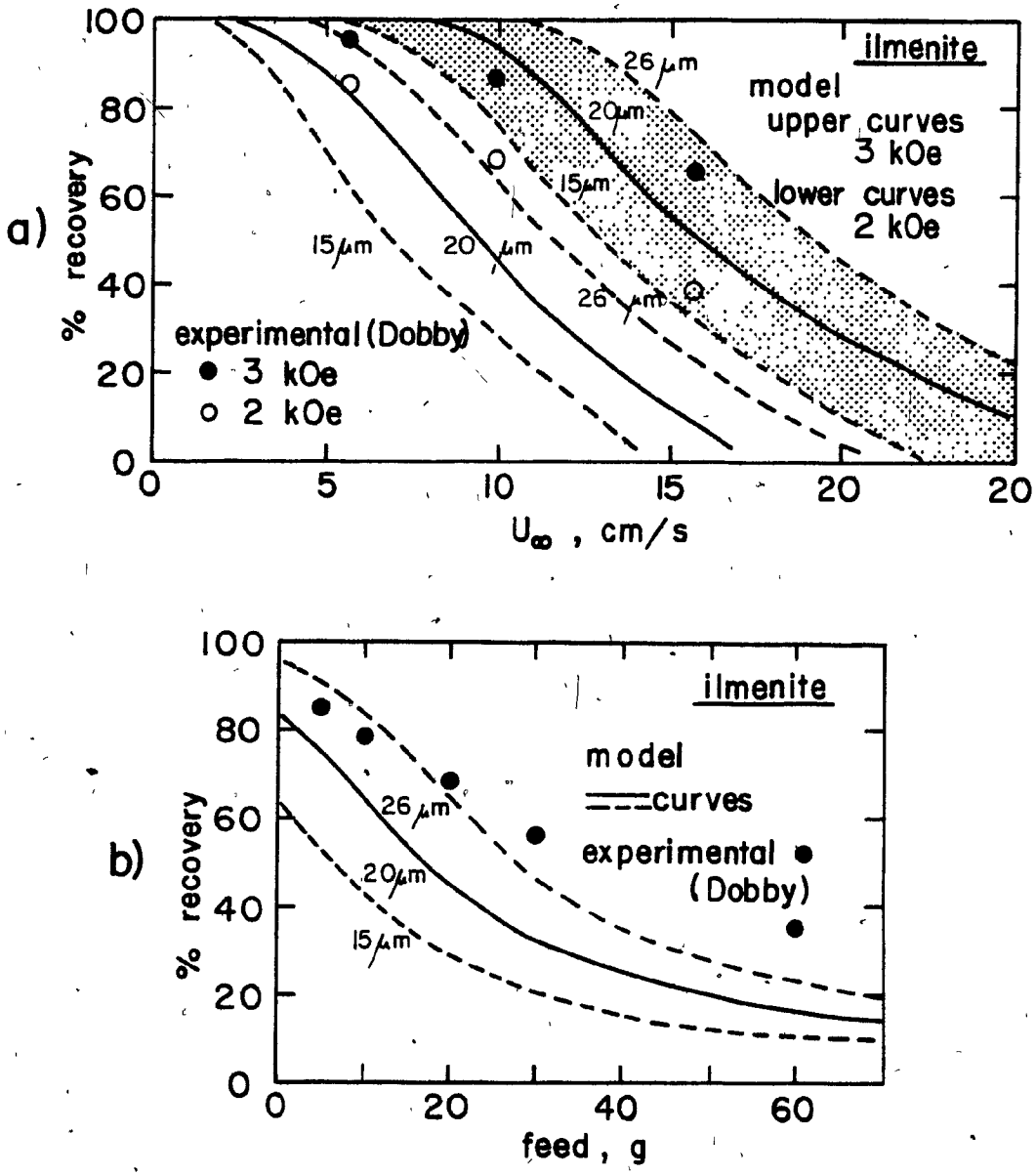

5-12 Experimental versus predicted recovery for ilmenite.
a) effect of velocity, $2b = 20.0$ μm, $H_a = 2.0$, 3.0 kOe
b) effect of feed mass, $2b = 20.0$ μm, $H_a = 2.0$ kOe, $U_\infty = 9.9$ cm/s

well with measurement when the influence of the size range (15-26 μm) is incorporated. The results of a series of tests in which increasing mass (5-60 g of 20 μm ilmenite at 2.0 kOe and 9.9 cm/s) was fed to the matrix are presented in Figure (5-12b). As the amount of feed increases and the matrix approaches the fully loaded state, both experimental and predicted recoveries begin levelling off, with the model tending to again underestimate recovery by about a factor of two.

Recovery of sphalerite and chalcopyrite (minerals with considerably lower magnetic susceptibilities than either hematite or ilmenite) as a function of particle size was also tested against the model. In pure form these minerals are known to be true paramagnetics. The small spontaneous magnetizations (σ_o) detected by the magnetometer measurements (see Table (4-4)) were, therefore, attributed to minute quantities of impurities either present in the original ore (e.g. pyrrhotite) or possibly picked up during previous testwork since the samples had been reused. Susceptibility was treated as constant with $\kappa = \kappa_\infty$ and $M_o = 0$. Figure (5-13) shows the results at 10 kOe and flowrates of 5.7 cm/s for the chalcopyrite and 9.9 cm/s for the sphalerite. Agreement is good, the model tending to underestimate at low recovery and overestimate at high recovery as was the case for ilmenite and hematite.

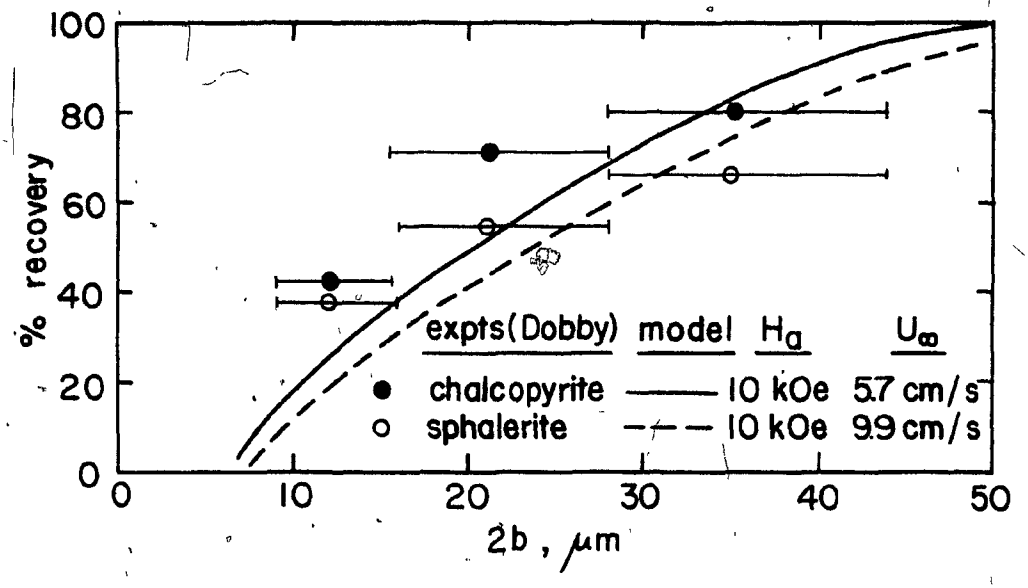

5-13 Experimental versus predicted recovery. Sphalerite (U_∞ = 9.9 cm/s) and chalcopyrite (U_∞ = 5.7 cm/s) at H_a = 10.0 kOe.

VI. DISCUSSION

6.1 Theoretical Perspective

To date a large portion of the theoretical work relating to hgms has revolved around the development of trajectory models and determination of capture radii for paramagnetic particle systems. By neglecting gravity and considering only Stokesian fluid drag and magnetic force, the value of R_c has been shown to uniquely depend on $\frac{V_M}{U_\infty}$ with a contribution from the field perturbation term, A, if the ferromagnetic matrix is near or below magnetic saturation. The importance of the Stokes number (particle inertia/viscous force) for high speed flows and low density fluids has also been shown.[18]

In adapting these models to predictions of filter performance, generally very large fitting factors have been required to correlate experimental results with the developed theory. These factors often suggest that as low as 1-6% of the steel wool strands are actually behaving as modelled. Interaction and overlapping effects aside, the fact that 95% of the filter is not performing as expected poses the dual question of model validity and efficiency of the filter design. No doubt this perplexity helped to prompt the investigation of other events related to the retention of particles.

Some attention has been focussed on buildup profiles with a view to estimating the maximum retainable amount of material, notably the work of Luborsky and Drummond[22] and Watson[31,32] on modelling and Friedlaender *et al.*[38,39,40] on photographing the single wire case.

The comprehensive equilibrium buildup model of Liu et al.[41], developed from a theory based on Stokesian drag and simplified magnetic force, was carried through to final predictions of filter performance without fitted parameters. An assumption was that capture radius remained constant at the bare wire value until at fully loaded conditions it became zero. Liu's model, though correlating well with experiment, may not have been sufficiently tested by the scope of his test work. Although the initial theory considers cases having both particle and wire size of the same order (small $\frac{a}{b}$ ratio) as well as particle size much smaller than the wires (large $\frac{a}{b}$ ratio), Liu's complete model is developed for the small $\frac{a}{b}$ case only. Interestingly, a minimum $\frac{V_M}{U_\infty}$ of ≈ 0.6 for buildup to occur is predicted which seems at odds with some operational data from the clay industry[91] where material has been reported successfully captured at $\frac{V_M}{U_\infty} = 0.1$ and below.

To date, as noted previously, there has been less work on buildup than trajectory models and virtually all of this has considered magnetic steel wool as the matrix medium. Some theoretical work by Birss et al.[92] has been reported for woven screens and a number of experimental comparisons of steel wool, fibre metal (assumed to be expanded metal) and woven screens have been performed by Collan et al.[93]

The present buildup model would appear to slot into that gap in the theory which considers fine particles and larger wires (large $\frac{a}{b}$ ratio) such as occurs in many of the potential applications of hgms to mineral processing. Here, continuous devices employing metal matrices (400-1000 μm diameter) will be treating particles of the order 1-100 μm at relatively high slurry flow rates (5-20 cm/s).

Model Development

The current equations of the literature describing magnetic force between paramagnetic particles and infinitely long ferromagnetic wires have been modified to include materials exhibiting field dependent susceptibility of the general form $\kappa = \kappa_\infty + \frac{M_o}{H}$. The assumption that $\hat{M}_o$ orients itself parallel to $\hat{H}$, as in the case in the development of Equation (3.1-25), may not always be realized in practice but monocrystalline particles will tend toward this condition even if never fully achieving it. Although typically used to describe the magnetization of canted antiferromagnetics, such as the taconites cited by Pastrana and Hopstock[49], the field-dependent susceptibility relationship is also of a form rendering the equations applicable to paramagnetics containing ferrimagnetic impurities or inclusions. In view of the present potential for developing hgms as an alternative[5,7] to flotation and flocculation techniques[94] for fine particle recovery of taconites, the revised force equations would appear to have an immediate relevance to industrial processes.

Incorporation of the involved (but readily handled by computer or programmable calculator) self-consistent calculations required for the evaluation of wire demagnetization and A, the perturbation term, may be unnecessary at fields considerably in excess of those required for wire saturation. However, since the applied fields for the applications of interest lay below or near matrix saturation levels, incorporation of this variable was judged to be important for the full model. Also for this reason, Watson's $\frac{V_M}{U_\infty}$ is used in its general form $\frac{4b^2\kappa H_a{}^2 A}{9a\eta U_\infty}$, (where $A = \frac{2\pi M_w}{H_a}$), rather than as the limiting cases; $\frac{8\pi b^2 \kappa H_a M_s}{9a\eta U_\infty}$ (saturated

wires) and $\frac{4b^2\kappa H_a^2}{9a\eta U_\infty}$ (unsaturated wires), for which an abrupt discontinuity exists at the saturation value. This caution applies especially to the stainless steel which, as seen from Figures (4-18,19), saturates more slowly than does the pure nickel.

In defining fluid drag on the captured particles a different approach to traditional Stokesian drag, used indiscriminantly on occasion, perhaps, has been taken. The Blasius solution describing shear stress, τ_o, on a smooth cylinder in a free stream cross-flow, is used to approximate fluid drag on particles residing at the bottom of the developed boundary layer. Surface roughness due to the presence of the particles can be expected to increase drag. However, the effect should be small for hgms where wire Re well below those for transition to turbulent boundary layers[95] are found.

The fractional area of shear, f_b, an important quantity in the present approach to fluid drag, is admittedly difficult to isolate. The comparison made in Figure (3-9) suggests that those models having assumed an average boundary layer thickness and Stokes' Law (Luborsky and Drummond, Clarkson et al. and Liu et al.) will overestimate drag by roughly 50% above the Blasius approach with $f_b = \frac{\pi}{8}$. It is noteworthy that this difference is too small and not in the correct direction to account for the large fitting factors required by some of the models.

For ease of analysis, particle shape has been idealized as spherical, a geometry which minimizes the surface-to-mass ratio. This will maximize magnetic relative to fluid drag forces with the result that for any deviation from sphericity, the model should tend to underpredict fluid drag and, hence, overpredict buildup. A possible refinement for handling real particle shapes (Figure (4-21) serves as a use-

ful reminder of this problem) would be through a suitable choice of f_b.

Particle-on-particle friction has also been neglected relative to magnetic and fluid forces. This may not be fully justifiable for buildup near the front stagnation point where the radial to tangential magnetic force-ratio becomes large (see Figure (3-3)). Since friction is proportional to the radial force its effect will be a maximum in this frontal region. Choosing a value for the coefficient of friction is difficult, (Watson has suggested 0.3)[31], and precluded the accomodation of friction in the analysis.

Gravity, also recognized as a second order effect, is easily accounted for and its inclusion in the analysis permitted the examination of interesting variations such as top versus bottom feeding of the device.

The extent of downstream wire buildup or 'back-capture' is far from satisfactory resolution. Photographic evidence of Friedlaender et al.[87] (Figures (5-3c)) suggests that under conditions of sufficiently large Re_w (estimated at 40-60 based on the radius of upstream buildup, R_{as}), the extent of backcapture approaches and may exceed that on the front. There is speculation that what is observed in these photographs is an end of the wire effect on field and flow resulting in some localized backcapture of material. Although the mechanism of backcapture is not considered in the present model a provision exists permitting an estimate of such an effect on overall recovery in the full length matrix model. This backcapture effect is achieved by increasing the number of screens per segment variable (= S) to a value greater than actual.

Extending any single wire model to recovery through a length of screens is viewed as more hazardous than predicting single wire buildup. Analysis of fluid behavior is particularly troublesome. Assuming potential flow, Simons and Treat[27] investigated the collective fluid and magnetic disturbance in a regular but highly simplified lattice. They found the capture radius for a lattice fibre to differ significantly from the isolated fibre case. Deviation from free-stream conditions toward more disturbed flow are expected as Re_w increases to yield downstream eddies and vortex shedding in the wake of the wires. Such deviations can be expected to increase fluid drag on any particle buildup which occurs.[96]

The model accounts for overlapping wires and capture areas on a first-order-of-effect basis only, as outlined in Section 3.2. The screens themselves are assumed to behave independently, however; i.e. neighbour interactions such as shadowing of incoming particles and mutual magnetization of wires have been neglected. A method for estimating applied field amplification due to the latter has recently been reported by Yaniv et al.[97]

It is also worth remembering that the expanded metal in use industrially is neither a square lattice nor of cylindrical wires as modelled; however, the approximation is felt to be sufficiently valid in view of other assumptions.

In summary, numerous influences, phenomenon and complicating interactions are envisioned in the analysis, many of which may arguably be relegated to the status of second and third order effects. The consequences on recovery of some of primary importance will receive additional comment in the discussion.

6.2 Equilibrium Buildup

6.2.1 Profiles

General

The predicted fan-shaped equilibrium buildup profiles for hematite (Figures (5-1a,b,c)) are seen to be in agreement with the Lubórsky and Drummond 'case a' (Figure (2-6)) and Watson's 'growth' model (Figure (2-9)) as well as the photographic evidence of Friedlaender et al. (Figures (5-2,3)). This contributes to evidence against the elliptical outlines of the earlier models of Watson (Figure (2-7)) and others[24,28] and Lubórsky's 'case b' blade-like buildup (Figure (2-6)).

Note the predicted retention of particles beyond the 90° sector. This is a direct result of including the near field term, $\frac{Aa^2}{r^2}$, in the magnetic force equations. The quantity of material outside the 90° sector becomes particularly significant at applied fields below or near wire saturation where the A term is close to 1. At fields in excess of saturation predicted buildup bulges near the stagnation point; however, the assumption of an 'expanding cylinder' for fluid flow appears to remain justified, a priori.

Manganese Pyrophosphate ($Mn_2P_2O_7$)

Fortuitously, the current work of Friedlaender and Takayasu provided a suitable pool of experimental results against which to further test the model.

Comparison between photographs and predicted equilibrium profiles of $Mn_2P_2O_7$ (Figures (5-2,3)) show that, although the observed buildup is not entirely symmetrical, agreement between the shapes is

remarkably good. Some rounding at the outer corners of the actual buildup is evident. Alternatively, this could be viewed as a gradual increase in buildup radius toward the front. The possibility of a final contribution to particle accumulation in the frontal region being due to mechanical entrapment has previously been raised by Cowen et al.[35] and a discussion on the role of possible friction forces has been covered in Section 6.1.2.

Also intriguing in the Friedlaender photographs is the not insignificant quantity of material outside the predicted regions in the replusive areas on either side of the wire. This is particularly evident in Figure (5-2b). By again referring to Figure (3-3), one is reminded that only a weakly magnetic force acts radially (outwards) in this region. It must be considered a possibility that interparticle surface forces are sufficiently large to overcome this magnetic repulsion, thereby contributing to accumulation. Indeed, after studying 0.4 and 0.8 μm diameter ferrite precipitates in an hgms system, Collan et al.[93] suggested that such surface forces may play a larger role in retaining (very small) particles than the magnetic force itself. Another consideration is the frictional force which may again be playing a significant role in the retention of material since the tangential-to-radial force ratio (see Figure (3-3)) is large in this region.

At the wire surface the buildup angle approaches that predicted. This is not unexpected since the transition here from strong attraction to strong repulsion is much more localized than further away.

The experimental conditions relevant to Figure (5-2b) yield an Re_w of about 4 for the 125 μm diameter bare wire. Thus, it would seem that a key assumption in the development of the boundary layer

equations is violated, namely $Re_w >> 1$. Yet agreement between measured and modelled profiles remains good. If the Reynolds number based on the final accumulation radius is considered instead, Re_w is nearer 20, which is in the acceptable range. Hence, with this proviso, the applicability of the model is possibly extended to include even lower Re_w.

6.2.2 Saturation Buildup Radius

The $Mn_2P_2O_7$ results for R_{as} in Figures (5-5a,b,c) show the model adequately handles the effects of flow velocity and applied field both above and below nickel saturation magnetization. Even the 'knee', at about 8 cm/s in Figure (5-5b), for example, is present in both predicted and experimental curves. This good agreement is felt to be particularly important in that field and flow represent the two main operating variables of hgms devices.

As evident from Figure (5-4), the closely sized material nevertheless shows a considerable distribution of Stokesian equivalent diameter (SED). Also included in Figures (5-5a,b,c), therefore, are curves for the size limits covering 80% of the distribution, 4 to 13 μm, with a 50% passing size of 8 μm. The results reveal the considerable influence of particle size on R_{as} and underline the importance in this type of experimental work of isolating the narrowest size distribution possible.

The additional question is raised as to what definition of particle dimension is best suited for hgms and if an average size is itself an appropriate parameter. Ideally, some 'magnetic equivalent

diameter' should be obtainable but the SED values appear to adequately perform the task. This may be reasonable since the mechanics of both hgms and elutriation are a balance of body forces (magnetic and/or gravitational) and competing fluid drag.

In Figures (5-5a,b,c) the 50% passing size (8μm) underpredicts the velocity at which $R_{as} = 1$, and suggests that this condition may be better represented by the upper size of the distribution. It could be argued that R_{as} will always be governed by the largest size present. If, on the other hand, it is considered that fluid drag is larger than calculated for real, non-spherical particles, this could bring the predicted in line with the experimental evidence.

In view of the assumptions made and the range of particle sizes present the possibility of a fortuitous cancelling of errors being partly responsible for the good agreement should be entertained. As in grinding studies, where the 80% passing size is adequate for the models, so it may be in hgms that the 50% passing size will give good predictions as well. Some evidence supporting this postulate has been gathered here. The conclusion remains, therefore, that the model adequately predicts both equilibrium profiles and accumulation radii for single wires without resorting to fitting techniques.

6.3 Buildup on Wire Screens

6.3.1 Loading Behavior through the Matrix

Admittedly, the capture radius of a single wire is a difficult quantity to experimentally verify and for stacked wire screens in close proximity it is expected to be even more uncertain. At best, it may be

thought of as a mathematical tool which permits loading to proceed from zero toward the fully loaded condition. Various methods for relating R_c to the initial capture radius through a driving function, α, are found in Section 3.2.

Figure (5-9), showing the loading ratio $\frac{\gamma}{\gamma_m}$ through a matrix, is presented as an illustration of the way in which the model handles buildup internally. Curves for the lowest and highest $\frac{V_M}{U_\infty}$ considered (curves (1)and (4)for .15 and 2.8 $\frac{V_M}{U_\infty}$ respectively), appear to correspond to Watson's 'weak and strong coupling limit' description of separator performance. Experimental verification of such curves is difficult but progress in back calculating from an analysis of 'concentration breakthrough curves' for filter effluent has been reported by Collan. et al.(93,99)

If the objective of magnetic separation is seen as the maximum recovery or removal of a product then loading behavior similar to curve (4) in Figure (5-9) (i.e. an advancing front of fully loaded screens) will make the most efficient use of the available matrix volume. Under normal operating conditions, a fully loaded state for the entire matrix will rarely be achieved and the simulations suggested that overall $\frac{L}{L_m}$ was consistently in the range 0.6-0.9 for recoveries of 20-90% for the various minerals. For a given mineral, $\frac{L}{L_m}$ remained approximately constant even when the operating conditions and recoveries changed. The conclusion is that for reasonable changes in operating conditions, $\frac{L}{L_m}$ will not change significantly while the actual loading and, hence, recovery will behave similarly to the equilibrium loading, γ_v. The ability to predict γ_v is, therefore, seen as an important development in hgms design.

6.3.2 γ_v and N_L

As evident from Figure (5-7), the computer predicted γ_v for minerals of different susceptibility under a wide variety of conditions plot up very consistently against the loading number, N_L. This constitutes support for the numerous simplifying assumptions made in the derivation of N_L. Somewhat surprising is the remarkably good guide to the complex computer calculations which the simple equation,

$$\gamma_v = \frac{\varepsilon}{4}\{(\frac{N_L}{2.5})^{4/5} - 1\} \qquad (3.2\text{-}15)$$

(also plotted in the figure with $\varepsilon = 0.7$) provides. The simplification should tend to fall somewhat below the predictions since material retained beyond the 90^o segment is unaccounted for. This difference will be greater at lesser buildup, i.e. low N_L. Both the computer model and Equation (3.2-15) tend to a minimum N_L of 2.5 for particle retention; a value at which the magnetic and fluid drag forces are in a 1:1 balance.

The experimental results for hematite (in Figure (5-8)) showing γ_v versus N_L plot in a very similar fashion to the computer generated curve. Some difference should be expected, if only for the reason that expanded metal strands are an approximation of infinitely long cylindrical wires. The choice of magnetization data, either magnetometer or Frantz Isodynamic, will affect the amount of overprediction to a small degree but both must be viewed as being completely adequate for susceptibility determination.

If, as expected, the results for the two highest loadings drop somewhat (see Section 5.1.4) then the actual trend would appear to be

levelling out at a γ_v around 2. Such a levelling may result from the screen packing arrangement in which the individual laths are sufficiently close to be touching at points. If buildup on one screen has proceeded until the screen next to it physically prevents additional particles from accumulating, then a 'mechanical' rather than magnetic limit will have been reached. Testwork with increased spacing of the screens and at high N_L values should resolve this question.

The results have shown that for the type of hgms system under study, N_L is a fundamental grouping from which the equilibrium loading (γ_v) may be quantified with good accuracy. Watson's $\frac{V_M}{U_\infty}$ has been shown to be only one of several terms making up N_L. The inadequacy of $\frac{V_M}{U_\infty}$ in dealing with systems where large $\frac{a}{b}$ ratios and $Re_w >> 1$ predominate is due to the oversimplification arising from the analysis of fluid shear based on Stokes' Law. Boundary layer effects in these systems cannot be neglected. However, the simplifying assumptions associated with the development of the loading equation;

$$\gamma_v = \frac{\varepsilon}{4}\left\{\left(\frac{N_L}{C}\right)^{4/5} - 1\right\} \qquad (3.2\text{-}15)$$

more than compensate for loss of prediction accuracy over the full model if a good indication of γ_v behavior is sufficient.

6.4 Recovery Predictions versus Experiment

6.4.1 General

The comparisons in Figures (5-10a,b), (5-11a,b), (5-12a,b) and (5-13) show the fundamental model to adequately handle the effects

of changing particle size, applied field, flow velocity and magnetic susceptibility. Based on fundamental measurements alone, it should prove capable of predicting conditions required for the recovery of most minerals. This is seen as being of direct benefit to mineral processing in view of the very good correlation claimed for scale up from laboratory batch units to continuous industrial devices.[5]

Some aspects of the experimental versus predicted comparisons merit comment. Firstly, in the lower % recovery range where fully loaded matrix conditions are more likely to be approached, the model consistently underpredicts by roughly a factor of two. Taking the conditions of Figure (5-12b) as an example, it seems unlikely that the additional recovery is contributed by very-high localized gradients on the somewhat irregular expanded metal since such an effect would have been rendered negligible by the large feed mass (up to 60 g). This magnitude of underprediction is also evident in the equilibrium loading experiments of hematite at comparable N_L (i.e. N_L of 6-7 in Figure (5-8)). Obviously, predictions of lower range % recoveries are inherently more difficult than predictions nearing 100% recovery; differences between the real and modelled systems having their largest influence when only small amounts of material are retainable. It is worth remembering that criticism of the experimental testing of the model of Liu et al.[41] stems from the fact that they concerned themselves with the somewhat easier near-100%-recovery predictions.

Secondly, the measured recovery curves are not as steep as predicted. A distribution of real values rather than the unique quantity assigned when modelling will contribute to such a smearing effect. From

the point of view of the model, an underestimate in the rate of capture radius decrease (i.e. the driving function, α) would also lead to predictions of material more easily retained in the matrix and hence steeper % recovery curves than actual.

6.4.2 Sensitivity to Likely Effects

In view of the numerous influences discussed in Section 6.1, a brief investigation into the repercussions of the most likely and quantifiable of these seemed appropriate. Using the experimental conditions of Figure (5-10a) as a basis, the effect on % recovery of the following were investigated:

a) Wire diameter of 600, rather than 800 μm (for the same mass of screen). This refects the uncertainty in estimating the diameter.

b) 1.5 X applied field to simulate amplification due to mutual screen magnetization (estimated from the analysis of Yaniv *et al.*[97] for a screen half-spacing-to-diameter ratio of 0.56).

c) Employing Frantz Isodynamic rather than magnetometer magnetization data for the hematite.

d) Choosing initial R_c considerably larger; using an approximation cited by Watson[100] for low $\frac{V_M}{U_\infty}$ (< 1):

$$R_c = \frac{1}{2}\left\{\frac{V_M}{U_\infty} + A\left(\frac{V_M}{U_\infty}\right)^{0.5}\right\}$$

e) Assuming back capture equivalent to front capture, an assumption used by Liu *et al.*[41]

As seen from Figures (6a,b,c,d,e), each of the adjustments displaces the curve toward higher values of recovery. Field amplification and back capture (Figures (6b,e)) have the effect of adding 25-30 recovery %, while the Frantz Isodynamic data and assuming 600 μm wire (Figures (6c,a)) show less influence; adding 15-20 recovery % to the original curve. The rather considerable R_c change altered the curve by only 5-10 recovery % (Figure (6-d)).

In all probability, each of these contributes something to the true system and would help in explaining the factor of two under-prediction at low recovery. On the other hand, influences not considered such as greater drag from flow disturbances in the matrix and increasing fluid velocity as the volume of magnetics builds would tend to push the true curve down, especially for buildup approaching maximum. The preceeding analysis does suggest that events such as field amplification and back capture in the matrix might have considerably more influence in correctly predicting material recovery than would tying down the final intricacies of capture radii. As such they constitute a rather promising area for further study.

6.5 Magnetization Measurements

The Frantz Isodynamic force balance approach is an accepted method for determining the susceptibility of paramagnetic minerals at the mineral engineering level of interest.[101] Greater accuracy and the study of unusual magnetic behavior requires complex devices generally available only to physicists. An extension of the Frantz theory has permitted the field dependent susceptibility of canted antiferromagnetic-

6-1 The sensitivity of predicted recovery to various effects as a function of particle size. Hematite test (dashed line) having; $H_a = 3.0$ kOe, $U_\infty = 9.9$ cm/s, 39 stainless steel screens of 800 μm diameter, $\kappa_\infty = .00114$ emu/cm^3-Oe, $M_o = 1.62$ emu/cm^3 is reference.

a) 600 μm versus 800 μm diameter wire

b) $H_a = 4.5$ kOe versus $H_a = 3.0$ kOe

c) $\kappa_\infty = .000115$ emu/cm^3-Oe, $M_o = 2.70$ emu/cm^3, Frantz Isodynamic data versus magnetometer data

d) $R_c = \frac{1}{2}\left(\frac{V_M}{U_\infty} + A\left(\frac{V_M}{U_\infty}\right)^{0.5}\right)$

e) downstream capture equal to upstream capture

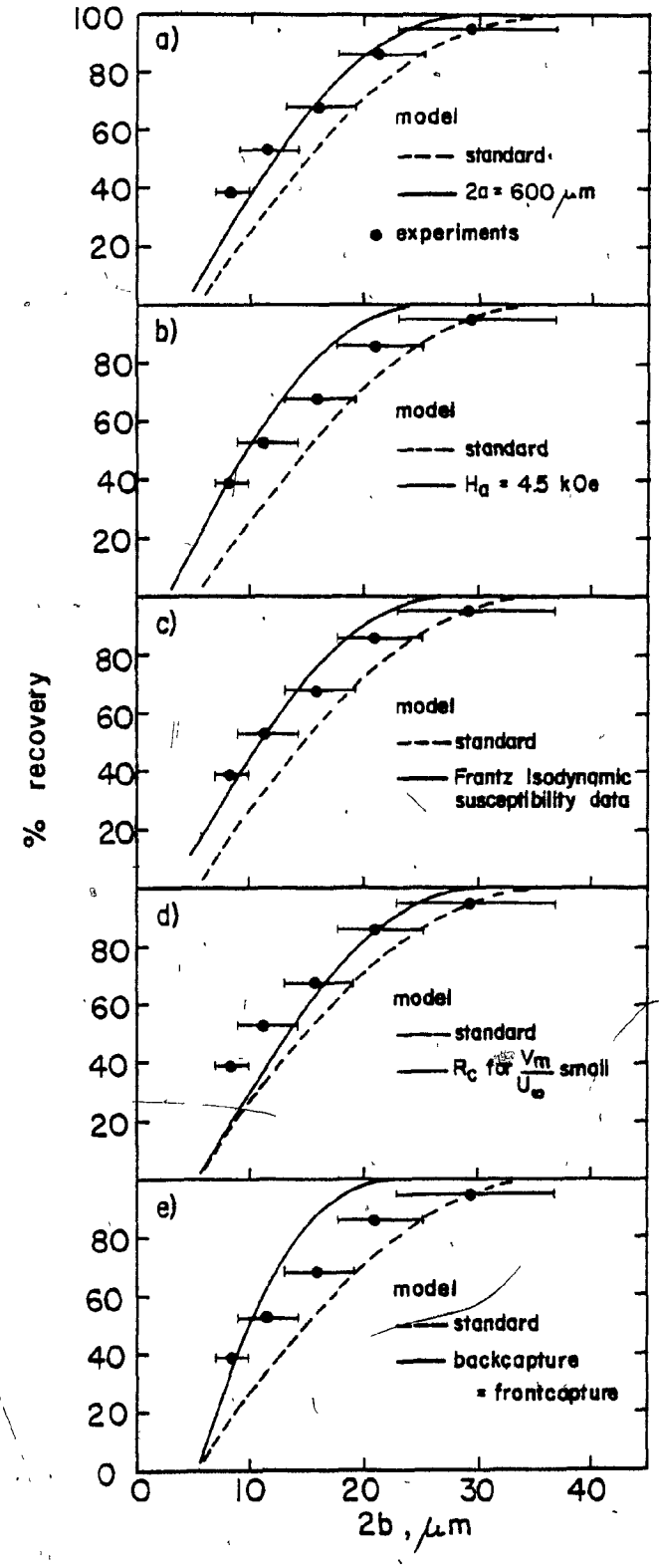
a)
model
standard
2a = 600 μm
experiments
b)
model
standard
H_a = 4.5 kOe
c)
model
standard
Frantz Isodynamic susceptibility data
d)
model
standard
R_c for $\frac{Vm}{U_\infty}$ small
e)
model
standard
backcapture
= frontcapture
% recovery
2b, μm
0
10
20
30
40
20
40
60
80
100

type materials, such as hematite, to be determined in terms of the spontaneous magnetization, σ_o, and the infinite field susceptibility, χ_∞. Excellent agreement between the Frantz and magnetometer generated values of χ_∞($\sim 21.8 \times 10^{-6}$ emu/g-Oe, Table (4-3)), attests to the viability of the Frantz method.

Interestingly, these values of χ_∞, albeit for a hematite from a particular location, are similar to those reported by Pastrana and Hopstock for some other natural hematites ($23\text{-}39 \times 10^{-6}$ emu/g-Oe) and for reagent grade α-Fe_2O_3 (26.5×10^{-6} emu/g-Oe). The extensive work presented here on Labrador type hematites would appear, therefore, to apply to hematites in general.

The Frantz generated σ_o (Table (4-3)), 0.52 emu/g, is 1.68 times the magnetometer value of 0.31 emu/g. Chevallier[102] has shown that σ_o for single crystals of hematite is dependent on the orientation between field and the crystal ternary axis (i.e. perpendicular to the basal plane of the rhombohedral structure). It is now known[103] that the canted antiferromagnetic moment lies in the basal plane such that when field and plane are parallel, the crystal magnetizes with a maximum σ_o. If the plane and field are perpendicular, no spontaneous magnetization occurs.[102] For a packed powder of randomly oriented monocrystals, the observed effect is an average of all possible orientations for which the resulting magnetization is roughly 2/3 that for the single crystal case.[104]

This ratio is very nearly that observed between the Frantz and magnetometer values. It is suggested that the packed powder in the magnetometer sample tube sees the averaged effect while individual crystals

in the chute of the Frantz are free to orient themselves in the field, thereby experiencing a greater σ_o. Hence, the difference in σ_o between Frantz and magnetometer determinations would appear to be real and due to anistropy effects related to crystal orientation.

Given that a particle undergoing capture in a magnetic separator is, within hydrodynamic limits, also able to freely orient itself in the field, it is argued that simple particle force balance methods like the Frantz yield values of susceptibility more appropriate to hgms study than methods involving bulk powders. Examples of bulk powder methods are the Gouy and the Faraday, used by Pastrana and Hopstock. Also, single particle force balances are not liable to potentially large errors due to minute quantities of strongly magnetic impurities. A reminder of this is Figure (4-14) showing the difference in magnetometer magnetization behavior between 'cleaned' and 'uncleaned' hematite.

A 3/2 correction applied to σ_o generated by bulk powder methods is also feasible provided the mineral sample is monocrystalline and known to spontaneously magnetize in one plane only. Of course, no correction is required for paramagnetics since they have no true σ_o component of magnetization.

One may, therefore, conclude that the Frantz method of susceptibility determination can be applied to magnetically complex minerals, such as hematite, and that magnetization values thus generated compare well with the traditional magnetometer methods, provided anisotropic effects are considered. This Frantz method should prove useful to the engineer since the device is widely available in the mineral industry

and easy to use compared with the relative scarcity and complexity of sophisticated magnetometers.

6.6 Concluding Remarks

Consideration of the shear force at the base of the developed boundary layer has resulted in an improved theoretical understanding of particle buildup in hgms. The static model as developed, in addition to comparison with the work of others (Watson, Hopstock and Pastrana and Friedlaender et al.), should prove useful in dynamic models where the changing profile of wire plus accumulating particles is required.

The development of the loading number, N_L, in predicting maximum loading is seen as a major advance in hgms design theory since it improves upon Watson's already established $\frac{V_M}{U_\infty}$. Although not yielding such detailed information as the full model, the loading number approach is particularly attractive because of its simplicity; it may be easily combined with any available matrix recovery model.

All parameters required for determining N_L may readily be obtained by the processing engineer; susceptibility representing the greatest challenge if, as recommended, book values are to be avoided. It was shown here that the Frantz Isodynamic separator, a simple and widely available device, is capable of susceptibility determination for even magnetically complex minerals such as hematite. The dry Frantz is limited by particle size ($\sim$ 10 μm) but the recent appearance of a wet Frantz[105] should extend this lower limit considerably since the role of interparticle surface forces will be further reduced. Certainly these devices are very compatible with hgms studies in general.

As a final point, it is again worth reminding that as the development of the classic boundary layer equations assumes Reynolds number much greater than 1, there exist potential situations in hgms of low flow rates, high viscosity fluids and/or fine wires where the applicability of the model will be exceeded.

VII. CONCLUSIONS AND FUTURE WORK

7.1 Conclusions

1. A fundamental static model of upstream particle buildup in hgms which considers Blasius-type fluid shear at the bottom of a changing boundary layer over a cylindrical wire has been developed.

2. The computer model is experimentally verified by photographs and data of $Mn_2P_2O_7$ buildup on nickel wire. Very good agreement is achieved for equilibrium profiles and saturation buildup radii as a function of field and flow rate.

3. The model is extended to simulate recovery through a stacked metal screen matrix of the type typically used for mineral processing applications of hgms. Agreement between experimental results and predictions for various minerals is judged to be good in view of the many assumptions required to bridge the conceptual to the real situation.

4. Particle buildup beyond a 90^o upstream sector, not considered in the literature, is shown to contribute significantly to recovery under conditions of wire magnetization below or near saturation.

5. The accomodation of field dependent susceptibility in some minerals, such as hematite, is shown to be important for predictions of recovery. This constitutes quantitative support for the claims of Pastrana and Hopstock.

6. A simplified form of the analysis shows loading, γ_V, to be uniquely dependent on the loading number, N_L:

$$\gamma_V = \frac{\epsilon}{4}\{(\frac{N_L}{2.5})^{4/5} - 1\}$$

where

$$N_L = \frac{2bH_a{}^2\kappa A}{a^{1/2}\rho_f U_\infty{}^{3/2}\nu^{1/2}}$$

7. The dependence of loading on N_L is confirmed through tests with hematite and a stainless steel expanded metal matrix.

8. N_L is, therefore, proven superior to Watson's $\frac{V_M}{U_\infty}$ as a descriptor of loading. N_L reduces mathematically to $\frac{V_M}{U_\infty}$ when $\frac{a}{b}$ and Re_w approach unity thus enabling $\frac{V_M}{U_\infty}$ to apply for certain conditions.

9. The Frantz Isodynamic separator is shown to be capable of providing accurate susceptibility measurements of the magnetically complex antiferromagnetics, such as hematite, as well as of paramagnetics. This allows the mineral engineer to determine with readily available equipment the value of an effective κ to be used in N_L.

10. The Frantz Isodynamic is especially suited to hgms studies, it appears, since it balances magnetic and particle forces in much the same way as a particle captured in the vicinity of a wire. A 3/2 correction to σ_0 is probably required for canted-antiferromagnetics when determined by bulk sample magnetometer methods. The Frantz method developed here eliminates the need to account for such anisotropic effects.

7.2 Claims for Original Research

1. The development and verification of a fundamental model of hgms without fitted parameters and capable of accurately predicting the effects of numerous variables on equilibrium buildup profiles, wire loading, and overall separator recovery.

2. The extension of the traditional magnetic force equations in hgms to include materials such as the canted anti-ferromagnetic hematite, exhibiting field dependent magnetic susceptibility of the form:

$$\chi = \chi_\infty + \frac{\sigma_o}{H}$$

3. Maximum loading, γ_v, is shown to be a function of the dimensionless grouping, $N_L = \frac{2bH_a^2\kappa A}{a^{1/2}\rho_f U_\infty^{3/2}\nu^{1/2}}$, which has been called the loading number.

4. Use of the Frantz Isodynamic Separator for field dependent susceptibility determination has been successfully developed and verified for hematite against the Foner vibrating sample magnetometer.

7.3 Suggestions for Future Work

1. The incorporation into the relevant force balance equations of interparticle forces (e.g. friction) in order that the potential of such effects, especially to frontal buildup and side accumulation beyond the 90^o sector, may be evaluated.

2. An experimental programme testing all the variables comprising N_L should be conducted, preferably using cylindrical wires.

3. A study into the hgms recovery of equally rigorously 'cleaned' and prepared multimineral and multisized feeds would be a logical extension of the present work which concerned itself with closely sized unimineral samples. This should include the analysis of both single-wire and full-filter size and mineral distributions.

4. Experimental and theoretical work is required on minimum recoverable size, with respect to both economical and technological limits.

5. Field amplification and back capture in filters were identified as having potentially major influence on performance and deserve further theoretical and experimental attention.

6. The matching of particle size with wire diameter and spacing should be examined with a view toward optimizing processing rate/recovery/economic performance.

BIBLIOGRAPHY

1. Oder, R.R., Proc. HGMS Symposium, M.I.T., May 22, 1973, Eds. Oberteuffer, J.A., Kelland, D.R., p.55.

2. Price, C.R., Abercrombie, W.F., Industrial Applications of Magnetic Separation, Liu, Y.A. (Ed.), IEEE Publication No. 78CH1447-2MAG, N.Y. (1979), p.14.

3. Yano, J., Eguchi, I., Industrial Applications of Magnetic Separation, ibid, p.134.

4. Oberteuffer, J.A., Wechsler, I., Marston, P.G., McNallan, M.J., IEEE Trans. Mag., Vol. MAG-11, No.5, Sept. 1975, p.1591.

5. Arvidson, B.R., Metallurgical and Economic Advantages of High Gradient Magnetic Separators, XII Int. Min. Proc. Congress, Sao Paulo, Brazil, Sept. 1977.

6. Private communication, B.R. Arvidson, Sala Magnetics, Cambridge, Mass., 1978.

7. Johannesen, N., Arvidson, B.R., Industrial Applications of Magnetic Separation, ibid, p.73.

8. Maxwell, E., Kelland, D.R., IEEE Trans. Mag., Vol. MAG-14, No.5, Sept. 1978, p.482.

9. Current research, CANMET Laboratories, Ottawa, May 1979.

10. Oberteuffer, J.A., Arvidson, B.R., Industrial Applications of Magnetic Separation, ibid, p.17.

11. Oberteuffer, J.A., IEEE Trans. Mag., Vol. MAG-10, June 1974, p.223.

12. Marston, P.G., Proc. High Gradient Magnetic Separations Symposium, May 22, 1973, M.I.T., Eds. Oberteuffer, J.A., Kelland, D.R., June 1973, p.25.

13. Kolm, H., Oberteuffer, J., Kelland, D., Scientific American 233 (5), 1975, p.46.

14. Finch, J.A., Smith, G.W., Minerals Sci. Engng., 11 (1), January 1979, p.36.

15. Melville, D., Paul, F., Roath, S., IEEE Trans. Mag., Vol. MAG-11, 1975, p.1701.

16. Zebel, G., J. Colloid Sci., 20, 1965, p.522.

17. Watson, J.H.P., J. Appl. Phys., 44, 1973, p.4209.

18. Lawson, W.F., Simons, W.H., Treat. R.P., J. Appl. Phys., 48, 1977, p.3213.

19. Luborsky, F.E., A.I.P. Conf. Proc., No.29, 1976, p.633.

20. Luborsky, F.E., Drummond, B.J., IEEE Trans. Mag., Vol. MAG-11, 1975, p.1696.

21. Watson, J.H.P., Proc. 6th Int. Cryogenic Engng. Conf., F4, 1976, p.223.

22. Luborsky, F.E., Drummond, B.J., IEEE Trans. Mag., Vol. MAG-12, 1976, p.463.

23. Cummings, D.L., Prieve, D.C., Powers, G.J., IEEE Trans. Mag., Vol. MAG-12, 1976, p.471.

24. Clarkson, C.J., Kelland, D., King, T.B., IEEE Trans. Mag., Vol. MAG-12, 1976, p.901.

25. Clarkson, C.J., Kelland, D.R., IEEE Trans. Mag., Vol. MAG-14, 1978, p.97.

26. Drehmel, D.C., Gooding, C.H., Proc. 2nd Pacific Chemical Engineering Congress (PACHEC '77), Vol. II, 1977, p.1265.

27. Treat, R.P., Lawson, W.F., Johnson, J.L., Industrial Applications of Magnetic Separation, ibid, p.159.

28. Stekly, Z.J.J., Minervini, J.V., IEEE Trans. Mag., MAG-12, 1976, p.463.

29. Himmelblau, D., 'Observation and Modelling of Paramagnetic Particle Trapping in a Magnetic Field', MIT Master's Thesis, June 1973.

30. Oberteuffer, J.A., IEEE Trans. Mag., Vol. MAG-9, Sept. 1973, p.303.

31. Watson, J.H.P., Filtration and Separation, May/June 1977, p.242.

32. Watson, J.H.P., presented at A Symposium on Deposition and Filtration of Particles from Gas and Liquids at Loughborough University, Sept. 1978.

33. Clarkson, C.J., 'The Modelling of High Gradient Magnetic Separation, and Its Application to Cold Rolling Mill Lubricants', M.I.T. Ph.D. Thesis, 1977, p.81.

34. Cowen, C., Friedlaender, F.J., Jaluria, R., IEEE Trans. Mag., Vol. MAG-11, 1975, p.1600.

35. Cowen, C., Friedlaender, F.J., Jaluria, R., IEEE Trans. Mag., Vol. MAG-12, 1976, p.466.

36. Cowen, C., Friedlaender, F.J., Jaluria, R., IEEE Trans. Mag., Vol. MAG-12, 1976, p.898.

37. Cowen, C., Friedlaender, F.J., Jaluria, R., IEEE Trans. Mag., Vol. MAG-13, 1977, p.1483.

38. Friedlaender, F.J., Takayasu, M., Rettig, J.B., Kentzer, C.P., IEEE Trans. Mag., Vol. MAG-14, (No.5), Sept. 1978.

39. Friedlaender, F.J., Takayasu, M., Rettig, J.B., Kentzer, C.P., IEEE Trans. Mag., Vol. MAG-14, (No.6), Nov. 1978.

40. Friedlaender, F.J., Takayasu, M., 'Video Recording of Particle Trajectories and Buildup of Single Wires in High Gradient Magnetic Separation, preprint of paper, 1979.

41. Liu, Y.A., Oak, M.J., Lin, C.J., paper for publication in the Chemical Engineering Progress Technical Manual, 'Coal Processing Technology', presented at Symposium on Novel Separation Techniques, Seventh Annual AIChE Meeting, Nov. 13-17, 1977, N.Y.

42. Telford, W.M., Geldart, L.P., Sheriff, R.E., Keys, D.A., Applied Geophysics, Cambridge, 1978, p.121.

43. Taggart, A.F., 'Handbook of Mineral Dressing', John Wiley and Sons, 1954, p.13-07.

44. Andres, U., 'Magnetohydrodynamic and Magnetohydrostatic Methods of Mineral Separation', Israel Universities Press, Jerusalem, Israel, 1976, Chapter 5.

45. Aharoni, A., IEEE Trans. Mag. Vol. MAG-12, 1976, p.234.

46. Stratton, J.A., 'Electromagnetic Theory', McGraw-Hill, 1941, p.261.

47. Cullity, B.D., 'Introduction to Magnetic Materials', Addison-Wesley, 1972, p.56.

48. Ref. 33, p.100.

49. Pastrana, J.M., Hopstock, D.M., Trans. Soc. Min. Engng., AIME, 262, 1977, p.1.

50. Currie, I.G., 'Fundamental Mechanics of Fluids', McGraw-Hill, 1974, p.83.

51. Geiger, G.H., Poirier, D.R., 'Transport Phenomena in Metallurgy', Addison-Wesley, 1973, p.31.

52. Schlichting, H., 'Boundary-Layer Theory', McGraw-Hill, 1968, p.26.

53. Arvidson, B.R., Sala Magnetics, personal communication, 1978.

54. Ref. 50, p.269.

55. idem, p.280.

56. idem, p.281.

57. Ref. 52, p.192.

58. Ref. 50, p.302.

59. Ref. 52, p.154.

60. idem, p.156.

61. idem, p.162.

62. Massey, B.S., Mechanics of Fluids, Van Nostrand Reinhold, 1975, p.292.

63. Bird, R.B., Stewart, W.E., Lightfoot, E.N., 'Transport Phenomena', John Wiley and Sons, 1960, p.59.

64. Ref. 52, p.204.

65. Kelly, E.M., Powder Technol., 4, 1970/71, p.56.

66. Ref. 51, p.103.

67. Akoto, I.Y., IEEE Trans. Mag., Vol. MAG-13, 1977, p.1986.

68. Bulman, W.E., 'Applications of the Hall Effect', technical literature supplied by Ohio Semitronics Inc., Columbus, Ohio, U.S.A.

69. Dobby, G.S., 'High Gradient Magnetic Capture of Mineral Particles', M. Eng. Thesis, McGill University, 1976.

70. Ref. 47, p.25.

71. Hess, H.H., Notes on Operation of Frantz Isodynamic Magnetic Separator, S.G. Frantz Co.

72. Gaudin, A.M., Spedden, H.R., 'Magnetic Separation of Sulphide Minerals', Publ. No. 1549, AIME, 1943.

73. Dobby, G., Nesset, J., Finch, J.A., to be published in Can. Met. Quarterly, Sept. 1979.

74. Ref. 43, p.13-02.

75. Partridge, A.C., 'Flotation and Adsorption Characteristics of the Hematite-Dodecylamine-Starch System, M. Sc. Thesis, McGill University, 1970, p.23.

76. Foner, S., Rev. Sci. Instr., 30, 1959, p.548.

77. Handbook of Chemistry and Physics, CRC Press, 56th Ed., 1975-76, p.E-120.

78. Gottschalk, V.H., Wartman, F.S., Report of Investigations 3268, 1935, U.S. Bureau of Mines, p.67.

79. Dobby, G., Finch, J.A., Powder Technol., 17, 1977, p.73.

80. Stoner, E.C., Phil. Mag. 36, p.803, 1945.

81. Kelsall, D.F., McAdam, J.C.H., Trans. Instn. Chem. Engnrs., 41, 1963, p.84.

82. Olivier, J.P., Hickin, G.K., Orr, C., Powder Technol., 4, 1970, p.257.

83. Allen, T., 'Particle Size Measurement', 2nd Ed., Chapman and Hall, 1975.

84. Berman, H., Amer. Miner., 24, p.434, 1939.

85. Ref. 77, p.F-1.

86. Ref. 77, p.D-172.

87. Unpublished photographs provided by Friedlaender, 1979.

88. Private communication from M. Takayasu, F. Friedlaender, 1978.

89. Am. Inst. Phys. Handbook, 3rd Ed., McGraw-Hill, 1972.

90. Private communication from M. Takayasu, F. Friedlaender, 1979.

91. Watson, J.A., private communication, Rindge, N.H., 1978.

92. Birss, R.R., Gerber, R., Parker, M.R., 2nd Conf. on Adv. Mag. Materials and Their Appl., IEE, London, Sept., 1976.

93. Collan, H.K., Janturen, J., Kokkala, M., Ritvos, A., Industrial Applications of Magnetic Separation, ibid, p.175.

94. Villar, J.W., Dawe, G.A., Min. Congr. J., 60, No.9, 1975, p.40.

95. ref. 52, Chapter XVII, Section g, p.509.

96. Clift, R., Grace, J.R., Weber, M.E., 'Bubbles, Drops and Particles', Academic Press, 1978, p.268.

97. Yaniv, I., Lin, I.J., Zimmels, Y., IEEE Trans. Mag., vol. MAG-14, November 1978, p.1175.

98. Watson, J.H.P., paper presented at Filtech. Conf., Sept. 1977.

99. Collan, H.K., Jantunen, J., Kokkala, M., Ritvos, A., IEEE Trans. Mag., vol. MAG-14, 1978, p.398.

100. Watson, J.H.P., IEEE Trans. Mag., vol. MAG-14, Sept. 1978, p.392.

101. McAndrew, J., Proc. Aus. I.M.M., 181, 1957, p.59.

102. Chevallier, R., Le Journal de Physique et le Radium, Tome 12, mars 1951, p.172.

103. ref. 47, p.176.

104. Van Vleck, J.H., Le Journal de Physique et le Radium, Tome 12, mars 1951, p.262.

105. U.S. Patent 4,102,780, July 25, 1978.

106. Thomas, G.B., 'Calculus and Analytic Geometry', Addison-Wesley, 1968, p.325.

APPENDIX I. DERIVATION OF THE MAGNETIC FORCE EQUATIONS FOR FIELD DEPENDENT SUSCEPTIBILITY.

As stated in Equation (3.1-13), the magnetic force on a particle is given by;

$$F_M = \frac{V}{2} \nabla(M_p \cdot H) \tag{A-1}$$

where the particle magnetization is represented by the 2-parameter equation:

$$M_p = M_o + \kappa_\infty H \tag{A-2}$$

Note that F_M, M_p and H are actually vector quantities.

Substituting for M_p in Equation (A-1) yields;

$$F_M = \frac{V}{2} \nabla(M_o H + \kappa_\infty H^2) \tag{A-3}$$

the assumption having been made that

$$M_o H \equiv M_o \cdot \bar{H}$$

The radial and tangential components of the field, H, are:

$$H_r = H_a \cos\theta\left(1 + A\frac{a^2}{r^2}\right) \tag{A-4a}$$

$$H_\theta = - H_a \sin\theta\left(1 - A\frac{a^2}{r^2}\right) \qquad \text{(A-4b)}$$

Squaring Equations (A-4a) and (A-4b) and combining terms, yields an expression in H^2;

$$H^2 = H_r^2 + H_\theta^2$$

$$= H_a^2\left(1 + 2A\frac{a^2}{r^2}\cos 2\theta + \frac{A^2a^4}{r^4}\right) \qquad \text{(A-5)}$$

By defining a field factor, f, such that;

$$f^2 = \frac{1}{4\left(1 + 2A\frac{a^2}{r^2}\cos 2\theta + \frac{A^2a^4}{r^4}\right)},$$

Equation (A-5) may be written:

$$H = \frac{H_a}{2f} \qquad \text{(A-6)}$$

In order to expand the expression in brackets in Equation (A-3) one requires the gradient operator in polar coordinates, i.e.

$$\nabla = \left(\frac{d}{dr}, \frac{1}{r}\frac{d}{d\theta}\right).$$

Making use of the Chain Rule which states that, in general,

$$\nabla H = \frac{d}{du}(H)$$

$$= \frac{1}{2\sqrt{(H)^2}}\frac{d(H)^2}{du}$$

$$= -\frac{1}{2H}\frac{d}{du}(H)^2$$

Equation (A-3) becomes:

$$F_M = \frac{V}{2}\left(\frac{d}{dr}, \frac{1}{r}\frac{d}{d\theta}\right)(M_o H + \kappa_\infty H^2)$$

$$= \frac{V}{2}\left(\frac{M_o}{2H} + \kappa_\infty\right)\left(\frac{d}{dr}, \frac{1}{r}\frac{d}{d\theta}\right)(H^2)$$

$$= C\left(\frac{d}{dr}, \frac{1}{r}\frac{d}{d\theta}\right)(H^2) \qquad \text{(A-7)}$$

where $C = \frac{V}{2}\left(\frac{M_o}{2H} + \kappa_\infty\right)$

and H^2 is given by Equation (A-5). Evaluating the gradient operation w.r.t. H^2 leads to;

$$\frac{d}{dr}(H^2) = H_a^2\left(2(-2)\frac{Aa^2}{r^3}\cos 2\theta + (-4)\frac{A^2a^4}{r^5}\right)$$

$$= -4H_a^2\frac{Aa^2}{r^3}\left(\cos 2\theta + \frac{Aa^2}{r^2}\right)$$

and

$$\frac{1}{r}\frac{d}{d\theta}(H^2) = \frac{H_a^2}{r}(2)2\frac{Aa^2}{r^2}(-\sin 2\theta)$$

$$= -4H_a^2\frac{Aa^2}{r^3}\sin 2\theta$$

Finally, the expressions for the radial and tangential components of magnetic force may be found, viz.;

$$F_{r_M} = C\frac{d}{dr}(H^2)$$

$$= -2VH_a\frac{Aa^2}{r^3}(\cos 2\theta + \frac{Aa^2}{r^2})(\kappa_\infty H_a + fM_o) \qquad \text{(A-8a)}$$

and $$F_{\theta_M} = C\frac{1}{r}\frac{d}{d\theta}(H^2)$$

$$= -2VH_a\frac{Aa^2}{r^3}\sin 2\theta(\kappa_\infty H_a + fM_o) \qquad \text{(A-8b)}$$

The total magnetic force is, then, simply;

$$F_{M_{total}} = \underline{V}\, H_a^2\frac{Aa^2}{r^3}(\frac{\kappa_\infty H_a}{f} + M_o) \qquad \text{(A-8c)}$$

which reduces to the well known expression for paramagnetics if $\kappa_\infty = \kappa$ and $M_o = 0$.

APPENDIX II. NEWTON'S METHOD

In general, Newton's Method[106] can be employed when seeking the real root of an equation of the form;

$$f(x) = 0$$

where $f(x)$ is an equation of any degree, even transcendental.

Provided that the derivative of $f(x)$, $f'(x)$, can be determined then a new function, $g(x)$, will yield a new approximation of the root as given by:

$$g(x) = x - \frac{f(x)}{f'(x)} \qquad \text{(Newton's Method)}$$

The accuracy of the solution is determined by the number of successive computations of $g(x)$ performed by the following iterative procedure.

previous guess → $g(x) = x - \frac{f(x)}{f'(x)}$ → new guess

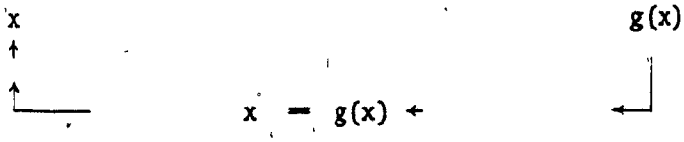

It is, however, sufficient to have an approximation of $f'(x)$ if exact differentiation is not possible. Hence, if $h(x) \approx f'(x)$, then

$$g(x) = x - \frac{f(x)}{g(x)} \qquad \text{(Modified Newton's Method)}$$

can be used.

In the application of this method both an initial guess for the root, x, and a convergence criterion for the difference between successive iterations, $|g(x) - x|$, is required.

Use was made of this technique to determine the wire magnetization, M_w, for an applied field, H_a, and for evaluating the roots of both radial and tangential net force equations.

a) Wire magnetization, M_w

$$f(H) = M_s \exp(-K/H) - \frac{(H_a - H)}{2\pi}$$

$$f'(H) = \frac{KM_s}{H^2} \exp(-K/H) + \frac{1}{2\pi}$$

initial guess: $H = \frac{H_a}{15}$

criterion for convergence: $\left|\frac{H - g(H)}{g(H)}\right| \leq 0.1\%$

b) Tangential net force, $F_{\theta_{net}}$

$$f(\theta) = -2VH_a \frac{Aa^2}{r^3} \sin 2\theta(\kappa_\infty H_a + fM_o) + V(\rho_p - \rho_f)g \sin\theta$$

$$+ f_b 4\pi b^2 \rho_f \left(\frac{U_\infty^3 \nu}{8r}\right)^{1/2} (9.861\theta - 3.863\theta^3 + .413\theta^5$$

$$- .0261\theta^7 + .00005\theta^9)$$

The modified Newton's Method is used since differentiation of the magnetic force term with respect to θ is rather complex. Hence, f is assumed constant in evaluating:

$$h(\theta) \approx f'(\theta)$$

$$= -4VH_a \frac{Aa^2}{r^3} \cos 2\theta(\kappa_\infty H_a + fM_o) + V(\rho_p - \rho_f)g \cos\theta$$

$$+ f_b 4\pi b^2 \rho_f \left(\frac{U_\infty^3 \nu}{8r}\right)^{1/2} (9.861 - 11.589\theta^2 + 2.065\theta^4$$

$$- .1827\theta^6 + .00045\theta^8)$$

initial guess: $\theta = \frac{\pi}{2}$ radians

criterion for convergence: $\left|\frac{\theta - g(\theta)}{g(\theta)}\right| \leq 0.01\%$

c) Radial net force, $F_{r_{net}}$

$$f(\theta) = -2VH_a \frac{Aa^2}{r^3}\left(\cos 2\theta + \frac{Aa^2}{r^2}\right)(\kappa_\infty H_a + fM_o) - V(\rho_p - \rho_f)g \cos\theta$$

Again, the modified Newton's Method is used to give:

$$h(\theta) \approx f'(\theta)$$

$$= 4VH_a \frac{Aa^2}{r^3} \sin 2\theta(\kappa_\infty H_a + fM_o) + V(\rho_p - \rho_f)g \sin\theta$$

initial guess: $\theta = \frac{\pi}{4}$ radians

criterion for convergence: $\left|\frac{\theta - g(\theta)}{g(\theta)}\right| \leq 0.01\%$

APPENDIX III. TESTWORK DATA

1. Hematite magnetization measurements by Foner vibrating sample magnetometer.

Cyclosizer Cone #	Regression Ranges: 1.0-2.5 kOe χ_∞**	1.0-2.5 kOe σ_o*	3.0-10 kOe χ_∞**	3.0-10 kOe σ_o*
1	.000224	1.36	.000127	1.62
2	.000215	1.38	.000126	1.61
3	.000198	1.18	.000109	1.44
4	.000204	1.35	.000103	1.60
5	.000254	1.44	.000107	1.85
average	.000219	1.34	.000114	1.62

* emu/gm
**emu/gm-Oe

2. Hematite magnetization measurements by the Frantz Isodynamic Separator.

I_{50} - current at which 50% of 1 g samples report to magnetics chute (amps)

θ - side slope of device in degrees

front slope: 35^{o} vibrator setting: 6

	Cyclosizer Cone #1					
	Sample 1		Sample 2		Cone #2	
θ	I_{50}	H*(kOe)	I_{50}	H*	I_{50}	H*
5	.063	.77	.065	.80	.044	.54
10	.132	1.62	.127	1.56	.125	1.54
15	.176	2.16	.183	2.25	.176	2.16
20	.233	2.87	.229	2.82	.228	2.80
25	.275	3.38	.227	3.41	.268	3.30
30	.313	3.85	.314	3.86	.315	3.87
35	.354	4.35	.356	4.38	.360	4.43
40	.400	4.92	.396	4.87	.386	4.75
45	.451	5.55	.451	5.55	.456	5.61
repeats						
10	.127	1.56				
15	.171	2.10				
20	.225	2.77				
30	.315	3.87				

*H = 12.3 x I_{50} (Equation (4.1-7)).

I_{50} data used in Equation (4.1-17) to generate χ_{∞} and σ_{o} values given in Table (4-3).

3. Specific gravity determination of hematite.

Sample	s.g.	repeat s.g.
1	5.2598	5.2598
2	5.2214	5.2214
3	5.2671	5.2550

Average: 5.2474 g/cm^3

Hematite samples isolated from cyclosizer cone #1.

Measurements made in toluene (s.g. .8632 at 24°C) employing Berman Density Balance.

4. Results of exploratory run on permanent magnet.

Test	Feed (g)	Magnetics (g)	Non-magnetics (g)	Field	Matrix
1,4	1	.23, .24	.67, .67	on	yes
2	5	.85	4.03	on	yes
3	3	.62	2.30	on	yes
5	9	1.26	7.70	on	yes
6	7	1.02	5.98	on	yes
7	11	1.41	9.56	on	yes
8	5	.12	4.79	off	yes
9	11	.27	10.65	off	yes
10	3	.13	2.88	off	yes
11	1	.06	.94	off	yes
12	9	.24	8.68	off	yes
13	7	.18	6.74	off	yes
14	18	.31	17.45	off	yes
15	18	1.74	16.10	on	yes
16	36	2.98	32.89	on	yes
17	36	0.78	35.09	off	yes
18	36	1.26	34.57	on	no

Conditions: water - temperature, 19°C; sodium silicate added as 1 kg/tonne solids
hematite - cyclosizer cone #2
$U_\infty = 4$ cm/s
matrix - 4 s. steel (1.39 g each) between 6 aluminum (4 upstream, 2 downstream, 1.51 g each)
$H_a \approx 0.78$ kOe

5. Results of runs on superconducting magnet.

Test	Cyclosizer Cone Fraction	U_∞ (cm/s)	H_a (kOe)	Weight % to Magnetics
1,6	3	5.5	2.08	79.56, 78.85
2	1	5.5	2.08	93.66
3	2	5.5	2.08	90.25
4	5	5.5	2.08	46.42
5	4	5.5	2.08	65.53
7	1	9.9	1.04	64.08
8	4	9.9	1.04	31.13
9,10	2	9.9	1.04	57.22, 58.04
11	3	9.9	1.04	43.05
12	5	9.9	1.04	21.04
13	2	15.2	4.13	81.42
14	1	15.2	4.13	84.63

Conditions: 20 g feed mass

matrix: 40 s. steel screens (1.41 g each)

water: temperature 20°C
sodium silicate added as 1 kg/tonne solids

6. Results of runs on CANMET Sala magnet.

Code	Feed (g)	Magnetics (g)	Magnetics* % of Feed	γ_m ($\frac{\text{g magnetics}}{\text{g matrix}}$)	γ_v ($\frac{\text{cm}^3 \text{ magnetics}}{\text{cm}^3 \text{ matrix}}$)
F	50	2.02	24.8	.363	.536
E	26	1.12	23.3	.201	.297
D	58 (2x)	3.70	31.4	.665	.982
A	15	0.45	33.3	.081	.120
B	93 (4x)	10.49	35.5	1.89	2.79
H	50 (2x)	3.36	29.8	.604	.892
D	58 (2x)	3.94	29.4	.709	1.047
C	62 (2x)	7.09	35.0	1.28	1.89
D	58 (2x)	3.55	32.7	.638	.942
G	26 (2x)	1.08	24.1	.194	.286

* greater than 20 ratio suggested from exploratory run for fully loaded condition.

Code	H_a (Oe)	A	U_∞ ($\frac{\text{cm}}{\text{s}}$)	2b (cm)	Cyclosizer Cone #	N_L*	N_L**	$\frac{V_M}{U_\infty}$***	$\frac{V_M}{U_\infty}$****
F	4240	.895	12.0	.00123	4	6.6	9.1	.248	.391
E	2580	.888	15.2	.00228	2	4.3	6.3	.385	.618
D	6710	.870	15.2	.00228	2	16.2	21.4	1.11	1.71
A	2580	.888	15.2	.00123	4	2.3	3.4	.112	.180
B	2580	.888	2.9	.00228	2	51.5	75.7	2.02	3.24
H	4240	.895	8.0	.00123	4	12.0	16.8	.372	.587
D	6710	.870	15.2	.00228	2	16.2	21.4	1.11	1.71
C	2580	.888	2.9	.00123	4	27.8	40.8	.587	.942
D	6710	.870	15.2	.00228	2	16.2	21.4	1.11	1.71
G	4240	.895	15.2	.00123	4	4.6	6.4	.196	.309

* M_o = 1.62 emu/cm^3, $\bar{f}$ = .42 (magnetometer data)
** M_o = 2.70 emu/cm^3, $\bar{f}$ = .42 (Frantz Isodynamic data)
*** M_o = 1.62 emu/cm^3, $\bar{f}$ = 0.5 (magnetometer data)
**** M_o = 2.70 emu/cm^3, $\bar{f}$ = 0.5 (Frantz Isodynamic data)

ρ_p = 5.25 g/cm^3
ρ_w = 7.75 g/cm^3

matrix: 4 s. steel screens (1.39 g each) between 6 aluminum (4 upstream, 2 downstream, 1.51 g/each).

APPENDIX IV

MAG6 PROGRAMME

```
*IN PROGRESS

C
C  MAG6. PROGRAM FOR MODELLING HGMS EQUILIBRIUM BUILDUP
C       ON CYLINDRICAL FIBERS OF UNIT LENGTH AND FOR
C       CALCULATING RECOVERY THROUGH A LENGTH OF SCREENS.
C       J.E. NESSET AND J.A. FINCH, MCGILL UNIVERSITY,
C       CANADA ( 1977 ).
C
C  PART 1: DETERMINATION OF EQUILIBRIUM PROFILE
C
/SYS TIME=32S
/LOAD WAT5
      REAL LOF,NT,LPS,NDOT,LMAX
      DIMENSION THETCT(200),THETCR(200),THETM(200),FN(200),FM(200),
     *DTHECT(200),DTHECR(200),DTHETM(200),R(200)
      DIMENSION RC(100),DMS(100),RLS(100),FLT(100),FAREA(100)
      REAL H,HO,LS(100)
 1    WRITE(6,5)
      READ(9,*) DIAP,RHOP,CHIP,SIGP,SF
      WRITE(6,15)
      READ(9,*) DIAW,RHOW,WMAGS,AH
      WRITE(6,25)
      READ(9,*) ETAF,VELF,RHOF
      WRITE(6,35)
      READ(9,*) ELLSQ,HO,G,DTHETS
      PI=3.141592654
      THETAS=DTHETS*PI/180
C
C  CALCULATE VARIOUS PARAMETERS FOR FORCE EQUATIONS
C
      RP=DIAP/2
      RW=DIAW/2
      VOLP=(4.0/3.0)*PI*(RP**3)
      FMT1=-2*VOLP*HO*(RW**2)
      FMT2=CHIP*HO
      ELL=SQRT(ELLSQ)
C
C  DET'N OF PERTURBATION TERM IN MAG FORCE EQ'N
C
      H=HO/15
 6    FH=WMAGS*EXP(-AH/H)-(HO-H)/(2*PI)
      DFH=(AH*WMAGS/(H**2))*EXP(-AH/H)+1/(2*PI)
      GH=H-FH/DFH
      DELH=(ABS(GH-H)/GH)*100
      IF(DELH.LE.0.1) GO TO 16
      H=GH
      GO TO 6
 16   H=GH
      AA=2*PI*WMAGS*EXP(-AH/H)/HO
C  CALCULATE THE MAG FORCE,FMT,AND DERIVATIVE,DFMT
      N=1
      THETCR(1)=PI/4.
      THETCT(1)=PI/2
 26   RR=RW+RP+(N-1)*RP*SQRT(ELLSQ)
      R(N)=RR
 36   FMT3=(AA/(RR**3))*SIN(2*THETCT(N))
      FACT=1/(2*(1+2*AA*((RW/RR)**2)*COS(2*THETCT(N))+(AA**2*((RW/RR)*
     **4)))**0.5)
      FMT4=SIGP*FACT
      FMT=FMT1*FMT3*(FMT2+FMT4)
      DFMT3=2*(AA/(RR**3))*COS(2*THETCT(N))
      DFMT=FMT1*DFMT3*(FMT2+FMT4)
C
C  CALCULATE DRAG FORCE,FDT,AND DERIVATIVE,DFDT
C
      SSC1=9.861*THETCT(N)-3.863*(THETCT(N)**3)+0.413*(THETCT(N)**5)-
     *0.0261*(THETCT(N)**7)+0.00005*(THETCT(N)**9)
      SSC2=RHOF*SQRT((VELF**3)*ETAF/(8*RR))
      FDT=SF*4*PI*(RP**2)*SSC1*SSC2
      DSSC1=9.861-11.589*(THETCT(N)**2)+2.065*(THETCT(N)**4)-0.1827*(T
     *HETCT(N)**6)+0.00045*(THETCT(N)**8)
      DFDT=SF*4*PI*(RP**2)*DSSC1*SSC2
```

```
C
C  CALCULATE GRAVITY FORCE,FG,AND DERIVATIVE,DFG
C
      FGT=VOLP*(RHOP-RHOF)*G*SIN(THETCT(N))
      DFGT=VOLP*(RHOP-RHOF)*G*COS(THETCT(N))
C
C  DET'N THE CRITICAL ANGLE,THETCT,WHERE FMT+FGT+FDT=0
C
      FT=FMT+FDT+FGT
      DFT=DFMT+DFDT+DFGT
      GT=THETCT(N)-FT/DFT
      DELT=(ABS(GT-THETCT(N))/GT)*100
      IF(DELT.LE.0.01) GO TO 46
      IF(GT.LT..0001) GO TO 46
      THETCT(N)=GT
      GO TO 36
 46   THETCT(N)=GT
C
C  CALCULATE RADIAL MAG FORCE,FMR,AND DERIVATIVE,DFMR
C
 48   FMR3=(AA/(RR**3))*(COS(2*THETCR(N))+(AA*(RW**2)/(RR**2)))
      FACT=1./(2*(1+2*(AA)*((RW/RR)**2)*COS(2*THETCR(N))+(AA**2*((RW/RR
     *)**4)))**0.5)
      FMR4=SIGP*FACT
      FMR=FMT1*FMR3*(FMT2+FMR4)
      DFMR3=-2*(AA/(RR**3))*SIN(2*THETCR(N))
      DFMR=FMT1*DFMR3*(FMT2+FMR4)
C
C  CALCULATE RADIAL GRAVITY FORCE,FGR,AND DERIVATIVE,DFGR
C
      FGR=-VOLP*(RHOP-RHOF)*G*COS(THETCR(N))
      DFGR=VOLP*(RHOP-RHOF)*G*SIN(THETCR(N))
C
C  DET'N THE CRITICAL ANGLE,THETCR,AT WHICH THE RADIAL FORCE IS
C                                                          ZERO
      FR=FMR+FGR
      DFR=DFMR+DFGR
      GR=THETCR(N)-FR/DFR
      DELT=(ABS(GR-THETCR(N))/GR)*100
      IF(DELT.LE.0.01) GO TO 58
      THETCR(N)=GR
      GO TO 48
 58   THETCR(N)=GR
C
C  CHECK FOR STOP CRITERION
C
      IF(THETCT(N)-THETAS)66,66,56
 56   N=N+1
      L=N-1
      THETCT(N)=THETCT(L)
      THETCR(N)=THETCR(L)
      GO TO 26
C
C  PART 2: MASS RECOVERY CALCULATIONS FOR A UNIT LENGTH OF FIBER
C  ( UNIT LENGTH=1 CM )
C
C  CHOOSE SMALLER OF RADIAL AND TANGENTIAL CRITICAL ANGLESFOR
C  PROFILE DET'N
C
 66   DO 86 I=1,N
      IF(THETCT(I).GT.THETCR(I)) GO TO 76
      THETM(I)=THETCT(I)
      GO TO 86
 76   THETM(I)=THETCR(I)
 86   CONTINUE
C
C  CALCULATE TOTAL NO AND MASS OF PARTICLES IN EACH LAYER AND
C  SUM
      DO 96 I=1,N
      PN(I)=0
      PM(I)=0
 96   CONTINUE
      PNT=0
      PMT=0
      DO 106 I=1,N
      PN(I)=THETM(I)*R(I)/(2*SQRT(ELLSQ)*RP**2)
      PM(I)=VOLP*PN(I)*RHOP
      PNT=PNT+PN(I)
      PMT=PMT+PM(I)
 106  CONTINUE
```

```
C
C  CONVERT ANGLES TO DEGREES
C
      DO 116 I=1,N
      DTHECT(I)=THETCT(I)*180/PI
      DTHECR(I)=THETCR(I)*180/PI
      DTHETM(I)=THETM(I)*180/PI
 116  CONTINUE
C
C  PRINT DATA ,CRITICAL ANGLES, RECOVERIES
C
      WRITE(6,10)
      WRITE(6,20) DIAP,RHOP,CHIP,SIGP,SF
      WRITE(6,30) DIAW,RHOW,WMAGS,AH
      WRITE(6,40) ETAF,VELF,RHOF
      WRITE(6,50) HO,H,AA
      WRITE(6,60) ELL,G,DTHETS
      WRITE(6,70)
      WRITE(6,80)(I,DTHECT(I),DTHECR(I),DTHETM(I),R(I),I=1,N)
      WRITE(6,90)
      WRITE(6,100)(I,PN(I),PM(I),I=1,N)
      WRITE(6,110) PNT,PMT
C
C
 5    FORMAT(' ','ENTER PARTICLE DIA,DENSITY,SP.SUSC,SP.MAGN,SHEAR AREA
     *')
 15   FORMAT(' ','ENTER FIBER DIA,DENSITY,SAT.MAGN,MAG CONSTANT')
 25   FORMAT(' ','ENTER FLUID VISCOSITY,VELOCITY,DENSITY')
 35   FORMAT(' ','ENTER ELLSQ,BACKGROUND FIELD,GRAV CONST,THETA STOP CRI
     *TERION')
 10   FORMAT('1',27X,'STATIC HGMS MODEL',//,'EXPERIMENTAL CONDITIONS ( A
     *LL UNITS CGS )')
 20   FORMAT(/,5X,'PARTICLE :  DIA ',F7.5,';  DENSITY',F5.2,';  SP.SUSCE
     *PT',E11.4,';',/,15X,'  SP.MAGN',E11.4,';  SHEAR AREA',F5.2)
 30   FORMAT(/,5X,'   FIBER :  DIA ',F6.4,';  DENSITY',F5.2,';  SAT.MAGN
     *',F7.1,';',/,15X,'  MAG.CONSTANT',F7.1)
 40   FORMAT(/,5X,'   FLUID :  VISCOSITY',F8.5,';  VELOCITY',F5.1,';  DE
     *NSITY',F6.1)
 50   FORMAT(/,5X,'   FIELD :  BACKGROUND',F7.0,';  FIBER',F7.0,';  PERT
     *URB TERM',F7.4)
 60   FORMAT(/,5X,'INTERLAYER DIST',F7.4,' RAD',';  GRAVITY',F6.1,';  ST
     *OP CRITERION',F5.1,' DEG')
 70   FORMAT(///,'RESULTS',/,5X,'LAYER',13X,'CRITICAL ANGLES (DEGREES)',
     *15X,'RADIUS',/,16X,'TANGENTIAL',5X,'  RADIAL',9X,'MINIMUM')
 80   FORMAT(' ',6X,I3,8X,F6.2,9X,F6.2,9X,F6.2,9X,F6.4)
 90   FORMAT(///,5X,'LAYER',12X,'PARTICLE RECOVERIES(ABS)',/,22X,'NUMBER
     *',11X,'MASS(GMS)')
 100  FORMAT(' ',6X,I3,9X,E12.5,5X,E12.5)
 110  FORMAT(/,5X,'TOTAL',9X,E12.5,5X,E12.5,//////)
C     PART 3:  MASS RECOVERY CALCULATIONS FOR A MATRIX OF NS
C              SEGMENTS; EACH SEGMENT OF SS SCREENS
C
      WRITE(6,115)
      READ(9,*) NO1
      IF(NO1.EQ.2) GO TO 137
 117  WRITE(6,105)
      READ(9,*) FM,SM,SS,NS,DIAV,M
C  CALCULATION OF VARIOUS PARAMETERS
C
      LPS=SM/(PI*RHOW*(RW**2))
      XAREA=(PI*DIAV**2)/4.
      CHIPO=CHIP+SIGP/HO
      VMVF=(2*CHIPO*(DIAP**2)*(HO**2)*AA)/(9*ETAF*RHOF*DIAW*VELF)
      LMAX=SS*2*LPS*PNT*VOLF*RHOP
      DT=1.0/M
      TT=DT
      KS=0
      DO 167 I=1,NS
      FLT(I)=1.0E12
 167  CONTINUE
      BMA=R(N-1)/RW
      CRLS=0.0
      IF(VMVF.LT.4.19) GO TO 187
      CRLS=(((((BMA-1)*(1-1.5*SQRT(3.)/(VMVF**.6667)))+1)**2)-1)/((BMA*
     **2)-1)
 187  CONTINUE
      KO=1
      KJ1=0
```

```
C
C DETERMINATION OF FIBER SPACING
C
      ROF=XAREA*2*PI*(RW**2)*RHOW/SM
      FSP=ROF-2*RW
C
C  CALCULATION OF INITIAL CAPTURE RADIUS AND FRACTIONAL AREA OF
C   CAPTURE
      IF(VMVF.GE.4.19) GO TO 47
      DO 57 I=1,NS
      RC(I)=0.5*VMVF
 57   CONTINUE
      GO TO 77
 47   DO 67 I=1,NS
      RC(I)=0.75*SQRT(3.0)*(VMVF**0.33333)
 67   CONTINUE
 77   RCI=RC(1)
      DO 177 J=1,NS
      LS(J)=0.0
 177  CONTINUE
 78   DO 87 I=1,NS
      IF(RC(I).GE.1.0) GO TO 79
      BETA=(FSP+RW)/(FSP+2*RW)
      GO TO 81
 79   BETA=(FSP+2*RW-RC(I)*RW)/(FSP+2*RW)
 81   FAREA(I)=BETA*2*RC(I)*SM/(PI*RW*RHOW*XAREA)
      IF(FAREA(I).GT.1.0) FAREA(I)=1.0
 87   CONTINUE
      EFA=FAREA(1)*SS
      IF(EFA.GT.1.0) GO TO 217
      GO TO 227
 217  WRITE(6,135)
      GO TO 117
 227  CONTINUE
C
C  CALCULATE RECOVERIES ON EACH SEGMENT FOR EACH TIME INCREMENT DT
C
      DMS(1)=FM*FAREA(1)*DT*SS
      SDMS=DMS(1)
      LS(1)=LS(1)+DMS(1)
      RLS(1)=LS(1)/LMAX
      DO 97 K=1,NS
      J=K+1
      IF(J.GT.NS) GO TO 207
      DMS(J)=(FM-SDMS/DT)*FAREA(J)*DT*SS
      SDMS=SDMS+DMS(J)
      LS(J)=LS(J)+DMS(J)
      RLS(J)=LS(J)/LMAX
 207  L=KS+1
      IF(L.GT.NS) GO TO 97
      IF(RLS(L).LT.0.99) GO TO 97
      KS=KS+1
      FLT(KS)=TT
 97   CONTINUE
      IF(KS.EQ.NS) GO TO 147
      IF(TT.GE.0.999) GO TO 147
C
C  ADJUST CAPTURE RADII FOR NEXT TIME INCREMENT
C
 600  TT=TT+DT
      DO 107 I=1,NS
      IF(RLS(I).LE.CRLS) GO TO 107
      ALPHA=(1-(((RLS(I)*((BMA**2)-1)+1)**0.5)-1)/(BMA-1))
      RC(I)=0.5*ALPHA*VMVF
 107  CONTINUE
      GO TO 78
C
C  SUM MASS RECOVERIES OVER ALL SEGMENTS
C
 147  SLS=0.0
      DO 157 J=1,NS
      SLS=SLS+LS(J)
 157  CONTINUE
      SRLS=SLS/(LMAX*NS)
      PFMR= SLS/FM*100.0
```

```
C
C  PRINT LOADING AND FRACTIONAL LOADING TIMES FOR
C  EACH SEGMENT AND FOR ENTIRE MATRIX
C
      WRITE(6,45)
      WRITE(6,55) FM,VMVF,NS,SS,SM,DIAV,M,RCI
      WRITE(6,65)
      WRITE(6,75)(I,LS(I),RLS(I),FLT(I),I=1,NS)
      WRITE(6,85) SLS,SRLS,PFMR
      WRITE(6,95)
      READ(9,*) NO2
      IF(NO2.EQ.1) GO TO 117
  137 WRITE(6,125)
      READ(9,*) NO3
      IF(NO3.EQ.1) GO TO 1
   45 FORMAT(//////,' ','MATRIX AND FEED CONDITIONS (ALL UNITS CGS,',
     *'TIME DIMENSIONLESS)')
   55 FORMAT(/,9X,'FEED : MASS',F6.1,';  MAG.FLUID VELOCITY',F6.3,
     *//,9X,'MATRIX : NO.SEGMENTS',I4,';  SCREENS/SEG',F3.0,'
     *';  MASS/SCREEN;',F6.2,/,11X,'MATRIX DIA',F5.2,';  NO. ',
     *'TIME INCREMENTS',I4,';  RC INITIAL',F6.4)
   65 FORMAT(' ',///,'RESULTS',/,31X,'MATRIX LOADING',/,5X,'SEGMENT',
     *11X,'MASS(GMS)',12X,'L/LMAX',12X,'TIME(.99)')
   75 FORMAT(' ',5X,I3,12X,E12.4,11X,F6.4,13X,F6.4)
   85 FORMAT(/,5X,'OVERALL',9X,E12.4,11X,F6.4,//,5X,'PERGENT',12X,
     *F6.2)
   95 FORMAT(///,'MORE MATRIX CALCULATIONS?(1=YES,2=NO)')
  105 FORMAT(' ','ENTER FEED MASS,MASS/SCREEN,SCREENS/SEGMENT,',
     *'NO. SEGMENTS,',//,7X,'MATRIX DIAMETER,NO. TIME INCREM',
     *'ENTS')
  115 FORMAT(///,'MATRIX CALCULATIONS?(1=YES,2=NO)')
  125 FORMAT(' ','MORE MODELLING?(1=YES,2=NO)')
  135 FORMAT(/,5X,'SEGMENT SIZE TOO LARGE; CHOOSE FEWER',
     *' SCREENS PER SEGMENT',//)
  127 STOP
      END
*END

*GO
```

Input/Output Hardcopy of MAG6

```
MAG6
*IN PROGRESS

          IGI032I * NULL PROGRAM
MAIN    = 00460C
009340 BYTES USED
EXECUTION BEGINS      5.9S
ENTER PARTICLE DIA,DENSITY,SP.SUSC,SP.MAGN,SHEAR AREA
?
.001 5.25 .000114 1.62 .39
ENTER FIBER DIA,DENSITY,SAT.MAGN,MAG CONSTANT
?
.08 7.75 1472 400
ENTER FLUID VISCOSITY,VELOCITY,DENSITY
?
.01 10 1
ENTER ELLSQ,BACKGROUND FIELD,GRAV CONST,THETA STOP CRITERION
?
3 3000 980 10
```

STATIC HGMS MODEL

EXPERIMENTAL CONDITIONS (ALL UNITS CGS)

PARTICLE : DIA 0.00100; DENSITY 5.25; SP.SUSCEPT 0.1140E-03;
SP.MAGN 0.1620E+01; SHEAR AREA 0.39

FIBER : DIA 0.0800; DENSITY 7.75; SAT.MAGN 1472.0;
MAG.CONSTANT 400.0

FLUID : VISCOSITY 0.01000; VELOCITY 10.0; DENSITY 1.0

FIELD : BACKGROUND 3000.; FIBER 323.; PERTURB TERM 0.8924

INTERLAYER DIST 1.7321 RAD; GRAVITY 980.0; STOP CRITERION 10.0 DEG

RESULTS

LAYER	CRITICAL ANGLES (DEGREES)			RADIUS
	TANGENTIAL	RADIAL	MINIMUM	
1	87.75	75.50	75.50	0.0405
2	86.88	73.56	73.56	0.0414
3	85.92	71.91	71.91	0.0422
4	84.84	70.48	70.48	0.0431
5	83.61	69.21	69.21	0.0440
6	82.18	68.08	68.08	0.0448
7	80.47	67.06	67.06	0.0457
8	78.36	66.13	66.13	0.0466
9	75.59	65.28	65.28	0.0474
10	71.53	64.50	64.50	0.0483
11	63.34	63.78	63.34	0.0492
12	0.00	63.11	0.00	0.0500

LAYER	PARTICLE RECOVERIES(ABS)	
	NUMBER	MASS(GMS)
1	0.61621E+05	0.16939E-03
2	0.61323E+05	0.16857E-03
3	0.61207E+05	0.16825E-03
4	0.61218E+05	0.16828E-03
5	0.61326E+05	0.16858E-03
6	0.61510E+05	0.16908E-03
7	0.61756E+05	0.16976E-03
8	0.62053E+05	0.17058E-03
9	0.62395E+05	0.17152E-03
10	0.62775E+05	0.17256E-03
11	0.62758E+05	0.17251E-03
12	0.66925E+00	0.18397E-08
TOTAL	0.67994E+06	0.18691E-02

```
MATRIX CALCULATIONS?(1=YES,2=NO)
?
1
ENTER FEED MASS,MASS/SCREEN,SCREENS/SEGMENT,NO. SEGMENTS,
      MATRIX DIAMETER,NO. TIME INCREMENTS
?
10 1.42 1 40 3.78 50
```

MATRIX AND FEED CONDITIONS (ALL UNITS CGS,TIME DIMENSIONLESS)

FEED : MASS 10.0; MAG/FLUID VELOCITY 0.146

MATRIX : NO.SEGMENTS 40; SCREENS/SEG 1.; MASS/SCREEN; 1.42
MATRIX DIA 3.78; NO. TIME INCREMENTS 50; RC INITIAL0.0730

RESULTS

	MATRIX LOADING		
SEGMENT	MASS(GMS)	L/LMAX	TIME(.99)
1	0.9760E-01	0.7163	******
2	0.9713E-01	0.7128	******
3	0.9666E-01	0.7093	******
4	0.9618E-01	0.7058	******
5	0.9570E-01	0.7023	******
6	0.9521E-01	0.6987	******
7	0.9472E-01	0.6952	******
8	0.9423E-01	0.6916	******
9	0.9374E-01	0.6879	******
10	0.9324E-01	0.6843	******
11	0.9274E-01	0.6806	******
12	0.9223E-01	0.6769	******
13	0.9173E-01	0.6732	******
14	0.9122E-01	0.6694	******
15	0.9070E-01	0.6656	******
16	0.9019E-01	0.6619	******
17	0.8967E-01	0.6580	******
18	0.8915E-01	0.6542	******
19	0.8862E-01	0.6504	******
20	0.8809E-01	0.6465	******
21	0.8756E-01	0.6426	******
22	0.8703E-01	0.6387	******
23	0.8649E-01	0.6348	******
24	0.8595E-01	0.6308	******
25	0.8541E-01	0.6268	******
26	0.8487E-01	0.6228	******
27	0.8432E-01	0.6188	******
28	0.8378E-01	0.6148	******
29	0.8323E-01	0.6108	******
30	0.8267E-01	0.6067	******
31	0.8212E-01	0.6027	******
32	0.8156E-01	0.5986	******
33	0.8100E-01	0.5945	******
34	0.8044E-01	0.5904	******
35	0.7988E-01	0.5862	******
36	0.7932E-01	0.5821	******
37	0.7875E-01	0.5779	******
38	0.7818E-01	0.5738	******
39	0.7761E-01	0.5696	******
40	0.7704E-01	0.5654	******
OVERALL	0.3506E+01	0.6432	
PERCENT	35.06		

```
MORE MATRIX CALCULATIONS?(1=YES,2=NO)
?
1
ENTER FEED MASS,MASS/SCREEN,SCREENS/SEGMENT,NO. SEGMENTS,
     MATRIX DIAMETER,NO. TIME INCREMENTS
?
30 1.42 1 40 3.78 50


MATRIX AND FEED CONDITIONS (ALL UNITS CGS,TIME DIMENSIONLESS)

        FEED :  MASS  30.0;  MAG/FLUID VELOCITY 0.146

        MATRIX :  NO.SEGMENTS  40;  SCREENS/SEG 1.;  MASS/SCREEN;  1.42
          MATRIX DIA 3.78;  NO. TIME INCREMENTS  50;  RC INITIAL0.0730


RESULTS
                                MATRIX LOADING
    SEGMENT          MASS(GMS)          L/LMAX          TIME(.99)
       1          0.1331E+00          0.9768          ******
       2          0.1330E+00          0.9764          ******
       3          0.1330E+00          0.9760          ******
       4          0.1329E+00          0.9756          ******
       5          0.1329E+00          0.9752          ******
       6          0.1328E+00          0.9748          ******
       7          0.1328E+00          0.9743          ******
       8          0.1327E+00          0.9739          ******
       9          0.1326E+00          0.9734          ******
      10          0.1326E+00          0.9730          ******
      11          0.1325E+00          0.9725          ******
      12          0.1325E+00          0.9721          ******
      13          0.1324E+00          0.9716          ******
      14          0.1323E+00          0.9711          ******
      15          0.1323E+00          0.9706          ******
      16          0.1322E+00          0.9701          ******
      17          0.1321E+00          0.9696          ******
      18          0.1321E+00          0.9691          ******
      19          0.1320E+00          0.9686          ******
      20          0.1319E+00          0.9681          ******
      21          0.1318E+00          0.9675          ******
      22          0.1318E+00          0.9670          ******
      23          0.1317E+00          0.9664          ******
      24          0.1316E+00          0.9659          ******
      25          0.1315E+00          0.9653          ******
      26          0.1315E+00          0.9647          ******
      27          0.1314E+00          0.9641          ******
      28          0.1313E+00          0.9635          ******
      29          0.1312E+00          0.9629          ******
      30          0.1311E+00          0.9623          ******
      31          0.1310E+00          0.9617          ******
      32          0.1310E+00          0.9611          ******
      33          0.1309E+00          0.9604          ******
      34          0.1308E+00          0.9598          ******
      35          0.1307E+00          0.9591          ******
      36          0.1306E+00          0.9584          ******
      37          0.1305E+00          0.9577          ******
      38          0.1304E+00          0.9570          ******
      39          0.1303E+00          0.9563          ******
      40          0.1302E+00          0.9556          ******

    OVERALL       0.5272E+01          0.9672

    PERCENT         17.57
```

```
MORE MATRIX CALCULATIONS?(1=YES,2=NO)
?
1
ENTER FEED MASS,MASS/SCREEN,SCREENS/SEGMENT,NO. SEGMENTS,
      MATRIX DIAMETER,NO. TIME INCREMENTS
?
40 1.42 1 40 3.78 50
```

MATRIX AND FEED CONDITIONS (ALL UNITS CGS,TIME DIMENSIONLESS)

FEED : MASS 40.0; MAG/FLUID VELOCITY 0.146

MATRIX : NO.SEGMENTS 40; SCREENS/SEG 1.; MASS/SCREEN; 1.42
MATRIX DIA 3.78; NO. TIME INCREMENTS 50; RC INITIAL0.0730

RESULTS

	MATRIX LOADING		
SEGMENT	MASS(GMS)	L/LMAX	TIME(.99)
1	0.1354E+00	0.9936	0.9200
2	0.1354E+00	0.9935	0.9200
3	0.1354E+00	0.9934	0.9200
4	0.1353E+00	0.9933	0.9400
5	0.1353E+00	0.9931	0.9400
6	0.1353E+00	0.9930	0.9400
7	0.1353E+00	0.9929	0.9400
8	0.1353E+00	0.9928	0.9400
9	0.1353E+00	0.9926	0.9400
10	0.1352E+00	0.9925	0.9600
11	0.1352E+00	0.9924	0.9600
12	0.1352E+00	0.9923	0.9600
13	0.1352E+00	0.9921	0.9600
14	0.1352E+00	0.9920	0.9600
15	0.1351E+00	0.9918	0.9600
16	0.1351E+00	0.9917	0.9800
17	0.1351E+00	0.9915	0.9800
18	0.1351E+00	0.9914	0.9800
19	0.1351E+00	0.9912	0.9800
20	0.1350E+00	0.9911	0.9800
21	0.1350E+00	0.9909	1.0000
22	0.1350E+00	0.9908	1.0000
23	0.1350E+00	0.9906	1.0000
24	0.1350E+00	0.9904	1.0000
25	0.1349E+00	0.9903	1.0000
26	0.1349E+00	0.9901	1.0000
27	0.1349E+00	0.9899	******
28	0.1349E+00	0.9898	******
29	0.1348E+00	0.9896	******
30	0.1348E+00	0.9894	******
31	0.1348E+00	0.9892	******
32	0.1348E+00	0.9890	******
33	0.1347E+00	0.9888	******
34	0.1347E+00	0.9886	******
35	0.1347E+00	0.9884	******
36	0.1347E+00	0.9882	******
37	0.1346E+00	0.9880	******
38	0.1346E+00	0.9878	******
39	0.1346E+00	0.9876	******
40	0.1345E+00	0.9874	******
OVERALL	0.5401E+01	0.9908	
PERCENT	13.50		

```
MORE MATRIX CALCULATIONS?(1=YES,2=NO)
?
2
MORE MODELLING?(1=YES,2=NO)
?
2
```